

AD-A054 730

TRW DEFENSE AND SPACE SYSTEMS GROUP REDONDO BEACH CALIF F/G 19/4
MEASUREMENTS IN AIRBLAST. PART A. OPTICAL TEMPERATURE MEASUREME--ETC(U)
OCT 77 R DOLL, L GLATT, P LIEBERMAN, P MOLMUD DNA001-77-C-0141

UNCLASSIFIED

TRW-29937-6001-RU-00

DNA-4421F

NL

1 OF 2
AD
A064 730





AD A 054730

MEASUREMENTS IN AIRBLAST

Part A—Optical Temperature Measurement

Part B—Novel Measurement Techniques

TRW Defense and Space Systems Group

One Space Park

Redondo Beach, California 90278

1 October 1977

Final Report for Period 28 February 1977 — 1 October 1977

CONTRACT No. DNA 001-77-C-0141

APPROVED FOR PUBLIC RELEASE;
DISTRIBUTION UNLIMITED.

THIS WORK SPONSORED BY THE DEFENSE NUCLEAR AGENCY
UNDER RDT&E RMSS CODE B344077462 HIICAXSX35501 H2590D.

Prepared for
Director
DEFENSE NUCLEAR AGENCY
Washington, D. C. 20305

DDC
RECEIVED
JUN 7 1978
B

AD-E300 210
12 FOR FURTHER TRAN

DNA 4421F

12

5

12 NOV. 1977
JDC FILE COPY

Destroy this report when it is no longer
needed. Do Not return to sender.



18 DNA, SBIK

UNCLASSIFIED

SECURITY CLASSIFICATION OF THIS PAGE (When Data Entered)

19 REPORT DOCUMENTATION PAGE		READ INSTRUCTIONS BEFORE COMPLETING FORM
1. REPORT NUMBER DNA 4421F AD-15300-210	2. GOVT ACCESSION NO.	3. RECIPIENT'S CATALOG NUMBER
4. TITLE (and Subtitle) MEASUREMENTS IN AIRBLAST Part A: Optical Temperature Measurement Part B: Novel Measurement Techniques		5. TYPE OF REPORT & PERIOD COVERED Final Report for Period 28 Feb 77 - 1 Oct 77
6. AUTHOR(S) R. Doll, P. Molmud L. Glatt, S. Pollack P. Lieberman		7. PERFORMING ORG. REPORT NUMBER TRW-29937-6001-RU-00
8. CONTRACT OR GRANT NUMBER(s)		9. PROGRAM ELEMENT, PROJECT, TASK AREA & WORK UNIT NUMBERS DNA 001-77-C-0141
10. PERFORMING ORGANIZATION NAME AND ADDRESS TRW Defense and Space Systems Group One Space Park Redondo Beach, California 90278		11. REPORT DATE 1 Oct 1977
12. CONTROLLING OFFICE NAME AND ADDRESS Director Defense Nuclear Agency Washington, D.C. 20305		13. NUMBER OF PAGES 176
14. MONITORING AGENCY NAME & ADDRESS (if different from Controlling Office) 12 175p.		15. SECURITY CLASS (of this report) UNCLASSIFIED
16. DISTRIBUTION STATEMENT (of this Report) Approved for public release; distribution unlimited.		15a. DECLASSIFICATION/DOWNGRADING SCHEDULE
17. DISTRIBUTION STATEMENT (of the abstract entered in Block 20, if different from Report)		
18. SUPPLEMENTARY NOTES This work sponsored by the Defense Nuclear Agency under RDT&E RMSS Code B344077462 HIICAXSX35501 H2590D.		
19. KEY WORDS (Continue on reverse side if necessary and identify by block number) Airblast Black Body Radiation Gas Species Neon Bag Method Optical Pyrometer Radioisotope Method Temperature Measurement Areal Density Measurement		
20. ABSTRACT (Continue on reverse side if necessary and identify by block number) Part A: Optical Temperature Measurement The measurement of temperatures generated in extreme explosive environments presents considerable experimental difficulties. The fact that these events take place over such a short duration and at high pressures and temperatures makes conventional temperature measuring methods ineffective. (over)		

DD FORM 1 JAN 73 1473 EDITION OF 1 NOV 65 IS OBSOLETE

UNCLASSIFIED

SECURITY CLASSIFICATION OF THIS PAGE (When Data Entered)

409 637

1/B

UNCLASSIFIED

SECURITY CLASSIFICATION OF THIS PAGE(When Data Entered)

20. ABSTRACT (Continued)

Optical methods possess the unique advantage of permitting temperature measurements without disturbing the shock front or combustion process and exhibit the quick response time necessary to obtain temperature histories. The optical measurement of gas species requires careful analysis so that measurements are made at wavelengths corresponding to emissions of substances normally found in the shock front or in the combustion products.

This study develops the theoretical background for choosing the correct wavelengths at a temperature range of interest. One and two color pyrometer theory is developed. Design and construction details are presented which outline the step-by-step procedures necessary to field a five channel optical temperature measurement system. Experimental results obtained from the DABS II-D tests are analyzed and compared with theoretical results. Problem areas associated with fielding the system are discussed along with recommended design improvements.

The test results presented clearly indicate the feasibility of using one and two color pyrometers for effectively measuring the temperature-histories for an explosively developed airblast shock front.

Part B: Novel Measurement Techniques

The deployment of instrumentation in a nuclear driven shock tunnel presents some very unique problems associated with this hostile environment. This study investigates the feasibility of two conceptual techniques to measure the density and temperature history of the shocked air along with a density history of any lofted debris entrained within the air shock.

The first technique is a gas bag and pyrometer experiment which is actually a method for providing a clean window into the air shock so that passive optical pyrometer equipment can be used to measure temperatures within the shock wave. The second technique is a radioisotope source method which uses two or more different frequency radioactive X-ray sources to measure areal density histories and tunnel wall translational displacement. The study shows that both techniques are clearly feasible from consideration of the basic physics concepts involved.

The study did not address the problem of hardware design solutions necessary for fielding these experiments, but outlines a series of study programs that should be conducted to answer the design questions that establish the high degree of confidence necessary for a successful program.

ACCESSION NO.	
NTIS	WHS Section <input checked="" type="checkbox"/>
DOC	Ext Section <input type="checkbox"/>
UNCLASSIFIED	<input type="checkbox"/>
JUSTIFICATION	
DISTRIBUTION/AVAILABILITY CODES	
Dist.	AVAIL. and/or SPECIAL
A	

UNCLASSIFIED

SECURITY CLASSIFICATION OF THIS PAGE(When Data Entered)

SUMMARY

PART A - OPTICAL TEMPERATURE MEASUREMENT

This study develops the theoretical background necessary for selecting the correct spectral intervals for one color and two color optical pyrometers used to determine the temperature history of explosively generated airblast environments.

To implement this theory a five channel optical pyrometer was designed, calibrated and tested. The design considerations separated into three different disciplines: mechanical installation, electronic signal amplification and optical design. The system consisted of two ultraviolet channels at 0.26μ and 0.36μ wavelengths to measure the high temperature airblast and three infrared channels at 1.9μ , 2.9μ , and 4.5μ wavelengths to measure the later arriving lower temperature combustion products.

In addition to the primary temperature history results, ancillary data on mean shock front velocity, estimate for depth of optical penetration of the radiometers and verification that the shock wave had an irregular front boundary were obtained. The primary results show good agreement of measured temperatures with expected temperatures. The two Hugoniot temperatures, computed from the predicted peak pressures of ~ 83 atmospheres (1225 psia) and from the "smoothed" value of recorded peak pressure of ~ 67 atmospheres extrapolated from downstream data, completely bound the measured radiation temperature histories. These measured temperatures suggest that the ratio of specific heats (γ) strongly effects the calculation of airblast temperatures. Hugoniot calculation at the above two pressures is sensitive to variations of γ , thus the choice of γ will impact the interpretation of test results. The results show that the often used $\gamma = 1.3$ mean specific heat ratio for pressure calculations at the shock front also is in reasonably good agreement with temperature test results for shock front pressures in the ~ 1300 psia to ~ 900 psia range.

Combustion product temperature information was not obtained due to electrical noise interference on the three infrared channels. The only data that could be verified was the 0.8 msec predicted arrival time for combustion products. The ultraviolet channels showed a steep drop in signal in the 0.8 to 1.0 msec range indicating the arrival of combustion products.

Conclusions from the DABS test can be summarized as follows:

- Successful operation of the ultraviolet and infrared channels was demonstrated in the field.
- Air shock temperature data was accurately measured by ultraviolet pyrometers and correlated with theoretical predictions
- The mechanical design of the open port installation provided protection against damage from the shock wave.

The main recommendation for improved performance is to redesign the electronic packaging to preclude any electronic noise interference with the infrared channels. The second recommendation would be for an overall package size reduction. This would be accomplished by providing for an optically transparent window, instead of the existing open port design, which would allow for a considerable size reduction and simplification of installation, calibration and operation.

PART B - NOVEL MEASUREMENT TECHNIQUES

This part of the study effort discusses the concept of deploying special techniques to measure the density and temperature histories within the interior of a nuclear driven shock tunnel. The extremely hostile environment makes conventional instrumentation ineffective. The implementation of any novel technique must first be based on sound physical principles, and secondly must lend itself to practical hardware design solutions. This study addresses the former question by presenting a feasibility analysis of the proposed two techniques. The latter question while not specifically studied, is addressed by listing a series of suggested areas of further study. In this later section, special design problems are identified.

The first technique discussed is the gas bag and pyrometer experiment for measuring the temperature inside the shock wave as it passes the observation station. The gas bag is a device which provides an optical "window" into the measured media so that passive optical pyrometer systems can be used to obtain temperature histories.

The second technique uses a radioisotope source in an active X-ray system in conjunction with a detector system to provide a measure of the areal density in the path of observation. Here, because areal density measurement will depend on the distance between source and detector, multi-frequency X-ray or γ -ray sources must be used which also will measure radial displacement of the tunnel walls.

The feasibility analysis presented in this study shows that the physical basis for each of these two concepts is sound and should provide the desired information. The study shows that the gas bag technique can work with the candidate cooled neon gas ($\sim 220^\circ\text{K}$). The radioisotope source method should give good results using two radioactive sources, one of Cobalt - 60 and the other of Ytterbium - 169. Analyses of the data provided by these two sources can yield histories of both areal density and radial displacement of the tunnel walls. There also is hope of using an additional Yb ¹⁶⁹ radioisotope X-ray emission frequency to separate areal densities owing to lofted debris from that of the shock compressed air.

Future study areas needed to evaluate both techniques are presented so that hardware design solutions can be evaluated and establish a high degree of confidence in the program.

PREFACE

Preparation of this report "Measurements in Airblast, Part A - Optical Temperature Measurement, Part B - Novel Measurement Techniques" was supported by the Defense Nuclear Agency under Contract No. DNA 001-77-C-0141, Program Element NWE 62710H, Project H11CAXS, Task Code X355 and work unit code 01 during the period 28 February 1977 through 1 October 1977.

TRW Systems Group is grateful to the University of New Mexico's CERF organization for providing facilities, to DABS test manager Mr. Oscar Hopkins for his cooperation and assistance, to Captain Dan Martens of AFWL for his support, to Messrs. Joe Renick and Joe Quintana of the AFWL for providing test results, and to the DNA program monitor Tom Kennedy for his support.

The authors also acknowledge the contributions of Mr. Charles Wood for his technical support in the field. To Messrs. Pat O'Neil, Ed Burchman, Bill Tierney, and Al Gibbs for their effort in the design, construction and checkout of the optical detector and associated electronics, to Ms. Jean Dorler and to Ms. Lore Agneessens for typing this manuscript.

TABLE OF CONTENTS

PART A - OPTICAL TEMPERATURE MEASUREMENT

1.0	INTRODUCTION	13
1.1	Objective	13
1.2	Background	13
1.3	Measurement Environment	14
1.3.1	Predicted Station Temperature and Pressure Values	18
2.0	THEORY	23
2.1	Spectral Region Selection Criteria for Optically Thick Gas Volumes	24
2.2	Spectral Region Selection	27
2.3	One and Two Color Pyrometer Systems	27
2.3.1	One Color Pyrometer Systems	28
2.3.2	Two Color Pyrometer Systems	28
2.4	Selected Wavelength Intervals for Two Color Pyrometers	29
2.4.1	Wavelength Selections for Shock Heated Air	29
2.4.2	Wavelength Selections for 4% CO ₂ Added to Air [DABS II-D-1]	30
2.4.3	Wavelength Selection for the Combustion Products	31
2.4.4	Summary of Wavelength and Pyrometer (Radiometer Pair) Selections	32
2.5	Information Presented in Appendices	35
2.5.1	Presentation of Radiating Species Information	35
2.5.2	Presentation of Opacity Data	35
3.0	OPTICAL SYSTEM PARAMETERS FOR THE DABS II-D-2 TEST	37
3.1	Radiometer Output Signals	43
4.0	ELECTRICAL SYSTEM FOR DABS II-D-2 TEST	45
4.1	Photovoltaic Circuit	45
4.2	Photoconducting Circuit	45
5.0	MECHANICAL INSTALLATION FOR DABS II-D-2 TEST	48
6.0	ANALYSIS OF THE DABS II-D-2 TEST DATA	53
6.1	Primary Results: Temperature Histories	53
6.1.1	Detailed Discussion of DABS II-D-2 Results	63
6.1.2	Comparison of Measures with Theoretical Temperatures	67
6.2	Secondary Results	69
6.2.1	Mean Shock Front Velocity	69

6.2.2	Lag Time Between the Two Ultraviolet Radiometers	71
6.2.3	Radiometer Signal Rise Times	73
7.0	CONCLUSIONS	75
8.0	RECOMMENDATIONS	76
8.1	Identification of Problem Areas	76
8.1.1	Electrical Interference on Infrared Channels	76
8.1.2	Optical Parallax	76
8.1.3	Optical Alignment	79
8.1.4	Electronic Packaging	79
8.2	Recommended Hardware Improvements	79
	BIBLIOGRAPHY	80
	APPENDIX A BLACK BODY RADIATION THEORY	81
A.1	Optimum Spectral Regions for Temperature Determinations	84
A.2	Wien's Law and Rayleigh-Jeans Law Approximations for Black Body Radiation Expressions	84
A.3	Error Analysis for "One Color" Radiometric Temperature Determination	85
A.4	Two Color Pyrometer Systems	87
A.5	Applicability of "Two Color Pyrometer" Techniques	87
A.6	Error Analysis for "Two Color" Pyrometer System	92
	APPENDIX B A BRIEF INTRODUCTION TO NOMENCLATURE OF MOLECULAR BAND SYSTEMS	99
B.1	Infrared Vibration Bands for Polyatomic Molecules	100
	APPENDIX C A BRIEF INTRODUCTION TO SOME RELEVANT SPECTRAL PARAMETERS	103
C.1	The Relation Between Absorption Cross Sections and Absorption Coefficients	103
C.2	Spectral Line Contour and Line Density Considerations	104
	APPENDIX D CONCENTRATIONS AND SPECTRAL DATA FOR RADIATING SPECIES MOLECULES	111
D.1	Radiating Species for Shock Heated Air	112
D.1.1	O_2 (S-R), NO (β) and NO (γ) Radiation	116
D.1.2	Free Electron [$e^-(ff)$] Radiation	119
D.1.3	Infrared Radiation from CO_2 and H_2O	120
D.1.3.1	Infrared Radiation from Air + 4% CO_2	121
D.2	Infrared Radiation from Combustion Products	122

APPENDIX E RESULTS OF OPACITY COMPUTATIONS	123
E.1 Air Species	123
E.2 Air + 4% CO ₂	129
E.3 Combustion Products	135
E.3.1 Carbon Soot	135
NOMENCLATURE	140

PART B - NOVEL DENSITY MEASUREMENT TECHNIQUES

1.0	INTRODUCTION	147
1.1	Objectives	147
1.2	Background	147
1.3	Proposed Techniques	148
1.3.1	The Gas Bag and Pyrometer Technique	148
1.3.2	Radioisotope Source Technique	149
1.4	Conceptual Feasibility	149
2.0	THEORY: A BRIEF OVERVIEW	150
2.1	Gas Bag and Pyrometer Experiment	150
2.2	Radioisotope Source Experiment	152
3.0	FEASIBILITY ANALYSIS	154
3.1	Gas Bag and Pyrometer Feasibility	154
3.2	Radioisotope Source System Feasibility	162
3.2.1	Reduction of Radioisotope Source Data	162
4.0	SUGGESTED AREA FOR FURTHER STUDY	168
4.1	Study Areas Associated With Gas Bag Pyrometer Experiment	168
4.1.1	Preheating of Downstream Air	168
4.1.2	Demonstration of Interface Matching	168
4.1.3	Determination of Optimum "Gas Bag" Material	168
4.1.4	Chemical Interaction of Vaporized Gas Bag and Air Shock Front	168
4.2	Study Areas Associated With The Radioisotope Source Experiment	169
4.2.1	Determination of Fraction of Lofted Material Entrained in the Air	169
4.2.2	Selection of Detector Study	169
4.2.3	Design Study to Narrow the Emittance And Acceptance Solid Angles	170
4.2.4	Study of Source and Detector Survivability	170
	BIBLIOGRAPHY	171

LIST OF ILLUSTRATIONS

PART A - OPTICAL TEMPERATURE MEASUREMENT

1-1	Pressure and Temperature Relations for Airblast	16
1-2	Pressure and Temperature Relations for Combustion Products	17
1-3	Predicted Shock Front Pressure and Arrival Times as a Function of Distance From the Explosive for DABS II-D	20
1-4	Predicted Temperatures as a Function of Distance from the Explosive for DABS II-D	21
2-1	DABS II-D Instrumentation Summary	33
2-2	DABS II-D-2 Instrumentation Summary	34
3-1	Schematic of Lens Occlusion Loss Through Circular Port Aperture	38
3-2	Transmittance Curves for the Five DABS II-D-2 Filters	39
4-1	Schematic of Optical Pyrometer Electronics	46
5-1	Schematic of Mechanical Installation	49
5-2	Photographs of Instrumentation Used to Measure Temperature History Data	50
6-1	DABS II-D-2 Experimental Results for Both One Color and Two Color Pyrometers	54
6-2	DABS II-D-2 Ultraviolet Radiometer Signal Tracings	55
6-3	Two Color Pyrometer Calibration Curve for the Ultraviolet Radiometers	61
6-4	One Color Pyrometer Calibration Curves for the Ultraviolet Radiometers	62
6-5	Variations in Theoretical Results as a Function of Gas Constant (γ) for Two Pressure Ranges of Interest	64
6-6	Delay of DABS II-D-2 Optical Signals With Respect to Fiduciary Pulse	70
6-7	Relating Lag Time Between Arrivals of the Two DABS II-D-2 Ultraviolet Radiometer Signals	72
6-8	Electronic System Response to a Fast (1 μ sec) Calibration Pulse	74
8-1	Pre-Test Optical Calibration Curves Recorded at the DABS-D-2 Site	77
8-2	Electrical Noise Recorded on Typical Infrared Channel During the DABS II-D-2 Test	78
A-1	Wavelength Dependence of Black Body Spectral Radiance	83
A-2	Error Reduction Factor for One Color Pyrometer	88
A-3	Black Body Spectral Radiance for Selected Wavelengths λ_1 and Wavelength Intervals, $\Delta\lambda_1$	89
A-4	Temperature Signals for Two Color Radiometers	90
A-5	Two Color Pyrometer Error Attenuation Factor (Equation A.19a): for Random Measurement Errors	95
A-6	Two Color Pyrometer Error Factor (Equation A.16b): For Systematic Measurement Errors of the Same Sign	96
A-7	Two Color Pyrometer Error Attenuation Factor (Equation A.19c): For Systematic Measurement Errors of Opposite Sign	97

C-1	Mean Spectral Line Densities for CO ₂ , CO, and H ₂ O in Selected Spectral Intervals	106
C-2	Pressure Broadened "Spectral Line" Half-Width, γ , for H ₂ O and CO ₂ in the Combustion Products, and for CO ₂ and for CO in 4% CO ₂ Added to Air	107
C-3	Spectral Line Profiles and Resultant Emission (Or Absorption) Patterns	108
D-1	Mole-Fractions in Dry Air at 10 Atmospheres	113
D-2	Spectral Distribution Curves Related to the Sun; Shaded Areas Indicate Absorption, At Sea Level, Due to the Atmospheric Constituents Shown	114
D-3	Comparison of the Near-Infrared Solar Spectrum with Laboratory Spectra of Various Atmospheric Gases	115
D-4	Spectral Intensity as a Function of Density Ratio	117
E-1	Temperature-Pressure Dependence of Mole Fractions in Air	124
E-2	Computed Absorption Coefficients for Air Molecules in the Near Ultraviolet and Violet Spectral Region	126
E-3	Mean Absorption Coefficient for N ₂ (Second Positive) and N ₂ ⁺ (First Negative) Band Structure	127
E-4	Computed Optical Thickness, τ , for Air at 0.26 μ and 0.36 μ Wavelengths	128
E-5	Mole-Fractions of CO ₂ and CO When 4% CO ₂ Added to Air	130
E-6	Spectral Absorption Coefficients (Smoothed), in Selected Spectral Intervals, for CO ₂ , CO and H ₂ O	131
E-7	Computed Optical Thickness Near 2.8 μ Wavelength for 4% CO ₂ in Air	132
E-8	Computed Optical Thickness for 4% CO ₂ Added to Air - 4.5 μ CO ₂ + CO Absorption Region	133
E-9	Computed Optical Thickness at 0.26 μ and at 4.5 μ for 4% CO ₂ Added to Air	134
E-10	Combustion Products Curves	136
E-11	Empirical (Mass-Density) Spectral Absorption Coefficients for Carbon Soot	137
E-12	Computed Optical Thickness, τ_c , of Carbon Partical Soot Carried by Combustion Gases	139

LIST OF ILLUSTRATIONS

PART B - NOVEL MEASUREMENT TECHNIQUES

2-1	Schematic of a Test Arrangement for the Gas Bag and Optical Pyrometer Experiment	151
2-2	Schematic of Proposed Radioisotope Source Experiment	152
3-1	Downstream Pressure for Moving Normal Shock, Upstream Temperature = 300°K, Upstream Pressure = 1 Atmosphere	156
3-2	Downstream Temperature for Moving Normal Shock. Upstream Temperature = 300°K, Upstream Pressure = 1 Atmosphere	157
3-3	Downstream Electron Density for Moving Normal Shock, Upstream Temperature = 300°K, Upstream Pressure = 1 Atmosphere	158
3-4	Downstream Pressure for Moving Normal Shock, Upstream Temperature = 300°K for Air; 232°K for Neon, Upstream Pressure = 1 Atmosphere	159
3-5	Downstream Temperature for Moving Normal Shock, Upstream Temperature = 300°K for Air; 232°K for Neon, Upstream Pressure = 1 Atmosphere	160
3-6	Downstream Electron Density for Moving Normal Shock, Upstream Temperature = 300°K for Air; 232°K for Neon, Upstream Pressure = 1 Atmosphere	161

LIST OF TABLES

PART A - OPTICAL TEMPERATURE MEASUREMENT

1-1	Predicted Station Parameters	22
4-1	Tabulated Expected Electrical Signal Range for Predicted Shock Tunnel Temperatures	47
A-1	Pyrometric Error Factor E(X) for One Color Pyrometer	86
D-1	Normal Composition of Clean, Dry Atmospheric Air Near Sea Level	111

PART B - NOVEL MEASUREMENT TECHNIQUES

3-1	P, Fractional Error in Areal Mass Determination as Functions of Areal Mass. (Using 100 Curie Sources of Co^{60} and Yb^{169} With 10 cm^2 Detectors and Time Resolution of 10^{-5}Sec)	155
4-1	Photon Emissions From Yb^{169} with Associated Absorption Coefficients of Si, N_2 or O_2 , and Al	169

PART A
OPTICAL TEMPERATURE MEASUREMENT

1. INTRODUCTION

1.1 Objective

The objective of this program was to demonstrate the practical application of using optical radiometers for measuring airblast temperatures. The dynamic airblast simulator (DABS) test series uses a high explosive charge to generate the shockwave. A airblast produced in this manner has three fundamental structural components of interest:

- Shock compressed air
- Combustion product gases
- Combustion product gases plus soot generated by explosives

Temperature measurements from all three regions are of prime interest in this program.

The theoretical background necessary for determining the proper wavelength selection is presented. A system required to measure these three regions must include both ultra-violet and infrared wavelengths. In addition the design, development and calibration as it relates to the fielding of the portable system is outlined. The three disciplines which encompass this phase of the program were mechanical installation, optical design, and electronic amplification of detector signal. Problems associated with each phase of these design parameters is discussed in the body of this report.

1.2 Background

During discussions with DNA/SPSS and AFWL/DED it was decided that new instrumentation systems should be developed to support the upcoming DABS II/HAVE HOST field tests. These two test series are in support of the MX full scale development program. HAVE HOST involves the interior and exterior air blast loading of scale model trench/shelter structures for MX concept validation, while the DABS II test series developed the phenomenology needed to simulate the dynamic air blast nuclear environment for MX related external structural loading. In particular for the DABS II test, there is a need to measure flow properties associated with the measured dynamic pressure wavefront anomalies. Thus, air blast patterns over the target area need to be determined along with temperature history at various ranges.

During the course of this program the cross-sectional dimension of the facility had been changed from a 0.191m.(3 ft.) diameter tube to the present configuration described below. Since much of the theoretical development was based on the smaller diameter test facility, and extrapolated to the larger configuration, this report will make a clear distinction between the two DABS II-D configurations by adding a -1 or -2 designation to the primary callout.

The final AFWL DABS II-D [1] (TRW DABS II-D-2) configuration consisted of an open ended trench with parallel concrete walls 1.83m (6 ft.) high and compacted soil floor 4.27m. (14 ft.) wide. The facility was inclosed with a prismatic roof 1.07m. (3.5 ft.) high from top of concrete wall to roof peak. The whole roof structure was covered with a sand overburden. The facility measured 36.2m. (119 ft.) long, with a steel reinforced concrete driver section at the closed end. This section contained the explosive charge which was distributed over 71% of the rear wall cross-sectional area. A TNT sensitized ammonium nitrate castable slurry explosive called IRETOL 30T22-C was used to generate the shockwave. The total weight of explosive was 823.7 kg. (1816 lbs.). This charge, when detonated, produced a planer airblast wave front which propagates down the length of the facility at a peak initial pressure of ~163 atmospheres (2400 psia).

The temperature at a given station of the airblast shock front can be calculated with good accuracy, based on either shock front velocity or shock front pressure measurements using the Rankine-Hugoniot relationship. The temperature in the airblast after passage geometry, and the multi-dimensional effects of the surrounding wall boundaries interacting with the shock front and the following high speed airflow. Recent advancements in computational modeling include the influence of mass addition and wall expansion effects on calculated temperature history.

Combustion products temperature history can be calculated based upon isentropic expansion from the explosive driver's Chapman-Jouguet detonation point. Results calculated from this relationship can vary since some of the explosives driving the air shock do not completely detonate and continue burning downstream of the detonation point. In addition, some of the gaseous chemical species are not in equilibrium at each pressure and temperature state during the available residence time within the shock tunnel. Further complications are present because the DABS II-D explosive had additives that result in fine particles of soot mixing with the combustion products. These fine particles must be considered in designing any temperature measurement system.

All these factors introduce uncertainty into the temperature calculation. This calculation is important, since a significant of the blast environment around a target is obtained by interaction with combustion product gases.

1.3 Measurement Environment

The measurement environment consists of air, chemical species and soot at continuously varying pressure and temperature states. The airblast peak pressure is established by the weight of explosives, explosive type, distance from explosive, and the length to diameter ratio of the shock tunnel as defined in section 1.2. For the DABS/HAVE HOST test series the airblast pressures of interest range from ~163 to ~41 standard atmospheres

(2400 to 500 psia). The corresponding time to half-pressure can be as small as 1 millisecond with times to zero-pressure from 5 to 10 milliseconds.

Any ideal airblast shock front can be represented by the Rankine-Hugoniot relationship

$$\frac{T_s}{T_1} = \frac{\left[\frac{P_s}{P_1} + \frac{\gamma + 1}{\gamma - 1} \right] \frac{P_s}{P_1}}{1 + \left[\frac{\gamma + 1}{\gamma - 1} \right] \frac{P_s}{P_1}} \quad (1.1)$$

The dashed line in Figure 1-1 represents this equation for a range of peak pressure (P_s) airblast shock fronts. The solid line curves branching off from the Rankine-Hugoniot curve represent the isentropic expansion of the gases as defined by

$$\frac{T_i}{T_s} = \left(\frac{P_i}{P_s} \right)^{\frac{\gamma - 1}{\gamma}} \quad (1.2)$$

For large pressure changes the isentropic expansion results in corresponding small changes in temperature. For example, note that for 200 atmosphere shock front pressures, the temperature is almost 1 ev (one electron volt = 11,604.9 °K). After severe isentropic expansion to a 75 percent reduction in shock pressure, the temperature only drops by 33 percent.

The combustion process is controlled by the Chapman-Jouguet detonation point ($P_{C-J} = 24,000$ ATM, $T_{C-J} = 2500$ °K). These combustion gases initially arrive with the contact surface after the pressure has fallen from its shock front pressure. For the case where the pressure at the shock front is 200 atmospheres, the combustion products may arrive at 100 atmospheres. This represents an isentropic expansion of the combustion gases from the Chapman-Jouguet state of 24,000 atmospheres to a contact surface pressure of 100 atmospheres. Moreover, the value of γ is unknown, but is in the range of 1.20 to 1.35 [2], and strongly influences the isentropic expansion. Figure 1-2 summarizes contact surface pressure and temperature combinations for isentropic expansion from the Chapman-Jouguet point for different values of γ . If the combustion products consist mostly of water vapor and nitrogen gases ($\gamma = 1.25$), the predicted lower bound contact surface temperatures, neglecting afterburning, stay below ~900 °K for pressures below ~150 atmospheres.

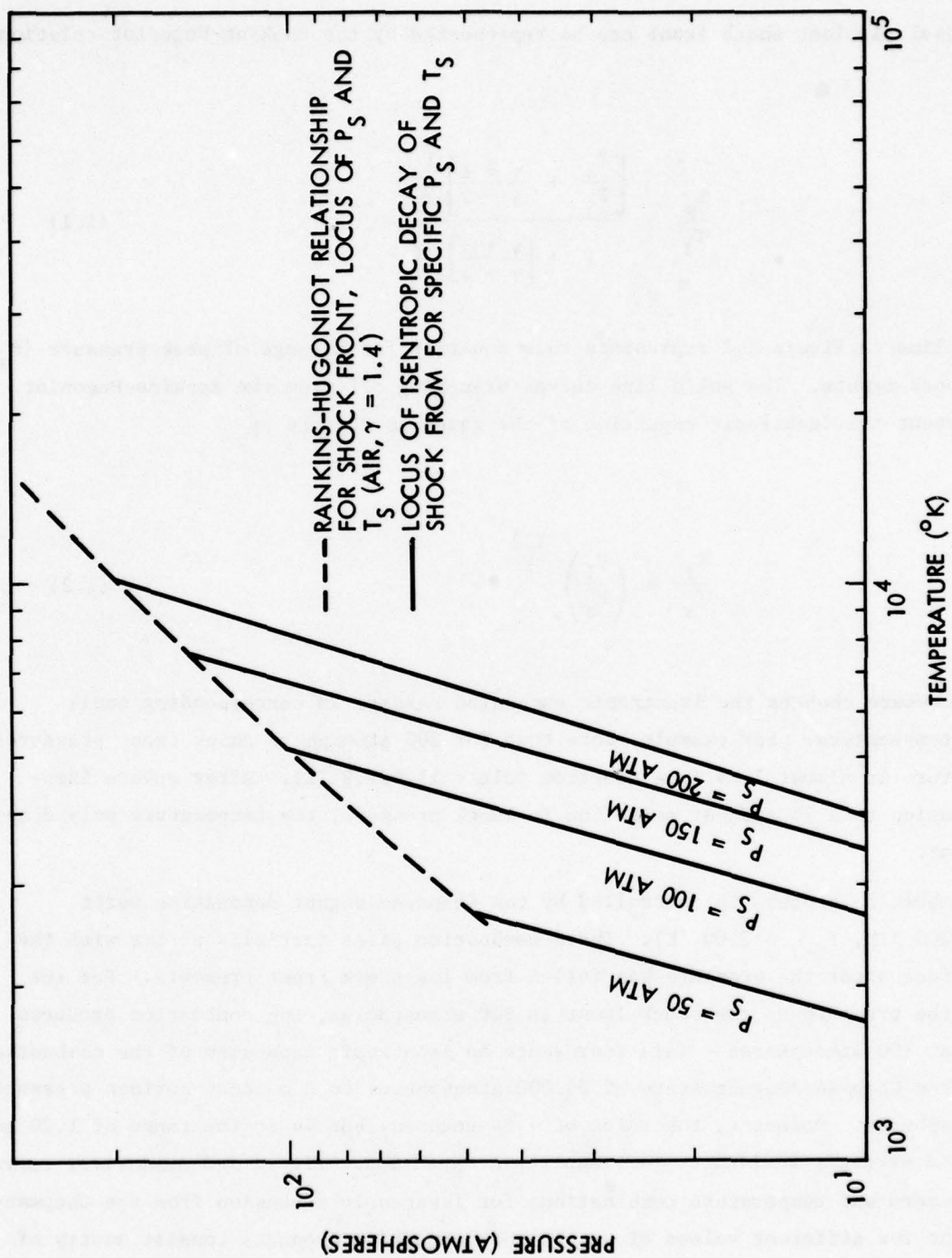


Figure 1-1. Pressure and Temperature Relations for Airblast

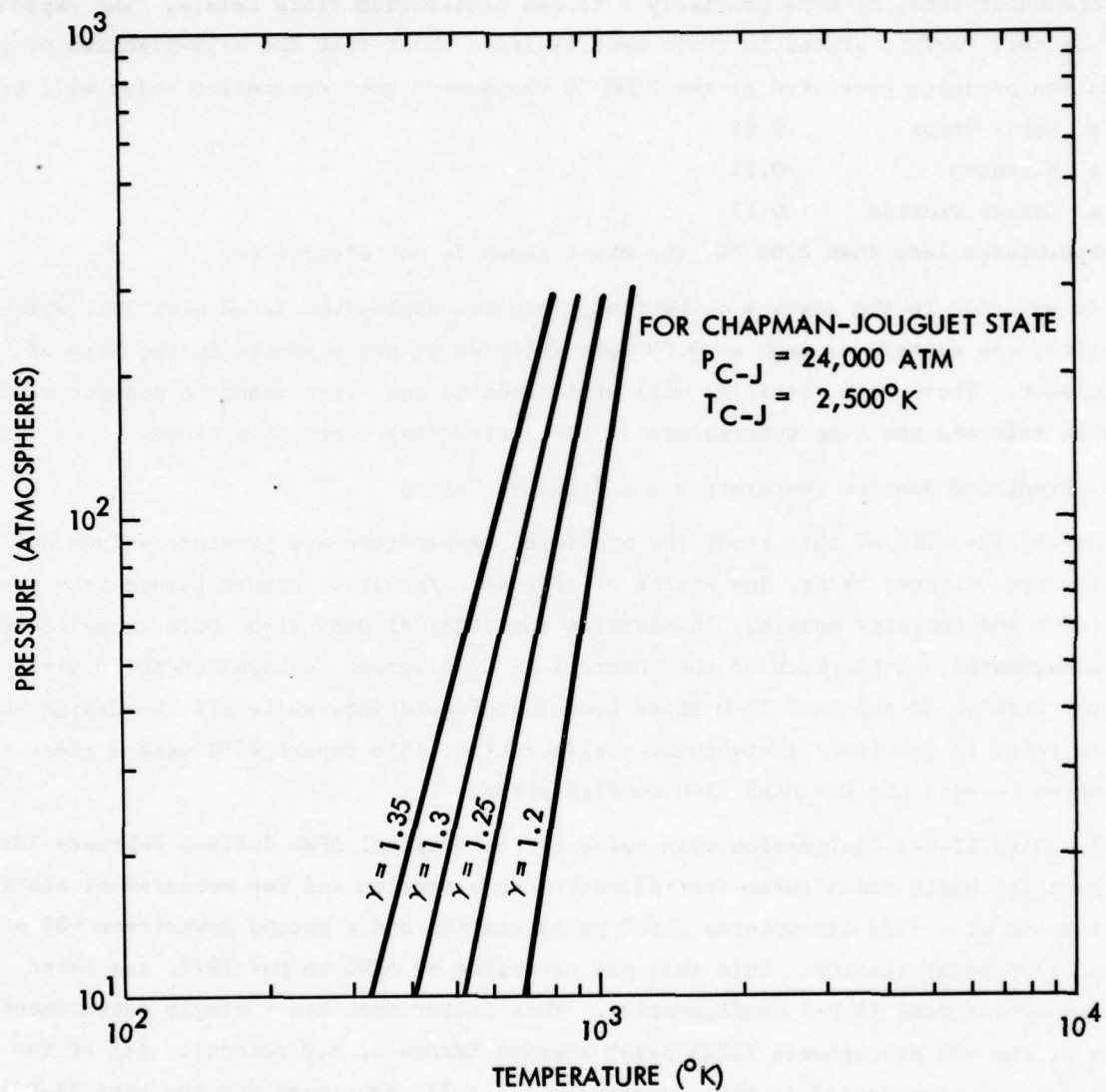


Figure 1-2. Pressure and Temperature Relations for Combustion Products

With the pressure and temperature limits of interest defined, additional information relating to the combustion constituents must be defined for radiometer spectral windows corresponding to black body radiation. Because of the time scale involved it is assumed that the chemical components created at detonation will be the same constituents propagated down the shock tube, or more precisely a frozen equilibrium state exists. The explosive manufacturer, IRETOL, states in their specification sheet that the mole-fraction of gaseous combustion products generated at the 2500 °K Chapman-Jouguet detonation point will be:

- Water Vapor 0.64
- Nitrogen 0.22
- Carbon Dioxide 0.13

At temperatures less than 2500 °K, the above gases do not dissociate.

In addition to the gaseous combustion products, explosives laced with TNT, which are fuel-rich, can contain as much as 0.03 mole-fraction of gas products in the form of carbon soot. These soot particles will arrive behind the air-combustion contact surface and will maintain the same temperature of the surrounding combustion gases.

1.3.1 Predicted Station Temperature and Pressure Values

During the life of this study the predicted temperature and pressure values had continually been updated by Mr. Joe Renick of AFWL as a result of data obtained from previous DABS tests and computer models. In addition the original DABS II-D shock tunnel configuration was updated. Since much of the theoretical development is based on the 0.91m. diameter version of the DABS II-D shock tunnel configuration, while all the design and test results refer to the final rectangular configuration, this report will make a clear distinction between the two DABS II-D configurations.

The DABS II-D-1 designation will refer to the original AFWL defined February 1977 configuration which had a three-foot diameter cross section and two measurement stations, one close-in at a ~122 atmospheres (1800 psia) station and a second downstream ~81 atmospheres (1200 psia) station. This shot was cancelled by AFWL in May 1977, and later replaced by the DABS II-D-2 configuration. This latter shot had a single measurement system at the ~83 atmospheres (1225 psia) station (range of 8.2 meters). All of the theoretical work presented in this report was initially developed for the DABS II-D-1 configuration, but is readily transferable to DABS II-D-2. Since the same explosive was planned for both shots, the temperature and pressure domain of the latter is completely within that predicted from the former. Originally two optical temperature measurement stations were planned for this DABS II-D-1 shot, corresponding to initial shock front arrival pressures of ~122 and 81 atmospheres (1800 and 1200 psia). Owing to the short

procurement time, existing DABS II-D-1 hardware had to be utilized for the DABS II-D-2 shot. This compromise situation only allowed for the fielding of a single station corresponding to a shock front arrival pressure of ~83 atmospheres (1225 psia).

For the original DABS II-D-1 shot the close-in station 1 was primarily for measuring combustion products while the further downstream station 2, which provided a longer duration between shock front arrival and contact surface arrival, would provide a clearer picture of airblast temperatures. This can be clearly seen in Figure 1-3 where shock front and contact surface arrival times are plotted with respect to range. The DABS II-D-2 location is situated near the original DABS II-D-1 station 2 location, thus providing a time duration of sufficient length to clearly record the airblast temperature, and with the remaining recording time to measure the combustion product temperatures.

Figure 1-4 presents TRW-predicted temperatures for the shocked air front at range dependent initial pressures, P_s , and after a isentropic pressure decay to $0.5 P_s$. It is assumed that the airblast combustion gases contact surface will pass the stations approximately when the pressure drops to $0.5 P_s$; there will be a pressure continuity, but with a sharp drop in temperature. Owing to afterburning, it is futile to attempt to predict temperatures of combustion products in the close range portion, thus the discontinuation of the combustion product curves at 15 meters in Figure 1-4. The only statement that can be made is to say that the expansion of the gases should ensure temperatures lower than the 2500 °K Chapman-Jouguet detonation point temperature. At the longer range, approximately 15 meters, the lower bound temperature computed for the assumption of no afterburning is shown for the combustion gases.

Table 1.1 gives intervals of pressure, temperature and time for stations 1 and 2 of DABS II-D-1 and the DABS II-D-2 station. The δt parameter is the predicted time interval between station arrivals of the shocked air front and the combustion gases contact surface. The equipment was designed to survive and record useful data for a total of 5 to 6 milliseconds from the onset of the shocked air front.

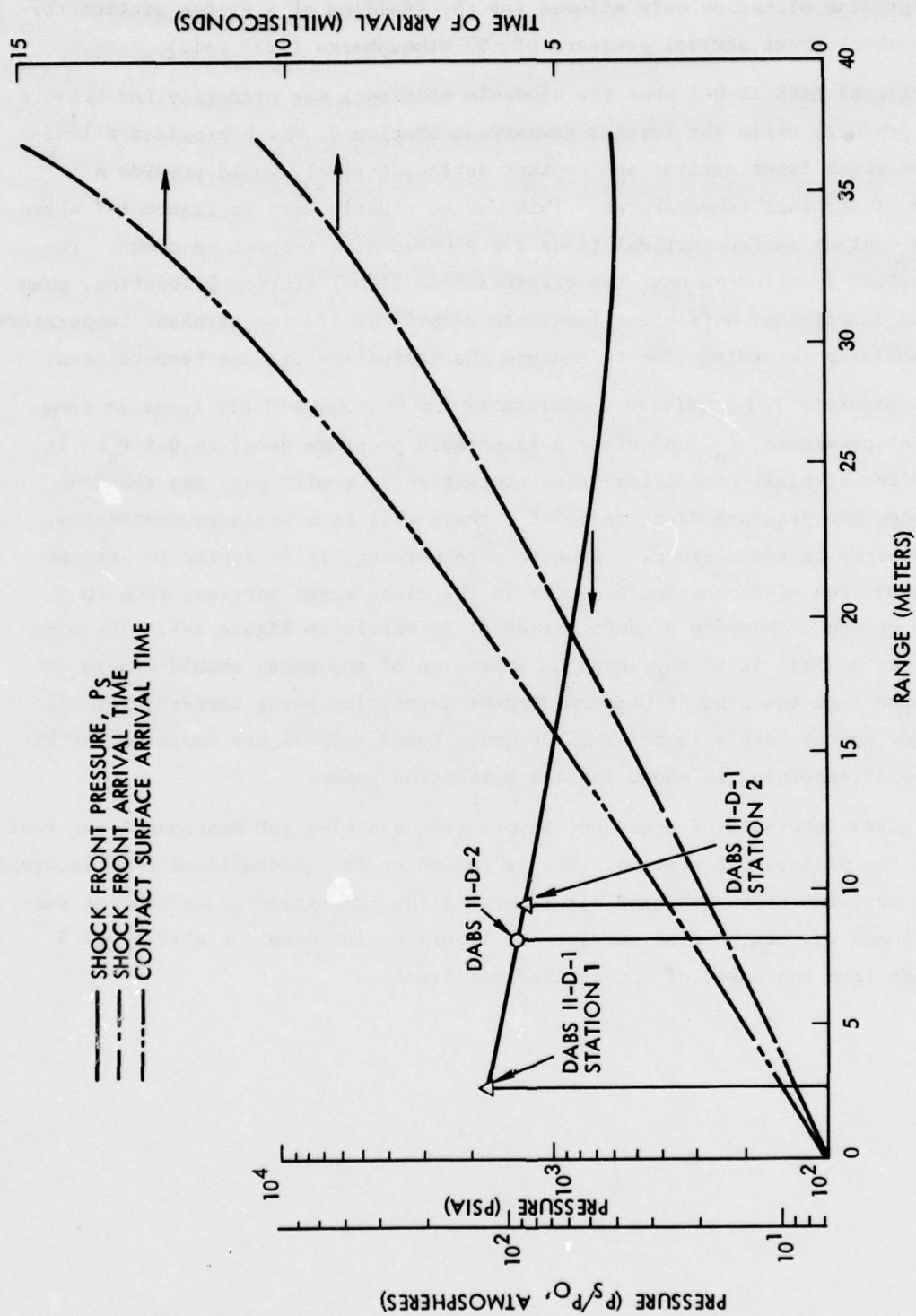


Figure 1-3. Predicted Shock Front Pressure and Arrival Times as a Function of Distance from the Explosive for DABS II-D

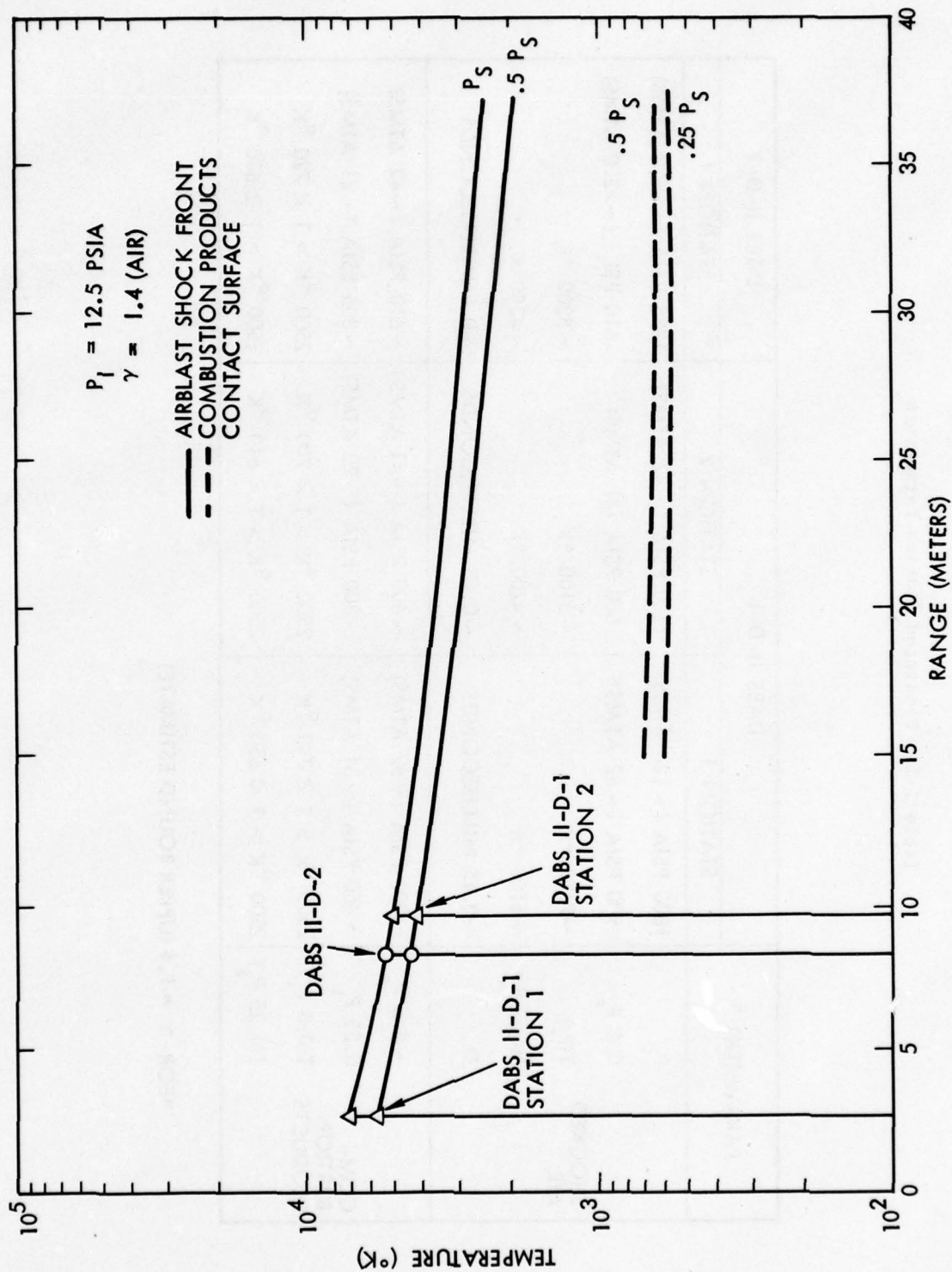


Figure 1-4. Predicted Temperatures as a Function of Distance From The Explosive for DABs II-D

Table 1-1. Predicted Station Parameters

PARAMETERS *	DABS II-D-1		DABS II-D-2
	STATION 1	STATION 2	STATION 1
SHOCKED AIR	P_s	1800 PSIA (~124 ATMS)	1225 PSIA (~83.3 ATMS)
	$0.5 P_s$	900 PSIA (~62 ATMS)	610 PSI (~42.0 ATMS)
	$T(P_s)$	~7600 °K	~5200 °K
	$T(0.5 P_s)$	~6100 °K	~4250 °K
	δt	~0.15 MILLISECONDS	~0.8 MILLISECONDS
COM- BUSTION PRODUCTS	$\sim 0.5 P_s$	~900 PSIA (~62 ATMS)	~610 PSIA (~42 ATMS)
	$0.25 P_s$	~450 PSIA (~31 ATMS)	~305 PSIA (~21 ATMS)
	$T(0.5 P_s)$	$2500\text{ }^\circ\text{K} > T \gtrsim 740\text{ }^\circ\text{K}$	$2500\text{ }^\circ\text{K} > T \gtrsim 720\text{ }^\circ\text{K}$
	$T(0.25 P_s)$	$2500\text{ }^\circ\text{K} > T \gtrsim 650\text{ }^\circ\text{K}$	$2500\text{ }^\circ\text{K} > T \gtrsim 630\text{ }^\circ\text{K}$

*FOR $\gamma = 1.4$ (UPPER BOUND ESTIMATE)

2. THEORY

The technical approach is to use the radiation emitted from the shock tunnel gases to determine its instantaneous temperature. Namely, by measuring the radiant energy transfer rate per unit projected area per unit solid angle and per unit spectral band width (directed spectral radiance, I), one can determine the temperature of the source. For the particular case of the thermodynamic equilibrium radiation, the spectral radiance, I , is called Black Body spectral radiance, I° .

A hypothetical black body is completely opaque to all wavelengths, λ , of optical radiation at all temperatures, T . It has an emissivity ϵ (radiant energy emission efficiency) equal to unity for all T and all λ . The equations for black body spectral radiance, $I^\circ(\lambda; T)$, are presented in Appendix A.

It is impractical to approximate a true black body except by artificial construction. Some solids and liquids are said to be gray bodies. These exhibit an emissivity, ϵ_{gray} , which while less than unity, shows relatively slow variation with temperature or wavelength over fairly broad $\Delta\lambda$ and ΔT intervals. Most real bodies, however, and particularly the gaseous volumes of current interest, exhibit large fluctuations of spectral absorptivity and emissivity both with changing wavelength and changing temperature. Kirchoff's Law states that the spectral emissivity $\epsilon(\lambda; T)$ and the spectral absorptivity $\alpha(\lambda; T)$ for any gases are equal for the same λ and T . In this report the curved parenthesis will always denote functional relationships, i.e., $\epsilon(\lambda; T)$, ϵ is a function of λ and T . The spectral radiance $I(\lambda; T)$ of the body is related to that of a black body at the same temperature by the expression:

$$I(\lambda; T) = \epsilon(\lambda; T) I^\circ(\lambda; T) \quad (2.1)$$

Black Body	$\epsilon = 1$	for all λ and for all T
Gray Body	$\epsilon = \epsilon_{\text{gray}} < 1$	ϵ_{gray} approximately constant over large $\Delta\lambda$ and ΔT regimes
Gases	$\epsilon(\lambda; T)$	large variation with λ and T , but $\epsilon(\lambda; T)$ may = 1 for selected $\Delta\lambda$ and ΔT regimes

For gas volumes, $\epsilon(\lambda; T)$ is strongly dependent upon the identity and relative proportions of the constituent gaseous species, and also upon the temperature and pressure in the volume and the length of optical path, L , through the volume. In a long path length of sufficiently high density and high temperature gas, spectral regions for a wavelength

interval, $\lambda_i \pm 1/2 \Delta\lambda$, can usually be found for which $\epsilon(\lambda, \Delta\lambda; T) \approx 1$, and for which $I(\lambda; T) \approx I^\circ(\lambda; T)$.

2.1 Spectral Region Selection Criteria for Optically Thick Gas Volumes

In general, it is considerably easier to determine wavelength (λ), bandwidth ($\Delta\lambda$), temperature (T) and temperature intervals (ΔT) regimes for which a specified gaseous layer of known constituent distribution, should exhibit a spectral emissivity, $\epsilon(\lambda, \Delta\lambda; T)$, closely equal to unity than to determine accurate values of spectral emissivity which depart appreciably from unity. The former approach, therefore, was selected for implementation.

The most general form of the simple exponential decay law for the transmission of optical radiation through a substance whose "optical thickness" τ increases from zero with increasing depth of penetration L , is,

$$I(\lambda) = I_0 \exp [-\tau(\lambda; L)] \quad (2.2)$$

$$I(\lambda) = I_0(\lambda) \text{ when } \tau = 0 \text{ (i.e. when } L = 0)$$

In various forms and applications, the preceding equation is known as Beer's Law, Lambert's Law, etc. While fairly valid for propagation through most types of semi-transparent solids and liquids, it is in general not directly applicable for propagation through gaseous layers for other than very closely monochromatic radiation. In the problem of current interest, where high pressures and high temperatures tend to blur the individual spectral lines of the gaseous constituents into pseudo continua (See Figure C-3b), an exponential decay law is again quite valid for application to relatively narrow but finite wavelength intervals $\lambda \pm 1/2 \Delta\lambda$ rather than to strictly monochromatic radiation. An overbar, i.e., $\bar{\tau}$, $\bar{\alpha}$, etc., will be used throughout this report to distinguish spectral parameters "smoothed" or averaged over a $\lambda \pm 1/2 \Delta\lambda$ interval from the corresponding monochromatic τ , α , etc., parameters. Using this overbar convention, the mean spectral absorptivity of a gaseous layer of spectrally averaged optical thickness $\bar{\tau}(\lambda, \Delta\lambda; P, T; L)$ is seen from the preceding equation to be represented by the expression:

$$\bar{\alpha}(\lambda, \Delta\lambda; P, T; L) = 1 - \exp[-\bar{\tau}(\lambda, \Delta\lambda; P, T; L)] \quad (2.3)$$

In writing Equation (2.3) it was assumed that τ and $\bar{\tau}$ are absorption rather than total "extinction" parameters. In any case, for gas layers, the scattering (or diffuse

reflection) contributions to "extinction" are generally of importance only in spectral regions of very weak absorption. If this is true, then Equation(2.3) is valid as an excellent approximation even for total "extinction" (absorption plus scattering) parameters.

Then applying the earlier mentioned Kirchoffs' Law to Equation(2.3) one can write:

$$\bar{\epsilon}(\lambda, \Delta\lambda; P, T; L) = 1 - \exp [-\bar{\tau}(\lambda, \Delta\lambda; P, T; L)] \quad (2.4)$$

$$\bar{\tau}(\lambda, \Delta\lambda; P, T; L) = \sum_{i,j} \bar{\tau}_{ij}(\lambda, \Delta\lambda; P, T; L) \quad (2.5)$$

with the summation extending over each j^{th} spectral band in the $\lambda \pm 1/2 \Delta\lambda$ region of interest for each i^{th} species of gas in the gaseous mixture. The individual "optical thickness" contributions, $\bar{\tau}_{ij}$, can in turn be exhibited in the form:

$$\bar{\tau}_{ij}(\lambda, \Delta\lambda; P, T; L) = \bar{k}_{ij}(\lambda, \Delta\lambda; T) \cdot L \cdot [N_i(P, T)/N_0] \quad (2.6)$$

Here $N_i(P, T)$ is the number density of the i^{th} species of radiating (and absorbing) molecules, in units of cm^{-3} , while N_0 is equal to $2.67 \cdot 10^{19}$ molecules of gas per cm^3 at standard temperature and pressure (STP). The optical path length is L . With elimination of the lower temperature boundary layers near the tube walls, L reduces to ~ 81 cm for DABS II-D-1 and to ~ 410 cm for DABS II-D-2. The $\bar{k}_{ij}(\lambda, \Delta\lambda; T)$ are spectral mean absorption coefficients specified in the units of "inverse reduced atmosphere centimeters" $[(\text{atm cm})^{-1}]$, or often more precisely, $(\text{atm cm} - \text{STP})^{-1}$ most commonly found in the literature. This does not mean, as is sometimes mistakenly assumed, that these absorption coefficients are evaluated under STP conditions. The rationale behind the preceding designation is that the multiplier, $L[N_i(P, T)/N_0]$, occurring in equation(2.6) can be said to represent an equivalent path length that would result if the i^{th} species gas were purified and reduced to STP conditions. This readily can be seen by first introducing the mole fraction, $\chi_i(P, T)$, where;

$$\chi_i(P, T) = N_i(P, T)/N(P, T) \quad (2.7)$$

Here, $N(P, T)$ represents the total number density of all gas particles per cm^3 at absolute temperature T and pressure P . Then, for the ideal gas assumption which is completely justified in the (P, T) domain of current interest,

$$N_i/N_o \cdot L \equiv \chi_i (N/N_o) \cdot L = \chi_i \cdot \frac{P \cdot T_o}{P_o \cdot T} \cdot L \quad (2.8)$$

The explicit (P, T) dependence of χ_i , N_i and N have been omitted in the preceding equation for convenience and also, when unambiguous, will often be omitted from later equations for the same reason. The subscript, o, on P, T or N, etc., will always indicate STP conditions. Thus, since the (P/P_o) ratio gives the pressure in units of standard atmospheres, the terms on both sides of Equation (2.8) are said to be in units of effective reduced (atm cm - STP).

A substitution of Equation (2.8) into Equation (2.6) yields:

$$\bar{\tau}_{ij}(\lambda, \Delta\lambda; P, T; L) = \chi_i(P, T) \bar{k}_{ij}(\lambda, \Delta\lambda; T) \cdot P/P_o \cdot T_o/T \cdot L \quad (2.6a)$$

The preceding equation is used when the mole-fractions, χ_i , rather than the species number densities, N_i , are the directly available data. The spectrally smoothed absorption coefficients \bar{k}_{ij} for the molecular and ionic species of interest generally were either directly available in the literature or could be calculated from data presented in the literature.

The fundamental absorption parameters are the monochromatic "per molecule cross sections", $\sigma(\lambda)$, rather than the somewhat arbitrarily defined monochromatic absorption coefficient counterparts, $k_{ij}(\lambda; T)$, or the $\bar{k}(\lambda, \Delta\lambda; T)$ parameters introduced in equation (2.6). The fundamental σ -cross sections are in general only weakly temperature dependent, but the k-coefficients can exhibit from one to several orders of magnitude variation with temperature within the temperature domain of current interest. The reason for this variation is related to the dependence of the k-(and \bar{k} -) parameters upon "excited state populations". A brief discussion of the relation between the k- and σ -parameters, and of the temperature dependence of the former is given in Appendix C.

To recap, a large fraction of the initial effort was spent in determining spectral regions for which either air or the combustion products could be expected to exhibit optical thickness, $\tau \gtrsim 3$. From equation (2.4) it can be seen that $\epsilon \gtrsim 0.95$ for $\tau \gtrsim 3$. Equation (2.6) or equation (2.6a) was used to predict $\bar{\tau}_{ij}(\lambda, \Delta\lambda; T)$ values from N_i , or χ_i , and $\bar{k}(\lambda, \Delta\lambda; T)$ values that were either available in the literature or could be computed from the in-house computer program TRW ACE.

2.2 Spectral Region Selection

The spectral intervals $\lambda \pm 1/2 \Delta\lambda$ investigated were all those between $\sim 0.25\mu$ and $\sim 5\mu$ wavelength for which the respective constituent gases (and carbon soot solids for the combustion products) were known to exhibit elevated temperature absorption bands that gave promise of possibly being useful and were not excessively expensive to implement. Optical instrumentation to view the very strong 15μ CO_2 band, for example, is approximately a factor of 10 more expensive than for wavelengths below $\sim 5\mu$. Also these detectors must use liquid helium cryostats. The longer wavelength apparatus also is very time-consuming and difficult to adjust in the field. The same applies to ultraviolet radiation at wavelengths much below 0.25μ where the hot air layer viewed would certainly be "optically thick". Moreover, normal temperature ambient air is completely opaque below $\sim 0.21\mu$ wavelength for even a few centimeter path lengths, and exhibits very strong absorption near 15μ wavelength for moderate path lengths. The high temperature radiation being investigated, therefore, would be at least partially absorbed in the far ultraviolet or in the 15μ wavelength CO_2 region.

2.3 One and Two Color Pyrometer Systems

The output voltage $V(\lambda, \Delta\lambda; T)$ of a radiometer filtered to respond to a $\lambda \pm 1/2 \Delta\lambda$ wavelength increment is directly proportional to the spectral radiance $I(\lambda, \Delta\lambda; T)$ being viewed. The proportionality factor, which is dependent upon the optical system, detector cell and amplifier parameters, is subject to either computation or preferably to empirical absolute calibration. If the spectral emissivity $\bar{\epsilon}(\lambda, \Delta\lambda; T)$ is known to be ≈ 1 [so that $I(\lambda, \Delta\lambda; T) \approx I^0(\lambda, \Delta\lambda; T)$] throughout the temperature regime of interest, then there is a unique one-to-one relationship between $I^0(\lambda, \Delta\lambda; T)$ and T , and hence between $V(\lambda, \Delta\lambda; T)$ and T . Equation (A.2b) in Appendix A gives the Black Body law relation between $I^0(\lambda, \Delta\lambda; T)$ and T . This equation could be solved for a somewhat awkward relation expressing T as a function of I^0 , and hence a function of the directly measured quantity V .

It is more convenient, however, to make calibration graphs representing both black body radiance $I^0(\lambda, \Delta\lambda; T)$ and signal voltage $V_s(\lambda, \Delta\lambda; T)$ as unique functions of T as the independent variable. Figure A-3 in Appendix A presents I^0 vs. T curves for five selected wavelength intervals $\lambda_i \pm 1/2 \Delta\lambda_i$. Figure 6-4, in Section 6.0 presents some equivalent V_s vs. T curves. Any one of these latter type of V_s vs. T calibration curves, together with the corresponding $\lambda_i \pm \Delta\lambda_i$ radiometer system is said to constitute a "one color" pyrometer.

A pair of radiometers filtered to respond respectively to $\lambda_i \pm 1/2 \Delta\lambda_i$ and $\lambda_j \pm 1/2 \Delta\lambda_j$ together with a $V_s(\lambda_i, \Delta\lambda_i; T)/V_s(\lambda_j, \Delta\lambda_j; T)$ vs. T calibration curve is said to constitute a "two color" pyrometer system. The V_s ratio vs. T curves are similar to the I^0 ratio vs. T curves shown in Figure A-4 Appendix A.

2.3.1 One Color Pyrometer Systems

It is possible to make fairly reliable temperature determinations at least over a limited temperature interval, with a one color pyrometer system such as was described in the preceding discussion. This type of "one color" pyrometer, however, suffers from the disadvantages of requiring accurate absolute calibration, a relatively narrow spectral region for accuracy and of falling off fairly rapidly in relative accuracy outside of a favorable temperature interval which is a function of the selected λ . As will be shown in Appendix A, the ultraviolet spectral region is most favorable for the measurement of very high temperatures, while the near infrared is most favorable for lower temperatures. This latter weakness possibly could have been overcome by the use of several "one color" pyrometer systems at different wavelengths $\lambda_i \pm 1/2 \Delta\lambda_i$ each selected for $\tau \gtrsim 3$.

2.3.2 Two Color Pyrometer Systems

All three of the preceding objections can be more readily met, however, by the use of several "two color" pyrometer systems, each consisting of a pair of radiometers for sufficiently separated high τ wavelength intervals, say $\lambda_i \pm 1/2 \Delta\lambda_i$ and $\lambda_j \pm 1/2 \Delta\lambda_j$. As will be seen in Appendix A, the "temperature signals" for a "two color" pyrometer is the spectral radiance ratio $[I(\lambda_i, \Delta\lambda_i; T)/I(\lambda_j, \Delta\lambda_j; T)]$. A "two color" pyrometer, depending as it does only upon the ratio rather than upon the absolute value of two input signals, does not require absolute calibration. It suffices to either have equivalent geometries and optical and electronic gain parameters for the two systems, or to be able to scale the differences in these factors accurately. Somewhat wider $\Delta\lambda$ filters are feasible, since again, the temperature signal does not depend so critically upon variations of the individual received spectral radiance increments, but only upon variations in their ratio. Finally, as will be seen from one of the curves shown in Figure A-4, it is possible to obtain acceptable accuracy over a temperature extending from over 8000 °K to less than 3500 °K by selecting one detector system centered on an ultraviolet wavelength and the other on a near infrared wavelength. The high and low temperature cut-offs are set more by the cost and gain of multiple decade amplifiers and low noise optimum detectors, and the cost of low noise transmission lines, than by the decay of the spectral radiance ratio temperature signal.

2.4 Selected Wavelength Intervals for Two Color Pyrometers

As was indicated in sub-section 2.2, the choice of wavelength intervals to be utilized was restricted to those between $\sim 0.25\mu$ and 5μ for which the optical thicknesses $\bar{\tau}(\lambda, \Delta\lambda; T; P)$ could be predicted to be ≥ 3 , if possible, for the (T, P) regimes of interest. Since the choices of pyrometer wavelength intervals are dependent upon the radiating molecular, atomic, ionic (or particulate) species being observed, they are different for the shock heated air volume than for the later arriving combustion products which consist primarily of H_2O , CO_2 and N_2 gases, and of particulate carbon soot.

2.4.1 Wavelength Selections for Shock Heated Air

After investigation into the high temperature optical thickness contributions $\bar{\tau}_{ij}(\lambda, \Delta\lambda; T, P)$ for λ between $\sim 0.25\mu$ and 5μ to be expected from air molecules, atoms and ions, it was determined that only the ultraviolet and short wavelength visible spectrum region for $\lambda < 0.38\mu$ gave any promise of sufficient opacity, i.e., $\tau > 3$, for shock heated normal air. It was determined that the best compromise wavelength intervals for natural air were $\lambda_1 \approx 0.26\mu$ and $\lambda_2 \approx 0.36\mu$, with $\Delta\lambda_1 \approx \Delta\lambda_2 \approx 0.01$ (100Å). A somewhat shorter wavelength would have been preferred for λ_1 , but was ruled out by optical system considerations. A longer wavelength for λ_2 was ruled out by the rapid fall-off with increasing wavelength of hot air opacity. As it is, the computed value of $\bar{\tau}(0.36\mu; 0.01\mu; T, P)$ falls below the critical values of 3 for pressure below ~ 45 atmospheres over much of the temperature interval of interest (see Table 1.1) for DABS II-D-1; for DABS II-D-2 the $\bar{\tau}$ value will be five times greater. The ($\lambda_1 = 0.26\mu$, $\lambda_2 = 0.36\mu$) pair are suitable primarily for temperatures in the $\sim 8000^\circ K$ to $\sim 3000^\circ K$ region and for pressures above ~ 40 or 50 atmospheres (owing to the diminishing opacity of the 0.36μ spectral region). [Pressures as low as 25 atmos. suitable for DABS II-D-2]

Outside of some relatively vary sharp atomic lines from N, O, Ar, Na and metallic impurities, it would appear that the only strong air radiation for temperatures of less than $8000^\circ K$ and wavelengths longer than 0.4μ comes from what are known as the molecular nitrogen first positive band system [$N_2(1+)$] and from the atomic oxygen radical O^- (free-bound) continuum (see Appendix D for explanation of these terms). However, computations using equation (2.6) showed that even at $T = 8000^\circ K$ and $P/P_0 \approx 130$ atmospheres, an optical thickness τ value of ~ 1 was the greatest to be expected in the $\sim 0.55\mu$ to $\sim 0.85\mu$ wavelength region for DABS II-D-1] where this radiation is the strongest. [For DABS II-D-2, the $\bar{\tau}$ values will again be approximately five times greater.]

Previous investigations have used the 0.55μ to 0.85μ wavelength spectral region for optical temperature determinations of flames, explosions, shock tube phenomena, etc. However, they may have been looking at other radiating species than those that

exist in normal shock heated air, or at higher pressure or longer optical paths. Also there are expensive and difficult to implement optical techniques that are more suitable for laboratory type environments than for one-shot field tests using expendable instrumentation. Some of these latter techniques use relatively high spectral resolution interferometers or scanning monochrometers to produce spectra of decidedly non-optically dense gases. The "rotational" or "vibrational" temperatures then are determined from the "back slopes" of the rotational structure of one or more "bands", or from the relative intensities of resolved vibrational bands (see Appendix B).

2.4.2 Wavelength Selections for 4% CO₂ Added to Air [DABS II-D-1]

Preliminary computations also showed quite conclusively that an 81 cm path of the hot air volume would not achieve the desired opacity in the near infrared spectral region between ~ 0.85 and 5μ . The strongest absorption in this region, from the CO₂ so-called 4.3μ wavelength band, still is too weak for the available optical path owing to the very low concentration of CO₂ in normal air. However, since it is very desirable to make pyrometer measurements at near infrared wavelengths in order to measure temperatures below ~ 4000 °K, it was suggested that $\sim 4\%$ CO₂ be added to the normal pre-shock air, either throughout the "tube", or in a thin plastic "balloon" containing the view volumes. It is shown in Appendix E that this small addition of CO₂ will produce suitable opacity not only in the very strong and broad CO₂ vibrational "fundamental band" centered on 4.3μ , but also in the much weaker vibrational "combination band" centered on 2.7μ . Allowing for the necessary tolerance in both the central positions and "widths" of relatively inexpensive and quickly available off-the-shelf filters, the best compromise positions for λ_3 and λ_4 , turned out to be 2.8μ and 4.5μ , respectively, with $\Delta\lambda_2$ and $\Delta\lambda_3 \approx 0.1\mu$ (see Figure 2-1).

The value of $\lambda_4 = 4.5\mu$ rather than 4.3μ was selected because as seen in Appendix D, CO₂ tends to dissociate into CO and O for temperatures much above 3000 or 3500 °K. The 4.5μ wavelength optical system will view: CO₂ at the lower temperatures up to ~ 3500 °K; CO₂ and CO at mid-temperatures between ~ 3500 °K and 4000 °K; CO from ~ 4000 °K to ~ 6500 °K; and both CO and electron free-free [$e^-(ff)$] radiation above ~ 6500 °K to ~ 8000 °K. Also, the natural CO₂ content of cold ambient air in the optical path will show very little absorption at 4.5μ and at 2.8μ ,

With the 4% CO₂ added to air, the 4.5μ wavelength interval will be "black", i.e., $\tau \gtrsim 3$, over virtually the full pressure interval of interest and for 1000 °K $\lesssim T \lesssim 8000$ °K (and owing to the e^- radiation, up to any higher temperature of interest). As a consequence, the 4.5μ λ_4 radiometer would pair not only with the 2.8μ radiometer, but also with the 0.26μ λ_1 radiometer to cover the temperature interval from ~ 3500 °K to

above 8000 °K. The lower and upper temperature cut-offs are set by considerations of excess dynamic range, of transmission line noise, and of the expense of extra high quality low noise detectors and amplifiers rather than by any lack of opacity or radiation signal fall-off. For DABS II-D-2 the addition of 4% CO₂ would have allowed the 2.8μ and 4.5μ infrared wavelengths to read the airblast temperature.

2.4.3 Wavelength Selections for the Combustion Products

It is relatively easy to show that the carbon particle soot arriving with the combustion products should be "black" at any near infrared (and probably visible) wavelength even for very low pressures of the order of 3 or 4 atmospheres or perhaps less. However, since this soot will lag the contact surface of the combustion produce and the shock heated air by some fraction of a millisecond the infrared wavelengths will be appropriate, thus wavelengths $\lambda_5 = 1.9\mu$ and $\lambda_6 = 4.3\mu$ were selected, again with $\Delta\lambda$'s of $\sim 0.1\mu$. The 1.9μ ratiometer will be viewing a relatively rather weak water vapor vibrational combination band, which owing to the mole-fraction of ~ 0.64 H₂O in the combustion products will nevertheless give values of $\tau \gtrsim 3$ over virtually the full pressure range of interest, particularly since the carbon soot should arrive before any marked drop-off in pressure occurs.

The wavelength of $\lambda_6 \approx 4.3\mu$ rather than the λ_4 value of $\sim 4.5\mu$ was initially selected for viewing DABS II-D-1 combustion product radiation in order to provide a capability of measuring temperatures of combustion gases below ~ 1000 °K before the arrival of the carbon soot particles within the station fields of view. At the time, it was thought that the lag time of the soot particle arrivals behind the contact surface might possibly be a fraction of a millisecond. The CO₂ absorption coefficients $\bar{k}_{CO_2}(\lambda, \Delta\lambda; T)$ are relatively independent of temperature for $\lambda \approx 4.3\mu$, but decay by several orders of magnitude as T decreases to ~ 500 °K for $\lambda \approx 4.5\mu$ (particularly for the $\sim 0.15\mu$ $\Delta\lambda$ increments which turned out to be available in off-the-shelf filters). Thus, the computed absorption optical thickness τ_{CO_2} remained well above the critical value of 3 throughout the full pressure range of interest for $\lambda \approx 4.3\mu$, but dropped below this value for T less than ~ 1000 °K, or possibly ~ 800 °K, for $\lambda = 4.5\mu$. For DABS II-D-2 the optical thickness τ_{CO_2} would have been five times greater.

An undesirable corollary, however, is that 4.3μ wavelength radiation, unlike 4.5μ wavelength radiation, is strongly absorbed by ambient air temperature CO₂. It is estimated that the $\sim 0.03\%$ CO₂ content of air in the ~ 12 foot optical path would absorb ~ 20 to 30% of viewed $\sim 4.3\mu$ wavelength radiation. This loss could have been corrected for by field calibrations, or measures could have been taken to replace the ambient air in the view path by non-absorbing dry nitrogen gas. In view of the short time available

for implementation, however, the latter procedure was not practical for the DABS II-D-2 shot. Also, the purchased off-the-shelf filter turned out to be centered on $\sim 4.25\mu$, where the ambient air absorption is even stronger than for $\sim 4.3\mu$.

The preceding ambient air absorption problem was resolved by a closer evaluation of the probable carbon soot lag time. It is believed that unlike larger particles, the expected sub-micron size soot particles arrive very close behind the contact surface. Since the arriving combustion products would be completely opaque at all near infrared wavelengths, there turns out to be no advantage in using a $\sim 4.3\mu$ rather than a 4.5μ radiometer. It thus was decided to substitute the latter radiometer for the DABS II-D-2 combustion products temperature measurements.

2.4.4 Summary of Wavelength and Pyrometer (Radiometer Pair) Selections

Figure 2-1 summarizes the radiometer wavelength selections, λ_1 through λ_6 , and their positioning at either Station 1 or Station 2, or at both stations for DABS II-D-1. As seen in Table 1.1, the close-in Station 1 for DABS II-D-1, will view the shock heated air for only ~ 0.15 milliseconds, and then spend the remainder of its brief lifetime viewing combustion products. Station 2, on the other hand, will see the shock heated air, now at reduced temperature and pressure, for ~ 0.85 milliseconds.

The hot air and air + 4% CO_2 viewing radiometers, filtered to respond to the four wavelengths centered respectively on $\lambda_1 = 0.26\mu$, $\lambda_2 = 0.36\mu$, $\lambda_3 = 2.8\mu$ and $\lambda_4 = 4.5\mu$ compromise three two-color pyrometers when taken in the pairs (λ_1, λ_2) , (λ_3, λ_4) , and (λ_1, λ_4) (see Figure A-4). It also is possible to interpret pyrometer data from the pairs (λ_1, λ_3) and (λ_2, λ_4) , but over more limited temperature intervals; λ_2 and λ_3 do not both view "black" radiation at overlapping temperature intervals.

The primary combustion product viewing radiometers originally were intended to be $\lambda_5 \approx 1.9\mu$ and $\lambda_6 \approx 4.3\mu$, but for reasons outlined at the end of the preceding sub-section, it was decided to substitute $\lambda_4 = 4.5\mu$ for λ_6 . In addition to the (λ_5, λ_4) pair however, combustion product temperature information also can be extracted from the (λ_3, λ_4) pair, and (less accurately) from the (λ_5, λ_3) pair. The (λ_3, λ_4) pair should be particularly useful for temperatures approaching $\sim 500^\circ\text{K}$ where the weaker voltage signal from the $\lambda_5 \approx 1.9\mu$ radiometer may tend to drop too close to the noise level.

Figure 2-2 summarizes the radiometer selection data for DABS II-D-2. As was shown in Table 1.1, ~ 0.8 milliseconds will be spent viewing the shock heated air, and the remaining few milliseconds of the equipment survival time will be devoted to the presumably cooling combustion products.

TEMPERATURE (°K)	MEDIA	ABSORBING MOLECULES	DETECTOR WAVELENGTH (μ)						DETECTOR	REQUIRED DYNAMIC RANGE (dB) VOLTS	STATION	
			λ ₁	λ ₂	λ ₃	λ ₄	λ ₅	λ ₆			1	2
			0.26	0.36	2.8	4.5	1.9	4.3				
800 - 3000	COMBUSTION PRODUCTS	H ₂ O CO ₂					●		Pb-Se	48 33	● ●	
4000 - 6200	AIR	O ₂ , NO(β), NO(τ), NO ₂	●						Si PIN DIODE	35	●	●
5800 - 8000			●							35	●	●
4000 - 8000				●						46	●	●
1000 - 4000	AIR & 4% CO ₂	CO ₂ CO ₂ & CO			●				Pb-Se	38 33	● ●	
3500 - 8000	AIR & 4% CO ₂	CO ₂ , CO, e ⁻ NO(β), NO(γ) O ₂ (S-R), O ⁻ , NO ₂	●			●	●		Pb-Se Si PIN DIODE	33 35		*

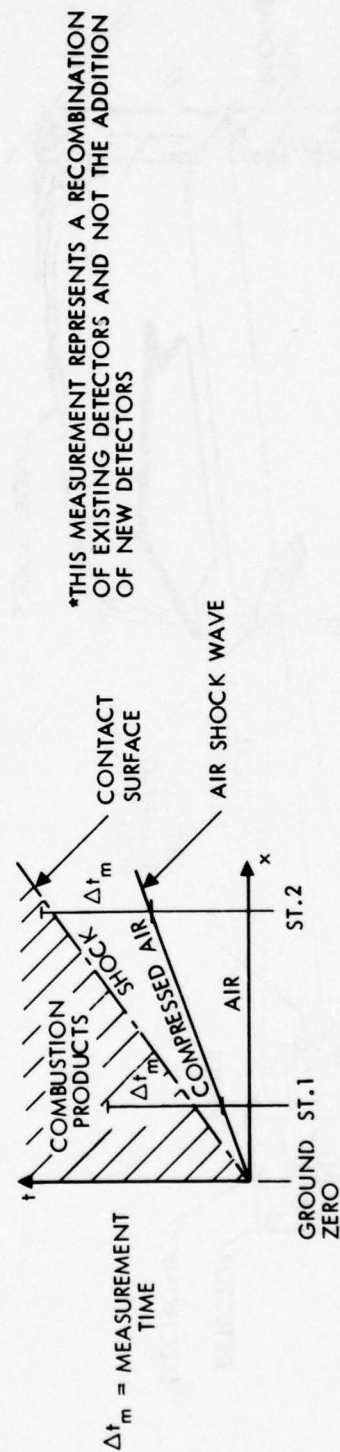
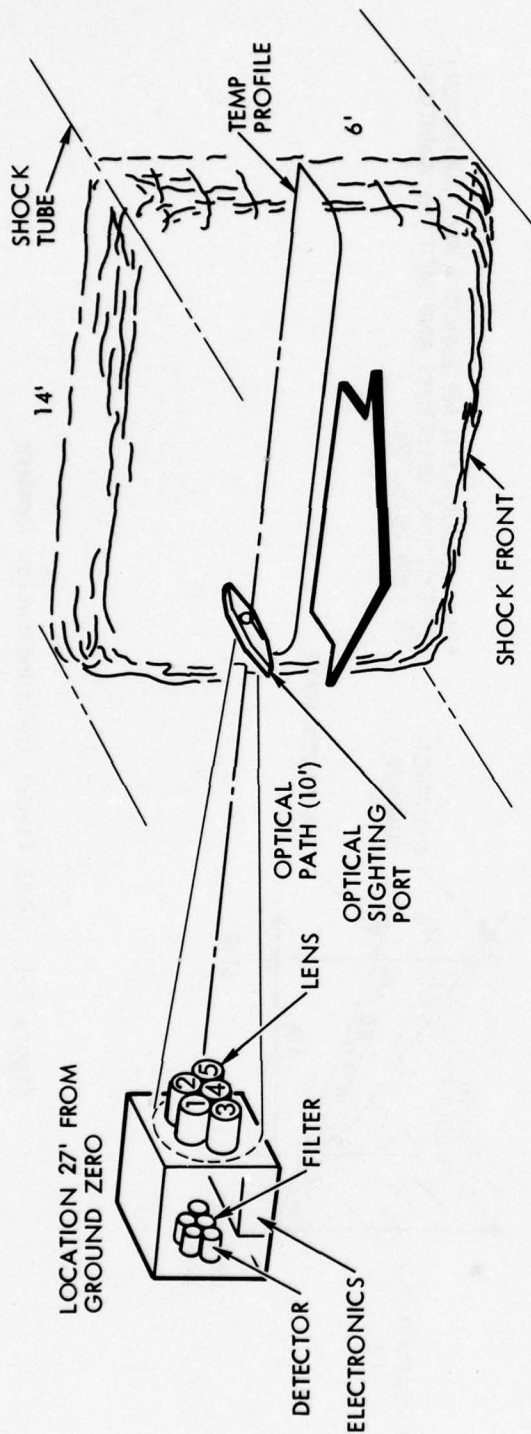


Figure 2-1. DABS II-D-1 Instrumentation Summary



POSITION	LENS			FILTER				DETECTOR	
	TYPE	FOCAL LENGTH	DIA	TYPE	CENTER (NOM)	BAND-WIDTH	TRANSMITTANCE	TYPE	RESPONSE RANGE max dB min
1	GLASS	20"	2"	I.R.	1.910 μ (1.9 μ)	0.160	58.5%	Pb-Se	50
2	CaF ₂	20"	2"	I.R.	2.85 μ (2.8 μ)	0.110	67.5%	Pb-Se	32
3	GLASS	20"	2"	U.V.	0.359 μ (0.36 μ)	0.0068	28.0%	Si PIN DIODE	30
4	CaF ₂	20"	2"	I.R.	4.49 μ (4.5 μ)	0.138	51.0%	Pb-Se	22
5	QUARTZ	20"	2"	U.V.	0.258 μ (0.26 μ)	0.024	17.5%	Si PIN DIODE	56

Figure 2-2. DABS II-D-2 Instrumentation Summary

2.5 Information Presented in Appendices

A detailed understanding of Black Body radiation theory and of molecular spectroscopy is not required for an understanding of this report, but a rudimentary understanding of the concepts and nomenclatures involved would be helpful. Appendices A, B and C present brief over-views of these topics for the reader who may not have been introduced to them previously, or who may wish to refresh his memory. Appendix A presents, without any attempt at derivation, the rudiments of Black Body radiation theory, and of criteria for the applicability of optical radiometer measurements for determining the radiation temperature of a volume of hot gases. It also discusses the selection of optimum spectral regions for observations, and presents generalized error analyses criteria for "one color" and "two color" pyrometer techniques. Appendix B presents a skeletal definition of some of the nomenclature of molecular spectroscopy. Appendix C presents a very brief discussion of the basic spectroscopic parameters of absorption "cross sections", and of the temperature and pressure dependence of spectral line contours, line "half widths", and the "spectral density of lines". It also shows how all of these parameters combine to define the spectrally smoothed absorption coefficients $\bar{k}(\lambda, \Delta\lambda; T)$ that generally are presented in the literature and which were used in this report to make required gas volume spectral opacity evaluations.

2.5.1 Presentation of Radiating Species Information

Appendix D presents a brief discussion of radiating species parameters for air, air plus 4% CO_2 and the H_2O , CO_2 and carbon soot combustion products for the DABS II-D shots. The selected radiometer wavelength intervals $\lambda_i \pm 1/2 \Delta\lambda_i$, were dictated by the spectral positions and strengths of the available radiating species absorption bands, together with the practical system considerations mentioned in sub-sections 2.2 and 2.3. The principal radiating species parameters of interest are the magnitudes and spectral positions of the spectrally smoothed absorption coefficients $\bar{k}_{ij}(\lambda, \Delta\lambda; T)$ and the number densities $N_i(P, T)$, or mole-fractions $\chi_i(P, T)$, for these species. As a corollary, the equilibrium persistence or decay of these species with increasing temperature also is important, as is the effect of increasing pressure upon relative species concentrations. All these topics are discussed and graphically presented in Appendix D.

2.5.2 Presentation of Opacity Data

As was previously stated, the somewhat arbitrary opacity criterion adopted in this report is that in the selected spectral regions, the mean optical thickness $\bar{\tau}(\lambda, \Delta\lambda; P, T)$ should be $\gtrsim 3$ so that the corresponding emissivity $\epsilon(\lambda, \Delta\lambda; P, T; L)$ would be $\gtrsim 0.95\%$. Appendix E graphically presents computed data to show that this criterion substantially is met for the selected $\lambda_i \pm 1/2 \Delta\lambda_i$ spectral regions for air,

air + 4% CO₂ and combustion products for the DABS II-D-1 configuration. As previously stated, the much longer path length for DABS II-D-2 insures that the corresponding τ values for the same (P, T) pair will be a factor of ~ 5 higher for this latter configuration. Thus, for temperatures below ~ 3000 °K, the radiation data for the DABS II-D-2 configuration could be used to predict temperatures for pressures that are lower by a factor of $1/5$ than the minimum that would have been reliable for the DABS II-D-1 configuration. With the lower pressures expected at the DABS II-D-2 station, species dissociation may tend to occur more rapidly and the decreased pressure factor might only be $\sim 1/3$ for temperatures above ~ 5000 °K.

3. OPTICAL SYSTEM PARAMETERS FOR THE DABS II-D-2 TEST

The optical system configuration for the DABS II-D-2 test is shown in Figure 3-1. Note that molecules located in the occlusion region (darkly shaded) will be obstructed by the aperture so that full illumination of the lens and detector is impossible, while molecules in the lightly shaded region will provide full illumination of lens and detector. The circular viewing port hole into the radiating gas volume is 2.8 cm (1 1/8 inches) in diameter. The objective lenses of all five radiometers are at a virtually equal distance, r , between ~308.8 and 308.2 cm (~121 1/3 inches) from this aperture, and all have 5.08 cm (2 inch) diameters, D , and optical transmissivities, β^{lens} , equal to 0.90. The lenses thus subtend solid angles, Ω , of $(\pi D^2/4r^2) = 2.134 \cdot 10^{-4}$ steradians from any point on the aperture. Since these parameters are all virtually equal, an indexing subscript would be superfluous for r , D , Ω , and β^{lens} . The spectral filter transmissivities, β_i^f , are all different, however, and thus need the i -indexing subscript.

The effective radiant power input to the i^{th} radiometer, filtered to respond to a narrow spectral interval centered on λ_i , is:

$$P_i^{\text{input}}(T) = S^g \cdot \Omega \cdot \beta^{\text{lens}} \cdot \int_{\lambda_i - m_i (\Delta\lambda_i/2)}^{\lambda_i + m_i (\Delta\lambda_i/2)} I^0(\lambda; T) \cdot \beta_i^f(\lambda) d\lambda \quad (3.1)$$

The symbol S^g represents the unoccluded increment of gas layer surface area which is actually focused within the square responsive area, $A^c = (0.4 \text{ cm})^2$, of each i^{th} radiometer detector cell. The measured filter transmissivities are shown in Figure 3-2a, b, c, d and e. It was found that the relatively inexpensive off-the-shelf spectral filters purchased all had roughly triangular spectral transmissivities, β_i^f , which did not all, however, drop off to zero as rapidly as was desirable. The integral in equation (3.1) must therefore be taken over some whole or fractional number m_i of full widths at half peak, $\Delta\lambda_i$, with the number varying from filter to filter. Except for the two broad and shallow ultraviolet filters centered on $\lambda_1 = 0.258\mu$ and $\lambda_2 = 0.359\mu$ equation (3.1) can be approximated with sufficient accuracy in the form:

$$P_i^{\text{input}}(T) \approx S^g \cdot \Omega \cdot \beta^{\text{lens}} \cdot I^0(\lambda_i; T) \cdot \beta_i^f(\lambda_i) \cdot (\Delta'\lambda_i/1\mu) \quad (3.1a)$$

with $\Delta'\lambda_i$ an approximation of the bandwidth that is sufficiently larger than $\Delta\lambda_i$ to account for contributions from the non-zero "wings" of the filter function outside of the $\lambda_i \pm \frac{1}{2}\Delta\lambda_i$ cut-offs of a hypothetical triangular filter; i.e., so that

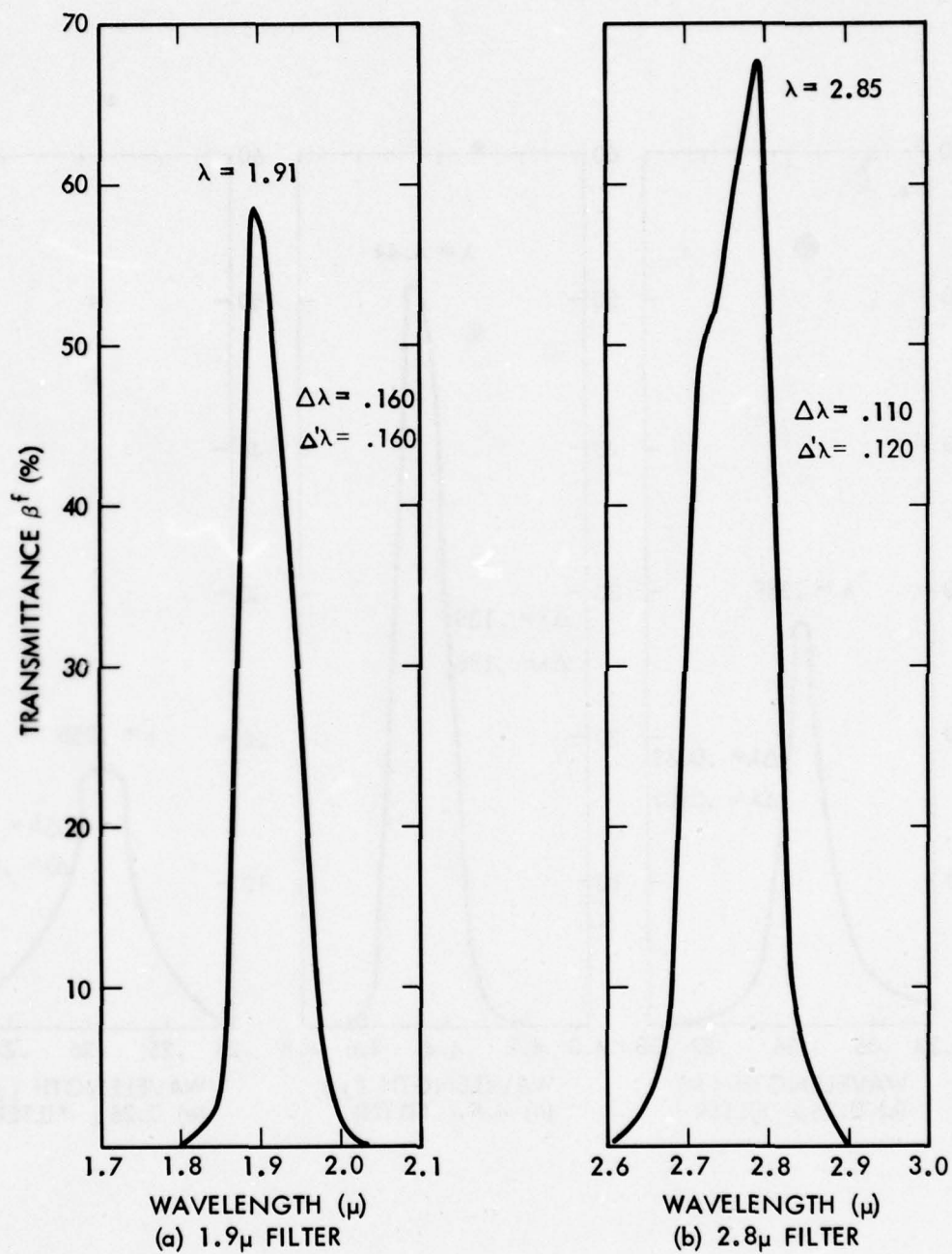


Figure 3-2. Transmittance Curves for the Five DABS II-D-2 Filters

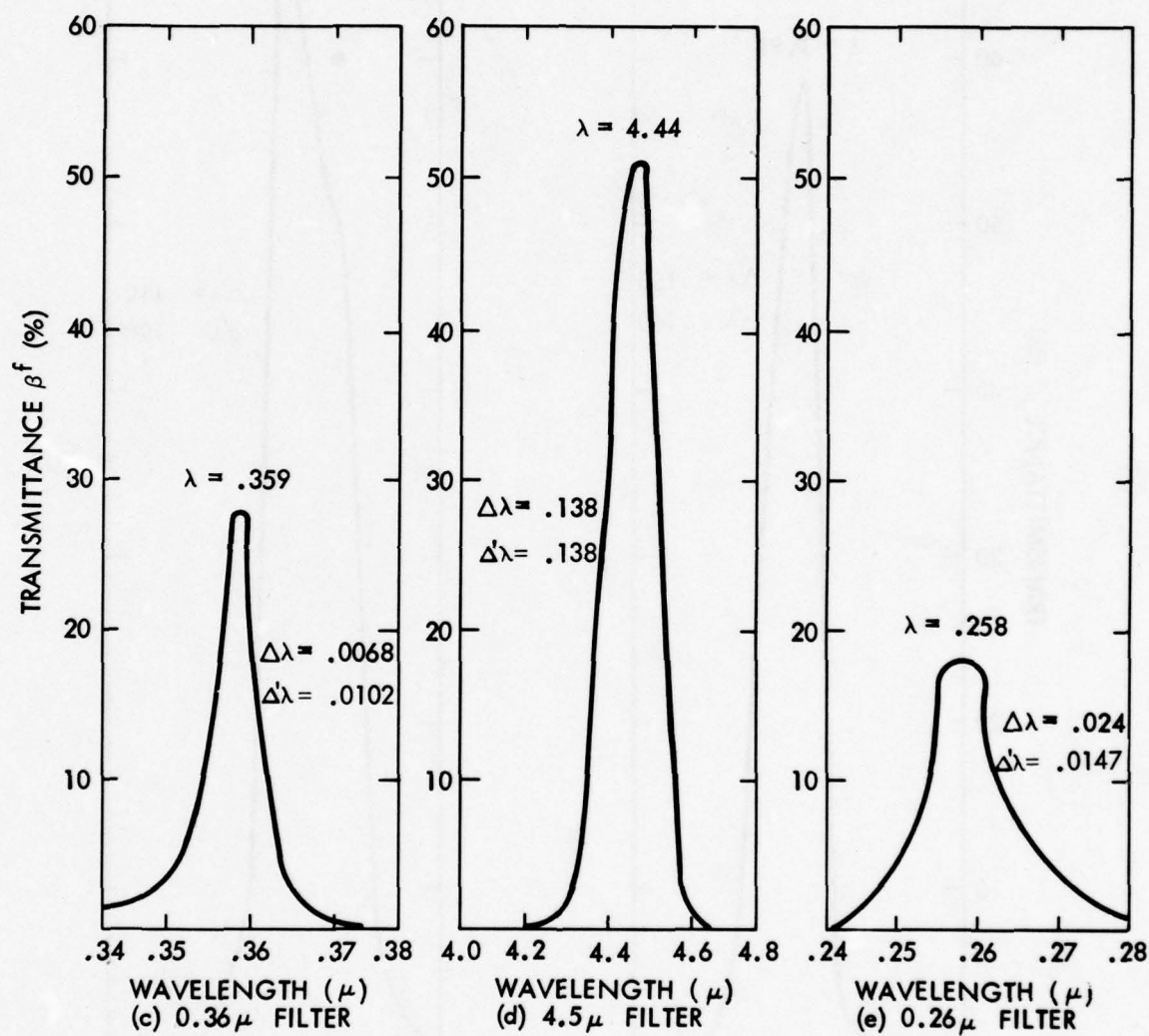


Figure 3-2. Transmittance Curves for the Five DABS II-D-2 Filters (Concluded)

$$\int_{-\infty}^{\infty} \beta_1^f(\lambda) d\lambda \approx \beta_1^f(\lambda_1) \cdot \Delta\lambda_1 \quad (3.1b)$$

The small square detector cell response surfaces of 0.16 cm^2 area, A^c , define incremental "viewing" solid angles, $\omega^c = (A^c/v^2)$. Here v represents the image distance, defined by the geometric optics relation:

$$1/v = 1/F - 1/u \quad (3.2)$$

As usual, the symbols u and F in the preceding equation represent the object distance and the lens focal length. The focal length F is equal to 50.8 cm (20 inches) for all five lenses. All these relationships are shown in Figure 3-1. If the object distance u is taken to be equal to r , the distance from the viewing port into the gas volume to the lenses, then $v = 60.83 \text{ cm}$ (23.95 inches). Although not necessarily accurate, as will be seen later, this $u = r$ assumption was implicitly assumed in the earlier definition of the solid angle Ω subtended from the port aperture by the lenses.

With the v -distances equal to 60.83 cm, the detector cell viewing solid angles ω^c will each subtend $4.324 \cdot 10^{-5}$ steradians, with square cross sections of $6.576 \cdot 10^{-3}$ radians on a side. As is seen in Figure 3-1, the projections of these ω^c solid angles onto the plane of the viewing port are (slightly distorted) squares that are $6.576 \cdot 10^{-3}r$, or 2.027 cm on a side. Neglecting optical blurring, the diagonals of these squares are equal to $\sqrt{2} \cdot 2.027 \text{ cm} = 2.866 \text{ cm}$, and thus project only very slightly beyond the 2.858 cm diameter of the port aperture. Consequently, only very small corner segments of the ω^c fields of view are blocked off from entry into the port hole.

The radiation to be observed, however, actually emanates from molecules within the gas volume, rather than from the plane of the port. Radiation originating from within the boundaries of conical surfaces determined by the lens circumferences and the port aperture have "clear shots" at the total lens surface, while radiation from molecules outside of this conical surface have at least some part of the lenses obstructed. This is again illustrated in Figure 3-1.

The ideal condition, then, is that the ω^c fields of view not only pass without obstruction through the port opening, but also lie completely within the unobstructed portion of the conical surface until after some characteristic depth of penetration is achieved. It is easy to show that, if this ideal condition had been achieved, the

observed radiation signals then would have been independent of the depth distribution of radiating molecules. For, the solid angle subtended by the lens (Ω) and the incremental detector cell projection (S^g) terms occurring in equation (3.1a) then would have been equal to $\pi D^2/4(r + \delta r)^2$ and $\omega^c(r + \delta r)^2$ respectively for molecules at depth δr . Thus, for a sufficiently large view port aperture to allow unobstructed lens illumination by the gas molecules within the viewing solid angles ω^c , the product of these two terms reduce to

$$S^g \cdot \Omega = (\pi D^2/4) \cdot \omega^c \quad (3.3)$$

Consequently, equations (3.1) and (3.1a) would become independent of $r + \delta r$ and hence of the δr depth distribution of the observed radiating molecules, and all detectors would have an optically unobstructed view of radiating gases across the width of shock tunnel to the opposite wall.

With the 5.1 cm (2 inch) diameter lenses of 51 cm (20 inch) focal length used, it would have required an approximately 3.6 cm (1.4 inch) diameter port opening to collect unobstructed radiation originating from molecules 45 cm deep into the gas volume. A 4.7 cm (1.6 inch) diameter port opening would have provided unobstructed observation for $\delta r < 200$ cm. The actual 2.86 cm (1 1/8 inch) diameter port opening utilized was originally designed for DABS II-D-1 and became a compromise design for DABS II-D-2.

For DABS II-D-2 the smaller than optimum diameter view port will not effect the validity of substituting equation (3.3) into equation (3.1) or (3.1a) for the combustion product observations, since the high opacity of the carbon soot will insure that virtually all of the radiation to be viewed will originate quite close to the view port, and moreover, for about the same small mean δr for all wavelengths. Since the optical thickness $\bar{\tau}$ should be quite large for the $\lambda_1 \approx 0.26\mu$ shocked air radiation, equation (3.3) also should be a valid approximation for the λ_1 radiometer. The only real problem will be with the interpretation of the $\lambda_2 \approx 0.36\mu$ radiometer data. The computed optical thickness $\bar{\tau}$ was relatively low for $\lambda \approx 0.36\mu$, particularly at the lower air shock pressures to be observed. A scaling of Figure E-4 shows that the observed radiation at this wavelength may originate from an average of some tens of centimeters within the gas volume when the shock front first fills the viewing port, and from an average of up to ~ 80 to 100 cm deep before arrival of the combustion products. It thus will be partially obscured from fully illuminating the lens. The $(S^g \cdot \Omega)_{0.36\mu}$ product may therefore have to be adjusted downward from the value given by equation (3.3), particularly as the pressure decreases from that of the initial shock front passage.

When equation (3.3) is valid, a substitution of the numerical values of the lens diameter, $D = 5.08$ cm, $\omega^c = 4.324 \cdot 10^{-5}$ steradians and $\beta^{lens} = 0.9$ reduce the term outside the integral in equation (3.1) to:

$$S^g \cdot \Omega \cdot \beta^{lens} \approx (\pi D^2/4) \cdot \omega^c \cdot \beta^{lens} = 3.105 \cdot 10^{-4} \text{ cm}^2 \quad (3.4)$$

Thus, the effective radiant power input to the i^{th} radiometer becomes:

$$P_i^{input}(T) \approx 3.105 \cdot 10^{-4} \text{ cm}^2 \int_{\lambda_i - m_i(\Delta\lambda_i/2)}^{\lambda_i + m_i(\Delta\lambda_i/2)} I^o(\lambda; T) \beta_i^f(\lambda) d\lambda \quad (3.5)$$

for equation (3.3) valid, and reduces to

$$P_i^{input}(T) \approx 3.105 \cdot 10^{-4} \text{ cm}^2 \cdot I^o(\lambda_i; T) \beta_i^f(\lambda_i) \cdot (\Delta'\lambda_i/1\mu) \quad (3.5a)$$

for equation (3.3) valid and the $\beta_i^f(\lambda)$ filter functions having sufficiently sharp cut-off past the filter bandwidth. The constant $3.105 \cdot 10^{-4} \text{ cm}^2$ term in equation (3.5) or equation (3.5a) will cancel out when radiant power input, or voltage signal output ratios are taken. Figure 3-2 shows the filter parameters $\beta_i^f(\lambda_i)$ and $\Delta'\lambda_i$.

3.1 Radiometer Output Signals

Let V_i represent the i^{th} radiometer output signal in units of either volts or amperes. Then,

$$V_i = P_i^{input}(T) \cdot R_i \cdot G_i \quad (3.6)$$

Here R_i represents the response of the i^{th} radiometer detector cell (and its associated pre-amplifier) in units of volts per watt for the infrared radiometers, and of ampere per watt for the $\sim 0.26\mu$ wavelength and $\sim 0.36\mu$ wavelength radiometers: while G_i represents the gain setting on the corresponding amplifiers. It is seen by comparison with equations (3.5) and (3.5a) that when the respective criteria for the validity of these equations are met, that:

$$(v_i/v_j) \approx \left\{ \frac{\left[\int I^o(\lambda; T) \cdot \beta_i^f(\lambda) \cdot d\lambda \right] \cdot R_i \cdot G_i}{\left[\int I^o(\lambda; T) \cdot \beta_j^f(\lambda) \cdot d\lambda \right] \cdot R_j \cdot G_j} \right\} \quad (3.7)$$

$$(v_i/v_j) \approx \left[\frac{I^o(\lambda_i; T) \cdot \beta_i^f(\lambda_i) \cdot (\Delta'\lambda_i/1\mu) \cdot R_i \cdot G_i}{I^o(\lambda_j; T) \cdot \beta_j^f(\lambda_j) \cdot (\Delta'\lambda_j/1\mu) \cdot R_j \cdot G_j} \right] \quad (3.7a)$$

As in equations (3.1) and (3.5), the integrals in equation (3.7) are taken over the respective wavelength intervals of effectively non-zero $\beta_i^f(\lambda)$ and $\beta_j^f(\lambda)$. Figure 2-2 gives the $\beta_i^f(\lambda_i)$ and $\Delta'\lambda$, for the five radiometer systems used in DABS II-D-2.

4. ELECTRICAL SYSTEM FOR DABS II-D-2 TEST

Once the detector center frequencies and predicted temperature range were established, the detection and signal conditioning circuit designs were determined as follows: two distinct circuit designs were required, a photovoltaic silicon PIN diode design for the two ultraviolet detector channels and a photoconductive lead-selenide design for the three infrared detector channels. Figure 4-1 shows the schematic of the total circuit hookup, from detector to tape recorder.

4.1 Photovoltaic Circuit

The optical signal from the silicon PIN diode is a single direction pulse whose output is amplified by a single stage current preamplifier. This amplified signal is then fed into a dual stage line driver amplifier system to transport the electrical signal over the 1500 feet of land line through RG58 coaxial cable to the instrumentation trailer, where the tape recording equipment was located.

The tape recorder input preamplifiers were set to provide D.C. offset so that the single-direction pulse would use the full scale minus to plus modulation of the recording band. In addition, to insure high resolution results the input signal was split for dual range recording of each channel. This resulted in a 20 to 1 difference in signal levels between the two channels. The tape recorder was operated in the FM mode, Group I wideband at 120 IPS tape speed.

4.2 Photoconductive Circuit

The lead-selenide circuit was designed with a single stage voltage preamplifier circuit. The preamplifier integrated circuit was located as close to the detector as possible to minimize high frequency roll off due to shunt capacitance between the lead-selenide preamplifier element and the input to the preamplifier. Similarly, controls were remotely located in the bottom of the optical detector box. The amplified signal was fed into a dual stage line driver stage. The electrical signal was transported over 1500 feet of land line to a recording set up similar to that described in section 4.1.

The expected minimum and maximum signal level corresponding to estimated temperature ranges for each channel is presented in Table 4-1. The dynamic range of the electronics is presented in terms of a dynamic range ratio in the same figure.

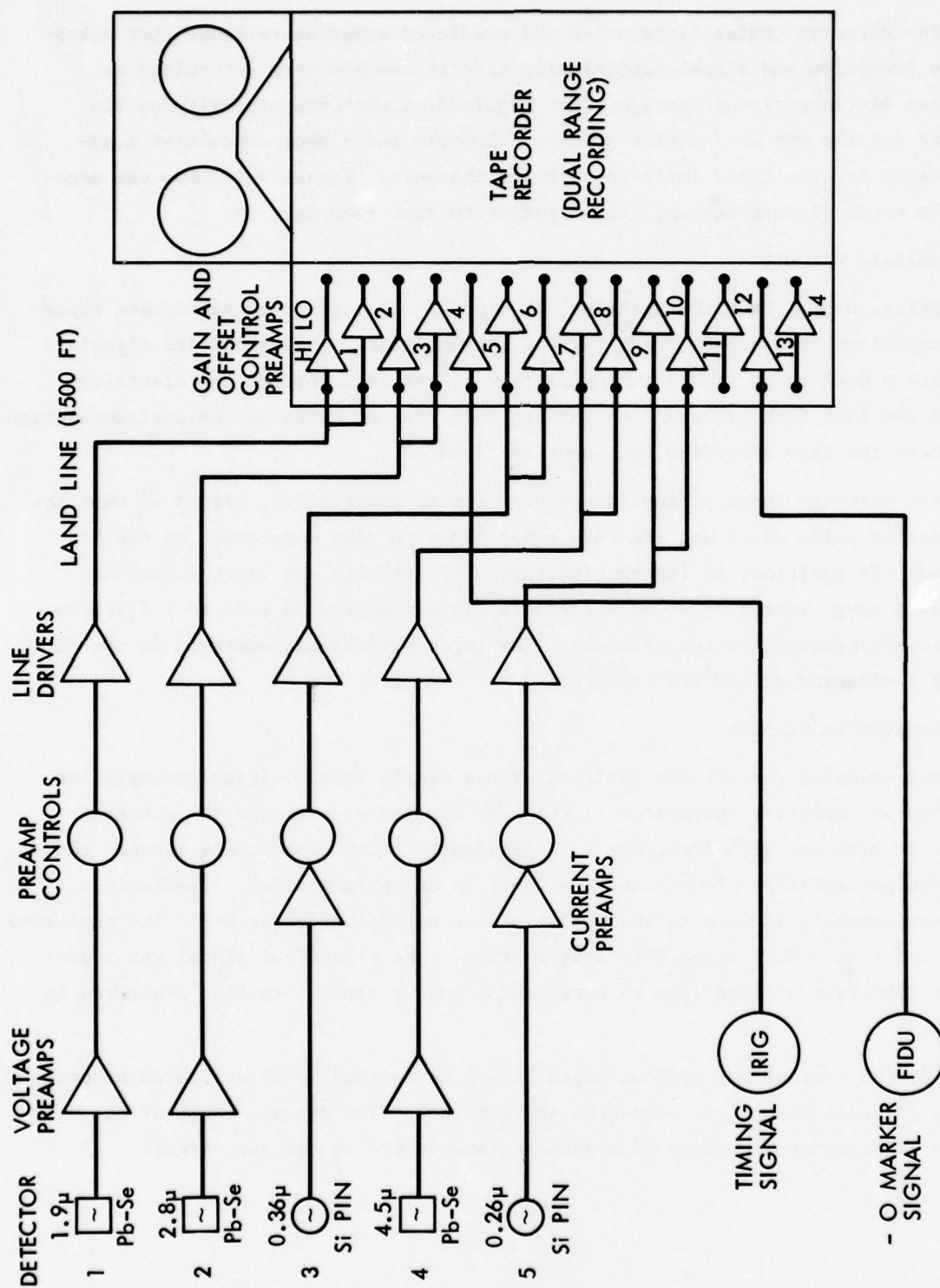


Figure 4-1. Schematic of Optical Pyrometer Electronics

Table 4-1. Tabulated Expected Electrical Signal Range
for Predicted Shock Tunnel Temperatures

NO.	TYPE	WAVELENGTH	TEMP RANGE		SIGNAL RANGE		DYNAMIC RANGE RATIO (MAX/MIN)
			MIN	MAX	MIN	MAX	
1	Pb-Se	1.9 μ	500 °K	800 °K	0.0092 mV	2.8 mV	50 dB
2	Pb-Se	2.8 μ	500 °K	800 °K	0.2 mV	8.3 mV	32 dB
3	Si PIN DIODE	0.36 μ	3300 °K	4300 °K	1.2 μ A	36.0 μ A	30 dB
4	Pb-Se	4.5 μ	500 °K	800 °K	0.7 mV	9.2 mV	22 dB
5	Si PIN DIODE	0.26 μ	3300 °K	4300 °K	0.003 μ A	1.8 μ A	56 dB

5. MECHANICAL INSTALLATION FOR DABS II-D-2 TEST

The primary purpose of the equipment pit installation design is to provide an optical window into the shock tube which will protect the optical radiometer/electronics from damage, and provide a stable seismic base during the 5 msec measurement envelope. A schematic depicting the side elevation section of the installation is shown in Figure 5-1 (not to scale).

The main functional components of the design are: 1) the wedged aerodynamic wing section which provides a window through the cooler boundary layer gases into the main shock region, the 2.86 cm (1 1/8 inch) diameter port provides the main optical aperture for viewing the shock wave, 2) the 4.57 cm (18 inch) long optical port provides a uniform cross sectional area which allows pressure and temperature values to remain constant for the first 0.15 msec of the test. This prevents the optical detectors from having to look through a cooler gas volume during the critical first stage compressed air shock, 3) the cylindrical cavity providing approximately a 100 to 1 area expansion, and along with the three baffle plates provide a means to reduce the final pressure at the instrumentation pit to a level compatible with equipment survival, 4) the three foam inserts were designed to accommodate ground displacement and attenuate the induced wave propagation through the soil, 5) the seismic mass was designed to provide an adjustable stable platform for placement of optics.

The pit was lined with a thin plastic sheet to keep moisture and dirt from the optical box prior to test. The addition of the lid wrapped with excess plastic sheet provided the system with protection from the elements during the check-out and calibration periods prior to the test. Finally a sand overburden was placed over the lid and baffle area to protect the pit from debris during the test.

Figure 5-2 is a series of photographs showing the actual instrumentation used to obtain the temperature history test data. Photograph (a) shows the complete instrumentation package, the black optical box on the right contains the lenses, filters, detectors and detector amplifier stages. The package on the right contains the power supply and line driver amplifiers.

Photograph (b) shows the interior of the optical box. The front panel contains five lens holders which can be adjusted for various focal lengths to maximize the signal at each detector. The rear panel has the five detector/filter assemblies mounted so that they remain parallel to the front lens plane. The bottom of the optical box contains the detector amplifiers and associated electronics. Photograph (c) provides a clear view of

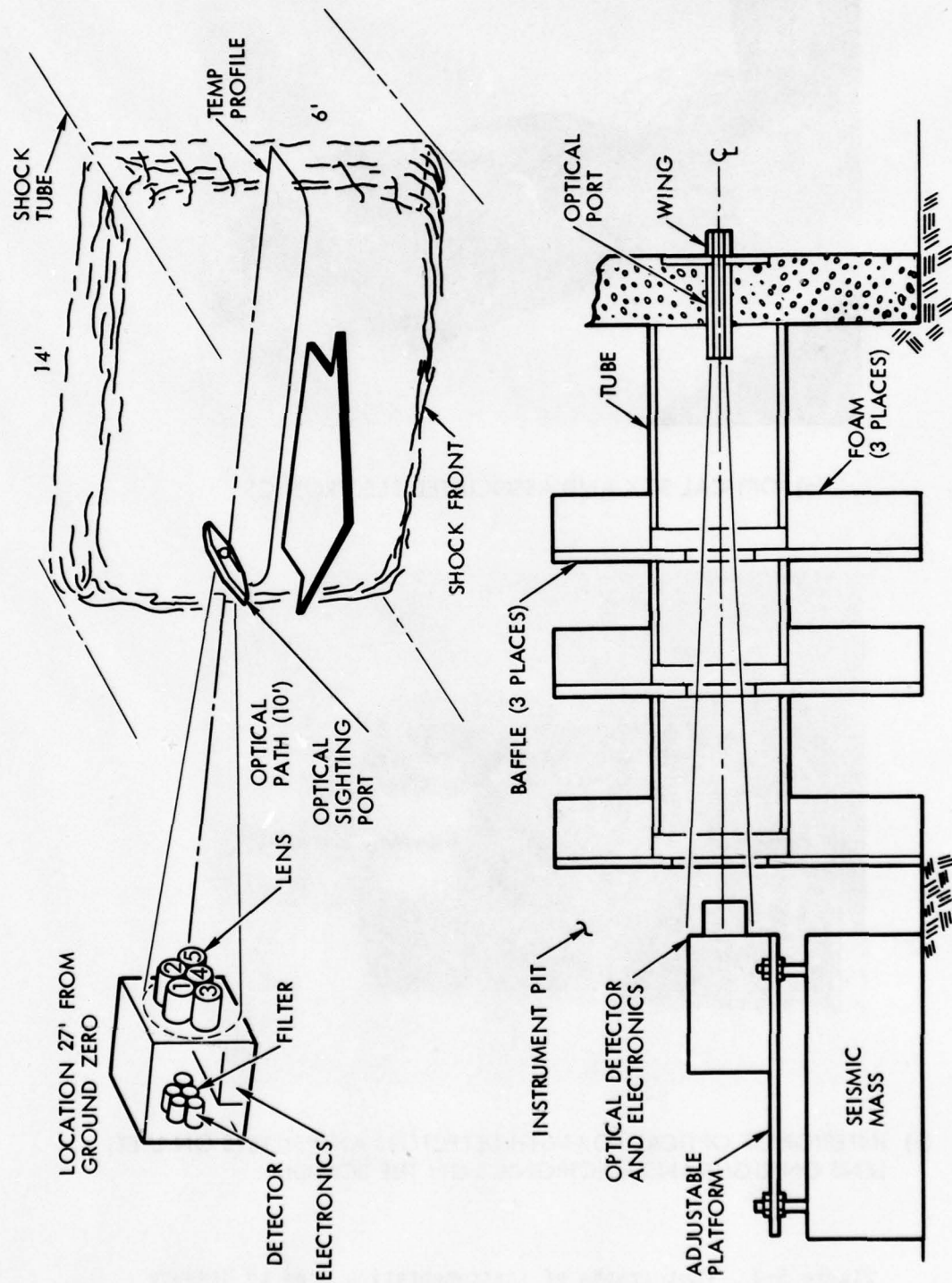
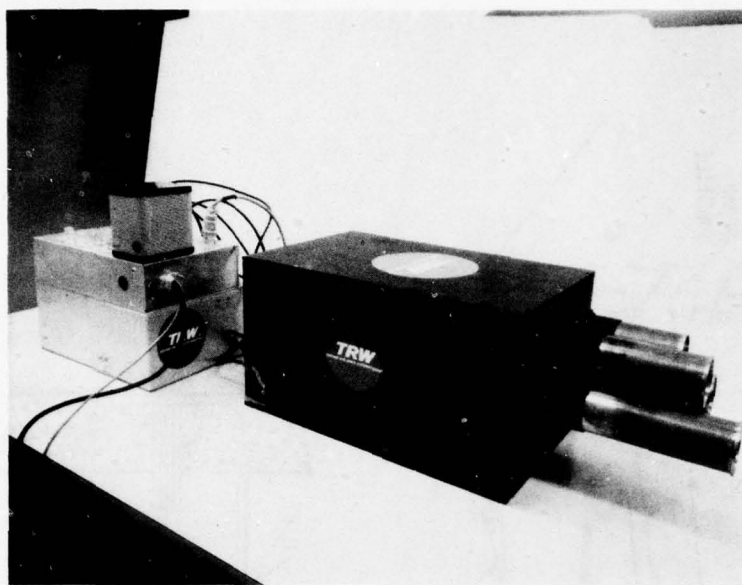
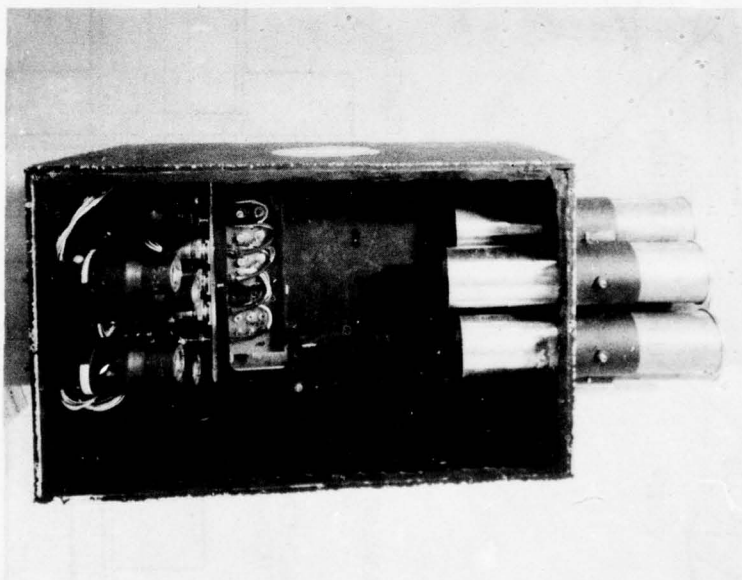


Figure 5-1. Schematic of Mechanical Installation



(a) OPTICAL BOX AND ASSOCIATED ELECTRONICS



(b) INTERIOR OF OPTICAL BOX WITH DETECTORS AND FILTERS ON LEFT, LENS ON RIGHT AND ELECTRONICS ON THE BOTTOM

Figure 5-2 Photographs of Instrumentation used to Measure Temperature History Data



(c) DETECTOR ASSEMBLIES WITH TWO OF THE FILTERS REMOVED



(d) FIELD INSTALLIZATION SHOWING EQUIPMENT IN INSTRUMENTATION PIT AFTER TEST

Figure 5-2 Photographs of Instrumentation used to Measure Temperature History Data (Concluded)

the detector/filter assembly. Two of the assemblies have their filters removed to expose the detectors inside. The upper detector is a lead-selenide photoconductive detector, while the bottom unit shows a silicone PIN diode photovoltaic detector.

The last photograph (d) shows the instrumentation pit at the test site. This photograph was taken after the test. The complete equipment package survived the test shock with the only damage occurring to the land lines. These coaxial lines were pulled out from the connectors on the rear instrumentation package, as clearly shown in the lower left of the photograph.

6. ANALYSES OF THE DABS II-D-2 TEST DATA

The optical temperature data generated by the DABS II-D-2 test consisted of two ultraviolet radiometer channels and three infrared radiometer channels. As mentioned earlier, the data obtained from the three infrared channels could not be interpreted due to spurious noise interference during the test. These signals saturated the electronics and rendered the infrared data meaningless. The results presented in sub-section 6.1 will consist of an analyses and interpretation of the ultraviolet channel data, while sub-section 6.2 will present a discussion of some secondary, non-temperature related inferences obtainable from the temperature history information.

6.1 Primary Results: Temperature Histories

The temperature history results for the DABS II-D-2 test are clearly shown in Figure 6-1. The data points shown on this figure were obtained by reading voltage values at selected time intervals from oscilloscope traces which had been reproduced from the master data tape. Figure 6-2 displays typical traces used to obtain these voltage-time data points. Next, these voltage readings were converted to temperature measurements by reading the calibration values off Figure 6-3 for the two color pyrometer temperatures and Figure 6-4 for one color pyrometer temperatures. All the 0.26μ and 0.36μ ultraviolet wavelength temperature data shown in Figure 6-1 were obtained in this manner.

The information presented in Figure 6-1 can be divided into five areas of interest.

- Precursor interval ($t < 0$)
- Air shock arrival at test station ($t = 0$)
- Compressed air shock interval ($0 \leq t < 0.8$ msec)
- Contact surface arrival at test station ($t \approx 0.8$ msec)
- Combustion products interval ($t > 0.8$ msec)

In addition, theoretical temperature envelopes representing the Rankine-Hugoniot relationship, with isentropic expansion of the shock compressed air are presented for comparison. The upper limit is defined by pre-test predictions from peak pressure of 83.3 atmospheres (1225 psia) at the 8.2 m (27 ft) station. The lower bound was obtained from AFWL post-test data [1] which presented a average peak pressure of 67.2 atmospheres (987 psia) at the same station. Both theoretical curves represent a constant gas constant of $\gamma = 1.3$. For convenience the arrival of the peak pressure at the station is used as the $t = 0$ time reference point.

The precursor region corresponds to forward scattered radiation arriving before the shock front enters the radiometer fields of view. A short and fairly reliable extrapolation of the forward scattered precursor temperature signal indicates that the

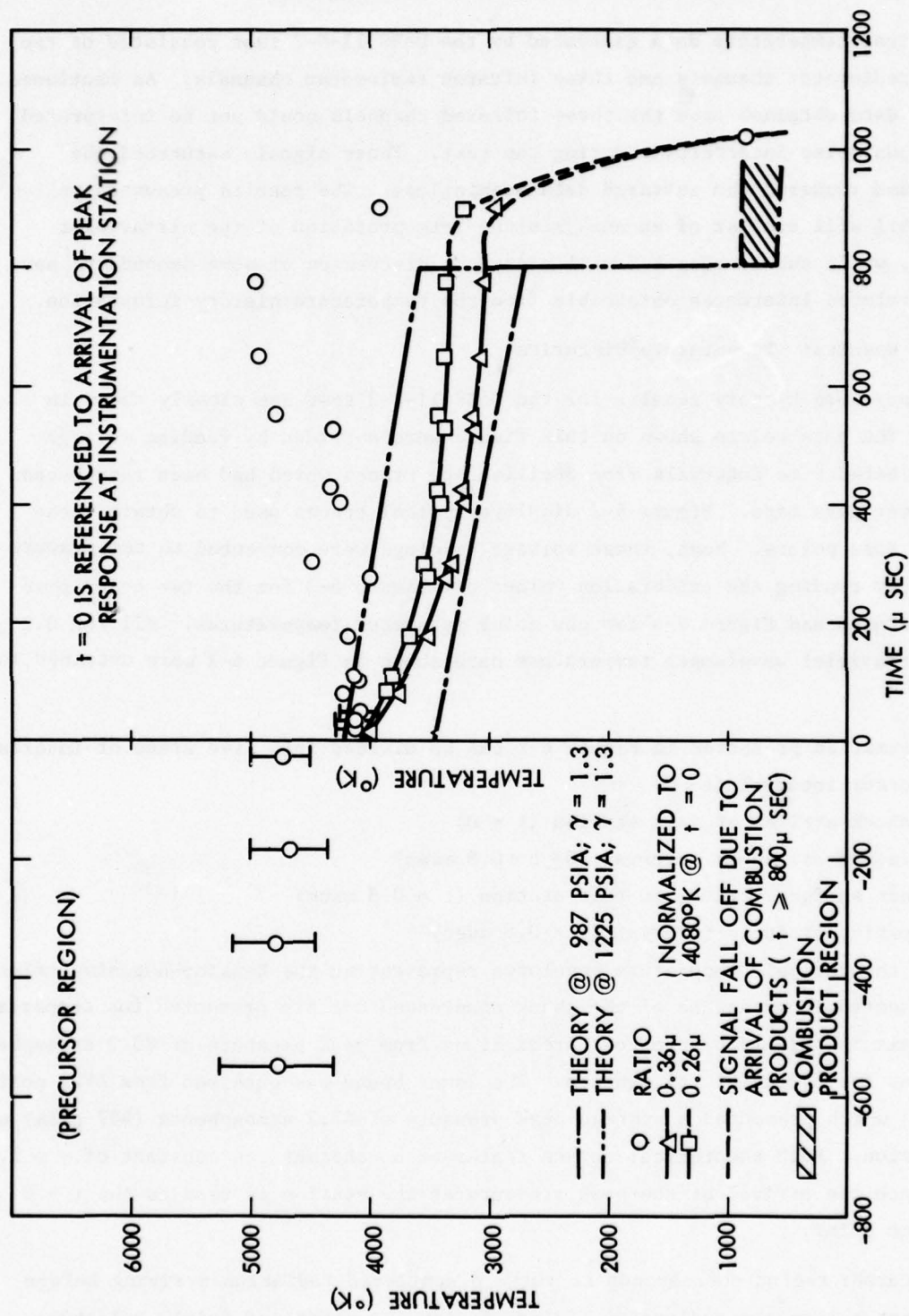
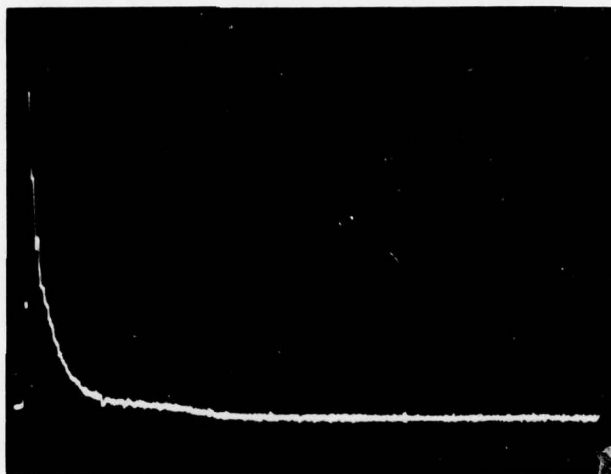
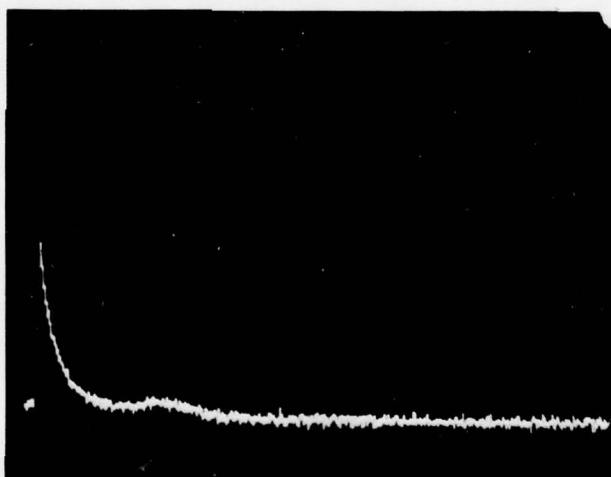


Figure 6-1. DABS II-D-2 Experimental Results for Both
 One Color and Two Color Pyrometers



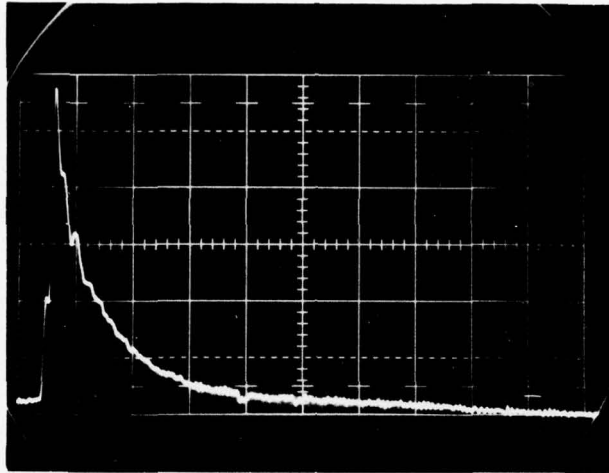
(a) 0.36 μ CHANNEL



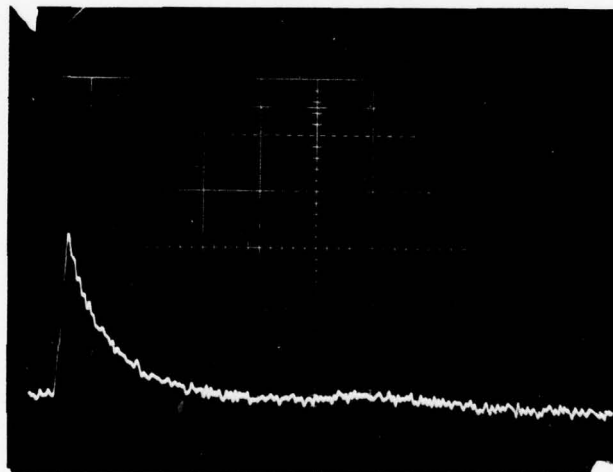
(b) 0.26 μ CHANNEL

TRACES (a) and (b): SHOCK FRONT ARRIVAL THROUGH SIGNAL DECAY INTO NOISE. VERTICAL SCALES ARE 0.5 VOLTS/CM AND HORIZONTAL SCALES ARE 312.5 μ SEC/CM, REAL TIME.

Figure 6-2. DABS II-D-2 Ultraviolet Radiometer Signal Tracings



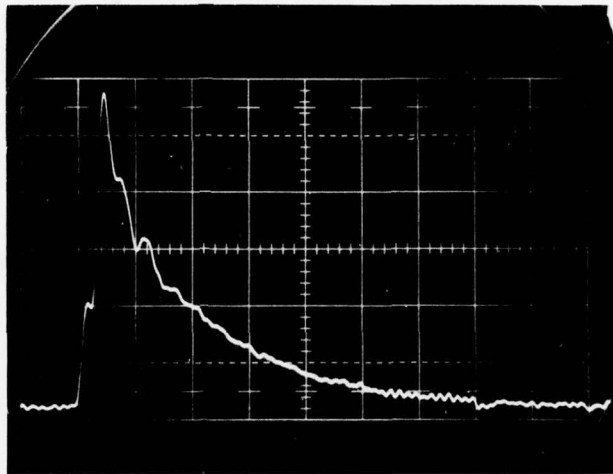
(c) 0.36 μ CHANNEL



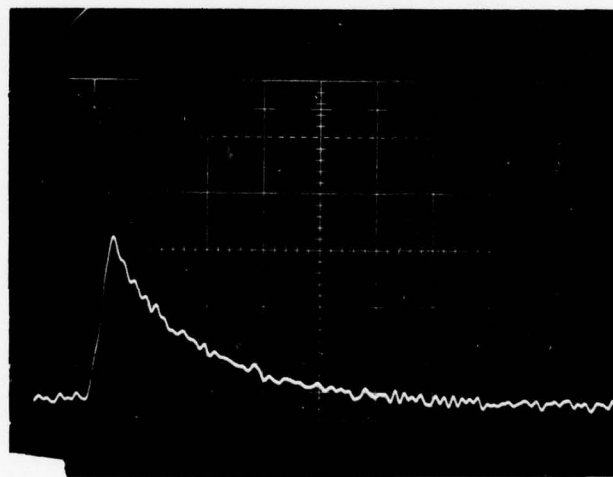
(d) 0.26 μ CHANNEL

TRACES (c) AND (d): SHOCK FRONT ARRIVAL THROUGH OPTICAL SIGNAL TAIL-OFF
 OWING TO ARRIVAL OF COMBUSTION PRODUCTS. VERTICAL
 SCALES ARE 0.5 VOLT/CM AND THE HORIZONTAL SCALES
 ARE 125 μ SEC/CM, REAL TIME.

Figure 6-2. DABS II-D-2 Ultraviolet Radiometer Signal Tracings (Continued)



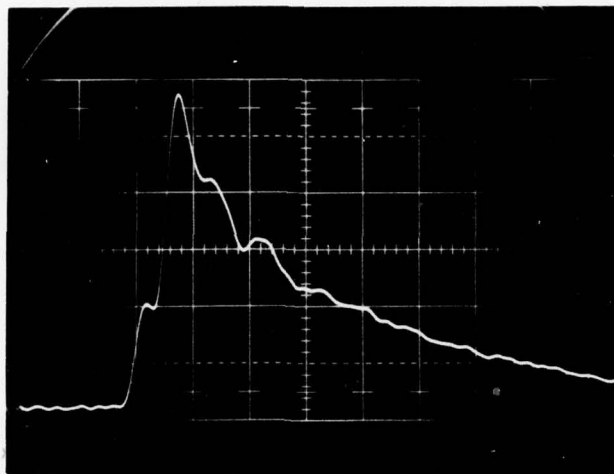
(e) 0.36 μ CHANNEL



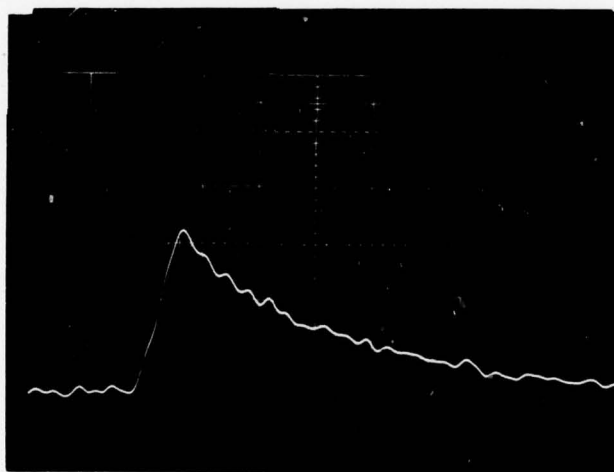
(f) 0.26 μ CHANNEL

TRACES (e) AND (f): TIME SCALE EXPANSION OF EARLY PORTIONS OF TRACES (c) AND (d) RESPECTIVELY. VERTICAL SCALES ARE 0.5 VOLT/CM AND HORIZONTAL SCALES ARE 62.5 μ SEC/CM, REAL TIME.

Figure 6-2. DABS II-D-2 Ultraviolet Radiometer Signal Tracings (Continued)



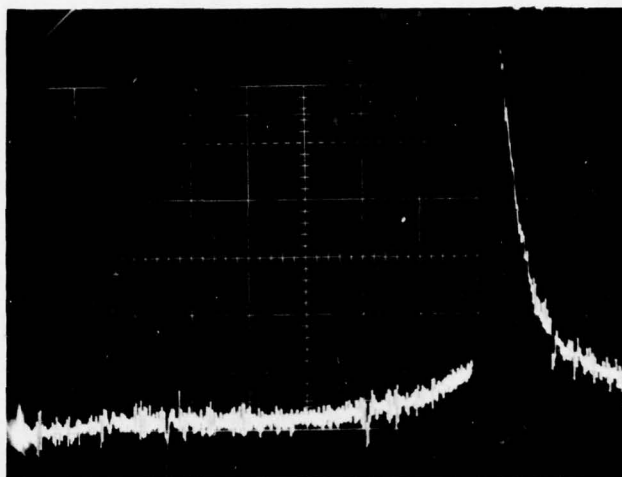
(g) 0.36 μ CHANNEL



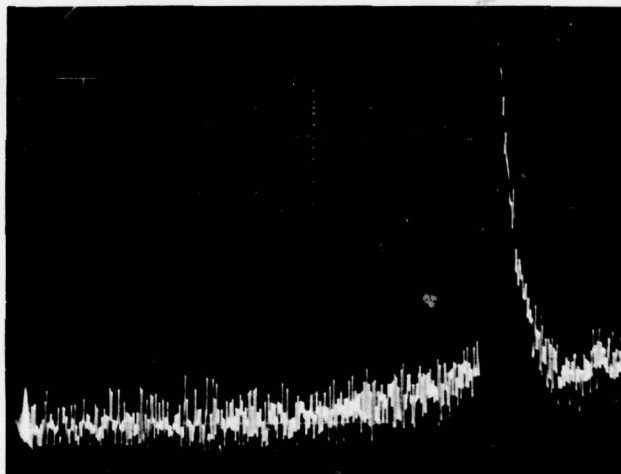
(h) 0.26 μ CHANNEL

TRACES (g) AND (h): A STILL FURTHER TIME SCALE EXPANSION OF VERY EARLY PORTIONS OF TRACES (c) AND (d) RESPECTIVELY. VERTICAL SCALES ARE 0.5 VOLTS/CM AND THE HORIZONTAL SCALES ARE 31.25 μ SEC/CM, REAL TIME.

Figure 6-2. DABS II-D-2 Ultraviolet Radiometer Signal Tracings (Continued)



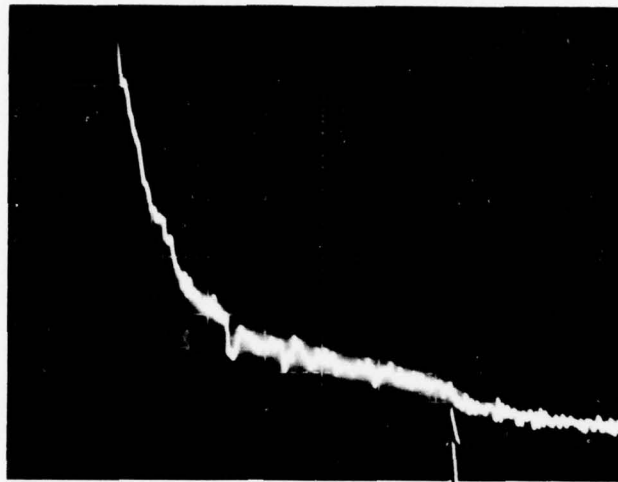
(i) 0.36 μ CHANNEL



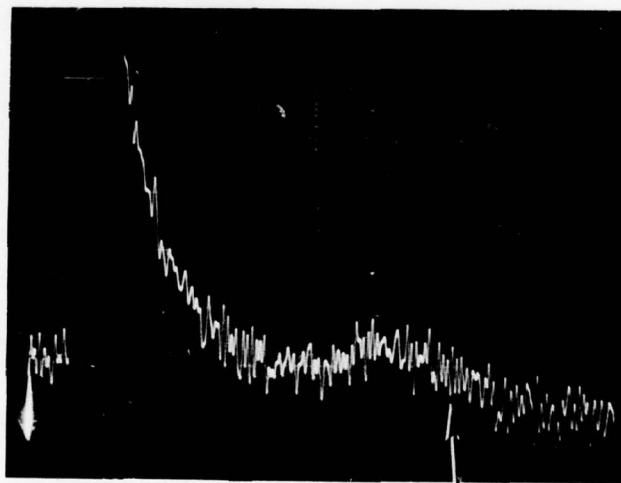
(j) 0.26 μ CHANNEL

TRACES (i) AND (j): EXPANDED SCALE OPTICAL RADIATION PRECURSOR SIGNALS OWING TO FORWARD SCATTERED RADIATION BEFORE ARRIVAL OF THE SHOCK FRONT AT THE OBSERVING STATION (+ NEGATIVE, SINCE ARBITRARILY SET EQUAL TO ZERO AT TIME OF PEAK PULSE ARRIVAL). VERTICAL SCALE IS 0.1 VOLT/CM AND THE HORIZONTAL SCALE IS 312.5 μ SEC/CM, REAL TIME.

Figure 6-2. DABS II-D-2 Ultraviolet Radiometer Signal Tracings (Continued)



(k) 0.36 μ CHANNEL



(l) 0.26 μ CHANNEL

TRACES (k) AND (l): RADIATION SIGNAL FALL-OFFS SHOWING ARRIVAL OF COMBUSTION PRODUCTS. VERTICAL SCALE IS 0.1 VOLT/CM AND HORIZONTAL SCALE IS 125 μ SEC/CM, REAL TIME.

Figure 6-2. DABS II-D-2 Ultraviolet Radiometer Signal Tracings (Concluded)

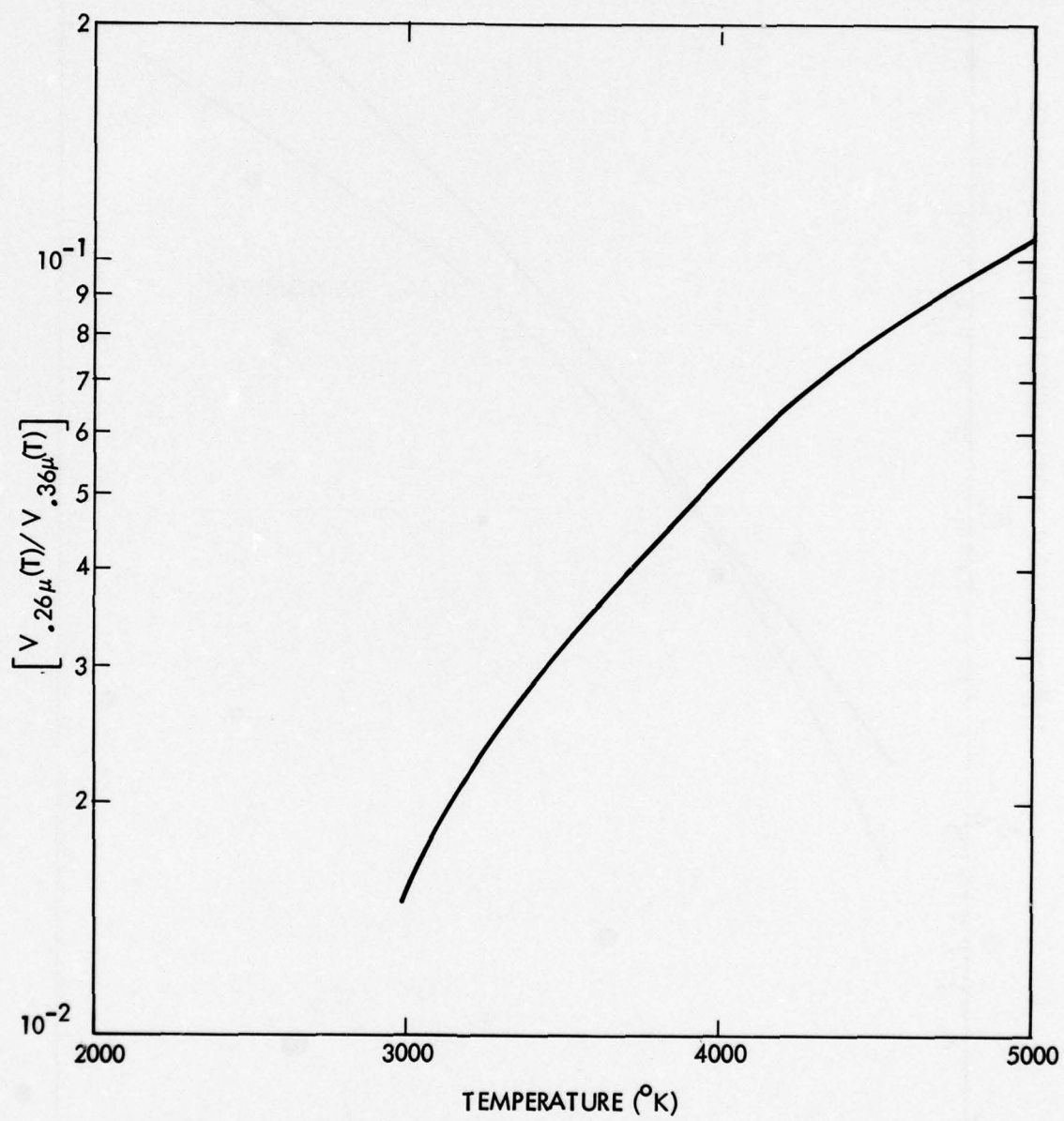


Figure 6-3. Two Color Pyrometer Calibration Curve for the Ultraviolet Radiometers

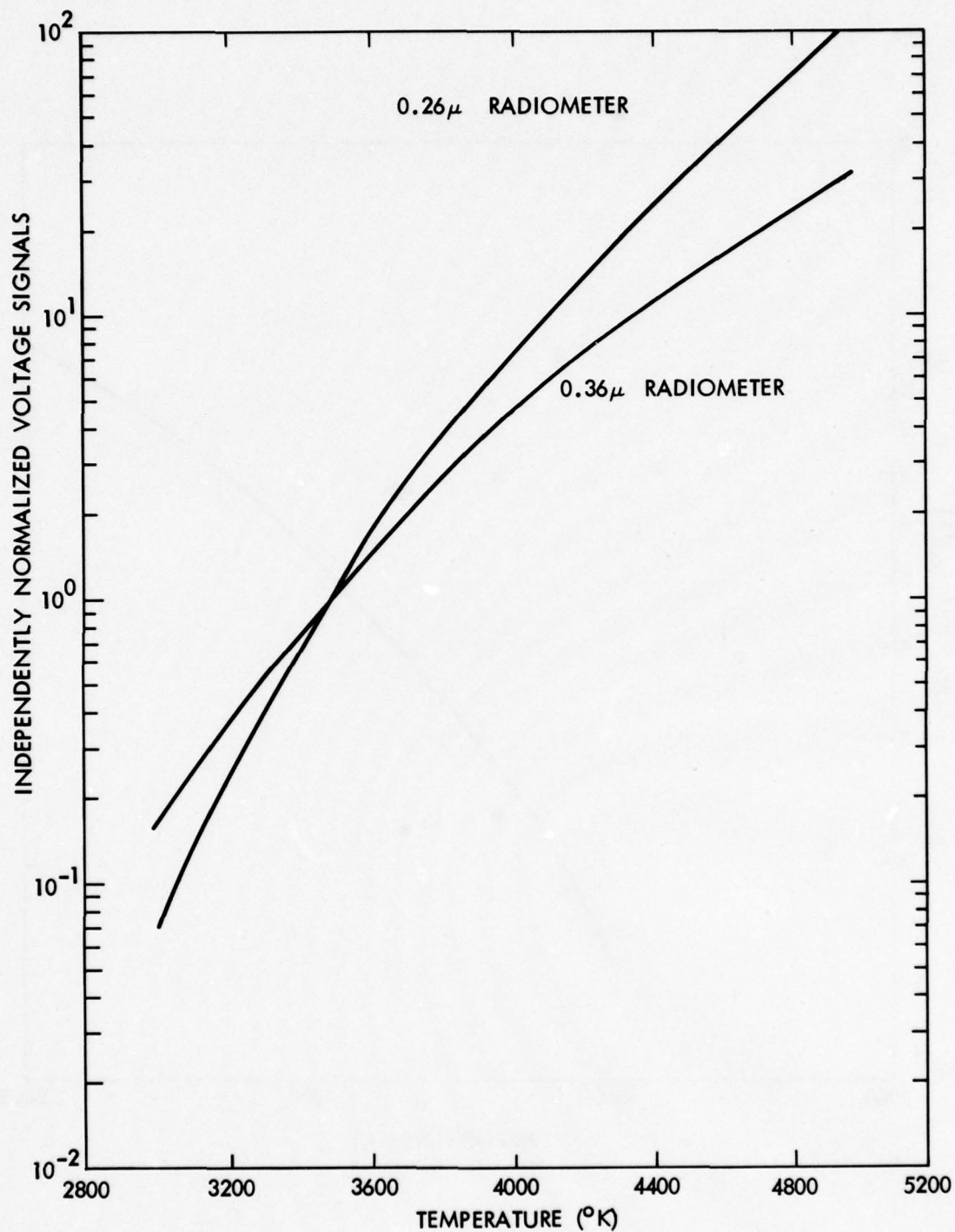


Figure 6-4. One Color Pyrometer Calibration Curves for the Ultraviolet Radiometers

mean temperature averaged over the entire shock front was of the order of $\sim 4600^\circ\text{K} \pm 250^\circ\text{K}$. At $t = 0$, corresponding to the arrival of the peak air blast pressure, the two color pyrometer temperature (near port) is 4080°K with random error of the order $\pm 50^\circ\text{K}$. As the shock front propagates downstream, the mean temperature of the viewed air volume in front of the port aperture decreases. Shortly before the arrival of the contact surface, at approximately $t = 0.78$ msec the mean temperature in the air volume as determined from the one color 0.26μ wavelength pyrometer is 3410°K within a random error of $\pm 100^\circ\text{K}$. Similarly, the one color 0.36μ wavelength pyrometer recorded a mean temperature of 3150°K (corrected), with a random error of $\pm 80^\circ\text{K}$. The above random error data was measured from recorded signal noise data that appears on the photographs in Figure 6-2.

The ultraviolet channels are incapable of measuring the low combustion product temperatures. Since the infrared data was lost, a mean absolute temperature for combustion product gases cannot be determined. The one color ultraviolet pyrometer readings shows a rapid drop off in signal level in the 0.85 to 1.0 msec range, thus indicating the arrival of the cooler combustion product gases. This value is within 0.05 msec of the predicted theoretical value.

The temperature curves exhibit the expected exponential decay between peak pressure and contact surface arrival times. The data is in good agreement with the theoretical values. Moreover, Figure 6-5 present data that graphically displays the sensitivity of these theoretical curves to changes in gas constant (γ) and pressure. These results show that the use of $\gamma = 1.3$ as a mean gas constant is supported by these test results.

A more detailed discussion of all the test results will be presented in the following sub-section.

6.1.1 Detailed Discussion of DABS II-D-2 Results

As mentioned in the preceding section, all the two color pyrometer temperature measurements used the Figure 6-3 theoretical voltage signal ratio versus temperature calibration curve for the 0.26μ and 0.36μ wavelength radiometer pair. It is similar to the I_1/I_2 versus temperature curve in Figure A-4 except that it applies directly to the measured voltage rather than spectral radiance ratios. The actual voltage ratio was computed by numerical convolutions from equation (3.7), since the transmission of the two spectral filters and particularly the 0.26μ wavelength bandpass filter, decayed too slowly to use the approximation of equation (3.7a).

The usable two color pyrometer data was limited to the precursor region ($t < 0$), the peak arrival time ($t = 0$) and approximately the first 20 μsec of the compressed air shock front. The accuracy of the two color pyrometer starts to decrease for $t > 20 \mu\text{sec}$ as will be discussed later. The two color pyrometer data is represented

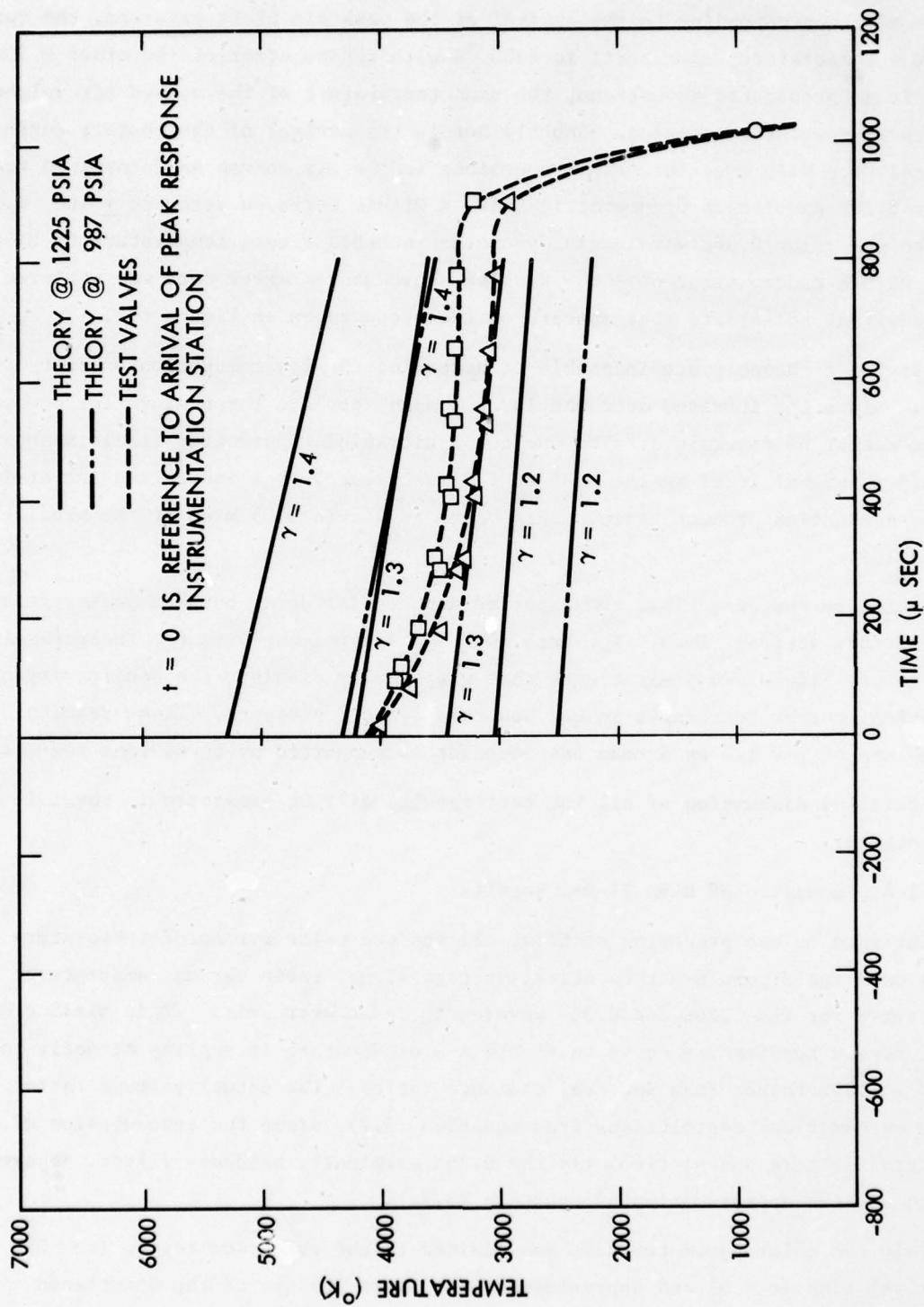


Figure 6-5. Variations in Theoretical Results as a Function of Gas Constant (γ) for Two Pressure Ranges of Interest

in Figure 6-1 by circles around each data point corresponding to $(V_{0.26\mu}/V_{0.36\mu})$ voltage ratios; error estimates are represented by the vertical bars.

The plotted points in the precursor region (negative t) indicates a large variance in measured real temperature. The gradual rise of the two voltage signals above their noise level (see Figures 6-1i and 6-1j) is almost certainly due to forward scattered radiation reflected off the chamber walls and into the radiometer fields of view. The emitting layer is probably a little deeper for the 0.36μ wavelength than for the 0.26μ wavelength radiation, but this difference in optical depth should be appreciably less than for the directly viewed radiation. Contributions to this forward scattered radiation should arrive from virtually the entire shock front rather than from the restricted local areas within the radiometer fields of view as is true for the directly viewed radiations. The large error ranges indicated arise from the low signal to noise ratios and, as a systematic error, from the difficulty in assessing "zero signal levels" from which the voltage is measured. The failure of the indicated temperature to decrease slightly with time probably is due to measurement errors. It is unlikely that the several hundred degree differential between the indicated forward scattered radiation temperature "points" and the peak response temperature, at $t = 0$, is due to systematic errors. It is more probable that the weight mean temperature over the entire shock front given by the forward scattered radiation is higher than the temperature of the gas near the port aperture. It also is possible that the diffuse reflectivity of the inner walls of the shock chamber could be slightly greater near 0.26μ than near 0.36μ , thus increasing the ratio of the 0.26μ signal to the 0.36μ signal in the precursor region so as to give the appearance of higher temperature than actually exists. It is difficult to obtain ultraviolet reflectivity coefficients in the literature to check this latter possibility.

The two theoretical envelopes indicate a dropping temperature after passage of the shock front past the observation station. The voltage signal tracing reproduced in Figures 6-1a through 6-1l exhibit decays consistent with dropping radiant power inputs, and hence dropping temperature. The plotted two color pyrometer data points (open circles in Figure 6-1), however, appear to show somewhat random oscillations about a rising rather than falling temperature pattern. This apparent inconsistency readily was explained by further analysis.

As was previously mentioned, shock heated air exhibits appreciably weaker absorption coefficients, and correspondingly deeper optical penetration, at 0.36μ than at 0.26μ . This would not have mattered if the necessary assumption of approximately uniform temperature in gas layers parallel to a presumably planar shock front were valid. (This assumption probably would have been more valid for the original DABS II-D-1 configuration than for the substitute DABS II-D-2 configuration with its appreciably smaller downstream range to chamber width ratio). It is clear, however, that the

0.26 μ wavelength radiometer is more sensitive to temperature variations occurring very close to the viewing port, while the 0.36 μ wavelength radiometer will respond more to temperature variations deeper into the shock chamber.

Very soon after the passage of the main shock front across the port aperture, a secondary perpendicular shock front is propagated down the 45.7 cm (18 inch) pipe projecting normally from the viewing port, (see Figure 5-1). It was initially expected that the air in this pipe would not differ appreciably in temperature, and if anything be slightly cooler, than the air in the main chamber adjacent to the viewing port. Further analyses revealed, however, that while this would be true for most of the pipe length, the diverted air will be heated by reflected shocks off the pipe inner surface during the first very few inches of propagation. This few inches is sufficient to strongly influence the radiation signal to the 0.26 μ wavelength radiometer, but would make relatively negligible contribution to the 0.36 μ wavelength radiometer signal.

It thus appears that only those two color pyrometer data points plotted in Figure 6-1 for $t < 20$ μ sec correspond to actual temperatures. The other two color pyrometer data points correspond merely to ratios of received spectral radiance emanating from overlapping gas volumes of different mean temperatures.

Insufficient empirical data exists for the accurate absolute calibration of the 0.26 μ and 0.36 μ wavelength radiometers as "one color pyrometers". Moreover, it is very difficult and expensive to obtain reliable black body (or pseudo black body) sources for ultraviolet wavelengths at temperatures above ~ 3000 $^{\circ}$ K to perform this absolute calibration. However, fairly reliable relative one color pyrometer calibration can be made, because the two color pyrometer data points for $0 < t < 20$ μ sec shown in Figure 6-1 represent meaningful mean temperature for the gas volume inside the main chambers and in the near vicinity of the viewing port. The numerator and denominator of equation (3-7) were previously computed for a selected set of temperatures in order to compute the two color pyrometer ratio curve shown in Figure 6-3. Theoretically, each of these quantities is proportional to the corresponding 0.26 μ and 0.36 μ wavelength radiometer output voltages for the corresponding temperature. The unknown constants of proportionality are eliminated by dividing each set of computed values through by its corresponding value for $T = 3500$ $^{\circ}$ K. The resulting one color pyrometer data evaluation curves are shown plotted in Figure 6-4. They are separately normalized to an arbitrary pseudo voltage signal of unity at $T = 3500$ $^{\circ}$ K, but are not normalized with respect to each other.

The best two color pyrometer estimate of temperature, evaluated from Figure 6-1, is $T = 4080$ $^{\circ}$ K at $t = 0$ (peak pulse). It is seen that for 4080 $^{\circ}$ K, the normalized one color pyrometer curves of Figure 6-4 give (pseudo) voltage readings of 5.1 "volts"

for the 0.36μ radiometer and 9.3 "volts" for the 0.26μ radiometer. When expanded to the same arbitrary vertical scale the signal voltage output tracings gave $t = 0$ readings of 51.0 for the 0.36μ wavelength radiometer and an average of 28.8 for the 0.26μ wavelength radiometer. The tracing readings for any later time t were first normalized to these respective $t = 0$ values before entering the corresponding one color pyrometer curve in Figure 6-4. This was done by multiplying the tracings vertical coordinate readings by $(5.1/51.0) = 0.10$ for the 0.36μ wavelength radiometer, and by $(9.3/28.8) = 0.323$ for the 0.26μ wavelength radiometer. The two resulting computed one color pyrometer temperature histories also are plotted in Figure 6-4. It is seen that they give reasonable appearing temperature decays, with the apparent mean temperatures differential between the two radiometers gradually increasing to $\sim 360^\circ\text{K}$ near 0.8 msec before the arrival of the combustion gases.

There possibly may be some fall off of emissivity below ~ 1 for the received 0.36μ wavelength radiometer radiation signal near 0.8 msec. The principal non-temperature related signal decay mechanism, however, is the partial occlusion of the radiation collecting lens by the edges of the port aperture. From the discussion in Section 3, it follows that as temperature and pressure decrease, and the relative radiation contributions from molecules progressively deeper behind the port aperture increase, this partial occlusion will cause increasing fractional signal loss in the 0.36μ wavelength channel. It is quite possible that this occlusion related signal loss, which does not effect the 0.26μ wavelength channel, is responsible for some fraction of the apparent temperature differential increases between the two channels.

6.1.2 Comparison of Measured with Theoretical Temperatures

The theoretical temperature pressure curves presented in Figures 1-1 through 1-4, and the data on Table 1.1 were based the somewhat idealized and simplified Rankine-Hugoniot relationships for shock front parameters (P_s, T_s), and upon similarly simplified isentropic decay theory for the relationship of temperature to pressure decay ratios behind the shock front at a given observation station. These relationships are given by equation (1.1) and (1.2) in section 1.0. The theories behind both these simplified equations utilize the convenient and empirically justified fiction that γ , the ratio of C_p the specific heat at constant pressure to C_v , that at constant volume (i.e., $\gamma = C_p/C_v$), remains constant during propagation of the shock front and also during the assumed isentropic expansion and cooling of the air behind the shock front [2]. Moreover, the figures and theoretically computed data presented in Section 1.3 used the additional first order assumption that γ was equal to its cold air value of 1.4, i.e., the γ -value in front of the shock. Also, from previous empirical observations it was assumed that the contact surfact, between the shocked air layer and the

combustion gases, would arrive at approximately half shock front pressure, i.e., when $(P_i/P_s) \sim 0.5$. From Figure 1-3 and Table 1.1 it is seen that the contact surface (or $P_i = 0.5 P_s$) was predicted to pass the DABS II-D-2 observation station ~ 0.8 msec after passage of the shock front. It can be seen in Figure 6-1 that this δt prediction was quite good.

It is quite obvious from theoretical considerations that γ really cannot and does not remain constant either on the propagating shock front or behind it. The partition functions of the constituent air molecules increase markedly with increasing temperatures, and with them, the internal energy contributions of these molecules to C_v . Thus, C_v must increase with temperature, and since $C_p = C_v + R$, the value of γ must correspondingly tend to decrease toward unity for very high temperatures. Moreover, the shocked air chemistry, as is shown in Figures D-1 and E-1, alters the mole fractions of constituent air species molecules, and thus alters the γ values as a function of pressure and temperature.

A higher order approximation to shocked air temperature pressure relations is to still use equations (1.1) and (1.2), but to substitute suitably selected effective mean values of γ for the first order $\gamma = 1.4$ approximation. A 1970 DASA report by H. L. Brode [2] presents data from which such effective mean shocked air γ values can be extracted for varying shock front pressures, P_s . Assuming these γ values to be approximately correct, and also that the shock front pressures P_s are known, corresponding shock front temperatures, T_s , can be computed from equation (1-1). Then isentropic decay temperatures, T_i , can be computed for selected (P_i/P_s) ratios from equation (1.2). This was done to generate the theoretical temperature curves shown in Figures 6-1 and 6-5, using the previously mentioned additional assumption that $(P_i/P_s) \sim 0.5$ at $t \sim 0.8$ msec after the shock front passage by the observation station.

It is seen in Section 1.3 that the predicted shock front pressure for the DABS II-D-2 observation station was $P_s \sim 83.3$ atmospheres (or 1225 psia). Allowing for pressure gage "overshoot", this value is reasonably consistent with pressure versus time charts sent to TRW by AFWL [1]. These pressure plots were measured at two stations, within 7.6 cm (3 inches) of one another, and 9.1 meters (29.86 ft) downstream from the driver wall. That is ~ 0.87 m (2.86 ft) downstream of the radiometer station (but on the opposite wall). The peak excursions ($t = 0$ values) of these two traces corresponded to pressures of ~ 88 atmospheres (~ 1300 psia) and ~ 102 atmospheres (~ 1500 psia), but were subject to reduction for "overshoot", so that an average value of the order of ~ 83 atmospheres (1225 psia) particularly at a station ~ 0.87 m (~ 2.86 feet) upstream, is not unreasonable. However, a more recent

telephone conversation with Mr. Joe Renick of AFWL indicated that shock front velocity data could be interpreted to imply a pressure of ~ 67 atmospheres (~ 987 psia) near the TRW radiometer station. The Brode report [2] (Figure 8, page 17) implies effective mean γ values of ~ 1.30 for $P_s \sim 83$ atmospheres (1225 psia) and ~ 1.32 for P_s 67 atmospheres (~ 990 psia). The corresponding T_s values computed from equation (1.1) are 4224 °K and 3641 °K respectively. For $P_s = 67.2$ atmospheres (987 psia) and $\gamma = 1.30$, the T_s value predicted by equation (6-1) is 3460 °K.

The constant γ approximation theoretical temperature curves shown in Figures 6-1 and 6-5 are merely straight lines connecting T_s points computed from equation (1.1) with corresponding T_i points computed from equation (1.2) for (P_i/P_s) set equal to 0.05 and positioned at the predicted station time increment of 0.8 msec after shock front arrival at $t = 0$. The two theoretical curves shown in Figure 6-1 are both for $\gamma = 1.3$, with the upper curve corresponding to $P_s = 83.3$ atmospheres (1225 psia) and the lower to $P_s = (67.2)$ atmospheres (987 psia). It is seen that these two curves bracket the experimental data. They also serve to show the variation in constant γ approximation theoretical temperature predictions corresponding to a change of assumed shock front pressure. The corresponding $\gamma = 1.32$, $P_s = 67.2$ atmospheres (987 psia) curve is not shown, since its variation from the $\gamma = 1.30$, $P_s = 67.2$ atmospheres (987 psia) curve is relatively small compared to the limited degree of validity of the constant γ theory and to the uncertainties in pressure determination.

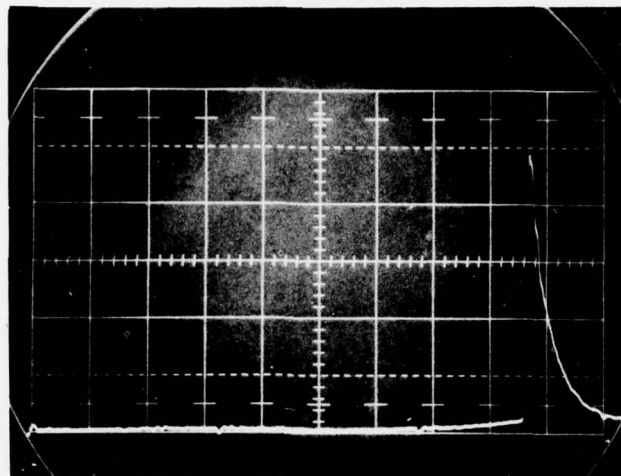
Figure 6-5 shows six constant γ theoretical curves, for $\gamma = 1.4$, 1.3, and 1.2, and for $P_s = 83.3$ atmospheres (1225 psia) and 67.2 atmospheres (987 psia) for each of these γ values. The $\gamma = 1.4$ value was chosen because the γ value for the air in front of the shock often is used for first order temperature predictions (i.e., in Section 1.3). The 1.2 value corresponds to the equilibrium γ value computed by an in-house TRW program for air at 4000 °K and 80 atmospheres (1176 psia) pressure. This set of curves serve to show the effects of variations of both shock front pressure and γ value assumptions on predicted temperatures, and to emphasize the necessity for making independent empirical temperature measurements.

6.2 Secondary Results

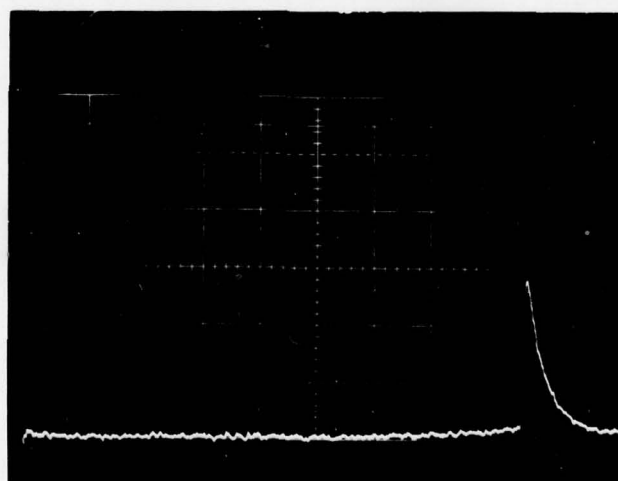
Inspection and analyses of the two ultraviolet radiometer signal tracings reveal some information in addition to the computed temperature data presented in the preceding section.

6.2.1 Mean Shock Front Velocity

Figure 6-6a and b, for the 0.36 μ and 0.26 μ wavelength radiometers respectively, show the delay time of these optical signals with respect to the fiduciary pulse which



(a) 0.36μ RADIOMETER SIGNAL



— 2.875 MS —

(b) 0.26μ RADIOMETER SIGNAL

TRACES (a) AND (b): THE VERTICAL SCALE IS 0.5 VOLT/CM AND THE HORIZONTAL SCALE IS 312.5μ SEC/CM, REAL TIME.

Figure 6-6. Delay of DABS II-D-2 Optical Signals With Respect to Fiduciary Pulse

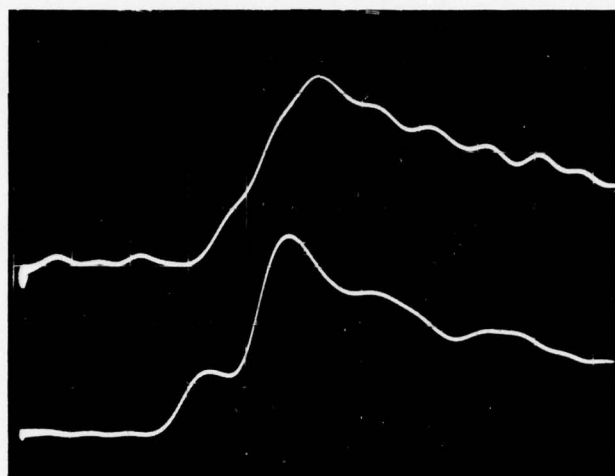
started the oscilloscope sweep. This fiduciary pulse also corresponds to the actual field electrical pulse which served to ignite the explosive that acted as the "shock piston". The vertical scales for these tracings are 0.5 volts/cm, while the horizontal time scale is $312.5 \mu \text{ sec/cm}$, real time. The time from the power pulse to initiation of the main optical signal pulses is 2.875 msec. Information received from AFWL personnel indicated a 1.2 msec delay between the ignition pulse and the beginning of shock front propagation. If this 1.2 msec is subtracted from the 2.875 msec optical signal delay time, then the computed mean velocity to the 8.2 m (27 ft) downstream station is $\sim (8.23 \text{ m} / 1.68 \cdot 10^{-3} \text{ sec}) = \sim 4.9 \cdot 10^3 \text{ m/sec}$ ($1.6 \cdot 10^4 \text{ ft/sec}$).

The preceding value of mean velocity during the first 8.2 meters (27 ft) of shock front propagation appears to be theoretically correct. The speed of ignition in the high explosive material itself should be of the order of $6.6 \cdot 10^4 \text{ m/sec}$ ($2 \cdot 10^4 \text{ ft/sec}$), and the indicated initial pressure of the combustion gases acting as the shock driver is of the order of 24,000 atmospheres. The initial shock front velocity of this order of $5.8 \cdot 10^3$ to $8.5 \cdot 10^3 \text{ m/sec}$ ($1.9 \cdot 10^4$ to $2.8 \cdot 10^4 \text{ ft/sec}$) are not unreasonable. Also, available theoretical curves appear to indicate an instantaneous shock front propagation speed of the order of $3.3 \cdot 10^4 \text{ m/sec}$ ($1 \cdot 10^4 \text{ ft/sec}$) for a pressure of ~ 81.6 atmospheres ($\sim 1200 \text{ psia}$) and temperature of $\sim 4000 \text{ }^\circ\text{K}$.

6.2.2 Lag Time Between the Two Ultraviolet Radiometers

As has been mentioned previously, the fields of view of the 0.36μ and 0.26μ wavelength radiometers are separated laterally by 15.2 cm (6 inches) and produce a parallax of ~ 0.0206 radians upstream and downstream of the approaching shock front (See Figure 2-2). It was expected that the 0.36μ wavelength radiometer would detect the approaching shock front slightly before the 0.26μ wavelength radiometer. The actual relative delay was found to be $\sim 7.5 \mu \text{ sec}$. This is shown in the expanded tracing segments presented as Figure 6-7 a, b. The time scale for these two segments is $12.5 \mu \text{ sec/cm}$, real time [0.2 msec/cm oscilloscope sweep], the signal amplitudes are not to scale.

If the theoretically indicated shock front propagation speed of $\sim 3.3 \cdot 10^4 \text{ m/sec}$ ($\sim 1 \cdot 10^4 \text{ ft/sec}$) is assumed, the $7.5 \mu \text{ sec}$ relative delay time indicates that the shock front entered the leading edge of the 0.36μ wavelength radiometer field of view $\sim 2.3 \text{ cm}$ (~ 0.9 inches) upstream of where it entered that of the 0.26μ wavelength radiometer. If the assumption were made that the shape of the shock front were such that the depths of penetration of these two fields of view into the shock chamber were the same for the initial detections, then a simple computation implies that this hypothetical first contact depth was $\sim 55.9 \text{ cm}$ (~ 22 inches). The virtually certain irregularities in the shock front, however, increase the uncertainty associated with the above 55.9 cm (22 inch) initial contact depth value.



→ | | ← 7.5 μ SEC

THE HORIZONTAL SCALE FOR BOTH TRACES IS 12.5 μ SEC/CM,
REAL TIME, (0.2 MSEC/CM OSCILLOSCOPE SWEEP)

LOWER TRACE: THE 0.36 μ RADIOMETER SIGNAL AMPLITUDE HAS A
VERTICAL SCALE OF 1 VOLT/CM

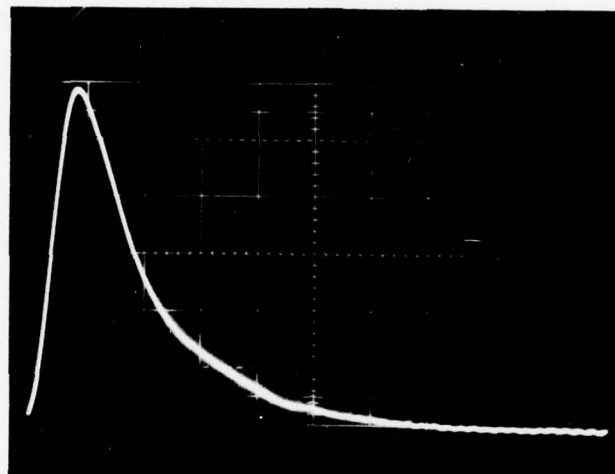
UPPER TRACE: THE 0.26 μ RADIOMETER SIGNAL AMPLITUDE HAS A
VERTICAL SCALE OF 0.5 VOLT/CM

Figure 6-7. Relative Lag Time Between Arrivals of the Two DABS II-D-2 Ultraviolet
Radiometer Signals

While some of the semi-oscillatory structure seen in Figure 6-7 probably can be attributed to noise or to instrument imperfections, much of it undoubtedly is real. It apparently indicates spatial, temporal and thermal irregularities in the propagating shock front. In particular, the pronounced hump occurring during the rise of the 0.36μ wavelength pulse, and some of the oscillations past this peak value, do not look at all like the passage of a thin uniform planar shock front oriented normal to the tunnel centerline. It will be remembered that the 0.36μ wavelength radiometer receives radiation from regions appreciably deeper into the shock chamber than does the 0.26μ wavelength radiometer. It seems evident, then, that the above data provides another fairly strong indication of shock front irregularities.

6.2.3 Radiometer Signal Rise Times

It also is seen in Figure 6-7 a, b that the rise times for the main pulse appear to be approximately 28 μ sec. for both ultraviolet radiometers. As is shown in Figure 6-8, the rise time of the equivalent electronic systems used on both radiometers is ~ 12 μ sec. A root mean square correction using this system response time modifies the observed rise times of the main pulses to ~ 25 μ sec., corresponding to complete filling of the radiometer field of view. Some attempts were made to correlate this rise time with shock front velocity, but too many uncertainties are involved to allow for meaningful correlation. These uncertainties include shock front non-planar geometrical and thermal structure and the unknown varying depths of optical penetration as the shock front first enters and eventually fills the radiometer fields of view.



THE HORIZONTAL SCALE IS $12.5 \mu \text{ SEC/CM}$, REAL TIME
(0.2 MSEC/CM OSCILLOSCOPE SWEEP). THE RISE TIME
IS SEEN TO BE $\sim 12 \mu \text{ SEC}$.

Figure 6-8. Electronic System Response to a Fast ($1 \mu \text{ sec}$) Calibration Pulse

7. CONCLUSIONS

This study has developed the necessary theoretical background for showing the feasibility of using properly designed one and two color pyrometer systems to measure the temperature history of explosively generated shock wave gases. The experimental data from the DABS II-D-2 field test were analyzed and showed excellent correlation with theoretical results. The information obtained from the design, calibration, installation and operation of this system provides a sound technical basis for designing a second generation optical pyrometer system that is compact in size, easy to install and simple to operate.

The main objective of this program was to demonstrate the practical application of using optical radiometers to measure airblast temperature histories. This goal was clearly demonstrated. The principle results can be summarized as follows:

- Successful operation of the ultraviolet and infrared channels was demonstrated in the field.
- Air shock temperature data was accurately measured by ultraviolet pyrometers and correlated with theoretical predictions
- The mechanical design of the open port installation provided protection against damage from the shock wave.

8. RECOMMENDATIONS

8.1 Identification of Problem Areas

The implementation of a new system usually uncovers certain problem areas that cannot be fully anticipated prior to the calibration, fielding and testing of the system. The DABS II-D-2 Temperature Measurement experiment was no exception. The only major problem involved the loss of all three infrared channels. The other problems were minor in nature and dealt with improved design changes or convenience changes for improved field operation.

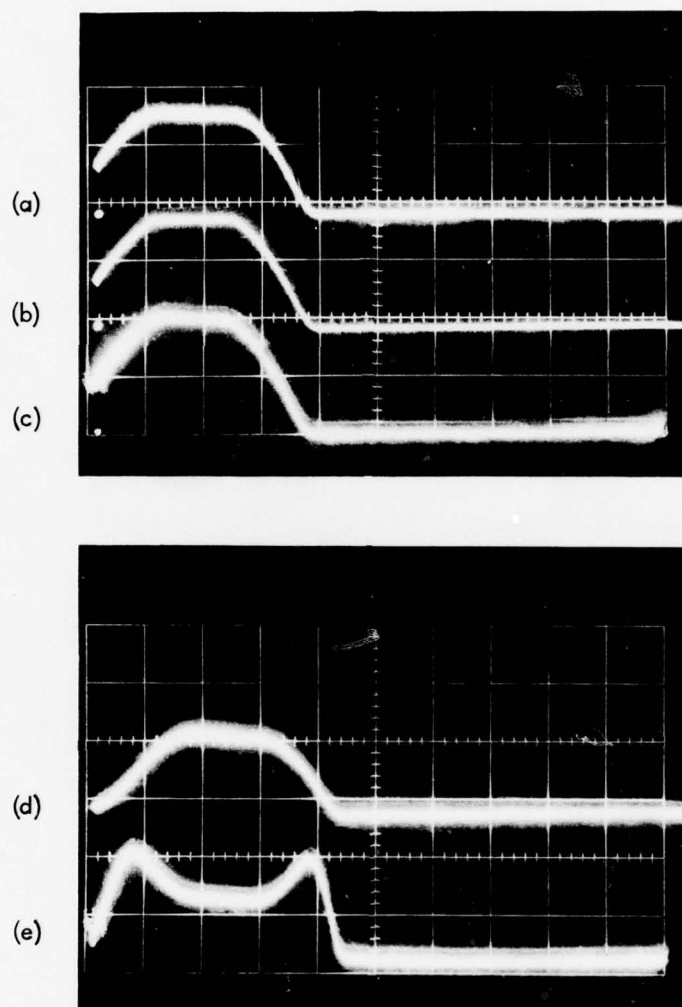
8.1.1 Electrical Interference on Infrared Channels

The infrared channels had been checked out and calibrated under full field conditions. Data from a pulsed light source was recorded in the instrumentation van and observed to be in proper working order (see Figure 8-1). The dry run, the day prior to the test, and a quick check three hours before detonation showed that the system was in perfect operating conditions. Trouble occurred during the electrical surge produced by the fiduciary pulse as shown in Figure 8-2. Close proximity of these cables to our experimental station and land line hook-up could have been a factor.

A preliminary evaluation indicates that the cause of the problem could have been the unshielded electrical leads on the infrared channels within the optical detector box. A one foot section of cabling from the voltage preamps to the preamp gain controls was unshielded. This cabling may have acted as an antenna for the 3000 volt detonation pulse. It is felt that proper shielding and grounding of all electrical circuits should be checked and corrected where necessary.

8.1.2 Optical Parallax

The two ultraviolet channels were located at either extreme in the five lens cluster. The lateral distance between channel 3 and channel 5 was 12.7 cm (5 inches) at the lens plane and approximately 15.2 cm (6 inches) at the detector plane. Thus allowing each detector to be focused on a different point in the shock front. This phenomenon was apparent from the different arrival times as discussed in Section 6.0. While the parallax allowed for calculation of the optical thickness of the 0.36μ wavelength channel, data within the shock wave was not observed at a point perpendicular to the optical axis. Repositioning the detectors with respect to the optical axis will solve any parallax problems.



HORIZONTAL TIME TRACE FOR ALL CHANNELS IS 1.25 MSEC/CM,
REAL TIME (20 MSEC/CM OSCILLOSCOPE SWEEP)

TRACE (a): THE 1.9 μ INFRARED RADIOMETER, CHANNEL 1

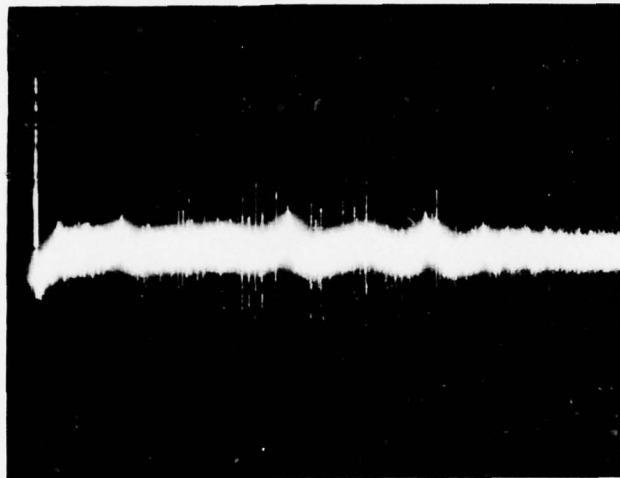
TRACE (b): THE 4.5 μ INFRARED RADIOMETER, CHANNEL 4

TRACE (c): THE 2.9 μ INFRARED RADIOMETER, CHANNEL 2

TRACE (d): THE 0.26 μ ULTRAVIOLET RADIOMETER, CHANNEL 5

TRACE (e): THE 0.36 μ ULTRAVIOLET RADIOMETER, CHANNEL 3

Figure 8-1. Pre-Test Optical Calibration Curves Recorded at the DABS II-D-2 Site



HORIZONTAL TIME TRACE IS 300 μ SEC/CM,
REAL TIME (0.5 SEC/CM OSCILLOSCOPE SWEEP)
VERTICAL SCALE IS 0.1 VOLT/CM

Figure 8-2. Electrical Noise Recorded on Typical Infrared Channel During the
DABS II-D-2 Test

8.1.3 Optical Alignment

The installation and set-up of the baffle/pit system was a time consuming job. The design and construction of an alignment jig would greatly alleviate this problem. Also the redesign of the system as proposed in subsection 8.2 would eliminate this problem.

8.1.4 Electronic Packaging

The main inconvenience associated with the electronics was the need to open the pit and remove the lid from the optical/detector box in order to activate the electronics power supply. Each opening increased the chance of damaging the electronics and optics from dust, moisture or debris. This problem can be easily eliminated by repackaging the electronics so that all switches necessary to activate the system are located in a remote control box outside the main pit. Then the optical box and pit can be sealed once the equipment is installed and aligned.

8.2 Recommended Hardware Improvements

The problems discussed in the previous subsection can be corrected. The infrared channels can be protected by shielding all electrical cabling between preamplifier circuit and controls. Optical parallax can be corrected by rearranging the position of the optics, the optical alignment made simpler by design of an alignment jig. The inconvenient arrangement of electrical switches can be alleviated by providing for external switching of electronics.

But the main recommendation for improvement of overall performance would be to reduce the package size. The key to this reduction would be the addition of a window (quartz or sapphire) optically transparent in the required wavelength region through which the shock wave would be observed. The addition of the window would provide protection from pressure without obscuring the radiation at the wavelength of interest. Without pressure to worry about, the detectors can be brought in close to the viewing port. A lens will still have to be used to collimate the light source. Care must be taken to limit the transmission loss through window and optics. The detector/optic package would be a small sealed unit already prealigned for easy installation. All electronics not required to be in proximity with a detector can be remotely located to improve reliability and eliminate interference from shock propagated through structure.

This new design would reduce installation and calibration time, allow placement of more units in a greater variety of locations, and many of the problem areas discussed in subsection 8.1 would become moot.

BIBLIOGRAPHY

- [1] Dynamic Airblast Simulator Test II-D Data Report, CERF Date Report AST-6, November 1977.
- [2] Brode, H. L., Height of Burst Effects at High Pressure, RM-6301-DSA, the Rand Corporation, Santa Monica, California; also, DASA 2506, Defense Atomic Support Agency, Washington, D. C., July 1970.
- [3] Herzberg, G., Molecular Spectra and Molecular Structure: I. Spectra of Diatomic Molecules, and II: Infrared and Raman Spectra of Polyatomic Molecules, D. Van Nostrand Co., Inc., Princeton, N.J., 1950.
- [4] Ludwig, C. B., Malkmus, W., Reardon, J. E., and Thompson, J. A. L., Handbook of Infrared Radiation From Combustion Gases, NASA SP-3080, NASA Marshall Space Flight Center, Huntsville, Alabama, 1973.
- [5] Handbook of Geophysical and Space Environments, Air Force Cambridge Research Laboratories, Office of Aerospace Research, Cambridge, Mass., 1965.
- [6] Lee, J. S., and Bobbit, P. J., Transport Properties at High Temperatures of CO₂-N₂-O₂-Ar Gas Mixtures for Planetary Entry Applications, NASA Technical Note NASATN D-5476, Washington, D. C., November 1969.
- [7] Menard, W. A. and Horton, T. E., Shock-Tube Thermochemistry Tables for High Temperature Gases; Volume 1 - Air, NASA Technical Report 32-1408 Jet Propulsion Laboratory, California Institute of Technology, Pasadena, California, November 1969.
- [8] Zel'Dovich, Ya. B. and Raizer, Ya. P., Physics of Shock Waves and High Temperature Hydrodynamic Phenomenon, Volume 1, Edited by Hayes, W. D. and Probstein, R. F., Academic Press, New York, London, 1967.

APPENDIX A: BLACK BODY RADIATION THEORY

Black Body radiation exhibits a unique relationship of absolute temperature T to Black Body hemispheric spectral radiant emittance $W^0(\lambda; T)$, and to Black Body spectral radiance $I^0(\lambda; T)$. That is, within any sufficiently narrow spectral interval, $\lambda_i \pm 1/2 \Delta\lambda_i$, there is a very useful one to one correspondence between $W^0(\lambda, \Delta\lambda; T)$ and T , and between $I^0(\lambda, \Delta\lambda; T)$ and T . Also, optical systems using photo-detector cells give a voltage signal output, V_s , directly proportional to the radiant power input impinging upon the objective element of the optical system and directed within a field of view, ω^c , that is focused upon the detector cell. Thus, a spectrally filtered radiometer optical system responsive only to a preselected $\lambda_i \pm 1/2 \Delta\lambda_i$ spectral interval and viewing Black Body radiation provides, in theory a direct measure of the spectral radiance $I^0(\lambda, \Delta\lambda; T)$, and hence of T .

Planck's original form of the Black Body spectral radiation law was specified in terms of total hemispheric spectral radiant emittance $W^0(\lambda; T)$ rather than the directed spectral radiance $I^0(\lambda; T)$. Planck's Law states that:

$$W^0(\lambda; T) = 2\pi c^2 h \lambda^{-5} [\exp(\frac{hc}{k\lambda T}) - 1]^{-1} \quad (A.1)$$

For present purposes, however, the formulation in terms of directed spectral radiance, $I^0(\lambda; T)$ is more applicable. For a "Lambertian surface", or for (as in the present application) "optically thick" layers of radiating gases:

$$I^0(\lambda; T) = \pi^{-1} W^0(\lambda; T) = 2 c^2 h \lambda^{-5} [\exp(\frac{hc}{k\lambda T}) - 1]^{-1} \quad (A.2)$$

In both equations (A.1) and (A.2) c , h , and k as usual symbolize, respectively, the speed of light, Planck's constant and Boltzmann's gas constant. The spectral wavelength, λ , is to be expressed in units of centimeters. Equation (A.2) often is exhibited in the convenient form:

$$I^0(\lambda; T) = c_1 \lambda^{-5} [\exp(c_2/\lambda T) - 1]^{-1} \quad (A.2a)$$

with the first and second radiation constants, c_1 and c_2 defined by the relations:

$$c_1 = 2 c^2 h = 1.1910 \cdot 10^{-12} \text{ watts cm}^2 \text{ ster}^{-1} \quad (A.3)$$

$$c_2 \equiv \frac{hc}{k} = 1.4388 \text{ (cm}^{\circ}\text{K)} \quad (A.4)$$

The definition given in equation (A.4) is universally used for c_2 , but the literature often contains alternative definitions for c_1 depending upon geometrical considerations and also depending upon whether the radiation quantities are expressed in wavelength units,

as is done here, or in wavenumber units as is often more convenient. In any case, the c_1 constant shortly will be eliminated from further consideration.

Typically, $I^0(\lambda; T)$ is presented in units of watts $[\text{cm}^2 \cdot \text{ster} \cdot (\text{micron-wavelength})]^{-1}$, although occasionally units of watts $[\text{cm}^2 \cdot \text{ster} \cdot (\text{cm-wavelength})]^{-1}$ or watts $[\text{m}^2 \cdot \text{ster} \cdot (\text{micron-wavelength})]^{-1}$, etc. are used. For application to finite spectral bandwidth measurements:

$$I^0(\lambda, \Delta\lambda; T) \approx I^0(\lambda; T) \cdot \left(\frac{\Delta\lambda}{1\mu}\right) = c_1 \lambda^{-5} \left[\exp\left(\frac{c_2}{\lambda T}\right) - 1\right]^{-1} \cdot \left(\frac{\Delta\lambda}{1\mu}\right) \quad (\text{A.2b})$$

In equation (A.2b) it was assumed that $I^0(\lambda; T)$ is given in units of watts $[\text{cm}^2 \cdot \text{ster} \cdot \mu]^{-1}$.

Figure A-1 presents log-log plots of $I^0(\lambda; T)$ against wavelength λ and also against wavenumber $\nu = [\lambda \text{ (in cm)}]^{-1}$ for selected values of absolute temperature T . It is seen that in log-log plots, the maximum values of $I^0(\lambda; T)$ for each T lie on a straight line. The equation of this parametric maxima curve, known as Wien's displacement law, is:

$$\lambda_{\max} T = c_2 / r_\lambda = 0.28978 \text{ (cm}^\circ\text{K)} = 2897.8 \text{ (}\mu^\circ\text{K)} \quad (\text{A.5})$$

where r_λ is defined below in equations (A.7), (A.8) and (A.9).

Also, the maximum values of $I^0(\lambda; T)$ for any T are given by the expression:

$$I^0(\lambda_{\max}; T) = 4.098 \cdot 10^{-16} (T/1^\circ\text{K})^5 \text{ watts } [\text{cm}^2 \cdot \text{ster} \cdot \mu]^{-1} \quad (\text{A.6})$$

Equations (A.5) and (A.6) are obtained by setting $\frac{dI^0(\lambda; T)}{d\lambda} = 0$

and solving for first λ_{\max} and then $I^0(\lambda_{\max}; T)$. Before differentiating, it is convenient to re-write equation (A.2a) in the form:

$$I^0(x) = c_1 (T/c_2)^5 x^5 [e^x - 1]^{-1}, \quad (\text{A.7})$$

where

$$x \equiv \frac{c_2}{\lambda T} \quad (\text{A.8})$$

The parameter r_λ (which equals 4.9651) that occurs in equation (A.5) is the positive root of the equation:

$$x = 5 [1 - \exp(-x)] \quad (\text{A.9})$$

It is evident from equation (A.7) that isothermal spectral radiance ratios $I^0(\lambda_1; T)/I^0(\lambda_2; T)$ are functions only of the dimensionless parameters $x_1 \equiv \frac{c_2}{\lambda_1 T}$ and $x_2 \equiv \frac{c_2}{\lambda_2 T}$. There exist several convenient condensed tables of radiometric quantities that tabulate only $I^0(x)/I^0(\lambda_{\max}; T)$ or corresponding $W^0(x)/W^0(\lambda_{\max}; T)$ etc., together with a short table of $I^0(\lambda_{\max}; T)$ etc.

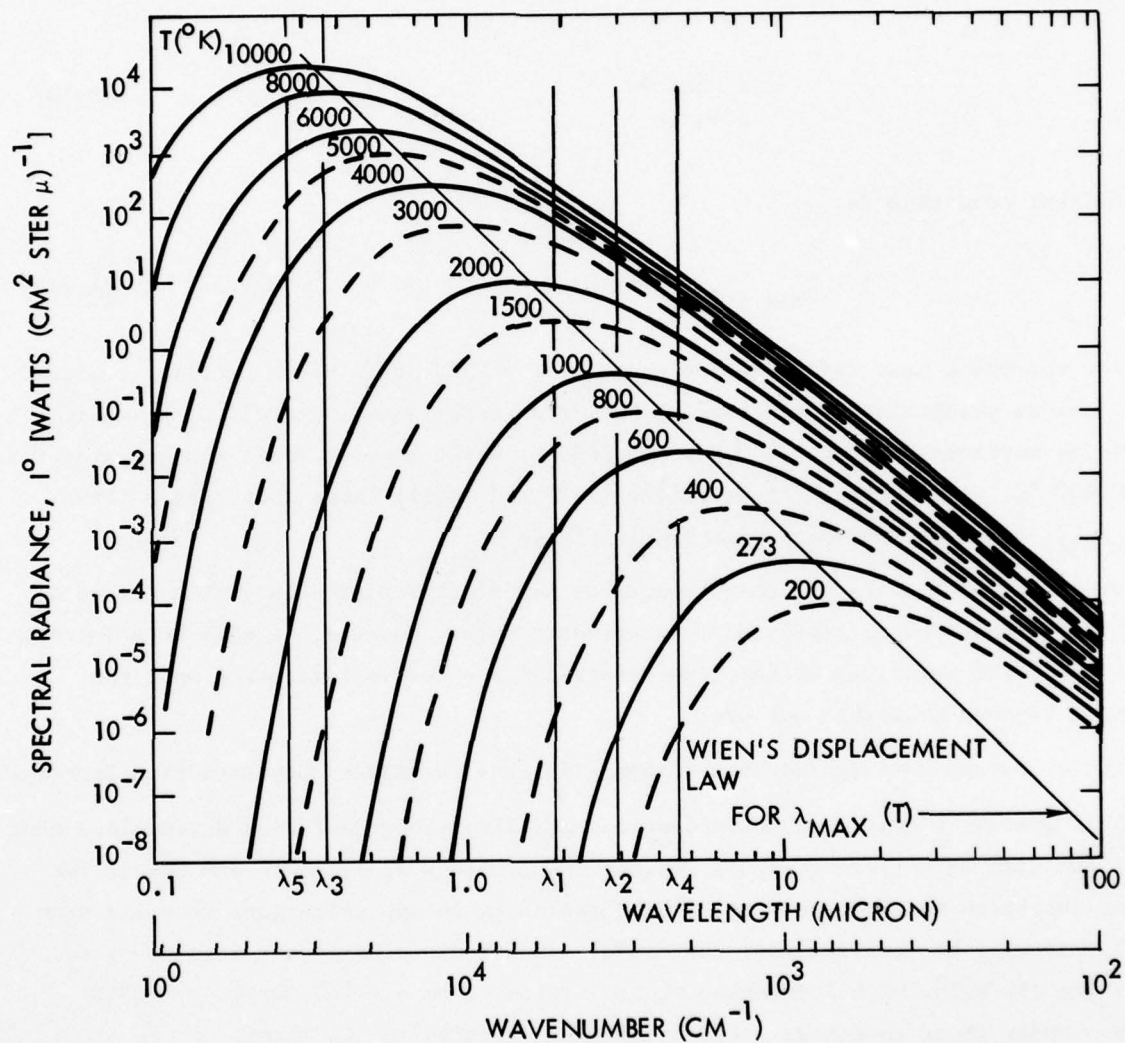


Figure A-1. Wavelength Dependence of Black Body Spectral Radiance

A.1 Optimum Spectral Regions for Temperature Determination

In radiation temperature measurements it would be preferable to choose wavelengths λ in spectral regions where the monochromatic spectral radiance changes relatively rapidly with a change in temperature. An expression for the wavelength, $\lambda_{\text{max diff}}$, at which the maximum change in $I^0(\lambda; T)$ occurs for a given change in T is found by solving the triple derivative expression:

$$\frac{\partial^3 I^0(\lambda; T)}{\partial^2 \lambda \partial T} \quad (\text{A.10})$$

The resultant condition is:

$$T \cdot \lambda_{\text{max diff}} = 2404 \text{ } (\mu \text{ } ^\circ\text{K}) \quad (\text{A.11})$$

Thus, for example a near infrared wavelength of $\lambda = 2.4\mu$ would be an excellent choice (other factors permitting) for measuring radiation temperatures near $1000 \text{ } ^\circ\text{K}$, while ultraviolet wavelengths near $\lambda \approx 0.24\mu$ ($= 2400 \text{ } \text{\AA}$) would be preferable for temperatures near $10,000 \text{ } ^\circ\text{K}$. A comparison of equations (A.5) and (A.11) shows that, for a fixed T , $\lambda_{\text{max diff}}$ falls on the short wavelength side of λ_{max} .

For radiation temperature measurements of non-Black Bodies such as the volume of hot radiating gases which represent the current problem, however, it will be seen that both physical and practical system constraints apply a severe limitation upon the wavelength regions available for use.

A.2 Wien's Law and Rayleigh-Jeans Law Approximations for Black Body Radiation Expressions

There are two widely used approximations for Black Body radiation expressions that find application to different (λ, T) regimes. Where they apply, both are useful for quick calculations and for analyses. The first of these approximations is valid when $x \gtrsim 2.5$. It will be recalled that the useful dimensionless parameter x is equal to $(c_2/\lambda T)$ [or $(hc/k\lambda T)$, with λ measured in cm - units ($1 \text{ cm} = 10^4 \mu$) for $c_2 = 1.4388 \text{ (cm } ^\circ\text{K)}$]. Under these conditions, equation (A.2a) reduces to the form:

$$I^0(\lambda; T) \approx c_1 \lambda^{-5} \exp(-c_2/\lambda T) \quad ; \quad \text{for } x \gtrsim 2.5 \quad (\text{A.12})$$

Equation (A.12) or its equivalent in terms of hemispheric radiant emittance $W^0(\lambda T)$ is known as "Wien's Law". The other approximation, known as the "Rayleigh-Jeans Law" is valid when $x \lesssim 0.15$. It then follows that equation (A.2a) reduces to the approximate expression:

$$\begin{aligned}
 I^0(\lambda; T) &\approx c_1 \lambda^{-5} (\lambda T/c_2) = (c_1/c_2) \lambda^{-4} T \\
 &\approx c_1 (Tx/c_2)^5 \cdot x^{-1} \quad ; \quad \text{for } x \lesssim 0.15
 \end{aligned}
 \tag{A.13}$$

A.3 Error Analysis for "One Color" Radiometric Temperature Determination

It can readily be shown that the fractional error in temperature determination by "one color" radiometer techniques is never greater than the corresponding fractional error in the measured spectral radiance. For, from equation (A.7) rewritten in the form:

$$\ln I^0(x) = \ln [c_1 \lambda^{-5}] - \ln (e^x - 1) \tag{A.7a}$$

and recognizing that,

$$\frac{dx}{dT} = - \frac{c_2}{\lambda T^2} = - x T^{-1} \tag{A.14}$$

it follows that

$$\frac{dT}{T} = \frac{dI^0}{I^0} \left[\frac{\exp(x) - 1}{x \exp(x)} \right] \equiv \frac{dI^0}{I^0} \cdot E(x) \tag{A.15}$$

The error multiplying factor $E(x)$ on the right hand side of equation (A.15) is < 1 for all values of x . This is very readily seen in the Wien's and Rayleigh-Jeans regime where equation (A.15) reduces to the respective approximations:

$$\begin{aligned}
 \frac{dT}{T} &\approx (x^{-1}) \cdot \left[\frac{dI^0(\lambda; T)}{I^0(\lambda; T)} \right] \quad ; \quad x \gtrsim 2.5 \\
 &\quad \lambda T \gtrsim 5.76 \cdot 10^5 \text{ } (\mu \cdot ^\circ K)
 \end{aligned}
 \tag{A.15a}$$

and

$$\frac{dT}{T} \approx [\exp(-x)] \cdot \left[\frac{dI^0(\lambda; T)}{I^0(\lambda; T)} \right]$$

$$\approx [1 - x] \left[\frac{dI^0(\lambda; T)}{I^0(\lambda; T)} \right] ; 0 < x \lesssim 0.15$$

$$\lambda T \gtrsim 9.6 \cdot 10^4 (\mu \cdot ^\circ K) \quad (A.15b)$$

In the intermediate $(\lambda; T)$ regime of $0.15 < x < 2.5$, the factor $[E(x) \equiv [e^x - 1]/(x e^x)]$ still remains less than unity and monotonically decreases with increasing x to finally approach x^{-1} asymptotically, as is seen from Table A-1.

TABLE A.1 PYROMETRIC ERROR FACTOR $E(x)$
FOR ONE COLOR PYROMETER

$x \equiv \frac{C_2}{\lambda T}$	$E(x)$	Wein's Approx. $E(x) \approx x^{-1}$	Rayleigh-Jeans Approx. $E(x) \approx (1-x)$
0.01	0.995		0.99
0.05	0.975		0.95
0.10	0.952		0.90
0.20	0.906		0.80
0.40	0.824		0.60
0.60	0.787		0.50
0.80	0.688	1.25	0.20
0.00	0.632	1.0	
1.50	0.518	N.G. 0.667	
2.00	0.432	0.500	
4.00	0.245	0.250	
8.00	0.125	0.125	

Table A-1 and the preceding discussion illustrate again, as was pointed out in the earlier discussion of equation (A.11) [concerning the wavelength $\lambda_{\max \text{ diff}}$ where the greatest change in $I^0(\lambda; T)$ occurs for a given change in T] that as the temperature regime of interest increases it would be preferable (if feasible) to utilize progressively shorter wavelengths λ so as to increase x and thus decrease the error factor E .

Figure A-2 is a plot of the "one color" pyrometric error factor ($E(x)$) against T for several selected values of wavelength, λ , ranging from 0.1μ to 10μ . It clearly shows, as does Table A-1, that the measurement error ($\delta I/I$) is always attenuated rather than amplified in determining fractional errors.

A.4 Two-Color Pyrometer Systems

Equation (A.2b) could be used to plot a $I^0(\lambda, \Delta\lambda; T)$ vs. T curve for a pre-selected fixed λ and $\Delta\lambda$, which in turn could be used in theory as a measure of T as a function of received radiation signal (i.e., output voltage from the $\lambda \pm 1/2 \Delta\lambda$ sensitive detector) if an absolute calibration is first made. However, in order to avoid the difficulties and inherent errors in an absolute calibration, and also the necessity and excessive cost of perhaps keeping $\Delta\lambda$ extremely narrow, it is often preferable to go to a more readily implemented "two color" (or "multi-color") system. These systems utilize two or more detector systems, each with similar geometry and each filtered to be responsive to different $\lambda \pm 1/2 \Delta\lambda$ spectral intervals. The temperature indicators then are the dimensionless spectral radiance ratios $I^0(\lambda_i, \Delta\lambda_i; T)/I^0(\lambda_j, \Delta\lambda_j; T)$. For reasons and compromises that will be explained in Appendix D, six different wavelength intervals $\lambda_i \pm 1/2 \Delta\lambda_i$ eventually were selected for use in DABS II-D-1. Five of these same wavelength intervals will be utilized in DABS II-D-2. Figure A-3 exhibits $I^0(\lambda_i, \Delta\lambda_i; T)$ vs. T curves for five of these six selections; the $\lambda_6 = 4.3\mu$ and $\lambda_4 = 4.5\mu$ curves (selected for use in observing combustion products and 4% CO_2 in air, respectively) lie too close together to exhibit separately on the chosen semi-log scale. The vertical lines superimposed on Figure A-1 also indicate the selected λ_i values. Figure A-4 exhibits the four "temperature signal" ratios of $[I^0(\lambda_i, \Delta\lambda_i; T)/I^0(\lambda_j, \Delta\lambda_j; T)]$ selected as most useful for determinations of radiometric temperature history in air, in air plus 4% CO_2 (presuming this addition would be allowed), and in the combustion gases.

A.5 Applicability of "Two-Color Pyrometer" Techniques

As has been previously stated, a "two-color pyrometer" consists of a pair of radiometers for which filters and detector cells have been selected to confine response to pre-selected spectral increments $\lambda_i \pm 1/2 \Delta\lambda_i$ and $\lambda_j \pm 1/2 \Delta\lambda_j$, respectively. Assuming that thermal equilibrium is a valid assumption for the radiating surface or volume being observed, it is clear that the "two-color pyrometer" can provide a useful estimate of the radiation temperature under any of the following sets of conditions:

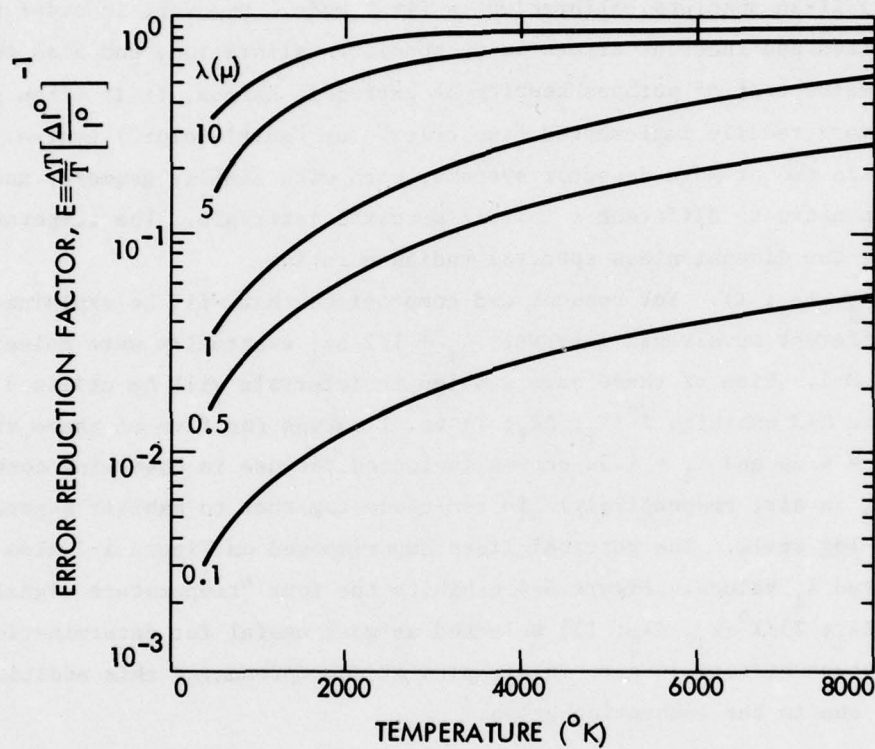


Figure A-2. Error Reduction Factor for One Color Pyrometer

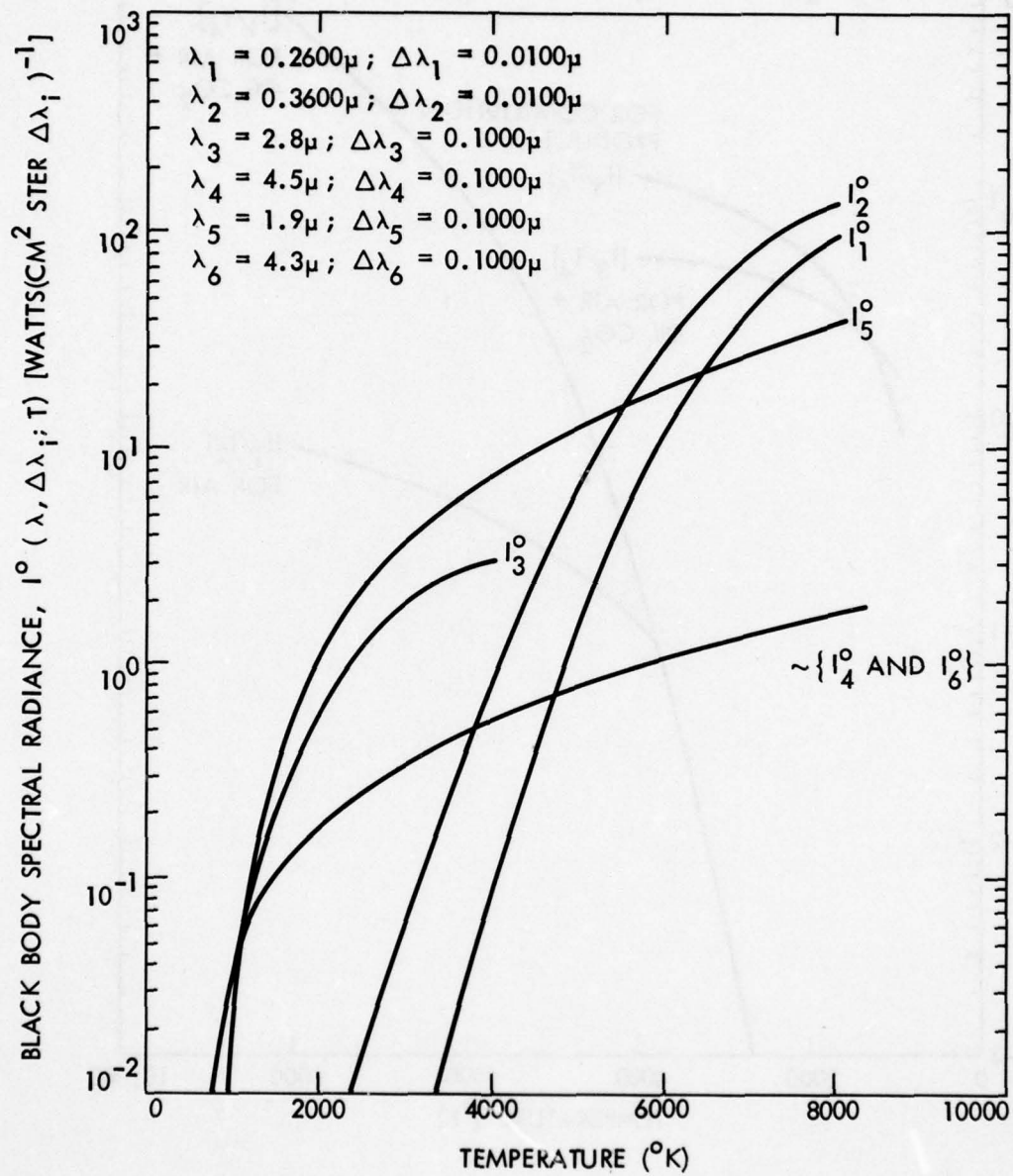


Figure A-3. Black Body Spectral Radiance for Selected Wavelengths λ_i and Wavelength Intervals, $\Delta\lambda_i$

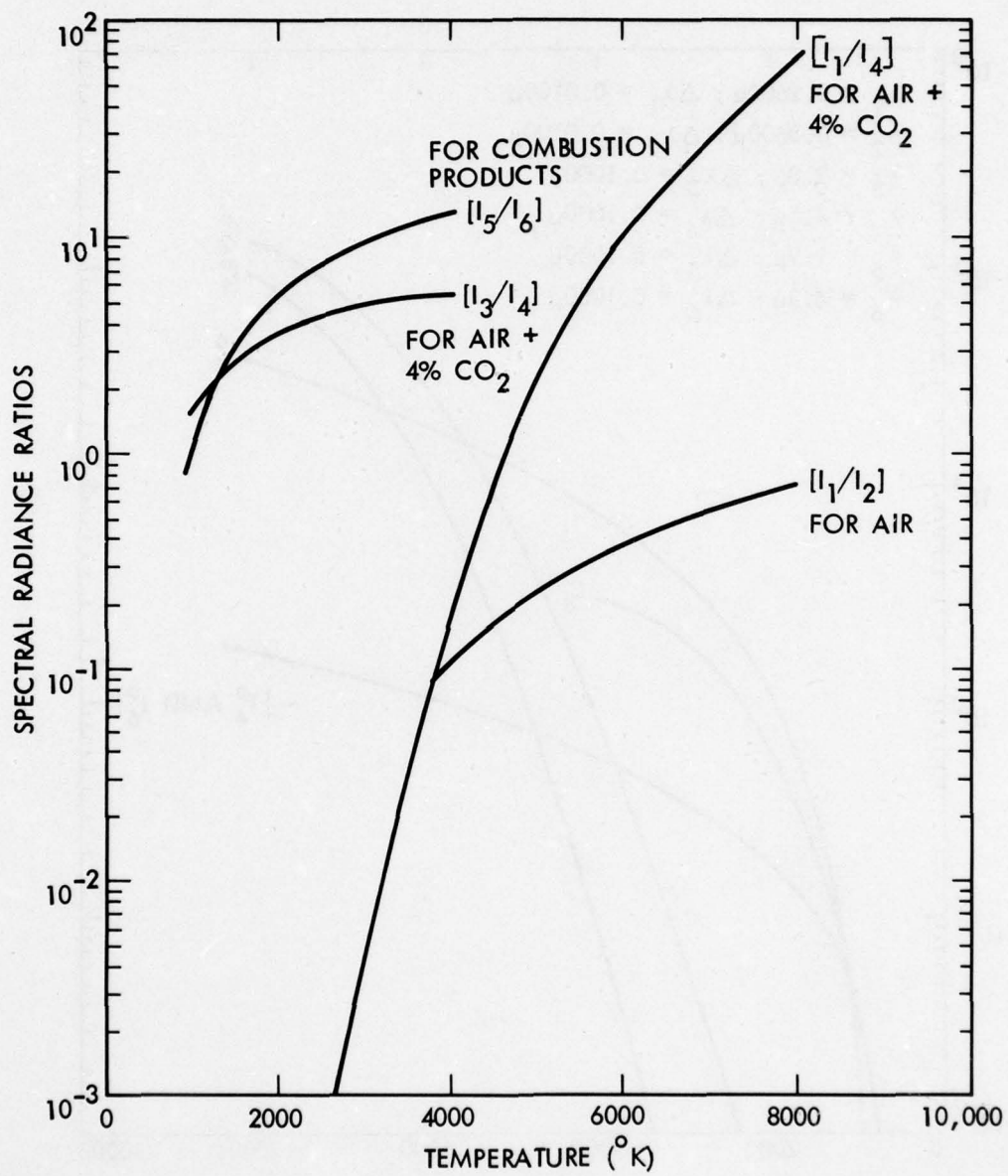


Figure A-4. Temperature Signals for Two Color Radiometers

I. Radiating object is a Black Body

$$\epsilon(\lambda_i, \Delta\lambda_i; T) = \epsilon(\lambda_j, \Delta\lambda_j; T) = 1 \text{ for all } \lambda \text{ and all } T$$

II. Radiating object is a Gray Body

$$\epsilon(\lambda_i, \Delta\lambda_i; T) = \epsilon(\lambda_j, \Delta\lambda_j; T) = \epsilon_{\text{gray}} < 1$$

ϵ_{gray} = some value < 1 , but essentially constant for all λ , $\Delta\lambda$, and T within some specified bounds.

III. The radiating volume is not "Black and Not Gray, and has a spectrally variable emissivity $\epsilon(\lambda, \Delta\lambda; T)$, but it is known that for the selected λ_i and λ_j intervals

$$\epsilon(\lambda_i, \Delta\lambda_i; T) \approx \epsilon(\lambda_j, \Delta\lambda_j; T) < 1$$

Over some T -interval of interest.

IV. The radiating volume has a spectrally variable emissivity

$$\epsilon(\lambda, \Delta\lambda; T), \text{ and}$$

$$\epsilon(\lambda_i, \Delta\lambda_i; T) \neq \epsilon(\lambda_j, \Delta\lambda_j; T) \text{ and}$$

$$\epsilon(\lambda_i, \Delta\lambda_i; T) < 1 \text{ and}$$

$$\epsilon(\lambda_j, \Delta\lambda_j; T) < 1$$

But both of the ϵ -values are accurately known or can be accurately computed over the T -interval of interest.

V. The Radiating volume again has spectrally variable emissivity, but for the pre-selected λ_i - and λ_j - intervals, the respective τ -values are both $\gtrsim 3$, so that,

$$\epsilon(\lambda_i, \Delta\lambda_i; T) \approx \epsilon(\lambda_j, \Delta\lambda_j; T) \approx 1$$

As was pointed out in the Introduction, Cases I and II are not applicable to gas volumes while Cases III and IV generally are very difficult to implement. Therefore, the only case of current interest is Case V. It will be shown in Appendix E that the set of six

wavelength intervals selected in Section 1.4.4 and its sub-sections correspond to suitably large τ -values >3 . A brief error analysis for "two color" pyrometers is presented in the subsequent sub-section.

A.6 Error Analysis for "Two-Color" Pyrometer Systems

It was stated in sub-section A.4 that the temperature signal for a "two-color" pyrometer is the ratio of measured spectral radiances:

$$R_{ij}(T) = I(\lambda_i, \Delta\lambda_i; T) / I(\lambda_j, \Delta\lambda_j; T) \quad (\text{A.16})$$

$$\text{or } R_{ij} = I_i / I_j \quad (\text{A.16a})$$

where the second form is a convenient shorthand. Then since,

$$\ln R_{ij} = \ln I_i - \ln I_j \quad (\text{A.17})$$

it follows that the fractional error in determining R_{ij} is given formally by the expression:

$$\frac{\delta R_{ij}}{R_{ij}} \approx \frac{\delta I_i}{I_i} - \frac{\delta I_j}{I_j} \quad (\text{A.18})$$

Here the $(\delta I_i / I_i)$ and $(\delta I_j / I_j)$ terms represent the fractional errors in measuring I_i and I_j , respectively. It is clear then, that if the errors were entirely random, that the predicted fractional error in R_{ij} would be given by the expression:

$$\frac{\delta R_{ij}}{R_{ij}} \approx \left[\left(\frac{\delta I_i}{I_i} \right)^2 + \left(\frac{\delta I_j}{I_j} \right)^2 \right]^{1/2} \quad (\text{A.18a})$$

(predicted for random measurement errors)

If the major errors in measuring I_i and I_j are systematic rather than random, then different types of error expressions would have to be used. If it were known that the systematic errors had the same sign, then

$$\left| \frac{\delta R_{ij}}{R_{ij}} \right| = \left| \frac{\delta I_i}{I_i} - \frac{\delta I_j}{I_j} \right| \quad (\text{A.18b})$$

(for systematic errors with $(\delta I_i) (\delta I_j) > 0$)

AD-A054 730

TRW DEFENSE AND SPACE SYSTEMS GROUP REDONDO BEACH CALIF F/G 19/4
MEASUREMENTS IN AIRBLAST. PART A. OPTICAL TEMPERATURE MEASUREME--ETC(U)

OCT 77 R DOLL, L GLATT, P LIEBERMAN, P MOLMUD DNA001-77-C-0141

UNCLASSIFIED

TRW-29937-6001-RU-00

DNA-4421F

NL

2 OF 2
AD
A054 730





If, on the other hand, it were known that the systematic errors had opposite signs, then

$$\left| \frac{\delta R_{ij}}{R_{ij}} \right| = \left| \frac{\delta I_i}{I_i} \right| + \left| \frac{\delta I_j}{I_j} \right| \quad (\text{A.18c})$$

(for systematic errors with $(\delta I_i)(\delta I_j) < 0$)

Now each of the $(\delta I/I)$ - quantities are related to $(\delta T/T)$ by the relation given in Equation (A.15), e.g.,

$$\left(\frac{\delta I_i}{I_i} \right) = E_i^{-1} (\delta T/T) \equiv \begin{pmatrix} x_i & e^{x_i} \\ e^{x_i} & -1 \end{pmatrix} (\delta T/T) \quad (\text{A.15a})$$

$$\text{where } x_i \equiv \frac{c_2}{\lambda_i T} = 1.4388 \times 10^4 (\mu \cdot ^\circ\text{K}) / (\lambda_i \cdot T) \quad (\text{A.8a})$$

when λ_i is specified in microns rather than in centimeters.

It follows, by combining equations of the forms (A.18) and (A.15), that if the δI measurements errors each could be resolved into three increments consisting respectively of random errors and systematic errors of the two types characterized in equations A.18b) and (A.18c), then:

$$\left| \frac{\delta T}{T} \right| \approx \left| E_i^{-2} + E_j^{-2} \right|^{-1/2} \left| \frac{\delta R_{ij}}{R_{ij}} \right| \quad (\text{A.19a})$$

for random measurement errors in I_i and I_j and with

$$\left(\frac{\delta R_{ij}}{R_{ij}} \right) \text{ given by Equation (A.18a) ;}$$

$$\left| \frac{\delta T}{T} \right| \approx \left| E_i^{-1} - E_j^{-1} \right|^{-1} \cdot \left| \frac{\delta R_{ij}}{R_{ij}} \right| \quad (\text{A.19b})$$

for systematic measurement errors in I_i and I_j and with $(\delta I_i)(\delta I_j) > 0$

and with $\left(\frac{\delta R_{ij}}{R_{ij}} \right)$ given by equation (A.18b);

and

$$\left| \frac{\delta T}{T} \right| \approx \left| E_i^{-1} + E_j^{-1} \right|^{-1} \cdot \left| \frac{\delta R_{ij}}{R_{ij}} \right| \quad (\text{A.19c})$$

for systematic measurement errors in I_i and I_j and with $(\delta I_i)(\delta I_j) < 0$

and with $\left(\frac{R_{ij}}{R_{ij}} \right)$ given by Equation (A.18c).

Figure A-5, A-6, and A-7 present plots of the three "two-color" pyrometer error factors given respectively, by equations A.19a, A.19b, and A.19c for selected (λ_i, λ_j) pairs. It is seen that the two error factors given by equations A.19a and A.19c are always error attenuators; i.e., the predicted $(\delta T/T)$ increments are always less than the corresponding random and systematic fractional error increments of $(\delta R/R)$. However, the error factor given by Figure A-6 for the equation A.19b relation for systematic error increments, such that $(\delta I_i)_{\text{systematic}} \cdot (\delta I_j)_{\text{systematic}} > 0$, sometimes becomes an "error amplifier" rather than an "error attenuator" (i.e., the error factor becomes greater than unity). This is seen to happen for $T \gtrsim 1800^\circ\text{K}$, $\lambda_i = 2.8\mu$ and $\lambda_j \approx 5\mu$. For the (λ_3, λ_4) pair of $(2.8\mu, 4.5\mu)$, this "error amplification" would occur for $T \gtrsim 1500^\circ\text{K}$. This "error amplification" is not particularly serious, however, since the error quantity being "amplified" is really of the type,

$$\left| \frac{\theta_i \delta I_i}{I_i} - \frac{\theta_j \delta I_j}{I_j} \right|$$

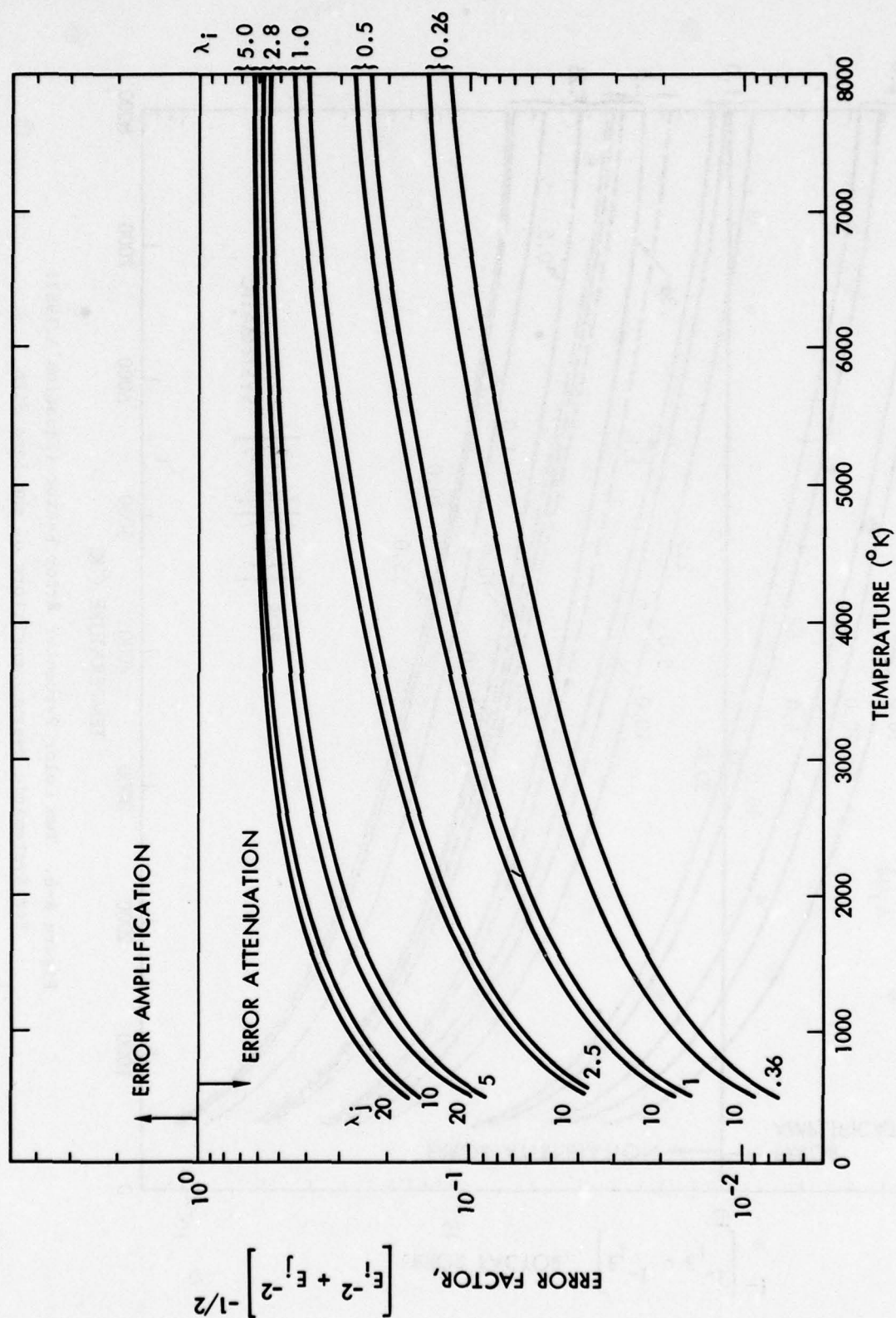


Figure A-5. Two Color Pyrometer Attenuation Factor (Equation A.19a):
For Random Measurement Errors

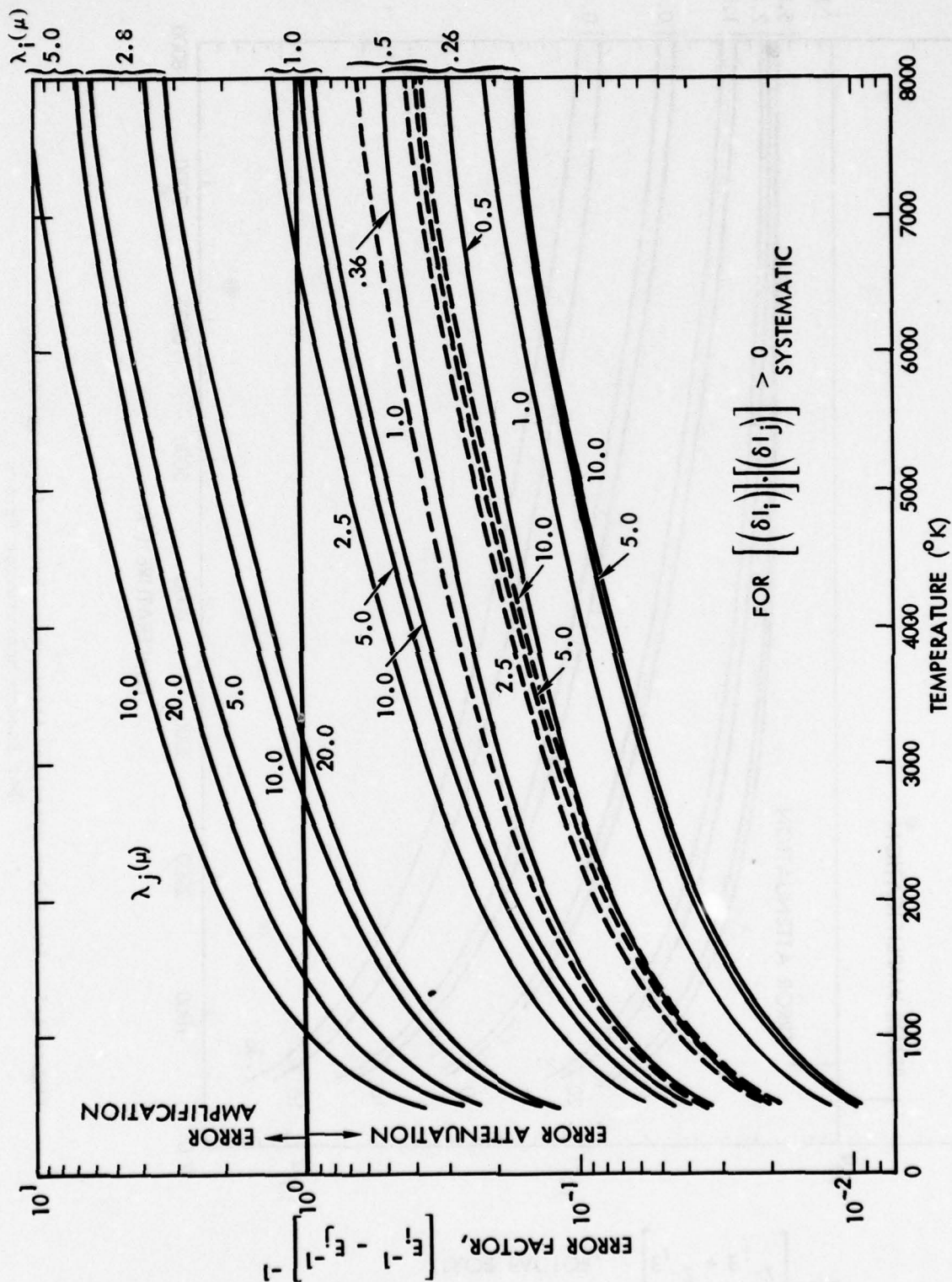


Figure A-6. Two Color Pyrometer Error Factor (Equation A.19b):
For Systematic Measurement Errors of the Same Sign

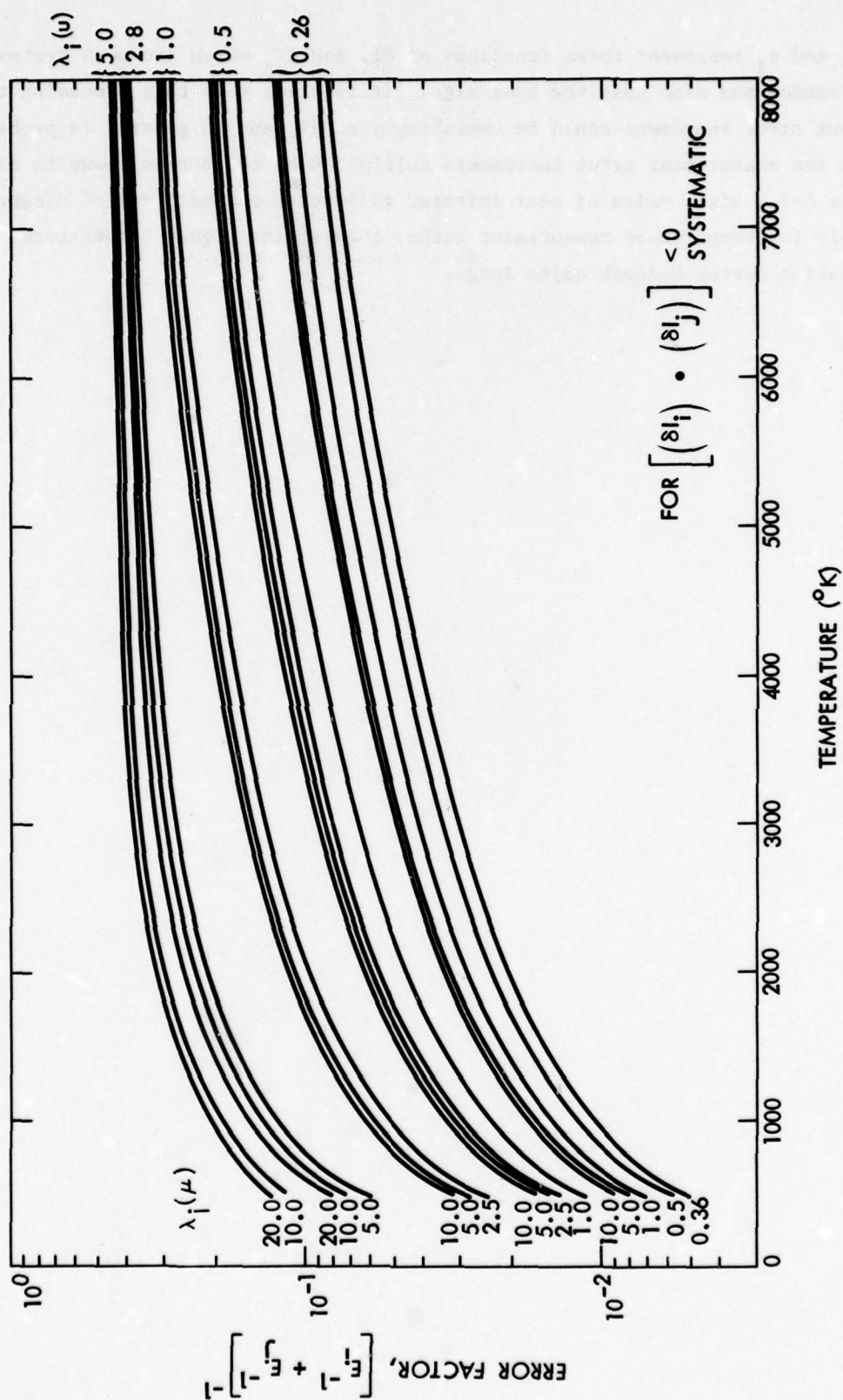


Figure A-7. Two Color Pyrometer Error Attenuation Factor (Equation A.19c):
For Systematic Measurement Errors of Opposite Sign

where the θ_i and θ_j represent those fractions of δI_i and δI_j which are both systematic rather than random and also have the same sign. It is clear that this preceding type of measurement error increment could be vanishingly small, and in general is probably smaller than the measurement error increments multiplied by the curves shown in either Figure A-5 or A-7. Also, pairs of near infrared radiometer channels are of use primarily for relatively low temperature measurement rather than at the higher temperatures where the amplification factor becomes quite large.



APPENDIX B: A BRIEF INTRODUCTION TO NOMENCLATURE OF MOLECULAR BAND SYSTEMS [3]

The designations of molecular electronic-vibration-rotation band systems are historical, being either named after one or more of the original investigators. or using names applied by an original investigator. Electronic energy levels are designated, more systematically, with the electronic ground state (or for a few molecules, the state that initially was mistakenly taken to be the electronic ground state) being designated by the symbol X. Then, the symbols A,B,C, etc. designate successively higher lying electronic states all of which have the same "multiplicity" as the X-state and thus are capable of "permitted" electric dipole transitions with the X-state or with each other. "Forbidden" transitions can occur but are very much weaker than "permitted" transitions. Electronic states with "multiplicity" differing from that of the ground state generally are designated by a lower case letter, a,b,c, etc., again in order of increasing electronic excitation.

Each electronic state of a molecule has associated with it a sequence of quantized vibrational energy sub-levels, and each of these, in turn has associated with it a sequence of quantized rotational energy levels. In general, the energy level separation is successively much greater between electronic states than between vibrational sub-levels of these states, and between these latter sub-levels than between the rotational sub-sub-levels.

For a given electronic transition the corresponding upper and lower energy levels are tagged by their corresponding electronic, vibrational and rotational quantum numbers designated by the symbols, n,v, and J respectively. Sometimes additional rotational quantum numbers, K,L, etc. also are required. For polyatomic molecules, v must be replaced by a set of vibrational quantum numbers, v_1, v_2, v_3 , etc. each designating the degree of vibrational excitation of the indexed normal vibrational modes 1,2,3, etc. For convenience, single and double "primes" are used to designate the respective upper and lower states in a transition. Thus (neglecting K,L. etc. and "fine" structure) the most general transition corresponding to a single spectral line of a diatomic molecule would be of type $(n'', v'', J'') \xrightarrow{\pm} (n', v', J')$, where the lower arrow represents absorption and the upper emission. For transitions between two specified electronic states, say A and X, these state-symbols are substituted for the n' and n'' symbols, i.e., $(X, v'', J'') \xrightarrow{\pm} (A, v', J')$. The totality of all such "lines" could be known as the A-X band system, etc. for the specified molecule. Instead, however, the band systems generally are designated by some historical name. Individual vibrational sub-"bands" within an electronic system correspond to all the allowed $J'' \xrightarrow{\pm} J'$ transitions for some specified pair of (v'', v') levels. These J-lines are restricted by "selection rules" to either only $\Delta J = J' - J'' = \pm 1$ or only $\pm 1, 0$. The nominal "center" of each band system is designated as ν_{00} (in cm^{-1} units) and corresponds to the sometimes hypothetical transition

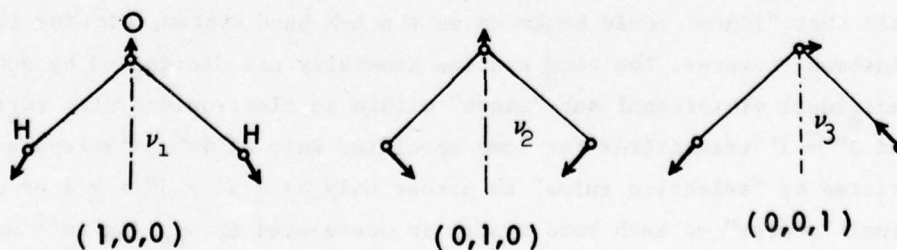
$(n'', v'' = 0, J'' = 0) \rightarrow (n' v' = 0, J' = 0)$. The relative intensities of the various vibrational sub-bands, and of the individual rotational "lines" within a band depend upon quantum mechanical considerations and also upon the relative population levels of each energy sub-state. The population levels, in turn, are very strongly temperature dependent through the Boltzmann distribution law.

Most infrared spectra consist of transitions between different vibrational-rotational sub-levels of the same electronic state, i.e., $n'' \equiv n'$. Except at very high temperatures,, the overwhelmingly predominant contributions are usually from the ground electronic state. Again, the totality of "allowed" transitions between all the rotational sub-levels of a pair of vibrational states are said to constitute a single vibrational band. For diatomic molecules this would be called a $(v'' \rightarrow v')$ -band. At low and moderate temperatures, only transitions with low v'' (i.e. 0, 1, 2 ..) are important. But as the temperature increases, higher vibrational levels become populated, and "hot band" transitions originating from higher v'' lower states begin to make increasingly important contributions. The spectral regions for the same $\Delta v = v' - v''$ tend to partially overlap, but as the temperature increases, the overall resultant band structure generally broadens and the region of maximum absorption or emission can shift very appreciably.

B.1 Infrared Vibrational Bands for Polyatomic Molecules

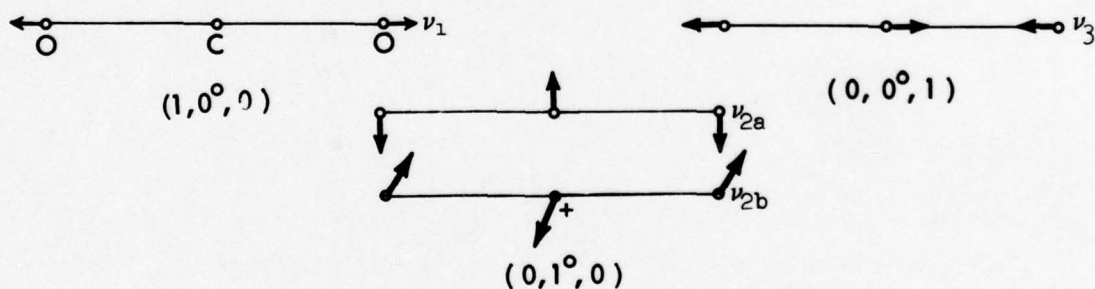
A polyatomic molecule consisting of n atoms generally has three non-quantized translational modes (i.e. in arbitrary x , y and z directions), three normal rotational modes, and $3n-6$ normal vibrational modes. "Linear molecules" such as CO_2 however, have one less normal rotational mode and one additional normal vibrational mode, since their moment of inertia about their figure axis is essentially zero.

The water vapor molecule, H_2O , for example, has the symmetry of an isosceles triangle with the O-atom at the vertex. Its three normal modes consist of symmetric and anti-symmetric "bond-stretching" vibrations labeled ν_1 and ν_3 , and a bond-bending vibration ν_2 . These three fundamental vibrations are symbolically represented below:



Any arbitrary vibrational mode is designated by the vibrational index triplet (v_1, v_2, v_3) with each v integer quantum number denoting the degree of excitational contribution by the corresponding fundamental mode. As was indicated below the preceding figures, $(1, 0, 0)$, $(0, 1, 0)$ and $(0, 0, 1)$ denote excitation of the first, second and third fundamental vibrational modes. Similarly, $(v, 0, 0)$, $(0, v, 0)$ or $(0, 0, v)$, where v is any non-zero integer, would indicate excitation of the v th harmonic [or $(v-1)$ th overtone] of the corresponding fundamental mode. If two or more of the v -integers are non-zero, i.e. $(v_1, v_2, 0)$, $(v_1, 0, v_3)$, $(0, v_2, v_3)$, or (v_1, v_2, v_3) , then the indicated excitation is said to be a "combination mode". Since diatomic molecules have only a single fundamental mode, they can have fundamental and harmonic mode excitation, but no combination modes.

The linear CO_2 molecule (more accurately represented as $\text{O} = \text{C} = \text{O}$ really has four fundamental vibrational modes, consisting also of symmetric and anti-symmetric bond-stretching modes ν_1 and ν_3 and two equivalent (doubly degenerate) bond-bending modes both represented by the symbol ν_2 and indexed by ν_2^ℓ , where the ℓ -superscript represents a pseudo rotational quantum number resulting from a combination of degenerate vibrational modes. The most general mode designation is (v_1, v_2^ℓ, v_3) , with fundamental, harmonic, and combination modes defined as before. The fundamental vibrational modes are symbolized below. The designations for harmonic and combination modes are similar to those for water vapor.



The very strong CO_2 absorption centered near 4.3μ wavelength arises from a "fundamental band". At low temperatures the absorption (or emission) is mostly from rotational lines of the fundamental ν_3 , or $(0, 0^0, 0) \leftrightarrow (0, 0^0, 1)$ transition. As the temperature increases, however, transition of the type $(v_1, v_2^{\ell''}, v_3) \leftrightarrow (v_1, v_2^{\ell'}, v_3 + 1)$ with

$(v_1 + v_2 + v_3) \geq 1$ make increasingly important contributions. The much weaker CO₂ absorption centered near 2.7 μ wavelength is a combination band. At low temperatures it arises primarily from the "accidentally degenerate" (and "Fermi-Resonant") pair of transitions $(0, 0^0, 0) \xrightarrow{\pm} (0, 2^0, 1)$ and $(0, 0^0, 0) \xrightarrow{\pm} (1, 0^0, 1)$. As the temperature increases, there are increasing contributions from "hot band" transitions of the type, $(v_1, v_2, v_3) \xrightarrow{\pm} (v_1, v_2, +2, v_3 + 1)$ and $(v_1, v_2, v_3) \xrightarrow{\pm} (v_1 + 1, v_2, v_3 + 1)$, [the ℓ and ℓ' superscripts are omitted for convenience] with $(v_1 + v_2 + v_3) \geq 1$.

The relatively very weak H₂O absorption band centered near 1.87 is also a combination band. At low temperatures it arises primarily from the $(0, 0, 0) \xrightarrow{\pm} (0, 1, 1)$ vibrational transition. With increasing temperature, there are "hot band" contributions of the type $(v_1, v_2, v_3) \xrightarrow{\pm} (v_1, v_2 + 1, v_3 + 1)$, again with $(v_1 + v_2 + v_3) \geq 1$.

APPENDIX C: A BRIEF INTRODUCTION TO SOME RELEVANT SPECTRAL PARAMETERS

It was mentioned in Section 1.4.1 that the absorption coefficients $k_{ij}(\lambda; T)$ are arbitrarily defined parameters. It will be recalled that the indexing subscripts designate the j^{th} band system [see Appendix B] of the i^{th} molecular (or ionic) species which may exhibit spectral activity in the $\lambda \pm \frac{1}{2} \Delta\lambda$ spectral region of interest. [For an atomic species, the j subscript would index an individual atomic "line".] The truly fundamental spectroscopic parameters are the "absorption cross sections", $\sigma_{ijm}(\lambda, \lambda_m)$, for the individual m^{th} line contours, each centered on some $\lambda = \lambda_m$ within the band system. In the wavenumber domain, which is more convenient for analyses, the cross sections would be represented as $\sigma_{ijm}(\nu, \nu_m)$ with the line center wavenumber position $\nu_m = \lambda_m^{-1}$ if λ is given in centimeters. In either representation, the σ 's are given in units of cm^2 per molecule of the i^{th} species that is in a proper electronic lower state to give rise to absorption in the j^{th} band system. [see Appendix B.] The k to σ relationship will be discussed in Sub-Section C.1.

Other very important parameters, which together with the absorption cross sections determine the spectrally smoothed mean absorption coefficients, $\bar{k}_{ij}(\lambda, \Delta\lambda; T)$, are the spectral widths and shapes of the individual "line" contours and the separations of adjacent spectral lines. These considerations will be discussed in Sub-Section C.2.

C.1 The Relation Between Absorption Cross Sections and Absorption Coefficients

The absorption coefficients, k_{ij} , are related to the fundamental cross sections, σ_{ijm} , by the defining equation:

$$k_{ij}(\lambda; T) = N_0 \cdot \sum_m \left[\frac{N''_{ijm}(T)}{N_i(T)} \right] \cdot \sigma_{ijm}(\lambda, \lambda_m) \quad (\text{C.1})$$

Here N''_{ijm} represents the population number density, in units of cm^{-3} , for the fractions of the i^{th} species molecules whose state of internal excitation corresponds to that lower energy state from which absorption transitions can produce the m^{th} spectral line (centered on λ_m) of the j^{th} band system. As in Section 1.4.1, N_0 represents the $2.67 \cdot 10^{19}$ molecules cm^{-3} corresponding to an ideal gas at STP conditions, while N_i represents the total number density of i^{th} species molecules in cm^{-3} . An explicit representation of the pressure dependence of N_i and N''_{ijm} has been omitted in equation (C.1) because the (N''_{ijm}/N_i) ratio is not pressure dependent. The summation in equation (C.1) extends over all of those m -indexed spectral lines whose centers, λ_m , lie sufficiently close to λ to make a significant contribution to $k_{ij}(\lambda; T)$.

The spectrally "smoothed" parameters $\bar{k}_{ij}(\lambda, \Delta\lambda; T)$ result from averaging the quantities expressed by equation (C.1) over some suitable $\lambda \pm \frac{1}{2} \Delta\lambda$ spectral interval. It is seen that a substitution of these \bar{k}_{ij} -values into equation (1.6) would cancel out the (N_i/N_o) -term occurring in the latter equation, leaving the more fundamental lower state population density terms $N''_{ijk}(T)$.

For the assumption of thermodynamic equilibrium, the (N''_{ijm}/N_i) ratios in equation (C.1) exhibit the familiar Boltzmann exponentially dependent temperature distribution. This Boltzmann dependence causes the $k(\lambda; T)$ [and consequently the corresponding $\bar{k}(\lambda, \Delta\lambda; T)$] values given by equation (C.1) to exhibit very strong temperature variation when the lower state energy levels for the j^{th} spectral "Band system" belong to a highly excited electronic state [see Appendix B]. Let E''_{ij} represent the generally dominant electronic portion of the total energy of the lower state. Then the (N''_{ijm}/N_i) are very small when $kT \ll E''_{ij}$ (the k in the kT terms represents the Boltzmann gas constant), and increase exponentially with increasing T as kT first approaches and then exceeds E''_{ij} ; it is seen from equation (C.1) that the $k_{ij}(\lambda)$ absorption coefficients also increase proportionately.

The increase of the $k_{ij}(\lambda; T)$ parameters with T is much less marked when the lower states for the absorption "band system" belong to the ground electronic state (as is virtually always true for infrared vibration-rotation bands where both upper and lower electronic states are the same electronic ground state). Even here however, increases in temperature increase the populations of more highly excited vibration (and rotation) levels and, as was discussed in Appendix B, tends to introduce absorption in the so-called "hot bands". That is, the summation in equation (C.1) will include significant contributions from a larger number of m -indexed "lines".

C.2 Spectral Line Contour and Line Density Considerations

The absorption coefficients $\bar{k}(\lambda, \Delta\lambda; T)$ used in the present computations are all spectrally smoothed mean values rather than spectrally fine structured monochromatic values. The smoothing, however, is generally over ~ 25 to $\sim 50 \text{ cm}^{-1}$ which are much narrower sub-intervals than the ~ 0.01 and $\sim 0.1 \mu \Delta\lambda$ -values assumed in this report. Also, wherever these smoothed values exhibit sharp fluctuations within a $\Delta\lambda$ -interval of interest either a minimum or at least a low average was taken. Even so one need be concerned with the possibility of some of the actual $k(\lambda; T)$ values within a $\Delta\lambda$ -radio-meter filter transmission region falling appreciably below the $\bar{k}(\lambda, \Delta\lambda; T)$ -values used. This could occur, generally only at low temperature and low pressures, when the "line packing factor" (γ/d) drops below unity. Here γ represents the individual spectral "line" contour half widths (at half-amplitude), while d is the distance between the centers of adjacent spectral "lines".

In the (P,T)-regime of current interest, the spectral lines profiles are completely dominated by collision rather than Doppler effects. The relative line profiles, as functions of wavenumber frequency ν in the vicinity of $\nu = \nu_m$ are given by the collision profile relation:

$$A(\nu, \nu_m) = \gamma[\nu - \nu_m]^2 + \gamma^2]^{-1} \quad (C.2)$$

The $A(\nu, \nu_m)$ parameter introduced here is directly proportional to the $[N''_{ijm}(T)/N_i(T)] \sigma_{ijm}(\nu, \nu_m)$ that would occur in equation (C.1) if it were rewritten in terms of wavenumber rather than wavelength. It is seen that the maximum $A(\nu, \nu_m)$ value occurs when $(\nu - \nu_m) = 0$, and is equal to γ^{-1} . $A(\nu, \nu_m)$ -values of $(1/2\gamma)$, $(1/5\gamma)$, $(1/10\gamma)$, $(1/17\gamma)$... occur respectively when $\nu - \nu_m = \pm \gamma$, $\pm 2\gamma$, $\pm 3\gamma$, $\pm 4\gamma$, The pressure broadened "half widths" γ have relatively complicated dependence upon temperature and species partial pressures of each of the constituent gases [4]. Quite often, however, a sufficiently good approximation is given by a relation of the form:

$$\gamma \approx \gamma_0 (P/P_0) \cdot (T_0/T)^{0.5} \quad (C.3)$$

More accurate expressions (see Reference [4], pages 218, 219 and 223) use the partial pressures of the various constituent gases, with various γ_{ij} rather than γ_0 and additional powers of (T_0/T) -terms which differ from 0.5. It was found that the more complicated relations were not needed in the current problem except for application to H_2O . The very strong dipole moment of this molecule required the use of a $(T_0/T)^1$ term as well as several $(T_0/T)^{1/2}$ terms multiplied by mole-fractions of CO_2 , N_2 etc.

Figure C-1 shows mean values of the "line packing" factor, \bar{d}^{-1} , for the 4.3 and 2.7 μ centered CO_2 bands at 600 and 3000 °K, the 1.87 μ centered H_2O band at the same temperatures, and a portion of the CO - band centered at 4.9 μ (but extending past 4.5 μ). Figure C-2 gives corresponding γ -values [computed from the more correct Reference 3 equation rather than the equation (c.3) approximation] for CO_2 , CO, and H_2O both as they would occur in 4% CO_2 + air and in the DABS II-D combustion products.

Figure C-3 gives schematic representations of the relative line profiles $A(\nu, \nu_m)$, and of "line packing" for hypothetical sets of constant intensity equally spaced "lines" for which the (γ/d) factor is equal to 1, 0.5, and 0.25 respectively. The latter three sub-figures also show $k(\nu)$ -curves, with $k(\nu)$ (proportional to the absorption coefficient) given by the relation:

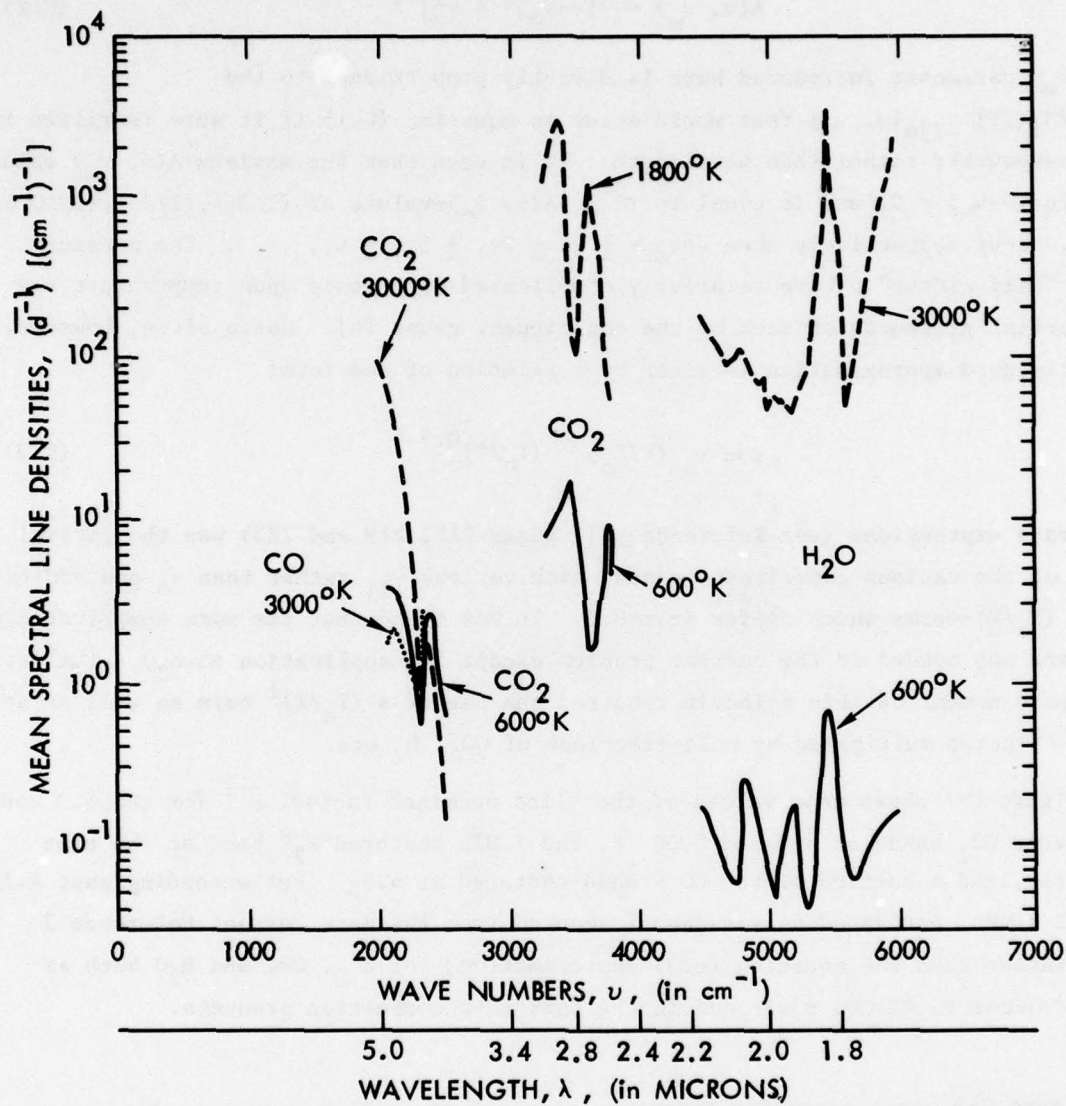


Figure C-1 Mean Spectral Line Densities for CO₂, CO, and H₂O in Selected Spectral Intervals

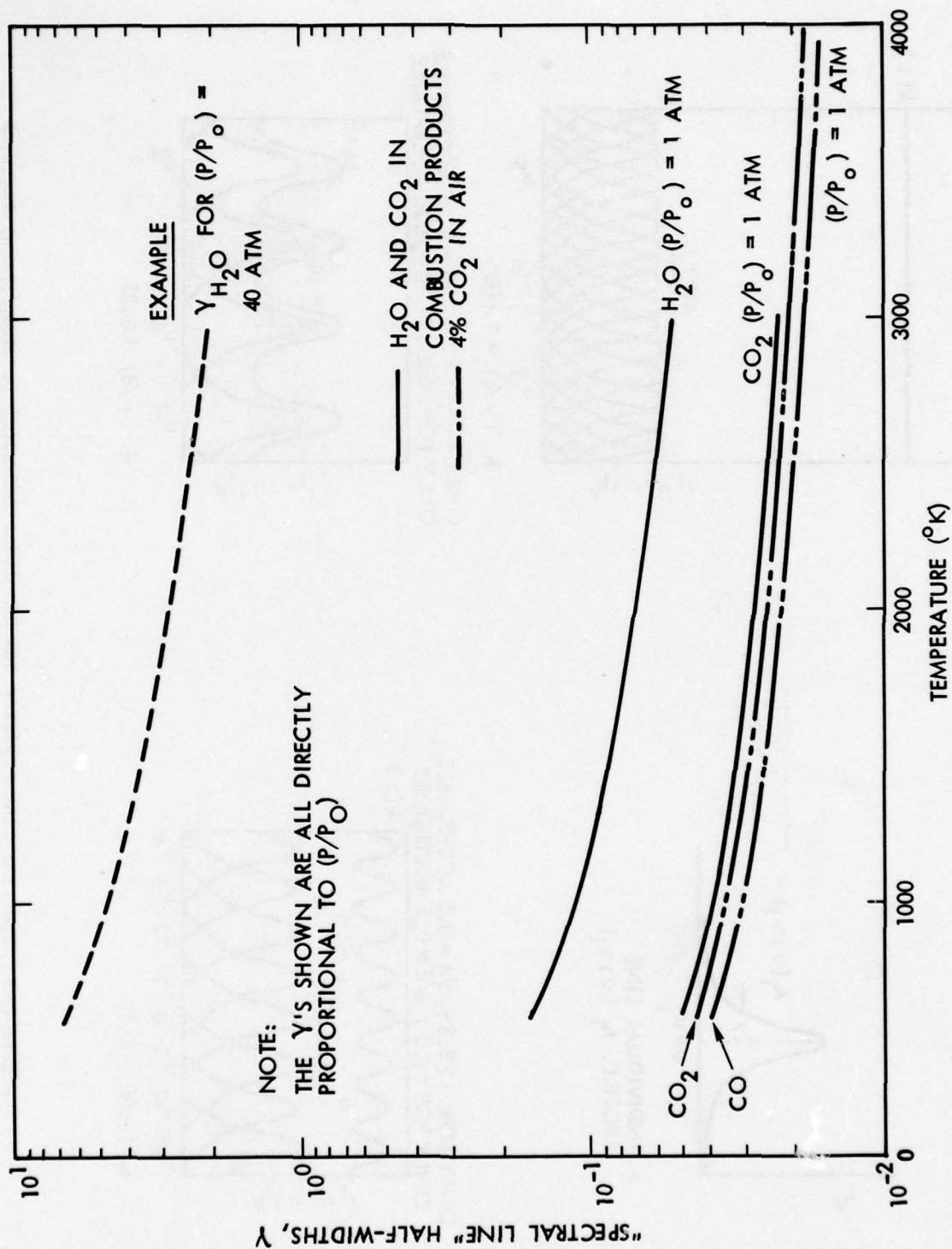
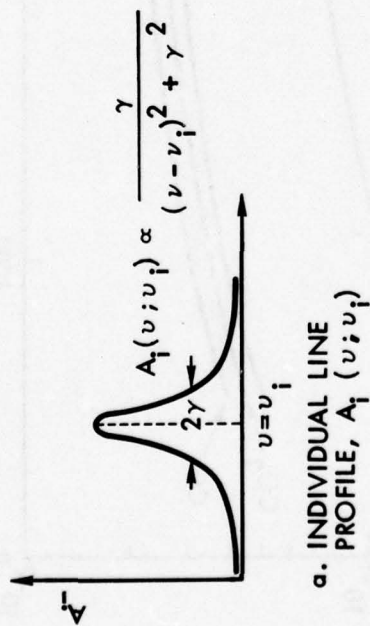
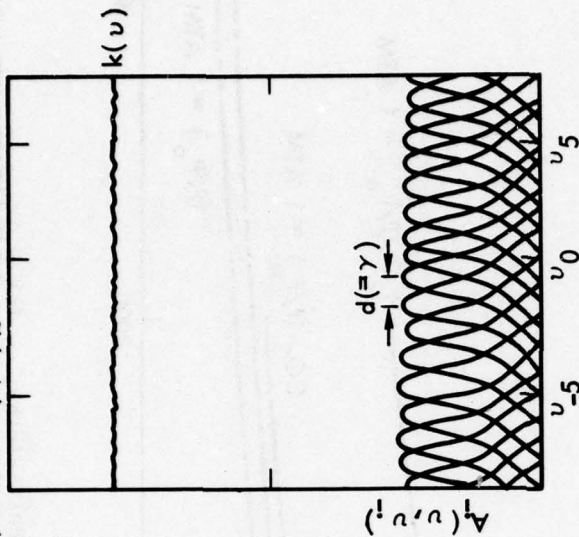


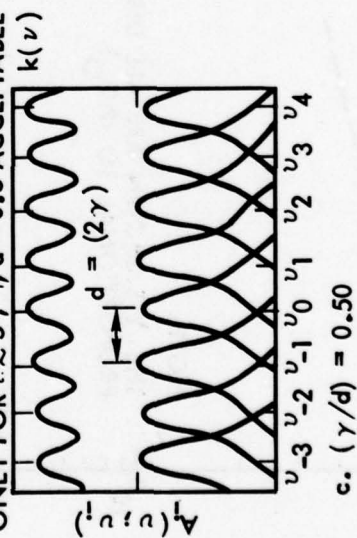
Figure C-2. Pressure Broadened "Spectral Line" Half-Widths, γ , for H_2O and CO_2 in the Combustion Products, and for CO_2 and CO in 4% CO_2 Added to Air



$(\gamma/d) \geq 1$ AND $(\gamma/\bar{d}) \geq 1$ BOTH ACCEPTABLE FOR $\tau \geq 3$



ONLY FOR $\tau \geq 3.3$; $\gamma/d = 0.5$ ACCEPTABLE
ONLY FOR $\tau \geq 5$; $\gamma/\bar{d} = 0.5$ ACCEPTABLE



ONLY FOR $\tau \geq 6$; $(\gamma/d) = 0.25$ ACCEPTABLE
ONLY FOR $\tau \geq 10$; $(\gamma/\bar{d}) = 0.25$ ACCEPTABLE

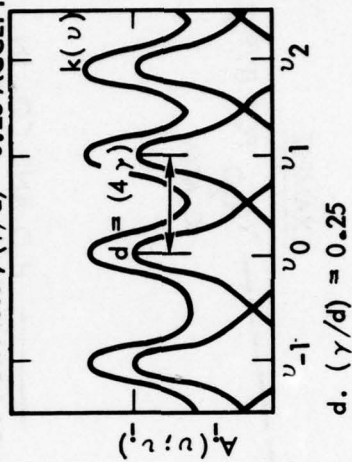


Figure C-3. Spectral Line Profiles and Resultant Emission (or Absorption) Patterns

$$k(\nu) \equiv \sum_{m=-\infty}^{\infty} A(\nu, \nu_m)$$

A mean value horizontal $\bar{k}(\nu)$ line also is drawn in for the $(\gamma/d) = 0.5$ and 0.25 representations, but is too close to $k(\nu)$ to show for the $(\gamma/d) = 1$ representation. The fluctuation of $k(\nu)$ is equal to $\pm 8.5\%$ for $(\gamma/d) = 0.5$, and to $\pm 60\%$ when $(\gamma/d) = 0.25$.

It should be realized that the γ -values are directly proportional to (P/P_0) if species mole-fractions remain relatively constant. Thus an isothermal two-fold increase in pressure would convert a $(\gamma/\bar{d}) = 0.25$ spectral region into a $(\gamma/\bar{d}) = 0.5$ spectral region, and the latter into a $(\gamma/\bar{d}) = 1$ spectral region. Similarly, an appropriate increase in temperature, while it would tend to decrease γ , could excite enough additional "hot lines" to produce the same effect. Thus, as we stated previously, the concern about low (γ/d) -values and a consequent drop of portion of $k(\lambda; P, T)$ below the corresponding $\bar{k}(\lambda, \Delta\lambda; P, T)$ is generally relevant only for low T and low P values. For this reason it was not considered worthwhile to expend any of the limited time and funds available on a literature search for high temperature O_2 and NO , etc., γ - and d -values.

When (γ/d) drops below unity, an upward adjustment of minimum $\bar{\tau}$ -values is required, since the actual $\tau(\lambda, \Delta\lambda; T, P)$ -values fluctuate from their mean value $\bar{\tau}$ in direct proportion to the fluctuation of the k -values about their \bar{k} . Also, in real spectra, any computed (γ/\bar{d}) value implies the possibility of still lower spectrally fine grained (γ/d) values within the $\delta\lambda$ (or $\delta\nu$) smoothing interval. Figure C-3b, c and d also give the listings of the increased $\bar{\tau}$ -values (over $\tau \gtrsim 3$) which are estimated to be required for the corresponding (γ/d) , and (γ/\bar{d}) values for the figures. It is estimated that $(\gamma/d) = 0.5$ and $(\gamma/\bar{d}) = 0.5$ are acceptable for τ -values $\gtrsim 3.3$ and $\gtrsim 5$ respectively; while $(\gamma/d) = 0.25$ and $(\gamma/\bar{d}) = 0.25$ are acceptable for respective τ values $\gtrsim 6$ and $\gtrsim 10$.

After investigation, it turned out that the increased minimum τ criteria for low (γ/d) was pertinent only to the 1.9μ water vapor spectral region of the λ_5 -radiometer. The reason for this was the proverbial "ounce of prevention"; i.e., care was taken, whenever possible, to select the radiometer $\Delta\lambda$ -increments where \bar{d}^{-1} line density did not fall too low. The increased τ confidence interval for the 1.9μ band is hatched in Figure E-10b of Appendix E.

APPENDIX D: CONCENTRATIONS AND SPECTRAL DATA FOR RADIATING SPECIES MOLECULES

Table D-1, extracted from Reference [5], shows the accepted normal composition of dry atmospheric air near sea level. Water vapor concentration is not shown, since it is very highly variable both spatially and temporarily. An appropriate mean value of H_2O concentration would be of the order of 0.002 or 0.003%, but the relative variations are so large as to make this mean value of very little use. It is seen that the major normal constituents of atmospheric air are N_2 and O_2 , followed by Argon and CO_2 . As air temperature is increased however, first O_2 (and CO_2), and then N_2 tend to dissociate, forming NO, O, N and other species. Figure D-1, extracted from Reference [6], gives mole-fractions of major dry air constituents for temperatures of from $1000^{\circ}K$ to $8000^{\circ}K$, and for a pressure of (P/P_0) equal to 10 (standard sea level) atmospheres. As will be seen from data to be presented in Appendix E, the mole-fraction distributions

Table D-1 Normal Composition of Clean, Dry Atmospheric Air Near Sea Level

Constituent Gas	Gas Symbol	Content (% by volume)	Molecular Weight*
Nitrogen	N_2	78.084	28.0134
Oxygen	O_2	20.9476	31.9988
Argon	Ar	0.934	39.948
†Carbon dioxide	CO_2	0.0314	44.00995
Neon	Ne	0.001818	20.183
Helium	He	0.000524	4.0026
Krypton	Kr	0.000114	83.80
Xenon	Xe	0.0000087	131.30
Hydrogen	H_2	0.00005	2.01594
†Methane	CH_4	0.0002	16.04303
Nitrous oxide	N_2O	0.00005	44.0128
†Ozone	O_3	Summer: 0 to 0.000007 Winter: 0 to 0.000002	47.9982 47.9982
†Sulfur dioxide	SO_2	0 to 0.0001	64.0628
†Nitrogen dioxide	NO_2	0 to 0.000002	46.0055
†Ammonia	NH_3	0 to trace	17.03061
†Carbon monoxide	CO	0 to trace	28.01055
†Iodine	I_2	0 to 0.000001	253.8088

*On basis of C^{12} isotope scale for which C^{12} equals 12.0000.

†The content of these gases may undergo significant variations from time to time or from place to place relative to the normal.

are strongly dependent upon pressure as well as upon temperature. The equilibrium concentrations of O_2 , CO_2 and N_2 (and later CO and NO) decay appreciably less rapidly as the pressure increases. It is evident from Figure D-1, however, that NO becomes a major constituent of high temperature air and that any CO_2 present tends to dissociate to CO (and O) for temperatures much above $\sim 3000^\circ K$.

At normal temperatures and pressures, atmospheric air is relatively very transparent in the visible and near ultraviolet spectral regions. This fortunate lack of opacity occurs because at normal atmospheric temperatures all the really strong N_2 and O_2 absorption bands occur in the "vacuum ultraviolet" wavelengths shorter than $\sim 2100 \text{ \AA}$. Below about 2000 \AA , a few centimeters of air, at one atmospheric pressure, are completely opaque owing to the N_2 and O_2 absorption. The earth's high altitude ozone layer serves as protection against near ultraviolet radiation in the ~ 2100 to $\sim 3000 \text{ \AA}$ region, transmitting only the less hazardous "sunburn" ultraviolet wavelengths above $\sim 3000 \text{ \AA}$. However, it can be seen from Table D-1 that near sea level (and up to ~ 20 kilometers altitude) the normal (but highly variable) "parts per million" ozone concentration is relatively low. In the relatively short path lengths of current interest, then, the ozone absorption spectral region is available for use. Except for some relatively very weak "forbidden transition" O_2 absorption near 0.78μ , N_2 and O_2 also are transparent in the infrared. Virtually all of the atmospheric infrared absorption and re-emission of solar radiation, so important to the earth's "heat budget", is due to the minor atmospheric constituents, and primarily to H_2O and CO_2 . Figures D-2 and D-3, also extracted from Reference [5], present solar spectra (spectra of the sun as transmitted through earth's atmosphere) for spectral regions extending respectively from ~ 0.2 to 3.2μ and from 1 to 16μ . Figure D-3 also shows laboratory absorption spectra for H_2O and CO_2 and some of the other minor atmospheric constituents listed in Table D-1.

D.1 Radiating Species for Shock Heated Air

For high temperature radiation or absorption by shock heated air, an investigation has demonstrated that the three most important molecular band systems are those historically designated as O_2 -Schumann-Runge [O_2 (S - R)], NO (β) and NO (γ). In the notation presented in Appendix B, these are respectively the ($B \rightarrow X$) system for the O_2 molecule and the ($B \rightarrow X$) and ($A \rightarrow X$) systems for the NO molecule. Their ν_{00} -positions are $49,163 \text{ cm}^{-1}$, $45,440 \text{ cm}^{-1}$ and $44,138 \text{ cm}^{-1}$ respectively.

It was found, in spite of the relatively large amounts of N_2 present, that N_2 -band systems made only relatively very minor contributions to air radiation or air

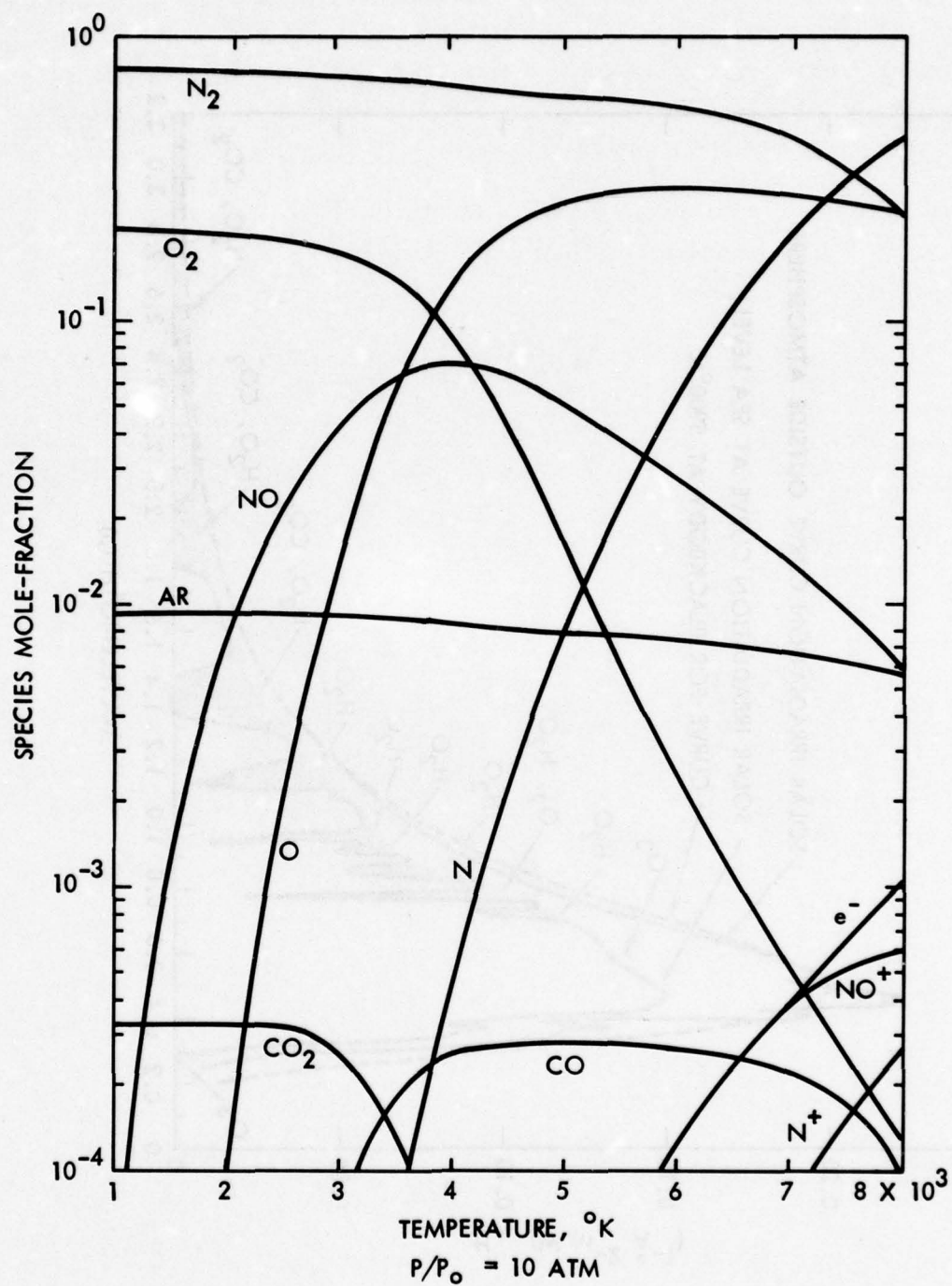


Figure D-1. Mole Fractions in Dry Air at 10 Atmospheres

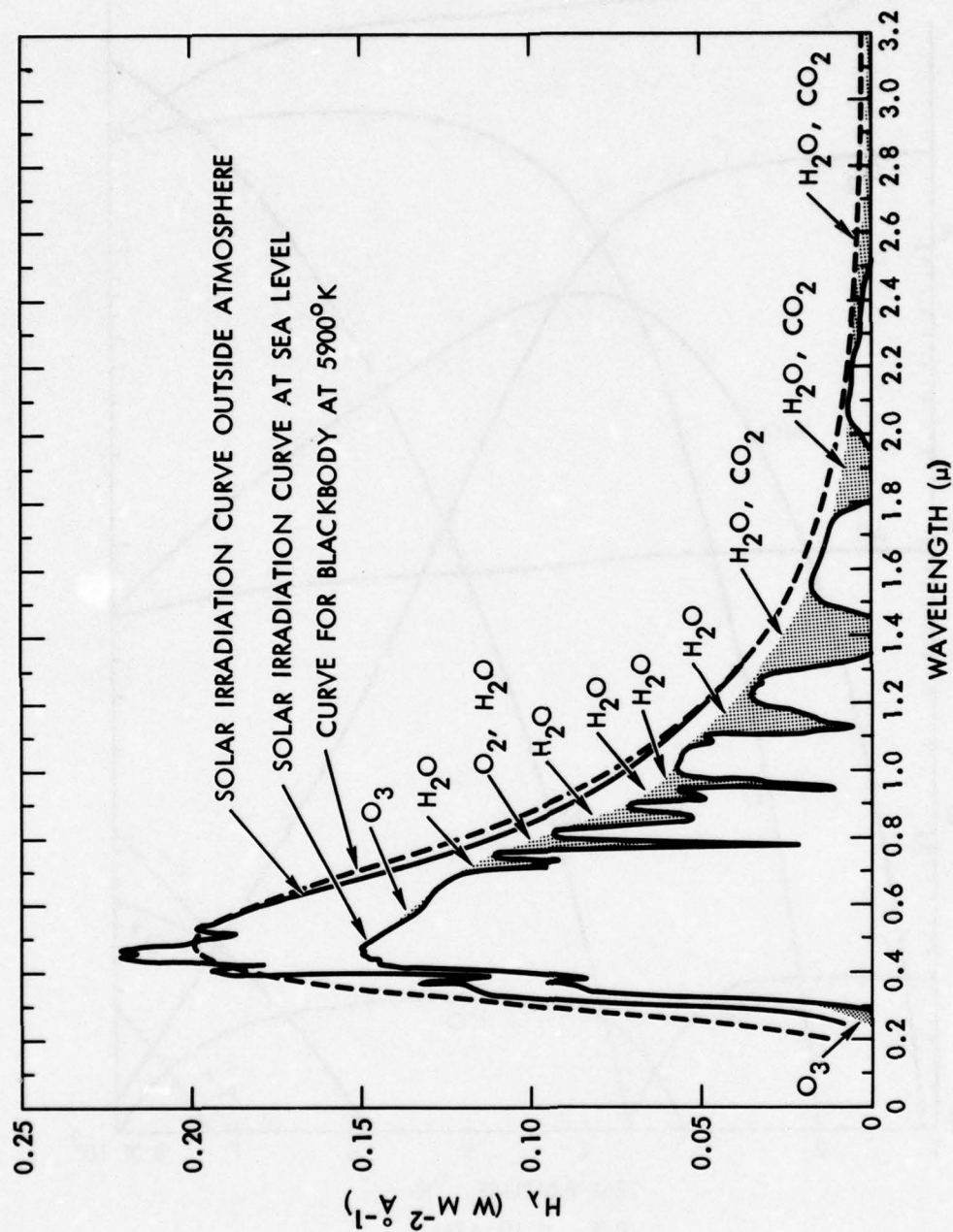


Figure D-2. Spectral Distribution Curves Related to the Sun; Shaded Areas Indicate Absorption, at Sea Level, Due to the Atmospheric Constituents Shown

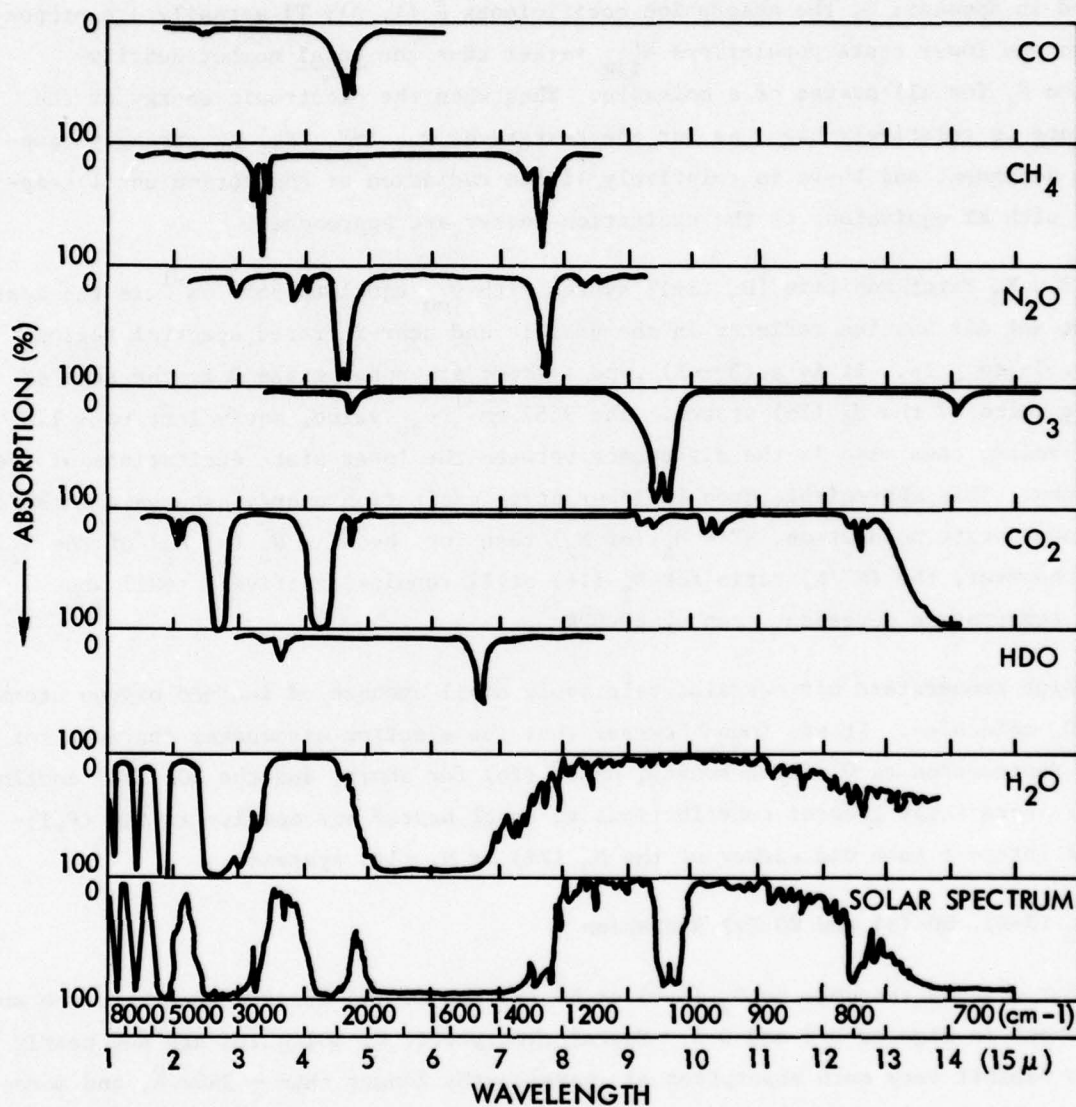


Figure D-3. Comparison of the Near-Infrared Solar Spectrum with Laboratory Spectra of Various Atmospheric Gases

opacity within the spectral region and temperature interval of interest. The N_2 Second Positive [$N_2(2+)$] with $\nu_{00} = 29,670 \text{ cm}^{-1}$ is a ($C \leftrightarrow B$) type system and the highly excited lower electronic state is only relatively sparsely populated even at 8000°K . As was described in Appendix C, the absorption coefficients $\bar{k}_1(\lambda, \Delta\lambda; T)$ actually are proportional to the lower state populations N''_{ijm} rather than the total number density population N_1 for all states of a molecule. Thus when the electronic energy of the lower state is relatively high, as for the B-state of N_2 , (N''_{ijm}/N_1) is strongly temperature dependent and there is relatively little radiation or absorption until temperatures with kT equivalent to the excitation energy are approached.

The N_2 First Positive [$N_2(1+)$] system with ν_{00} equal to 9557 cm^{-1} is the most important hot air species radiator in the visible and near-infrared spectral region from $\sim 0.55\mu$ to $\gtrsim 1\mu$. It is a ($B \leftrightarrow A$) type system; its upper state B is the same as the lower state of the $N_2(2+)$ system. The 9557 cm^{-1} ν_{00} value, equivalent to ~ 1.2 electron volts, thus also is the difference between the lower state excitations of the two systems. This appreciable drop in lower state excitation energy assures a markedly higher lower state population, $N'' = N_A$ (of N_2) than for the $N'' = N_B$ (of N_2) of the $N_2(2+)$ system. However, the (N''/N) ratio for $N_2(1+)$ still remains relatively small and strongly temperature dependent even at 8000°K .

High temperature air contains relatively small amounts of ionized oxygen atoms O^- and NO_2 molecules. It was found however that the electron attachment continua for O^- -atoms, represented as O^- (free-bound), or O^- (fb) for short, and the NO_2 (fb) continua both made appreciably greater contributions to shock heated air opacity in the (P,T)-regime of interest than did either of the $N_2(2+)$ or $N_2(1+)$ systems.

D.1.1 O_2 (S-R), NO (β) and NO (γ) Radiation

For obvious reasons, no O_2 (S-R) or NO (β) and NO (γ) spectra appear in the solar spectra shown in Figures D-2 and D-3. Normal atmospheric O_2 molecules are not nearly hot enough to exhibit very much absorption at wavelengths longer than $\sim 2400 \text{ \AA}$, and moreover the O_2 (S-R) absorption region is masked by the much stronger (for cold molecules) absorption by the high altitude O_3 layer in the ~ 2100 to $\sim 3000 \text{ \AA}$ region. Also, normal atmospheric air contains at most only very minute proportions of NO (see Table D-1).

Figure D-4, extracted from Reference [7] presents both computed curves for radiation from individual hot air species and empirical data resulting from measurements of this radiation in shock tube experiments. The authors of the referenced report [7]

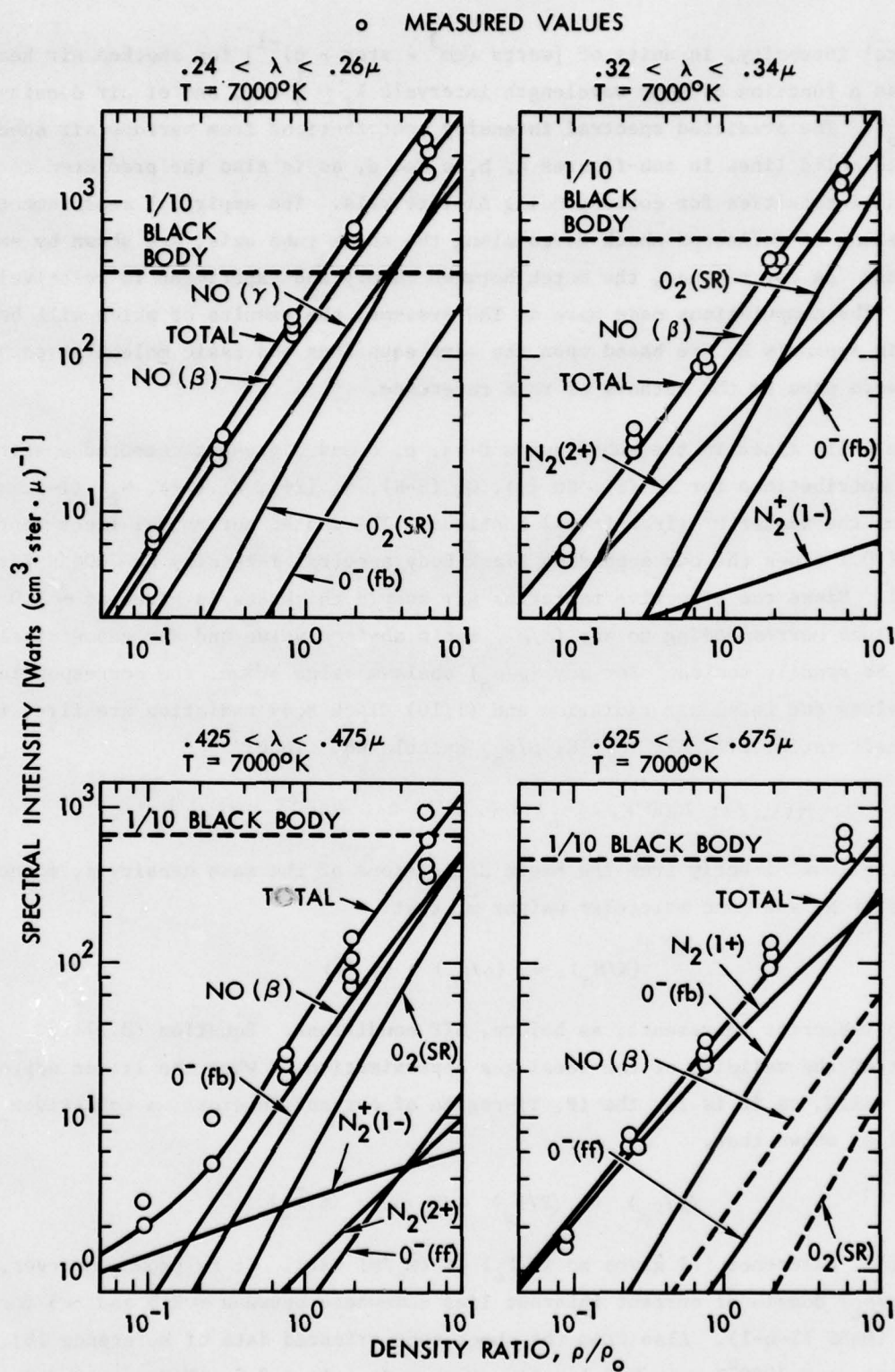


Figure D-4. Spectral Intensity as a Function of Density Ratio

plot spectral intensity, in units of $[\text{watts (cm}^3 \cdot \text{ster} \cdot \mu)^{-1}]$ for shocked air heated to 7000°K as a function of four wavelength intervals $\lambda_1 \pm \frac{1}{2} \Delta\lambda_1$, and of air density ratio (ρ/ρ_0) . The predicted spectral intensity contributions from various air species are shown as solid lines in sub-figures a, b, c and d, as is also the predicted total air spectral intensities for corresponding $\Delta\lambda$ -intervals. The empirical measurements, made by looking at reflected shock waves along the shock tube axis, are shown by small open circles. As can be seen, the match between theory and experiment is relatively very good. The computations made here at TRW Systems, the results of which will be presented in Appendix E, are based upon the same equations and basic molecular parameter values as were used by the authors of this reference.

The solid lines in the sub-figures D-4a, b, c and d present computed spectral intensity contributions for NO (β), NO (γ), O_2 (S-R), N_2 (2+), N_2 (1+), N_2^+ (1-), and the O^- (fb) [and the weaker O^- (free-free)] continua. The dashed horizontal lines represent a factor of 0.1 times the corresponding Black Body spectral intensity at 7000°K for each $\Delta\lambda$ -interval. Since the effective radiating air sample thickness is given as ~ 1.0 cm, the τ_{air} values corresponding to any (ρ/ρ_0) ratio abscissa value and any geometrical path L can be readily scaled. For any (ρ/ρ_0) abscissa value shown, the corresponding ordinate values for total air radiation and (1/10) Black Body radiation are first read and then their ratio, $r(\lambda, \Delta\lambda; 7000^\circ\text{K}, \rho/\rho_0)$ calculated. Then:

$$\tau(\lambda, \Delta\lambda; 7000^\circ\text{K}, \rho/\rho_0) \approx 0.1r(\lambda, \Delta\lambda; 7000^\circ\text{K}, \rho/\rho_0) L \quad (\text{D.1})$$

It follows directly from the basic definitions of the mass density ρ , molecule number density N , and mean molecular weight \bar{m} , that:

$$(N/N_0) = (\rho/\rho_0) \cdot (\bar{m}_0/\bar{m}) \quad (\text{D.2})$$

where the 0 subscript represents, as before, STP conditions. Equation (D.2) is independent of the validity of the ideal gas approximation. When the latter approximation is valid, as it is for the (P, T)-regime of current interest, a comparison with equation (1.8) shows that:

$$(\rho/\rho_0) = (P/P_0) \cdot (T_0/T) \cdot (\bar{m}_0/\bar{m}) \quad (\text{D.3})$$

Unfortunately, Reference [7] gives no (P/P_0) or (\bar{m}_0/\bar{m}) data. It is known, however, that the (ρ/ρ_0) domain of current interest lies somewhere between ~ 2.5 and ~ 5 for $T = 7000^\circ\text{K}$ (DABS II-D-1). Also from the shock tube oriented data of Reference [8], it is known that at $\sim 7000^\circ\text{K}$ and $(P/P_0) = 113$ atm., (ρ/ρ_0) is $\gtrsim 3.7$. For $\rho/\rho_0 \approx 3.7$, the

application of equation (D.1) to Figures D-4a and b give τ -values of:

$$\begin{aligned}\tau(0.25\mu, 0.02\mu; 7000^\circ\text{K}, 113 \text{ atm}) &\approx 32 \\ \tau(0.33\mu, 0.02\mu, 7000^\circ\text{K}, 113 \text{ atm}) &\approx 9.6\end{aligned}\quad (\text{D.4})$$

The corresponding τ -values are seen to drop below 3 for the longer wavelengths.

Figure D-4 also shows that while the $\text{N}_2(2+)$ and $\text{N}_2^+(1-)$ radiation is dominant for very low (ρ/ρ_0) -ratios (i.e., at low pressures) for some wavelengths in the interval of interest, that their relative contribution decreases with increasing ρ/ρ_0 (and P/P_0) as the mole-fractions of NO and O_2 increase relative to those of N_2 (and of N_2^+). The dominance of $\text{N}_2(1+)$ radiation at wavelengths $> 0.625\mu$, and also the implication of relatively low τ values is shown in Figure D-4b.

D.1.2 Free Electron [$e^-(\text{ff})$] Radiation

Free electrons in gas volumes both radiate and absorb radiant energy when their momentum is altered by collisions with the other gas particles (molecules, atoms, ions, etc.). The free-free [$e^-(\text{ff})$] absorption coefficient generally is given in terms of actual geometrical path L rather than of atmosphere-centimeters [which as has been shown previously for molecular absorption, really would represent $(N_{e^-}/N_0) L$ rather than $(P/P_0)L$]. The geometric absorption coefficient for $e^-(\text{ff})$ absorption, to be multiplied by L to obtain τ_{e^-} is given by the expression:

$$k'_{e^-} \approx (1/c) \frac{\omega_p^2 \nu_{e^-}}{\omega^2 + \nu_{e^-}^2} \quad (\text{D.5})$$

Here ν_{e^-} , the collision frequency of the electrons with gas particles is within two significant figures equal to $1.0 \cdot 10^{11} (P/P_0) \text{ sec}^{-1}$. As usual, c represents the speed of light, equal to cgs units to $2.997925 \cdot 10^{10} \text{ cm sec}^{-1}$. The "plasma frequency", ω_p , in units of radians sec^{-1} , is given by the expression:

$$\omega_p^2 = 4\pi N_{e^-} (e)^2 (m_{e^-})^{-1} \quad (\text{D.6})$$

The symbol ω represents the radian frequency of the optical radiation absorbed or emitted. That is:

$$\omega = 2\pi c \lambda^{-1} \quad ; \quad \lambda \text{ in cm} \quad (\text{D.7})$$

In the optical frequency and pressure regime of interest, i.e., 2.5×10^{-5} cm $\lesssim \lambda \lesssim 5 \times 10^{-4}$ cm and $(P/P_0) < 200$ atmospheres, it is found that $\omega^2 \gg \nu_e^2$ and equation (D.5) simplifies to the form:

$$k'_{e-} \approx \frac{\omega_p^2 \nu_e}{(c \omega^2)} \approx \frac{(e)^2 1.0 \times 10^{11} \text{ sec}^{-1}}{\pi m_{e-} (c)^3} (P/P_0) \lambda^2 N_{e-} \quad (\text{D.8})$$

or for λ in μ [$1\mu \equiv 10^{-4}$ cm] rather than in cm,

$$k'_{e-} \approx \frac{(e)^2 1.0 \cdot 10^3 (P/P_0) \lambda^2 (\text{cm}^2 \mu^{-2} \text{ sec}^{-1}) N_{e-}}{\pi m_{e-} (c)^3} ; \lambda \text{ in } \mu \quad (\text{D.8a})$$

Substituting numerical (cgs) values for the electron charge, e^- , the electron mass m_{e-} and speed of light, c one obtains:

$$k'_{e-} \approx 2.99 \times 10^{-21} (P/P_0) \lambda^2 \cdot N_{e-} (\text{cm}^2 \cdot \mu^{-2}) \quad (\text{D.8b})$$

$\lambda \text{ in } \mu, N_{e-} \text{ in cm}^{-3}$

For the 81 cm optical path length assumed for DABS II-D-1

$$\tau_{e-} = k'_{e-} \times 81 \text{ cm} \approx 2.42 \times 10^{-19} (P/P_0) \lambda^2 \times N_{e-} \times (\text{cm}^3 \times \mu^{-2}) \quad (\text{D.9})$$

$\lambda \text{ in } \mu, N_{e-} \text{ in cm}^{-3}$

As an example, Reference [8] gives an N_{e-} concentration of $6.87 \cdot 10^{16}$ free electrons cm^{-3} at $T = 8131^\circ\text{K}$ and $(P/P_0) = 135.6$ (standard) atmospheres. By substituting into equation (D.9), one finds a τ_{e-} value of 45.7 at $\lambda_4 = 4.5\mu$. Owing to the λ^2 -dependence, however, the τ_{e-} contribution at the same temperature and pressure is only 0.15 for $\lambda_1 = 0.26\mu$ and 0.29 at $\lambda_2 = 0.36\mu$. The N_{e-} concentrations increase quite strongly with both temperature and pressure [8]. Even at the higher pressures and longer wavelengths of interest, the τ_{e-} contributions become negligible for T much below 6000°K .

D.1.3 Infrared Radiation from CO_2 and H_2O

In the infrared spectral region, virtually all observed spectral activity arises from transitions between vibration-rotation levels of the same electronic state, and

mostly of the ground electronic state. The NASA Handbook of Infrared Radiation From Combustion Gases [4] gives very convenient spectrally averaged absorption coefficients, $\bar{k}(\lambda; T)$ for the principal infrared vibration-rotation bands of CO_2 , H_2O , CO , NO , etc., for selected temperatures between 600 and 3000°K. It is readily seen from Figures D-2 and D-3 that CO_2 and H_2O are the most important infrared absorbing (and emitting) species in normal atmospheric air. As temperatures increase, the absorption bands tend to broaden, shift contour centers and intensify as transitions from successively higher lower state levels become important contributors. It was found, however, that even the strongest infrared band, that of the CO_2 fundamental centered near 4.3μ , could give a τ -value $\gtrsim 3$ for the DABS II-D-1 configuration only for $(P/P_0) \gtrsim 120$ atm. This is unfortunate since it is desirable to have at least one reliable near-infrared, radiometer, preferably near 5μ , for measurement of temperatures below 4000°K.

D.1.3.1 Infrared Radiation From Air + 4% CO_2

The addition of 4% CO_2 to the ambient air in the shock tube (before the shock occurs) would readily solve the preceding problem. As will be shown by graphs to be presented in Appendix E, the 4% CO_2 (which tends to dissociate to form CO at temperatures above $\gtrsim 3000^\circ\text{K}$), would provide for τ -values of $\gtrsim 3$ not only near 4.3μ wavelength, but also within the contours of the much weaker CO_2 "combination band" centered near 2.7μ wavelength. Wavelengths of $\lambda \approx 2.8\mu \pm 0.05\mu$ and $\lambda_4 \pm 4.5\mu \pm 0.05\mu$ were selected for observations of the air shock with 4% CO_2 added. The selections were influenced by the ready availability of relatively inexpensive off-the-shelf filters (which may be somewhat broader, however, at 4.5μ wavelength). The λ_4 -centered at 4.5μ rather than 4.3μ wavelength was chosen so as to be able to also observe the high temperature CO radiation which occurs as progressively more CO_2 dissociates with increasing T . It will be seen from Figure E-9, that the total τ -value at $\sim 4.5\mu$ wavelength should be $\gtrsim 3$ over virtually the total (P, T) regime of interest from less than 1000°K to over 8000°K . The lower temperature emission is from CO_2 and then CO_2 plus CO , and then only CO . As T increases $\gtrsim 6500^\circ\text{K}$, the e (ff) emission discussed in Section D.1.3 begins to first supplement, and then take over from the eventually dissociating CO molecules.

As was seen in Figure A-3, the 4.5μ wavelength radiometer can be combined not only with the $\lambda_3 = 2.8\mu$ radiometer for useful relatively low temperature measurements, but also with the $\lambda_1 = 0.26\mu$ radiometer to provide good coverage of the temperature interval from 3500 to above 8000°K . As remarked earlier in Section 1.4.4.3, the upper and lower temperature boundaries are set by practical rather than intrinsic limitations.

D.2 Infrared Radiation From Combustion Products

Preliminary indications are that the gaseous combustion products for the DAB II-D shots would be initially $\sim 64\%$ H_2O , $\sim 13\%$ CO_2 and $\approx 22\%$ N_2 . Both the O_2 and CO_2 would begin to dissociate with temperatures above $\sim 2500^\circ\text{K}$ but indications are that there is very little possibility of exceeding this temperature even if considerable afterburning of solid explosive fragments follows downstream; a maximum temperature of less than 1000°K is much more likely.

Radiometers with λ_5 centered on 1.9μ and λ_6 on 4.3μ were selected as the primary pyrometer pair to view combustion products. As can be seen from Figure D-3, the 1.8μ wavelength water vapor "combination band" to be viewed by the λ_5 radiometer is much weaker than (about 10% as strong as) the less conveniently located 2.7μ and 6.3μ wavelength H_2O "fundamental" bands. However, with the 65% of H_2O present, the computed $\tau(1.9\mu, 0.1\mu; T, P)$ values are $\gtrsim 3$ over virtually all of the range interest, particularly for $T \lesssim 2000^\circ\text{K}$. The 2.8μ wavelength radiometer channel also will be available to team with the 4.3μ wavelength channel as a (λ_3, λ_6) pyrometer useful at the lower combustion product temperatures. The λ_6 value of 4.3μ rather than a repeat of the 4.5μ λ_4 value was selected because it is more suitable at lower temperatures if there is a time lag in the arrival of the carbon soot particles, and because the high temperature CO radiation at 4.5μ wavelength is irrelevant to the combustion products; Figure E-10b shows the computed 1.9μ and 4.3μ wavelength $\tau(P, T)$ -values for the combustion products for the DABS II-D-1 configuration. The computed τ -values are very high for the 4.3μ wavelength channel (as they also would be at 4.5μ wavelength except for the lowest temperature values). At the same temperature and pressure, τ -values for the DABS II-D-2 configuration are five times as large as those for DABS II-D-1.

APPENDIX E RESULTS OF OPACITY COMPUTATIONS

All the opacity computations presented in the following sub-sections are for the DABS II-D-1 configuration. For the same temperature and pressure, the DABS II-D-2 τ -values would be a factor of 5 larger, owing to the longer path length of radiating gas being viewed.

E.1 Air Species

The opacity determining optical thickness parameters, $\tau(\lambda, \Delta\lambda; P, T)$ were computed, with approximate assumptions from equations (1.6) or (1.6a) for the six selected wavelength intervals $\lambda_i \pm 1/2\Delta\lambda_i$. The required thermal equilibrium mole-fraction values, $x_i(T, P)$, were computed for temperatures up to 5000°K from an available in-house program. Unfortunately, this program has not yet been extended to include chemistry reaction rates for temperatures above 5000°K. For temperatures above 5000°K and for $P/P_0 > 10$ atms. species number density values $N_i(T, P)$, rather than mole-fraction values, were extracted from extensive computed theoretical "shock tube chemistry" tables given in a JPL Report [7]. These tables listed N_i - values corresponding to different presumed temperature and pressure initial conditions for an "air" shock, and for a presumed resulting "moving shock", "standing shock", and "reflected shock". The temperatures, pressure ratios (P/P_0), density ratios (ρ/ρ_0), enthalpies, etc., are listed for each N_i -column. However, systematic distributions of temperature values, or of (P/P_0)-values for any temperature are not available, and the desired data must be gleaned by checking through each set of tables to find if any ($T, P/P_0$) pairs of interest are included. Although the data extracted by this gleaning process was appreciably less detailed than was desirable, there was still sufficient data to make useful interpolations and extrapolations.

Figure E-1 presents the resulting computed mole-fraction data for N_2 , O_2 , NO, CO_2 and CO in air for T varying from 1000 to $\sim 8000^\circ\text{K}$ and for pressure intervals of 10 atms $\leq P/P_0 \leq 125$ atms. The 10 atmosphere data was taken directly from the Langley Research Center NASA Technical Note by J. S. Lee and P. J. Bobbitt from which Figure D-1 was extracted [6]. It is seen that the dissociation of N_2 , O_2 and CO_2 , and the consequent formation of NO and CO, tends to be lowered as pressure increases. Thus O_2 , N_2 and CO_2 radiation tends to increase with increasing pressure. At the lower temperatures, the reverse is true for CO and NO radiation. As temperature increases, however, dissociation also tends to occur in NO and CO molecules, and this in turn is slowed by increase in pressure.

Mean spectral absorption coefficients for O_2 (S-R), NO (β), NO (γ), N_2 (2+), N_2 (1+), O^- (ff), the NO_2 continua, and N_2^+ (1-) were computed from formulae and data

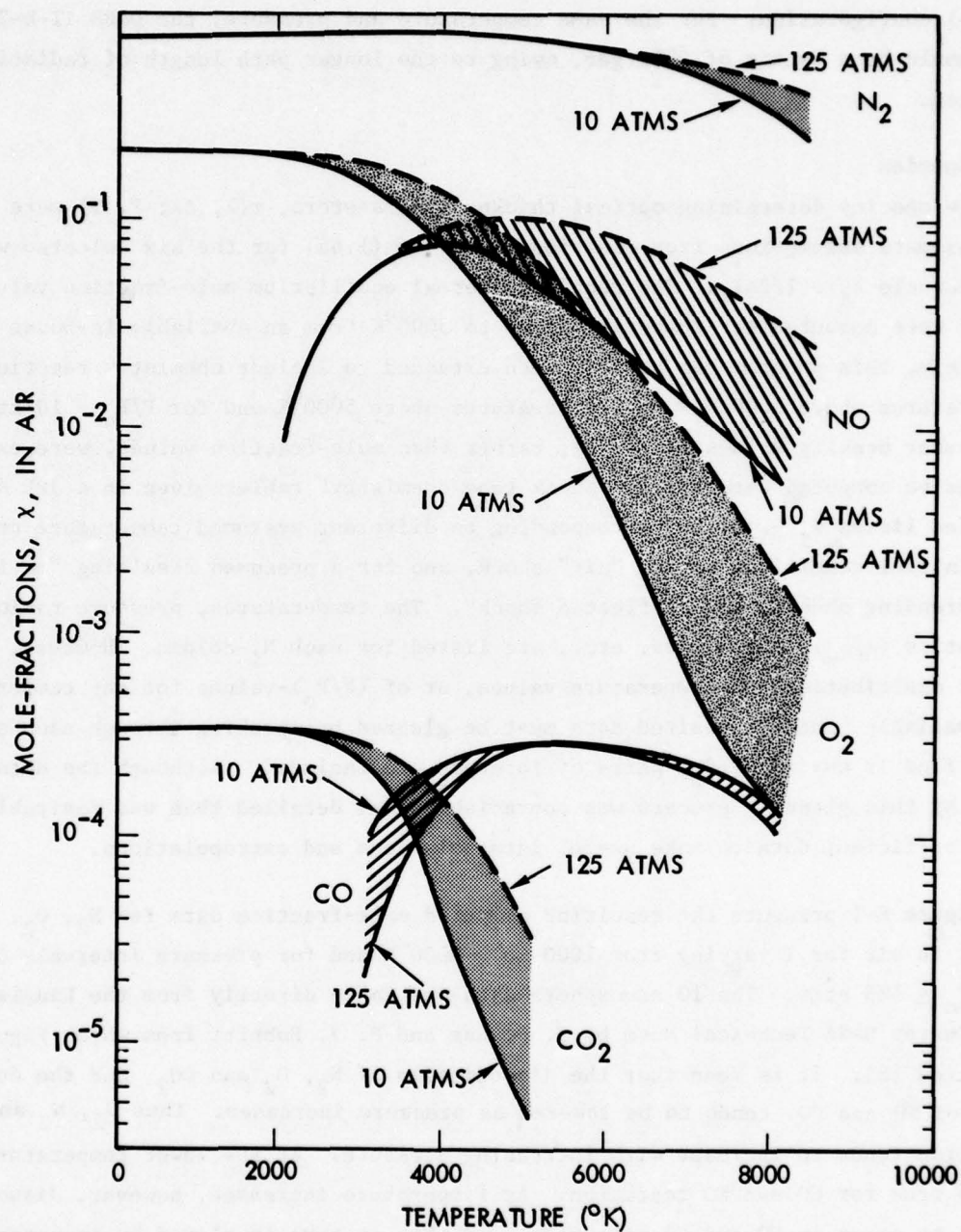


Figure E-1. Temperature-Pressure Dependence of Mole Fractions in Air

given (mostly in Chapter V. §21 of Volume I) in the excellent text by Zel'dovich and Raizer [8]. The reader should be warned, however, that there is a confusion in definition of their c_1 "concentration" parameter occurring on the formulae given on page 334 (and elsewhere) of this reference. For physical consistency, their c_1 cannot possibly be equal to (N_1/N_0) as appears to be implied by the somewhat obscure wording of their definition, perhaps owing to a mis-translation from the original Russian text. Rather, their entire $(c_1 \rho/\rho_0)$ term must be replaced by either (N_1/N_0) or by its equivalent $(\chi_1 N/N_0) = \chi_1 (\rho/\rho_0) \frac{\bar{m}}{m}$ [see Appendix D]. The data presented by Zel'dovich and Raizer was largely taken directly or adapted from the previously referenced paper [7] from which Figure D-4 was extracted.

Figure E-2 presents the absorption coefficients for O_2 (S-R), NO (β) and NO (γ) contributions computed from the Zel'dovich and Raizer equations for temperatures of 10,000, 8000, 6000, and 4000°K. It is seen that the O_2 (S-R) absorption (or emission) is the strongest, and that the NO (γ) radiation, is not only weaker than the NO (β) near 0.2600 μ , but drops off much more rapidly with increasing wavelength.

Figure E-3 presents similar data, but with 5000 rather than 4000 °K curves, for the N_2 (2+) and N_2^+ (1-) band systems. It is seen that the N_2 (2+) absorption is more than two orders of magnitude weaker than that for NO (β) near 8000 °K, and drops off very rapidly with decreasing temperature. Therefore, in spite of the relatively large N_2 concentrations, as shown in Figure E-1, the N_2 (2+) contributions to the computed τ 's were very minor. As previously mentioned (see Figure D-4), the N_2 (1+) spectral activity occurs mostly in the longer wavelength visible region and turned out to be too low to give τ 's > 1 for the DABS II-D-1 configuration.

The N_2^+ (1-) absorption coefficients are relatively very large as is seen (on the right hand ordinate scale) in Figure E-3. In the (T, P) regime of interest, however, the number density of N_2^+ ions was insufficient to provide more than very minor contributions to $\bar{\tau}$ (0.36 μ , 0.01 μ ; T, P).

Absorption coefficients for the O^- (fb) and NO_2 continua are not shown since their τ - contributions were computed directly without intervening χ_1 and \bar{k} computations from relatively very simple formulae and data given by Zel'dovich and Raizer.

Figure E-4 presents the results of opacity calculations for $\bar{\tau}_{air}$ (0.26 μ , 0.01 μ ; T, P) and $\bar{\tau}_{air}$ (0.36 μ , 0.01 μ ; T, P). As previously stated, the contributions were mostly from O_2 (S-R), NO (β) and NO (γ) at the shorter wavelength, and from the first

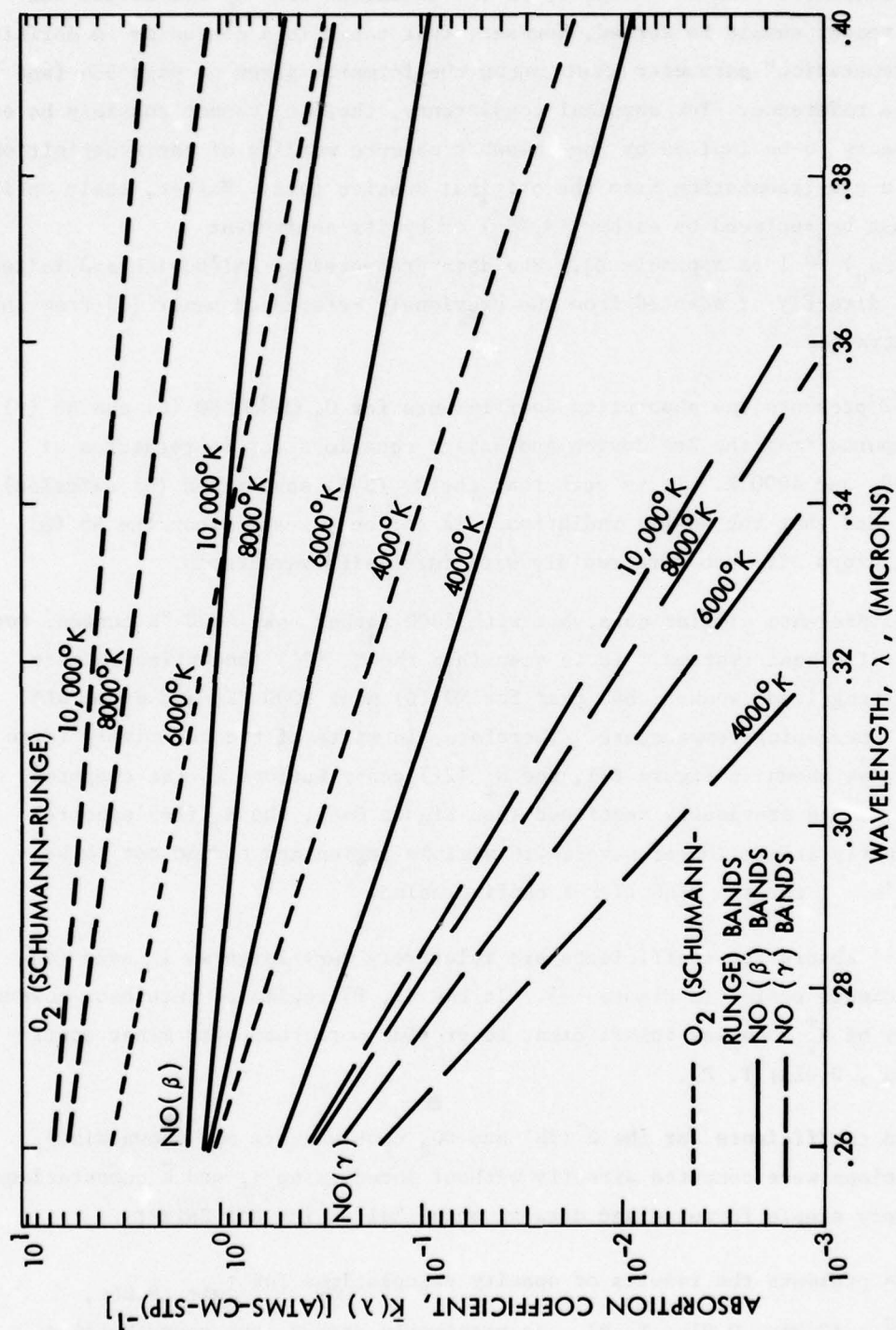


Figure E-2. Computed Absorption Coefficients for Air Modules
in the Near Ultraviolet and Violet Spectral Region

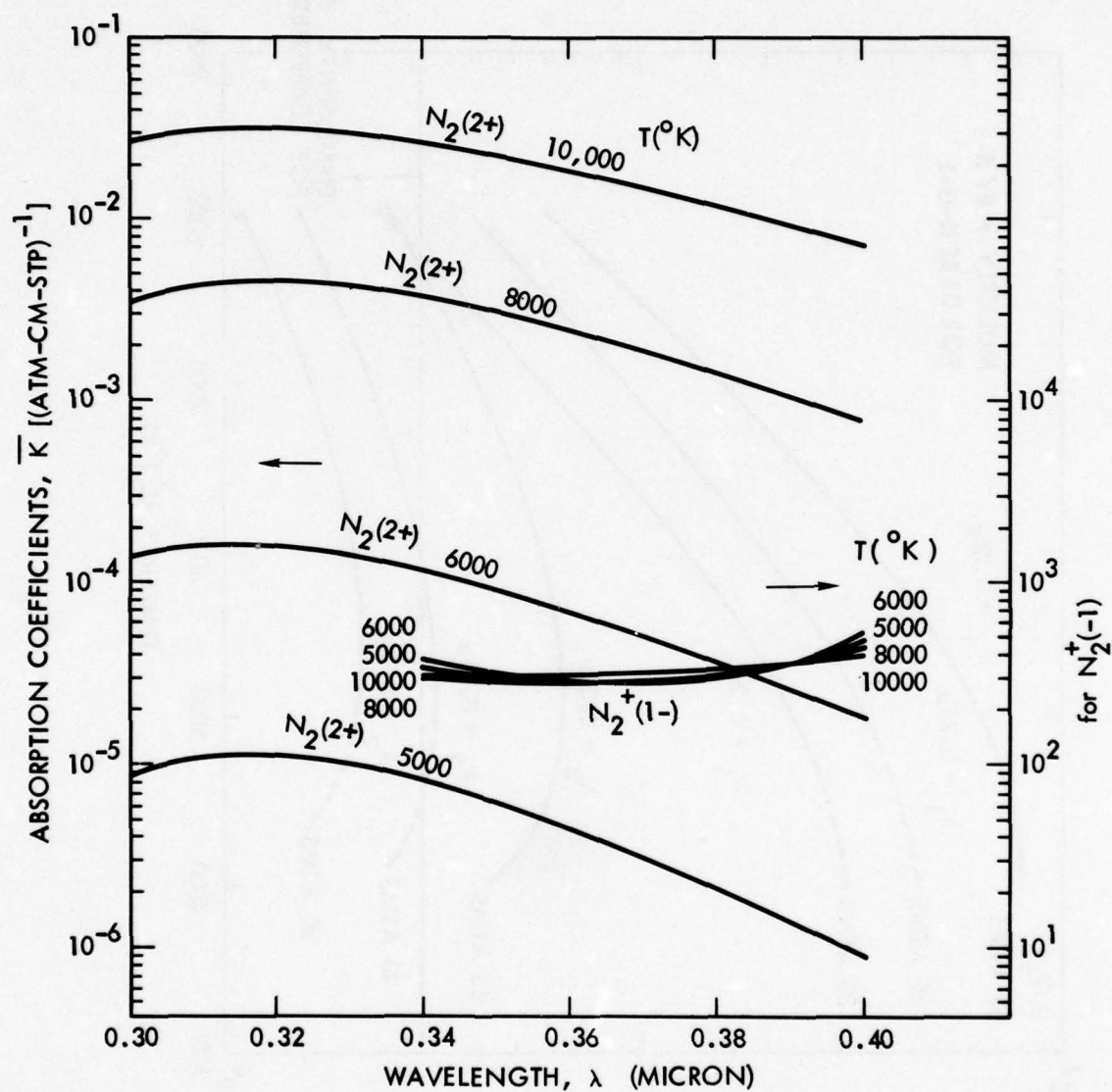


Figure E-3. Mean Absorption Coefficient for N_2 (Second Positive) and N_2^+ (First Negative) Band Structure

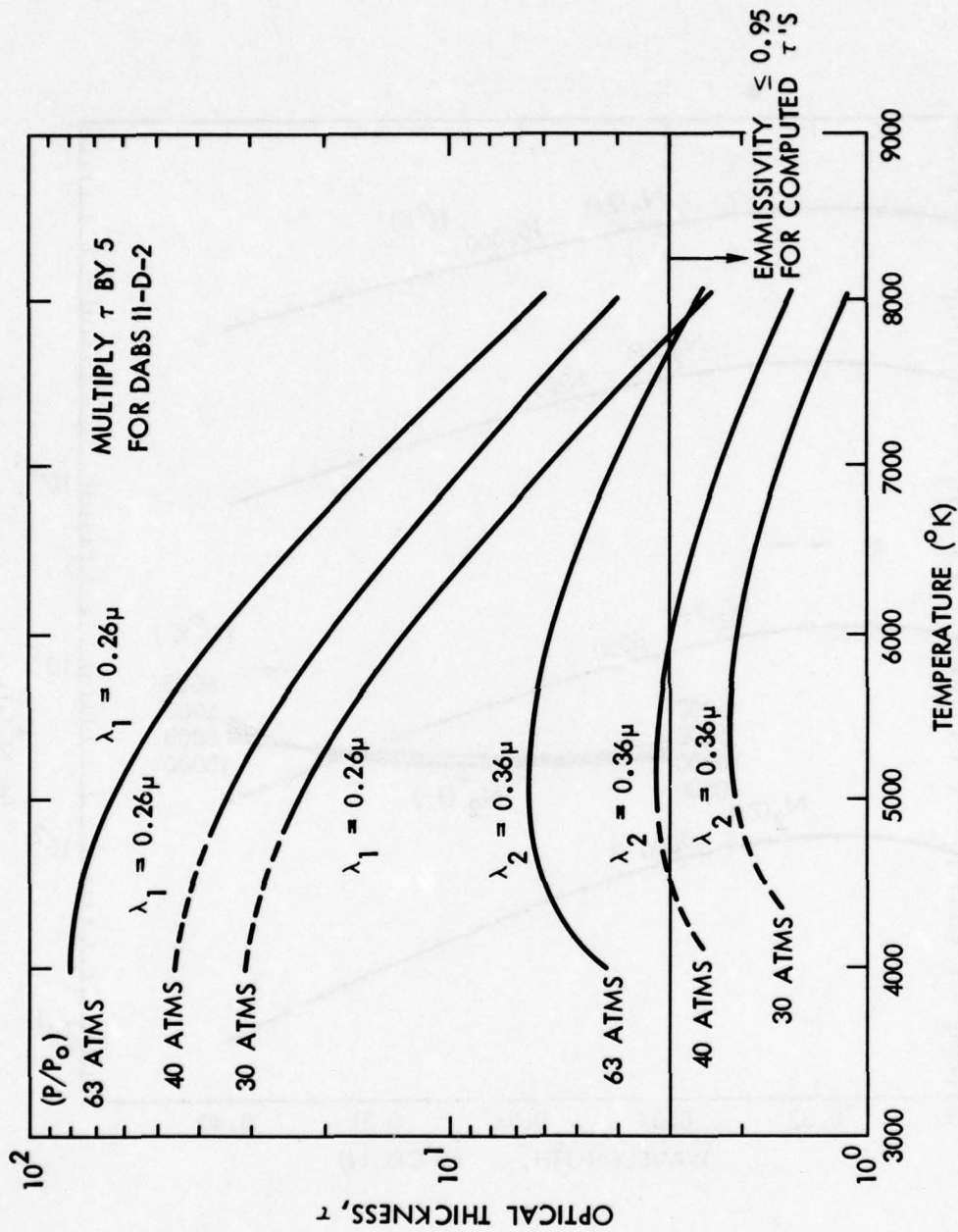


Figure E-4. Computed Optical Thickness, τ , for Air at 0.26μ and 0.36μ Wavelengths

two of these for 0.36μ wavelength. The NO_2 and O^- (fb) τ -contributions added up to as large as $\sim 8\%$ for some temperatures and pressures. It is seen that the 0.26μ wavelength radiometer will be viewing the equivalent of virtually black body radiation throughout the full range of the (T-P) regime of interest for both Station 1 and Station 2 of DABS II-D-1. This is not completely true however, of the 0.36μ wavelength radiometer for Station 2, where the air shock is predicted to arrive at ~ 82 atm. (1200 psia) and decay to ~ 41 atms. (600 psia) in 1 msec. Figures 1-3 and 1-4, and Table 1.1 show that the corresponding predicted air shock temperature interval is from $\sim 5100^\circ\text{K}$ to $\sim 4100^\circ\text{K}$. Figure E-4 shows that a pressure of ~ 50 atms, is required to keep $\bar{\tau}(0.36\mu, 0.02\mu; T, P)$ above ~ 3 near 4100°K . [τ 's 5 x greater for DABS II-D-2]

E.2 Air + 4% CO_2

Figure E-5 shows that temperature and pressure dependent mole-fractions of CO_2 and CO computed for 4% CO_2 added to the air. The computation for these curves was done on the in-house TRW program which is useful for $T \leq 5000^\circ\text{K}$, with small extrapolations to higher temperatures being guided by the 10 atms data of Reference [6]. Figure E-6 gives $\bar{k}(\lambda, \Delta\lambda; T)$ values for CO_2 , CO and H_2O (for later combustion gases use) taken from graphs and tables given by Reference [4].

Figures E-7 and E-8 show the respective values computed for $\bar{\tau}(2.8\mu, 0.1\mu; T, P)$ and $\bar{\tau}(4.5\mu, 0.1\mu; T, P)$. These plotted curves are not critically dependent upon the radiometer band centers $\lambda_3 \approx 2.8\mu$ and $\lambda_4 \approx 4.5\mu$, nor upon the assumed $\Delta\lambda$ intervals of 0.1μ as long as the spreads $\lambda \pm 1/2 \Delta\lambda$, remain within desired intervals. It is seen that the $\lambda_4, 4.5\mu$, radiometer should be looking at equivalent Black Body radiation for virtually all pressure values of interest and for temperatures from ~ 1000 to $> 6000^\circ\text{K}$. The 1000°K cutoff occurs because of the selection of $\lambda_4 \approx 4.5\mu$ rather than 4.3μ wavelength. The $\lambda_3, 2.8\mu$, radiometer, however begins to lose its usefulness for $T \geq 3500^\circ\text{K}$ at the lower pressure values. This is not particularly serious because the (λ_3, λ_4) pair of radiometers is of primary usefulness for $T \leq 3500^\circ\text{K}$.

The $\bar{\tau}_4$ -value shown in Figure E-8 are not complete, since they do not include e^- (ff) contributions, as computed from equation (D.9). Figure E-9 shows superimposed plots of $\bar{\tau}_1(0.26\mu, 0.01\mu; T, P)$ and $\bar{\tau}_4(4.5\mu, 0.1\mu; T, P)$ extending from $\sim 1000^\circ\text{K}$ to $\sim 8000^\circ\text{K}$, with the e^- absorption contributions now included in the latter curves. The upper and lower (P/P_0) pressure boundaries for the τ -regions shown are 125 and 30 atms. respectively. It readily is seen that the (λ_1, λ_4) pair both are looking at effectively "Black Body" radiation over virtually the full (P, T) regime of interest. However, signal fall off and transmission noise and dynamic range considerations, and the non-

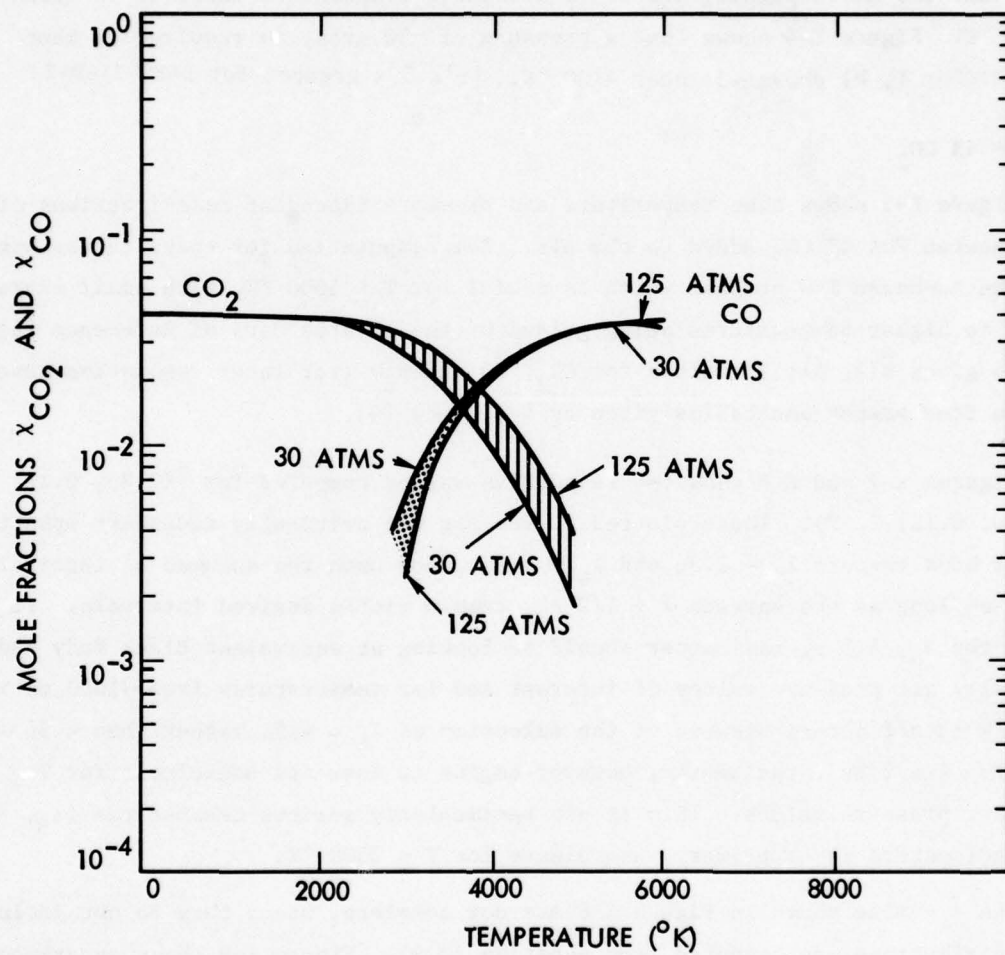


Figure E-5. Mole-Fractions of CO₂ and CO When 4% CO₂ Added to Air

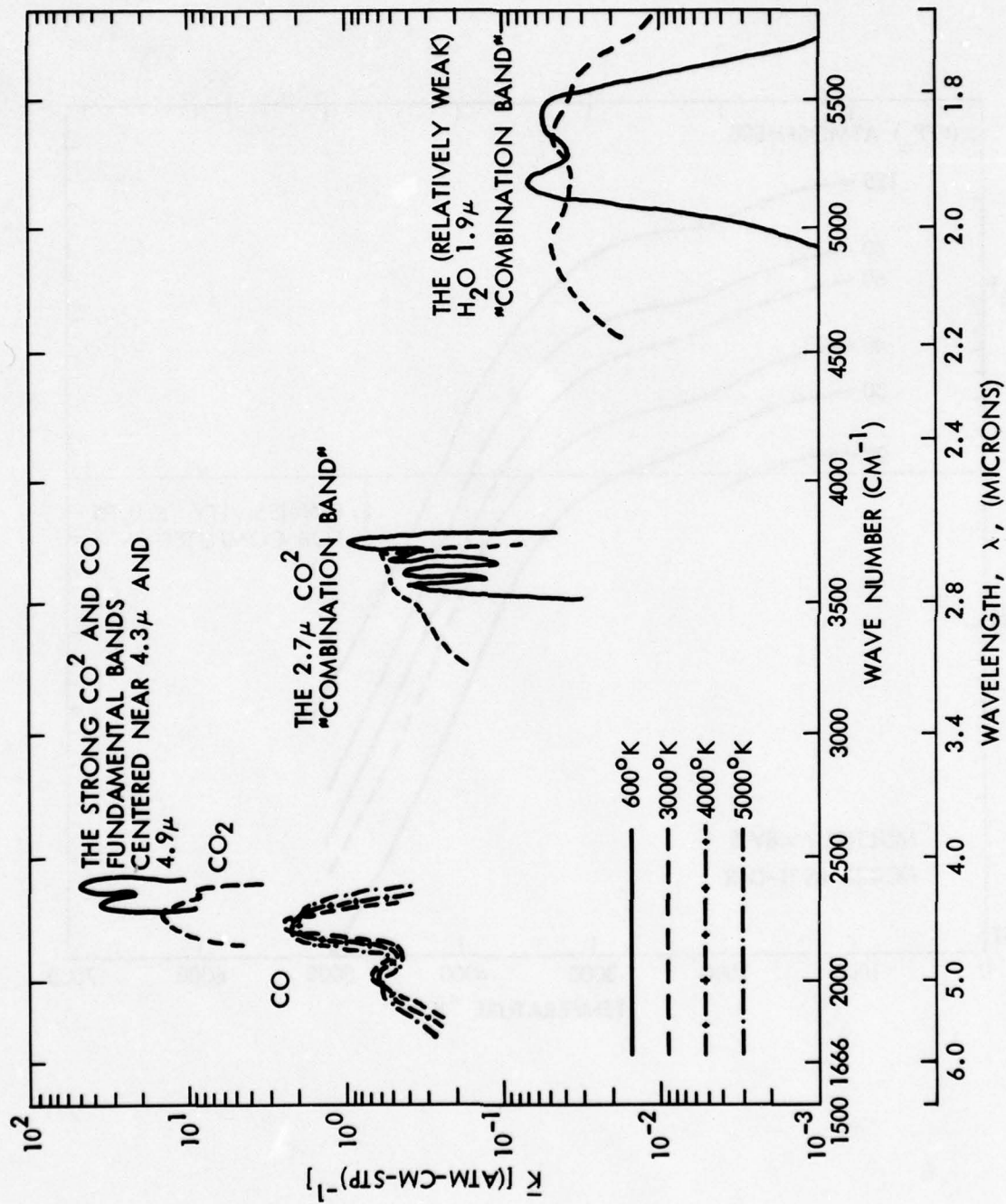


Figure E-6. Spectral Absorption Coefficients (Smoothed), in Selected Spectral Intervals, For CO_2 , CO and H_2O

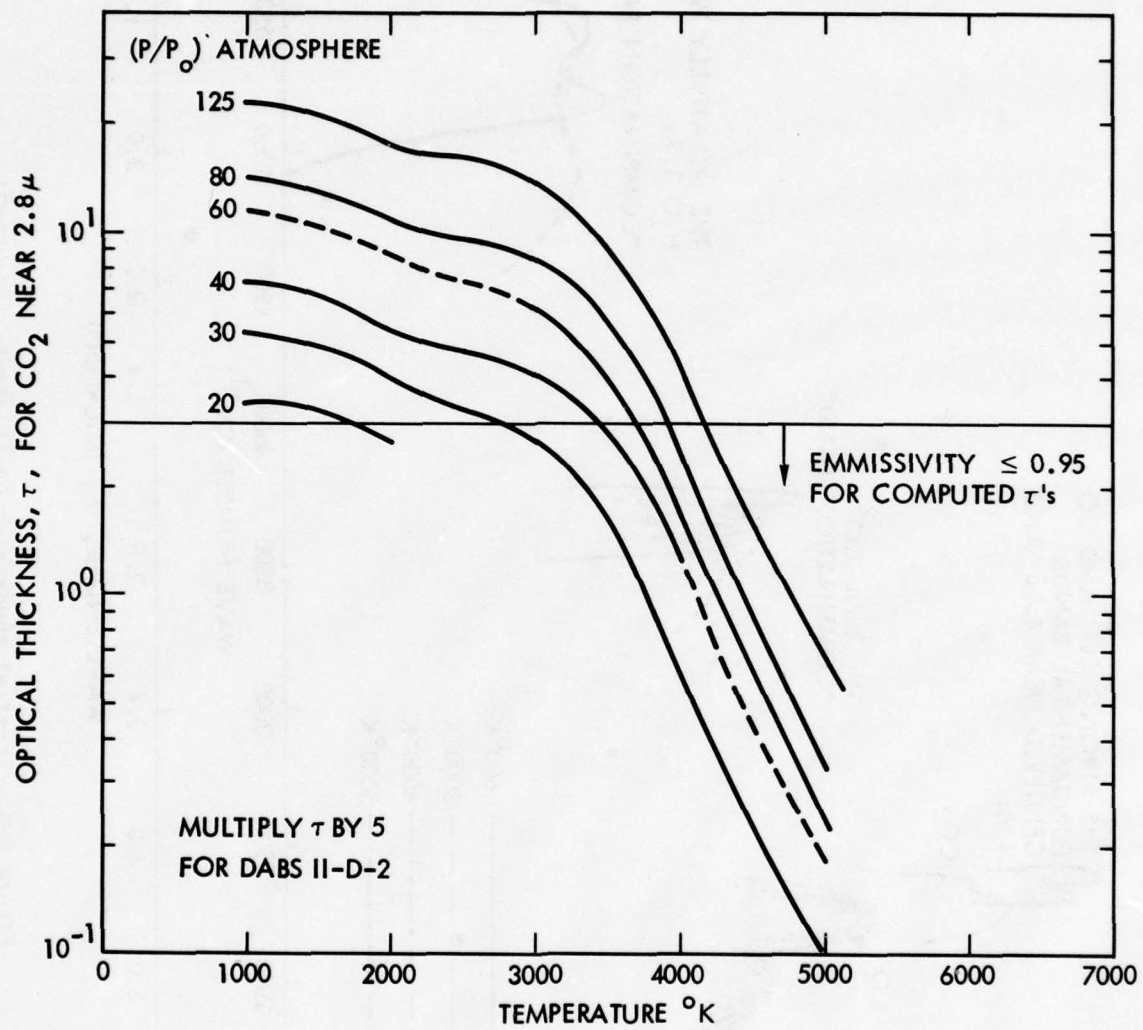


Figure E-7. Computed Optical Thickness Near 2.8μ Wavelength for 4% CO_2 in Air

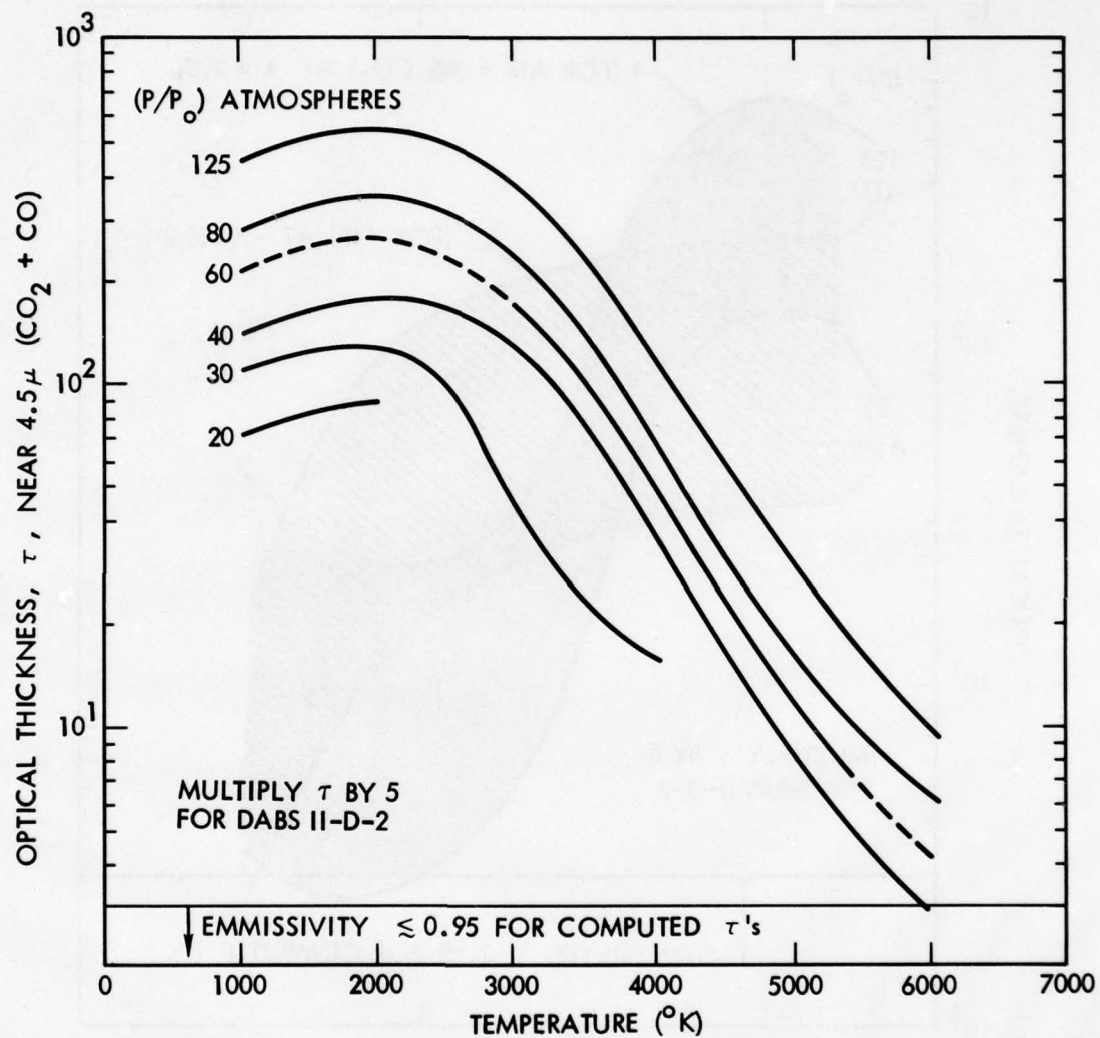


Figure E-8. Computed Optical Thickness for 4% CO_2
Added to Air - 4.5μ $\text{CO}_2 + \text{CO}$ Absorption Region

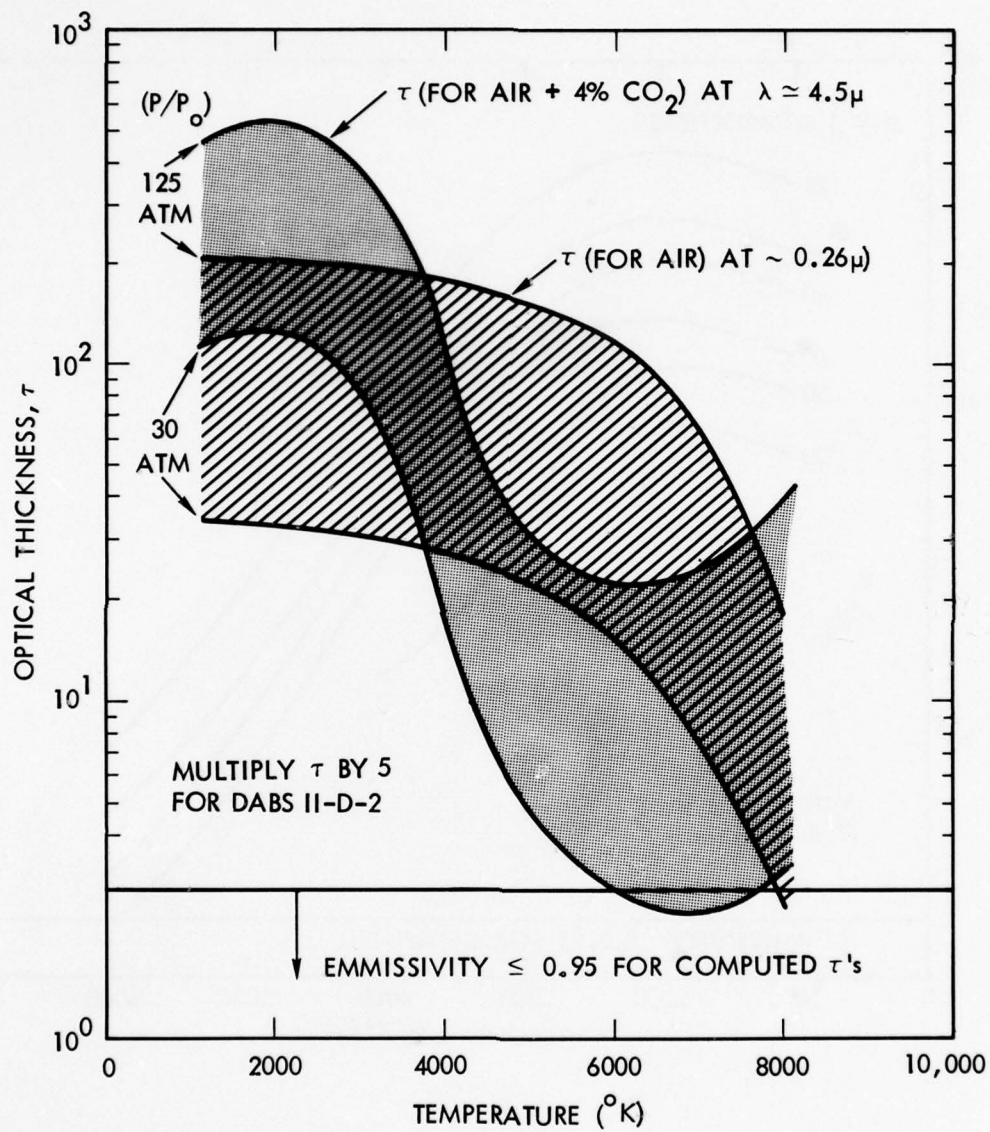


Figure E-9. Computed Optical Thickness at 0.26μ and at 4.5μ for 4% CO_2 Added to Air

expendability of higher priced optimum detectors and low noise amplifiers, etc., would tend to restrict the useful field operations range of the λ_1 radiometers to $T \geq 3000$ °K.

E.3 Combustion Products

Figures E-10a shows computed values of mole-fractions of CO_2 and of H_2O in the combustion products. The corresponding $\bar{k}(\lambda, \Delta\lambda; T)$ values were shown in Figure E-6. Figure E-10b shows the computed values of $\bar{\tau}_5(1.9\mu, 0.1\mu; T, P)$ and $\bar{\tau}_6(4.3\mu, 0.1\mu; T, P)$. The cross-hatched portion at the lower left of the 1.9μ wavelength τ_5 region indicates an "area" where the low density spectral "line packing" in low temperature H_2O creates some doubt of reliability. However, the arrival of carbon soot following closely behind the air combustion gas contact surface would soon insure virtually complete opacity. It now appears that the carbon soot lag time is negligible.

The temperature limits for the combustion products, assuming no afterburning, is not predicted to rise much above 800 °K at most. However, these predictions are for isentropic expansion, and do not include afterburning, which possibly could raise these temperatures to ~2500 °K. For this reason, Figure E-10 calculations were carried out to 3000 °K.

E.3.1 Carbon Soot

Figure E-11 presents empirical near infrared spectral absorption coefficients k_c for carbon particle soot at temperatures ranging from 300 to 2600 °K. The figure was extracted from the NASA Handbook of Infrared Radiation From Combustion Gases (page 228) [4]. As is indicated by its title, the ordinates represent mass-density rather than number density coefficients. In order to obtain the desired τ_c values, therefore, these ordinates must be multiplied by the product of optical path length L with the mass-density, ρ_c , of carbon soot, rather than by $(N_1/N_0) \cdot L$ as was true for the molecular gas absorption coefficients. This is shown in equation E.1 below.

$$\tau_c = \rho_c k_c L \approx \left(\chi_c \cdot \frac{m_c}{m_{\text{gas}}} \cdot \rho_{\text{gas}} \right) \cdot k_c (L)$$

$$\chi_c \left(\frac{m_c}{m_{\text{gas}}} \right) \approx \left(\frac{1.4}{41.5} \right) \left(\frac{12}{24.25} \right) \cdot 1.67 \cdot 10^{-2} \quad (\text{E.1})$$

$$\rho_{\text{gas}} \approx 1.08 \cdot 10^{-3} \left(P/P_0 \right) \left(\frac{273.2 \text{ °K}}{T} \right) \text{ gm cm}^{-3}$$

$$L \approx 81 \text{ cm} \quad (\text{For DABS II-D-1})$$

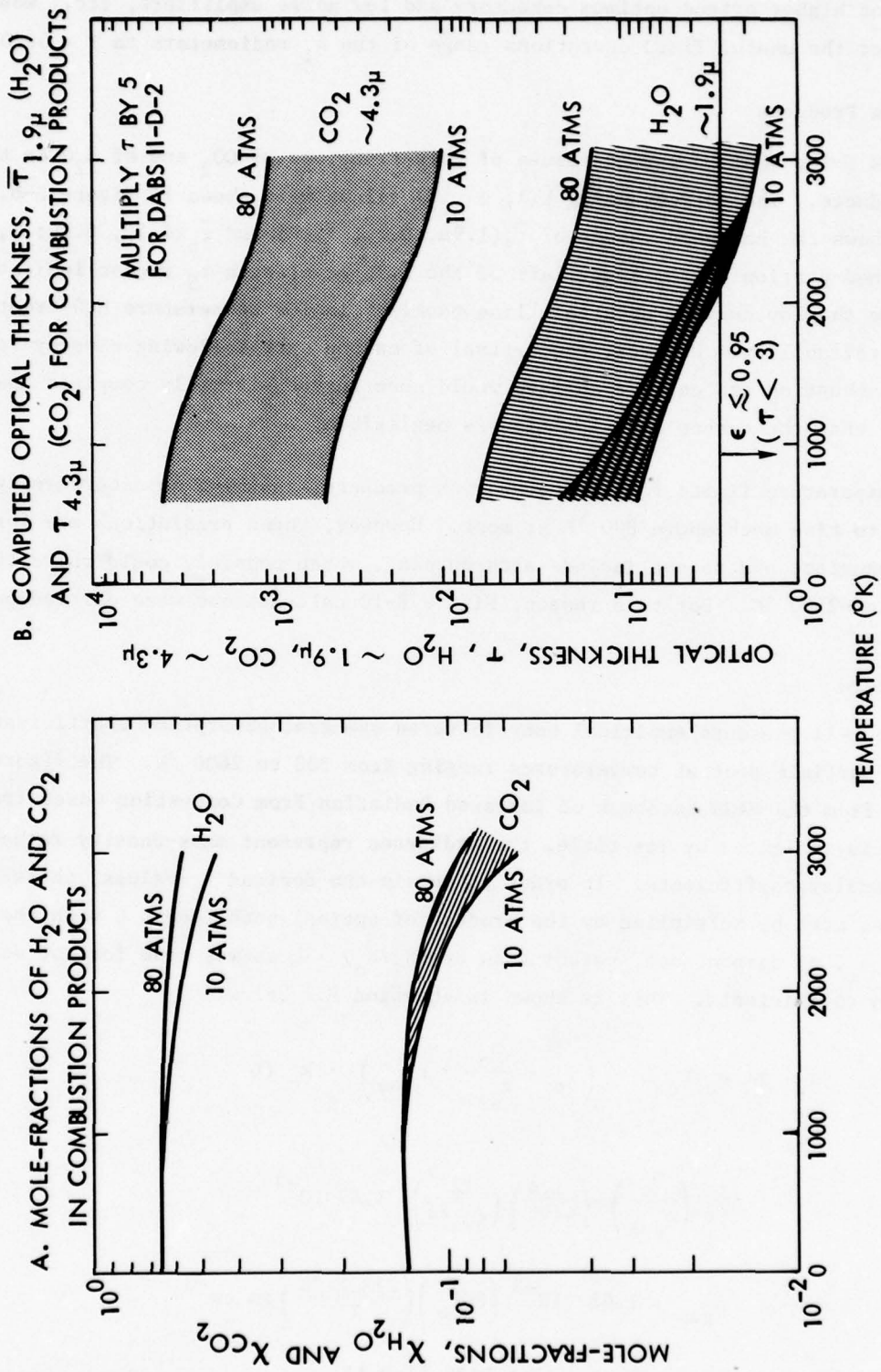


Figure E-10. Combustion Products Curves

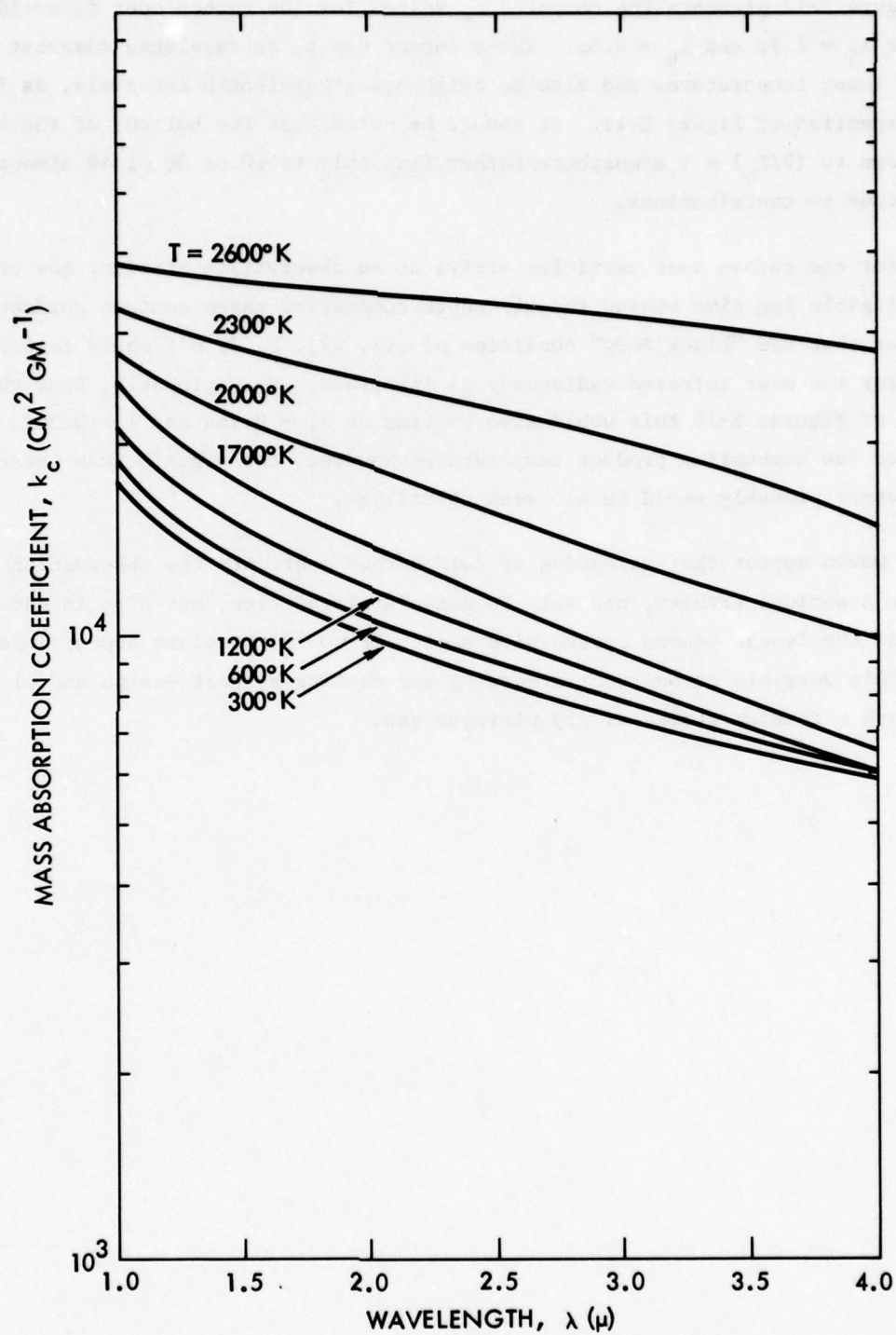


Figure E-11. Empirical (Mass-Density) Spectral Absorption Coefficients for Carbon Soot

Figure E-12 presents the computed τ_c values for the carbon soot from ~ 500 to 2500°K for $\lambda_5 \approx 1.9\mu$ and $\lambda_6 \approx 4.3\mu$. These curves can be extrapolated somewhat to higher and lower temperatures and also to neighboring wavelength intervals, as is seen from an inspection of Figure E-11. It should be noted that the bottoms of the hatched-in areas go down to $(P/P_0) = 1$ atmosphere rather than only to 10 or 30 or 40 atmospheres as for gaseous τ - contributions.

After the carbon soot particles arrive at an observation station, now presumably with a negligible lag time behind the air shock combustion gases contact surface, it would appear that the "Black Body" condition of $\epsilon(\lambda, \Delta\lambda_i; P, T) \approx 1$ would certainly be satisfied for the near infrared radiometer $\Delta\lambda$ intervals. Very probably, from the appearance of Figures E-10 this would also be true at $\lambda_1 \approx 0.26\mu$ and $\lambda_2 \approx 0.36\mu$. At the expected low combustion product temperatures however, the signals from these latter two radiometers probably would be too weak to utilize.

It would appear that streaming of cold carbon soot into the observation port could cause a serious problem, not only in data interpretation, but also in data observation if the lenses become coated with soot. It would therefore appear imperative to combat this possible carbon soot streaming and coating by port design and also possibly with a counter stream of dry nitrogen gas.

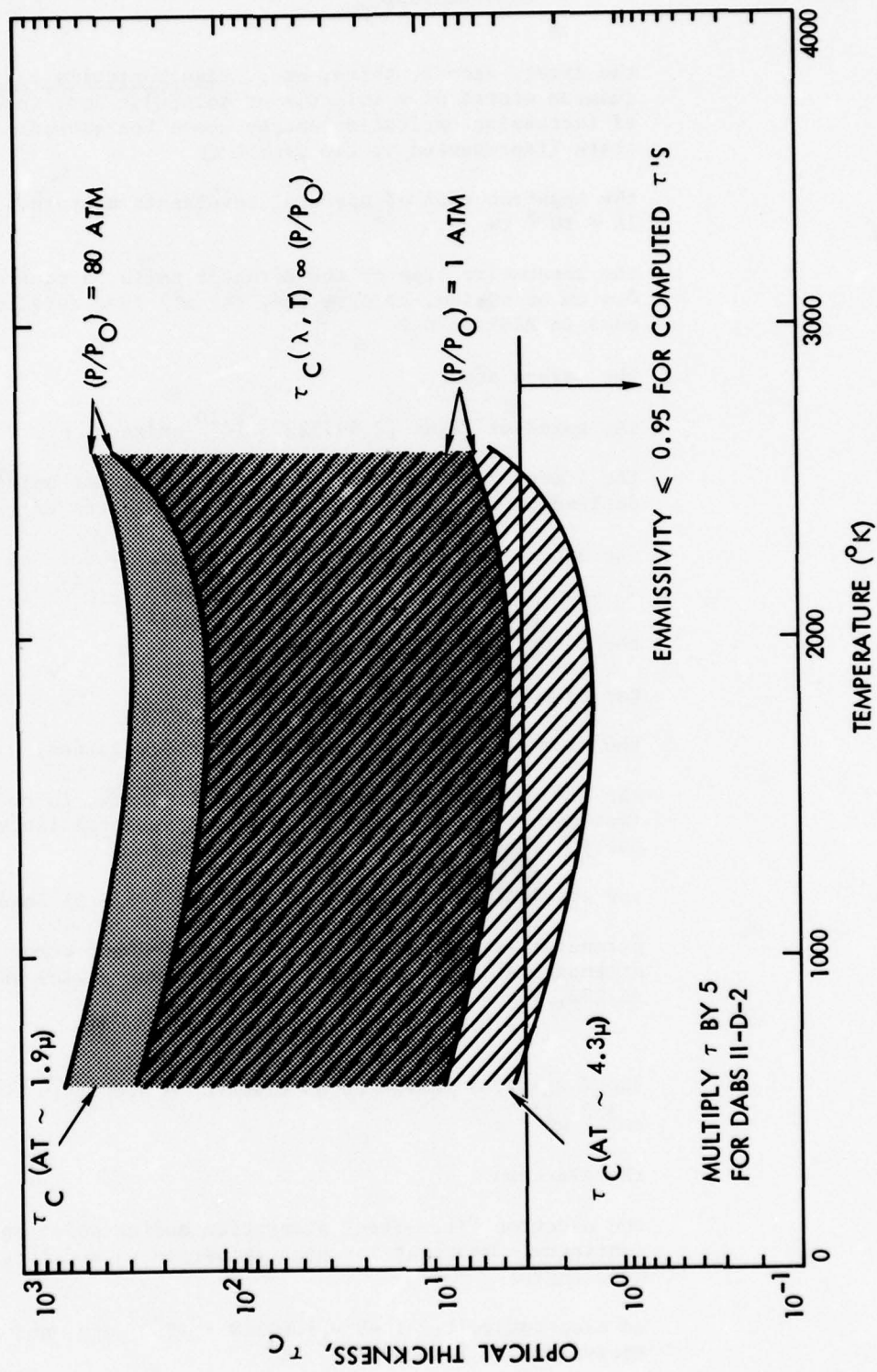


Figure E-12. Computed Optical Thickness, τ_c , of Carbon Particulate Soot Carried by Combustion Gases

NOMENCLATURE

A, B, C, ...	the first, second, third, etc., <u>electronically excited</u> quantum states of a molecule or molecular ion, in order of increasing excitation energy above the ground electronic state (represented by the symbol X)
\AA	the Angstrom unit of spectral wavelength measure. $1\text{\AA} = 10^{-8} \text{ cm}$
A^c	the responsive area of the detector cells, a square, 0.4 cm on a side, or 0.16 cm ² , for all five detectors used in DABS II-D-2
C	the carbon atom
c	the speed of light [$2.997925 \cdot 10^{10} \text{ cm/sec}$]
c_1	the 'first radiation constant', here (but not universally) defined as $c_1 = 2 c^2 h = 1.1910 \cdot 10^{-12} \text{ watts cm}^2 \text{ ster}^{-1}$
c_2	the second radiation constant, universally defined as $c_2 = (hc/k) = 1.43880 \text{ (cm } ^\circ\text{K)} = 1.43880 \cdot 10^4 \cdot (\mu ^\circ\text{K)}$
CO	the carbon monoxide molecule
CO ₂	the carbon dioxide molecule
D	the diameters of the lenses = 5.08 cm (2 inches)
$d, d_{ij}(\lambda; T)$	the strongly temperature dependent distance, in cm ⁻¹ (wavenumber) units, between adjacent spectral lines (for the j^{th} band system of the i^{th} species)
$\bar{d}, \bar{d}_{ij}(\lambda, \Delta\lambda; T)$	the spectral mean value of d over a $\lambda \pm 1/2 \Delta\lambda$ interval
E, E_i	pyrometer error factors (mostly "measurement error attenuators"). See Appendix A, equations (A.15) and (A.19a, b, c).
e	the (negative) charge on an electron = $4.80298 \cdot 10^{-10} \text{ cm}^{3/2} \text{ gm}^{1/2} \text{ s}^{-1}$
e ⁻	the electron
e ^{-(ff)}	the electron "free-free" absorption and emission spectral continuum, important for high temperatures and long wavelengths
eV	an electron volt. $1 \text{ eV} = 1.60210 \cdot 10^{-12} \text{ erg}$, and is equivalent to $1.16049 \cdot 10^4 ^\circ\text{K}$

F	the focal length of the lenses = 50.8 cm (20 inches for each lens used)
(ff)	indicating a free-free spectral transition during non-capture, but inelastic, collisions between electrons and atoms, molecules or ions, or between molecules and ions, etc.
(fb)	an ionization, dissociation or capture transition leading to a spectral continuum
G_i	the amplifier gain factor for the i^{th} radiometer system
h	Planck Constant = $6.6256 \cdot 10^{-27}$ ergs
H_2O	the water vapor molecule
$I^0, I^0(\lambda; T)$	Black Body spectral radiance, in units of watts $[\text{cm}^2 \text{ ster } \mu]^{-1}$ or the equivalent
$I, I(\lambda; P, T; L)$	spectral radiance from a surface element of a layer of hot gases, in the same units as for I^0 . $I = I^0 \cdot \epsilon(\lambda; P, T; L)$
$I_i^0, I^0(\lambda_i; T)$	Black body spectral radiance for a specific set of $\lambda_1, \lambda_2, \dots, \lambda_n$ values
$\bar{I}_i^0, \bar{I}^0(\lambda_i, \Delta\lambda_{ij}; T)$	Black Body spectral radiance mean value averaged over the interval $\lambda_i \pm 1/2 \Delta\lambda_i$ for a specific set of $\lambda_1, \lambda_2, \dots, \lambda_n$ values
J, J', J''	the principal <u>rotational</u> quantum number of a molecule, ion or atom. J' and J'' correlate to the respective <u>upper</u> and <u>lower</u> quantum states in a spectral transition
$^{\circ}\text{K}$	degrees Kelvin; $0^{\circ}\text{K} = -273.15^{\circ}\text{C}$
k	the Boltzmann Constant = $1.38054 \cdot 10^{-16}$ erg $(^{\circ}\text{K})^{-1}$
$k_{ij}, k_{ij}(\lambda; T)$	the "spectral absorption coefficient" in units of inverse atmosphere-centimeters as conceptually reduced to STP conditions $[(\text{atm cm} - \text{STP})^{-1}]$. See Appendix C, Section C.1 for clarification of the meaning. The ij dummy indices refer to the j^{th} band system of the i^{th} spectrally active species.
$\bar{k}_{ij}, \bar{k}_{ij}(\lambda, \Delta\lambda; T)$	the spectral mean value of the above parameter, as averaged over a $\lambda \pm 1/2 \Delta\lambda$ spectral interval
k'_e	the (geometric) absorption coefficient for $e^-(\text{ff})$ spectral activity
L	optical (geometrical) path length through an absorbing and emitting media (here a layer of gas)
\bar{m}_0	mean molecular weight of gas particles at STP conditions

m_{e-}	electron rest mass = $9.1091 \cdot 10^{-28}$ gm
m_i	molecular (or atomic) weight of the i^{th} species of spectrally active molecule, atom or ion
$\bar{m}, \bar{m}(P, T)$	mean molecular weight of gas particles at pressure P and temperature T
N	the nitrogen atom
$N, N(P, T)$	number density of gas species particles, in units of cm^{-3} [i.e., total number of particles, of all gas species, per cm^3]
$N_i, N_i(P, T)$	number density of i^{th} species particles, in units of cm^{-3}
N_o	number density of gas particles at STP conditions $N_o = 2.67 \cdot 10^{19} \text{ cm}^{-3}$
N'_{ijk} and N''_{ijk}	the number densities of i^{th} species particles excited to the respective upper and lower quantum states to generate the k^{th} spectral line of the j^{th} band system. [See Appendix C, Section C.1]
$N_{e-}, N_{e-}(P, T)$	number density of electrons, in units of cm^{-3}
N_2	the nitrogen molecule
N_2^+	the singly ionized nitrogen molecule
$N_2(1+)$	the "first positive" spectral band system of the N_2 molecule, corresponding to a $(B \rightarrow A)$ -type electronic transition and with its "origin" near 1.05μ
$N_2(2+)$	the "second positive" spectral band system of the N_2 molecule, corresponding to a $(C \rightarrow B)$ -type electronic transition, and with its "origin" near 0.3370μ
$N_2^+(1-)$	the "first negative" spectral band system of the molecular nitrogen ion N_2^+ , corresponding to a $(B \rightarrow X)$ -type electronic transition, and with its "origin" near 0.391μ
NO	the nitric oxide molecule
NO (β)	the "beta-band system" of the nitric oxide molecule, corresponding to a $(B \rightarrow X)$ -type electronic transition, and with its "origin" near 0.2201μ
NO (γ)	the "gamma-band system" of the nitric oxide molecule, corresponding to an $(A \rightarrow X)$ -type electronic transition, and with its "origin" near 0.2266μ
NO_2	the nitrogen dioxide molecule

$\text{NO}_2(\text{fb})$	the spectrally very broad nitrogen dioxide free-bound continuum
n' and n''	the principal <u>electronic</u> quantum numbers correlated to the respective upper and lower quantum states of a spectral transition
O	the oxygen atom
O^-	the negative oxygen ion, with a single additional attached electron
$\text{O}^-(\text{fb})$	the broad free-bound spectral continuum of the negative oxygen atomic ion
P	gas pressure, in units of standard atmospheres or pounds per square inch, absolute (psia)
P_o	one standard (sea level) atmosphere = 760 mm Hg = 14.7 psia
(P/P_o)	gas pressure in units of standard atmospheres
P_s	shock <u>front</u> pressure (at time of initial arrival of any specified observation station)
P_i	predicted isentropic decay pressure at some time after passage of shock front (Section 1.3)
P_c	combustion products pressure
P_i^{input}	the effective radiant power input to the i^{th} radiometer system (See equation 3.1)
R_i	the response factor of the i^{th} radiometer cell, in amps output, per watt input for $\lambda_i = 0.26\mu$ and 0.36μ , and in volts output per watt input for $\lambda_i = 2.8\mu$, 4.5μ and 1.9μ
R_{ij}	the ratio, $(\bar{I}_i/\bar{I}_j) \approx (\bar{I}_i^0/\bar{I}_j^0)$ for both ϵ_i and ϵ_j near unity. This R_{ij} ratio is the basic "temperature signal input for a two color pyrometer system
r	the distance from a lens to the viewing port aperture
δr	the distance of a viewed radiating molecule behind the viewing port aperture
s^g	the incremental projected area of the radiating gas layer <u>actually</u> focused within the responsive area A^c of a detector cell [See Section 3]
T	gas temperature in units of $^{\circ}\text{K}$
T_o	standard temperature = 273.15 $^{\circ}\text{K}$

T_s	shock <u>front</u> temperature (at time of initial arrival of any specified observation station; corresponds to P_s)
T_i	predicted isentropic decay temperature at some time after passage of shock front (Section 1.3, corresponds to P_i)
t	time
δt	time interval between arrival of shocked air front and combustion products contact surface at any station
Δt_m	available measurement time interval between initial arrival of shocked air front and destruction of measuring apparatus at any station [Figure 2-5]
u	the geometrical optics object distance with weighted mean value of $(r + \delta r)$ varying slightly for each radiometer
v	the geometrical optics image distance (in practice, the adjustable set distance between a detector cell and its lens)
v_i	the i^{th} radiometer output signal in units of volts for the infrared radiometers and units of amperes for the 0.26 μ and 0.36 μ radiometers
v	the vibrational quantum number for a diatomic molecule (or diatomic molecular ion). v takes on the values 0, 1, 2, 3 ... depending upon the degree of vibrational excitation
$(v_1, v_2, v_3, \dots, v_m)$	a set of vibrational quantum numbers corresponding to each of the m normal vibrational modes, v_i , of a polyatomic molecule (or molecular ion). Each v_i can assume the values 0, 1, 2, 3, ... depending upon the degree of excitation of the corresponding normal mode v_i within an arbitrary combinational mode [see Appendix B, Section B.1]
$v', \text{ and } v''$	the vibrational quantum numbers corresponding to the respective upper and lower excitation states for a spectral transition in a diatomic molecule
$(v'_1, v'_2, \dots, v'_m), (v''_1, v''_2, \dots, v''_m)$	the <u>sets</u> of vibrational quantum numbers corresponding to the respective upper and lower excitation states for a spectral transition in a polyatomic molecule
x, x_i	the analytically and computationally useful dimensionless parameter equal to $c_2/\lambda T$ or $c_2/\lambda_i T$

$\alpha(\lambda; P, T; L)$	spectral absorptivity of a layer of absorbing gases of thickness L , temperature T and pressure P . The α -parameter also depends very strongly on the proportions of different gas species in the layer
$\bar{\alpha}(\lambda, \Delta\lambda; P, T; L)$	the spectral mean value of the preceding α -parameter over a $\lambda \pm 1/2\Delta\lambda$ spectral interval
$\beta_i^f(\lambda)$	the spectral filter transmissivity at wavelength λ , for the arbitrary i th radiometer filter used on DABS II-D-2
β^{lens}	the spectrally flat transmissivity of the lenses used on DABS II-D-2. $\beta^{\text{lens}} \approx 0.90$ for each of the five lenses
γ	ratio of specific heat at constant pressure to specific heat at constant volume; $\gamma = C_p/C_v$
γ_0	the value of γ at STP conditions
$\gamma, \gamma_{ij}(P, T)$	the half width at half peak, in units of cm^{-1} , of a (conceptually) isolated spectral "line". See Appendix C, Section C.2, and equation (C.3) and adjacent discussion for P - and T -dependence of γ
(γ/d)	the strongly temperature and pressure dependent dimensionless "packing factor", or "packing ratio", of spectral lines
(γ/\bar{d}) or $\overline{(\gamma/d)}$	the spectral mean value, over a suitable $\lambda \pm 1/2 \Delta\lambda$ interval, of the above "packing factor"
Δ, δ	indicating incremental values
$\epsilon, \epsilon(\lambda; P, T; L)$	spectral emissivity of a layer of emitting gases of thickness L , temperature T , and pressure P (also very strongly dependent upon proportions of different gas species in the layer). From Kirchhoff's Law, $\epsilon(\lambda; P, T; L) = \alpha(\lambda; P, T; L)$
$\bar{\epsilon}, \bar{\epsilon}(\lambda, \Delta\lambda; P, T; L)$	the spectral mean value of the preceding ϵ - parameter over a $\lambda \pm 1/2 \Delta\lambda$ interval
λ, λ_i	optical radiation wavelength, measured in units of microns (μ), angstrom units (\AA), or centimeters (cm). The dummy subscript i indicates one of a set of specific wavelengths
$\Delta\lambda, \Delta\lambda_i$	incremental wavelength intervals centered on λ or λ_i , usually referring to optical filter bandpass or to spectral regions of strong absorption or emission.
$\Delta'\lambda_i$	the effective width, somewhat larger than $\Delta\lambda_i$, for a spectral filter bandpass that fails to decay as rapidly as is desirable.

μ	one micron (or micrometer). $1\mu = 10^4 \text{ \AA} = 10^{-4} \text{ cm} = 10^{-6} \text{ m}$
ν, ν_i	optical radiation wavenumber spectral positions. When λ is measured in cm units, then $\nu = \lambda^{-1}$ and $\nu_i = \lambda_i^{-1}$
ν_{00}	the "origin" of an electronic band system
ν_e	the collision frequency of electrons with gas particles, in units of sec^{-1}
$\Delta\nu, \Delta\nu_i$	incremental wavenumber increments centered on ν or ν_i
$\rho, \rho(P, T)$	gas density, in units of gm cm^{-3}
ρ_0	gas density at, or reduced to, STP conditions
$\tau, \bar{\tau}$	optical thickness and spectral mean value of optical thickness
$\bar{\tau}_{ij}(\lambda, \Delta\lambda; P, T; L)$	contribution to spectral mean optical thickness by j^{th} band system of i^{th} species gas particle
$\bar{\tau}_{ij}, \bar{\tau}_{ij}(\lambda, \Delta\lambda, \chi_i P, T; L)$	the spectrally averaged optical thickness contribution, in the $\lambda \pm 1/2 \Delta\lambda$ spectral interval, from the j^{th} spectral band system of the i^{th} species gas particles. The $\chi_i P$ product in the abstract functional representation of τ_{ij} can be replaced by the corresponding species partial pressure P_i , or species number density N_i
$\chi_i, \chi_i(P, T)$	the mole fraction of i^{th} species of gas particles (molecules, atoms or ions)
ω	the "optical frequency" of spectral radiation (used only in Appendix D, Section D.1.2 for $e^-(ff)$ radiation), with $\omega = 2\pi c \lambda^{-1}$
ω_p	the "plasma frequency", again used only in Appendix D, Section D.1.2 [see equation D.6)]
ω^c	the detector cell solid angle field of view. $\omega^c = A^c v^{-2}$, where v is the geometrical optics "image distance", i.e., the distance between the lens and the detector cell
$\Omega = \Omega(D, r)$	the solid angle subtended by a lens from any point on the viewing port aperture. $\Omega = (\pi D^2/4r^2) \approx 2.134 \cdot 10^{-4}$ steradians for each lens used.
$\Omega = \Omega(D, r + \delta r)$	the solid angle subtended by a lens from a radiating gas molecule a distance δr behind the port aperture. $\Omega(D, r + \delta r) = [\pi D^2/4(r + \delta r)^2]$
primes, ' and ''	single and double primes, ' and '', are used to indicate parameters belonging to the respective "upper" and "lower" quantum states in any "bound-bound" spectral transition

PART B
NOVEL MEASUREMENT TECHNIQUES

1. INTRODUCTION

1.1 Objectives

The objectives of the theoretical study described herein were to establish the conceptual feasibility of deploying novel instrumentation to measure temperature histories and density histories within the interior of a nuclear driven shock tunnel. This study will only address the basic physics concepts rather than present hardware design solutions. Specifically, it was considered desirable to investigate procedural techniques to measure the density and temperature history of the shocked air before, during and after the passage of the shock front, and the density history of any lofted debris. It is virtually certain that the tunnel walls will undergo transitory displacement during the passage of the shock. Since this displacement, if not considered, could readily distort the interpretation of the data, it is desirable to have measurements of the local wall displacement history. To sum up, the objectives of these proposed novel measurements are to obtain:

- Density and temperature histories of shocked air
- Density history of lofted debris
- Translational displacement history of tunnel walls in the tunnel radial direction

1.2 Background

These types of measurements have not been made previously. During the Marvel experiments [1, 2 and 3], a series of measurements were made for various parameters associated with the shock generated by the detonation of a 2.2 KT nuclear explosive at one end of a one meter diameter horizontal tunnel 122 meters long. The only experiments looking directly along the axis into the shocked air viewed the advancing shock front with luminosity instrumentation placed at the far end of the tunnel. In addition, a series of light-pipe photodetectors were placed in side alcoves to measure time of arrival of the shock front. The former instrumentation saw mostly the precursor radiation emitted by the optically dense radiation heated air well in advance of the actual shock front. Owing to the extremely high temperature and pressure air in and behind the shock front, the time of arrival photodetectors only responded to the radiation emitted within a few centimeters of their immediate vicinity. Thus no real measurements were made of state parameters within the interior of the shocked air.

To date, measurements of the type proposed in this report have not been accurately made in such extreme environments (temperatures above 12,000 °K and pressures of ~1000 atmospheres).

1.3 Proposed Techniques

This report will discuss two techniques which will provide the means for obtaining the needed measurement histories presented above. The proposed techniques are:

- Gas bag method
- Radioisotope method

The first technique, the "gas bag method", is not a measurement technique per se, but a method for providing an optical window into the interior region of the shock front. This would permit the use of passive two color (or multi-color) optical pyrometers for determining temperature histories of the shocked air.

The second technique, the "radioisotope method" is an active X-ray system using two or more different frequency radioactive X-ray sources with detectors to measure areal density histories and tunnel wall translational displacement. The density history would consist of measurements of the initially arriving shocked air and the later arrival of shocked air plus lofted debris. These measurements along with the wall displacement histories will be used to resolve the separate areal density contributions of air and lofted debris.

1.3.1 The Gas Bag and Pyrometer Technique

The concept of two color or multi-color optical pyrometers has been fully discussed and their usefulness demonstrated in Part A of this report. In a nuclear driven shock tube experiment, however, temperatures and pressures are both much higher than in the DABS II-D experiments, and more hostile to instrumentation system survival and performance. Moreover, the higher temperatures and pressures result in greatly increased radiation thus causing even a few centimeter layer of shocked air to be completely opaque. Also precursor radiation tends to arrive well in front of the shock owing to the intense radiation heating of the downstream air. This radiation heated downstream air tends to be "black" and thus completely obscures the actual shock front radiation from any optical instrument looking upstream.

The "gas bag method" proposes to use a very thin and transparent walled plastic bag of rectangular cross-section, filled with a noble gas to act as a window into the shocked air region that is to be viewed. Theoretical calculations show that neon cooled to ~ 220 °K is the best candidate material for this window to date. Neon will be suitably transparent and still match the air parameters sufficiently well to minimize any reflected shock heating.

1.3.2 Radioisotope Source Technique

It is well known that X-ray absorption measurements can be used to provide a sensitive measure of the areal mass density of the material in the path of a collimated X-ray beam. One approach for implementing this technique would be to use an expensive and relatively fragile X-ray generating machine to provide a source of X-rays. A second approach, which is considerably less expensive and easier to implement in very hostile nuclear generated shock conditions, is to utilize commercially available radioactive X-ray sources imbedded in a rugged ceramic matrix. Owing to the large radioactive source strengths desired, these will not be off the shelf items, but will be prepared to order in the size and shape desired. They will still be orders of magnitude cheaper than manufactured X-ray generating devices. Also commercially available radioactive sources generally radiate in one or more discrete X-ray or γ -ray frequencies rather than over a very broad spectral band as do the X-ray machines. Since both the radioactive sources and detectors are so compact, there is no difficulty in using them in pairs, triplets, etc.

1.4 Conceptual Feasibility

The conceptual feasibility of the preceding two techniques will be established by the results presented in Section 3. The feasibility of designing operating hardware systems to implement the techniques looks promising but still requires further study. Some specific areas that require further study are outlined in Section 4. Many of these problem areas could be resolved by implementing scale tests. Also, the theoretical study should be pushed further by including the important effects of radiative heating upon the shocked and pre-shocked air parameters. First, however, a brief overview of the physical principles invoked for each of the two techniques is presented in Section 2 below.

2. THEORY: A BRIEF OVERVIEW

2.1 Gas Bag - Pyrometer Experiment

In a nuclear driven air shock the temperatures and pressures of the shocked air can be expected to exceed those encountered in the DABS II-D tests by at least an order of magnitude. The peak temperatures and pressures to be encountered depend of course upon the magnitude of the explosion and upon the downstream position of the observation station. But in the HYBLA GOLD test for example, even for moderately far downstream stations it is expected that the temperatures will exceed 12,000 °K and the pressures will exceed 1000 atmospheres. For these, and considerably lower pressures and temperatures, the air behind the shock is expected to be opaque to optical radiation. This opacity is due to bound-free electron transitions, inverse bremsstrahlung absorption, and the pseudo continuum resulting from the conjunction of closely spaced pressure broadened discrete spectral lines [see Part A, Appendices B and C]. There also will be very appreciable radiative heating of air well downstream from the propagating shock front. The air heated by this precursor radiation may itself become opaque, and radiate as a black body at some considerably lower temperature than that of the air immediately behind the front. Thus a new technique is required to make the shocked air temperature measurements penetrate further than a few centimeters from the tunnel walls.

The conceptual procedure for looking deeper into the shocked air was to design a "gas bag" to act as an optical window into the region to be observed. The gas bag is to consist of a thin transparent plastic membrane filled with an inert gas that would remain transparent to the spectral wavelengths to be observed. The noble gases, helium, neon, argon, etc., and mixtures thereof, were selected for inspection since their ionization and excitation potentials are high, and under ordinary conditions they are transparent in broad spectral regions. It was desired to match conditions at the bag-air shock interface so that there would be very little super heating by shock reflection. Computer computations were made with the TRW ACE code and with an acquired JPL code [4]. It was found that the computed electron density predicted for the shock passing through most of these gas bag candidate gases was much higher than desirable. These predicted high electron densities would lead to opacity owing to inverse bremsstrahlung absorption. The surviving candidate gas is cooled neon. Calculations made with the JPL code indicate that a transition from air to neon cooled to ~220 °K will suffer very little reflected shock, and that for shocked air temperatures below ~9,000 °K and pressures below ~500 atmospheres the neon will remain transparent.

It is expected, of course, that the plastic membrane containing the neon will vaporize when hit by the shock. Preliminary approximate diffusion and turbulent mixing

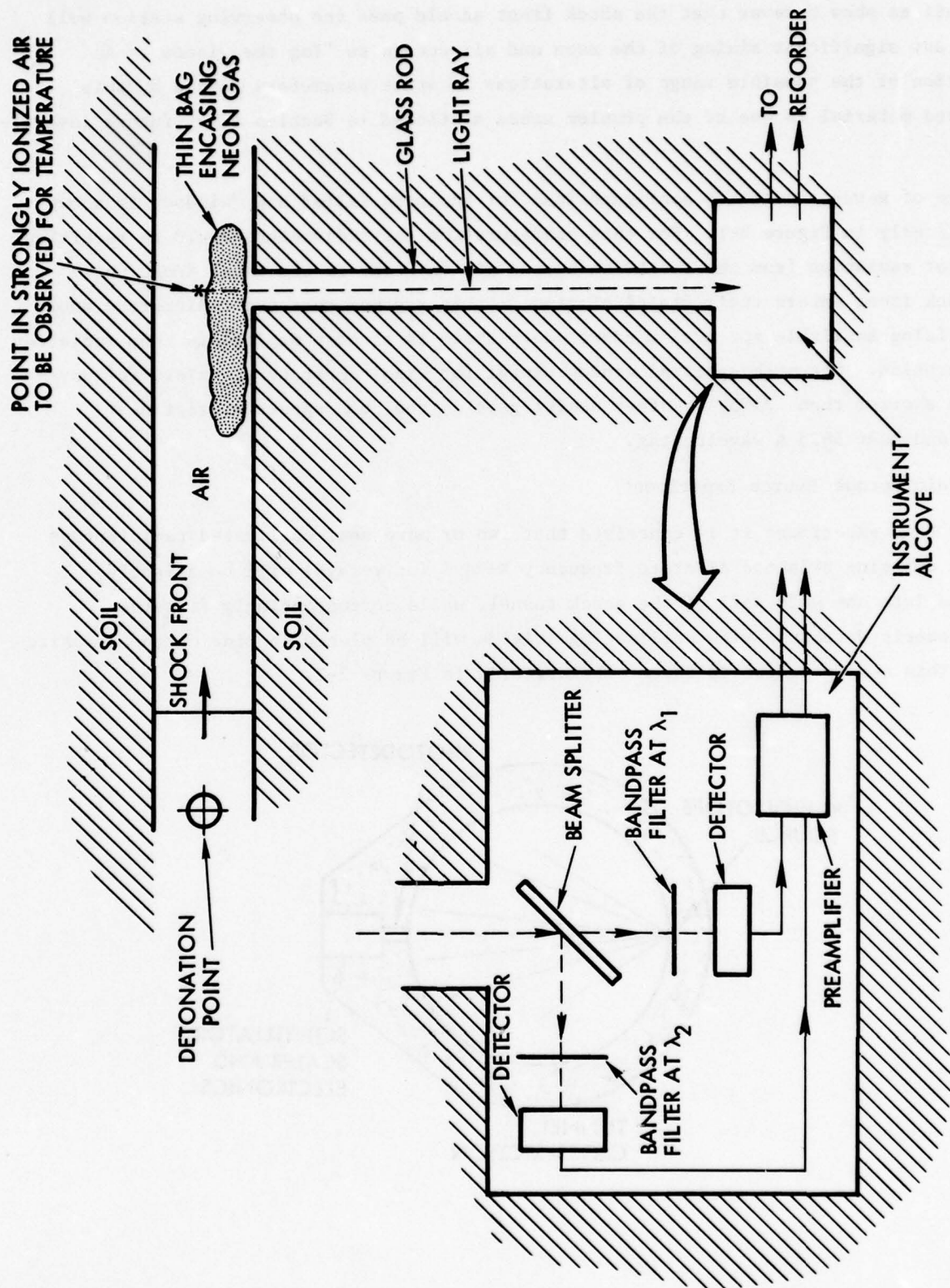


Figure 2-1. Schematic of a Test Arrangement for the Gas Bag - Optical Pyrometer Experiment

computations show however that the shock front should pass the observing station well before any significant mixing of the neon and air occurs to "fog the window". An evaluation of the possible range of alterations in state parameters caused by this vaporized material is one of the problem areas mentioned in Section 4 for future investigation.

One of several possible configurations for the neon filled bag "window" is shown schematically in Figure 2-1. For this configuration the radiometers would be receiving precursor radiation from the radiation heated air in front of the shock front until the shock front enters their fields of view. It is assumed that the radiometers would be utilizing available spectral windows where there is at most negligible neon radiation or absorption. One such spectral window useful for high temperatures exists for wavelengths shorter than 2595 \AA . Other useful gaps in the neon spectrum exist near 7000 \AA and near 5625 \AA wavelengths.

2.2 Radioisotope Source Experiment

In this experiment it is conceived that two or more semi-collimated radioisotope sources emitting selected discrete frequency X-rays (or γ -rays) will be slightly recessed into one side wall of the shock tunnel, while correspondingly filtered monochromatic detectors with collimating shields will be placed in line on the opposite wall. This configuration is shown schematically in Figure 2-2.

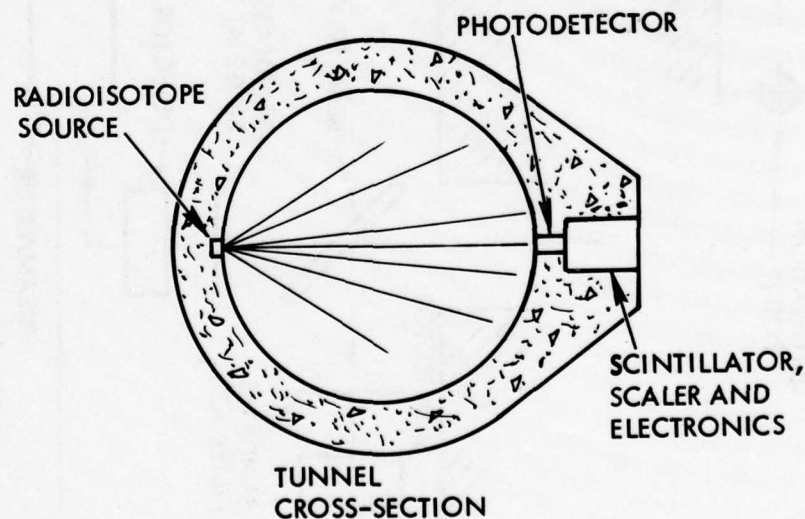


Figure 2-2. Schematic of Proposed Radioisotope Source Experiment

A main consideration of the design will concern the interaction between X-rays and matter which takes the form of: (1) photoelectric absorption; (2) Compton scattering; and (3) elastic scattering. The second process results in a photon of lower energy, and thus lower frequency, than the original X-ray photon and generally traveling in an altered direction. Even if these photons are deflected back into the detector by subsequent collisions, they will not be passed by the spectral filter on the detector. Multiple elastically scattered X-ray photons, however, are subject to being accepted by the detector just as if they were primary beam photons. The Compton scattered photons also would register on the detector unless this detector system is designed for frequency (or photon energy) discrimination. Thus it is preferable for diagnostic purposes to use a monochromatic source system with a relatively restricted solid angle output with a spectral filtered detector system with a narrow acceptance angle. The acceptance of any appreciable proportion of multiply scattered radiation, either elastic or Compton, would be treated just as if it were directly transmitted radiation by the detector and make interpretation of the data difficult.

The attenuation of a beam of X-rays upon passage through matter is primarily dependent upon the areal density, or mass per unit projected areas of the matter traversed. For this reason the X-ray absorption coefficient, β , is expressed in units of inverse areal density, usually $\text{cm}^2 \text{gm}^{-1}$. The areal mass density parameter generally symbolized by μ (not to be confused with wavelength nomenclature used in Part A) is given in units of gm cm^{-2} . When a monochromatic beam of X-rays traverses through matter of areal density μ , the intensity of the X-ray photons left in the original beam obey the familiar Lambert-Beer law:

$$I = I_0 e^{-\beta\mu} \quad (2.1)$$

Here I_0 is the original beam intensity, β is the inverse areal density absorption coefficient for X-rays of that particular energy (or photon frequency), and μ is the areal density of the matter penetrated by the beam. But, as previously indicated, an X-ray detector with a large acceptance angle will receive not only the direct unscattered radiation but also some portion of multiply scattered radiation. The corresponding effective attenuating law would have to be solved by iterative techniques, but not in as simple a relationship as given by equation (2.1)

3. FEASIBILITY ANALYSIS

3.1 Gas Bag and Pyrometer Feasibility

In order to determine the feasibility of the neon bag "window" a survey of the neon spectrum was made to show the existence of wide windows in the optical region. Next the inverse bremsstrahlung absorption in the shock heated neon was computed. The computer code results are presented which show the feasibility of matching condition at the air-bag interface so that there are no reflected shocks.

From the spectrum search some attractively large gaps in the spectrum of neon were found. A wavelength of 7700 Å is quite far from the nearest line, 7839 Å of neon which is quite weak. Another good wavelength appears to be 5625 Å; nearest neon lines are 5589 Å and 5653 Å, both of which are weak. Monatomic nitrogen (which should be expected in the shock heated air behind the gas bag) has a weak line at 5617 Å. Also to be found in air and possibly as an impurity in neon is argon which has a weak line at 7724 Å.

Line broadening and Doppler broadening are not expected to cause any appreciable absorption at 5625 Å and definitely not at 7700 Å. This can be shown as follows: The particle density of the shock heated neon is $6 \cdot 10^{20} \text{ cm}^{-3}$. Assuming a collision cross-section of $2 \cdot 10^{-16} \text{ cm}^2$ and a mean speed of $4 \cdot 10^5 \text{ cm/sec}$ for neon, one gets a collision frequency of $5 \cdot 10^{10} \text{ sec}^{-1}$. This will provide the line broadening $\Delta\nu$, and $\Delta\lambda = \lambda^2 \frac{\Delta\nu}{c}$. Setting $\Delta\nu = 5 \cdot 10^{10}$, $\lambda = 10^{-4} \text{ cm}$, one finds $\Delta\lambda = \frac{5}{3} \cdot 10^{-8} \text{ cm}$ or about 2 Å. Thus, one can expect negligible contributions by line broadening of adjacent lines to absorption at 5625 Å and 7700 Å.

The next concern is the absorption due to inverse bremsstrahlung. The electron density is given by the equation

$$\frac{X^2 N}{1-X} = \frac{(g_A^+ g_e)}{g_A} \left(\frac{2\pi m k T}{h^2} \right)^{3/2} e^{-\frac{I}{kT}}$$

where N is the number density $(\text{cm})^{-3}$ of species to be ionized and X its fractional ionization potential, g_A^+ , g_A and g_e are the statistical weights of the ionized atom, the neutral atom and the electron. Using the values appropriate for neon, $I = 21.47 \text{ eV}$, $kT = 1 \text{ eV}$, $g_e g_A^+ / g_A = 12$, $N = 6 \cdot 10^{20} \text{ cm}^{-3}$, one finds $X = 3 \cdot 10^{-6}$ and electron density $n_e = 7 \cdot 10^{16} \text{ cm}^{-3}$. Now in order to complete the computation of inverse bremsstrahlung an estimate of the electron-atom collision frequency is needed. From gas discharge data one finds the electron-neon cross section $\approx 2 \cdot 10^{-16} \text{ cm}^2$. The electron speed at 1 eV

is $6 \cdot 10^7$ cm/sec. Then ν , the collision frequency, is $6 \cdot 10^7$ cm/sec $\cdot 2 \cdot 10^{-16}$ cm² $\cdot 6 \cdot 10^{20}$ = $7 \cdot 10^{12}$ sec⁻¹.

The absorption coefficient in inverse bremsstrahlung is given by,

$$\beta = \frac{\omega_p^2 \nu}{2c(\omega^2 + \nu^2)} \approx \frac{n_e \nu}{18(\omega^2 + \nu^2)}$$

Take $\omega = 6\pi \cdot 10^{14}$ sec⁻¹, corresponding to $\lambda = 1\mu$. Then

$$\beta \approx \frac{7 \cdot 10^{16} \cdot 7 \cdot 10^{12}}{18 \cdot 36 \cdot 10^{29}} \frac{\text{neper}}{\text{cm}} \approx 7 \cdot 10^{-3} \frac{\text{neper}}{\text{cm}}$$

An early analysis assumed neon in the gas bag shocked to 1000 atmospheres and 12,000 °K. Under these conditions, the gas was essentially transparent in wide optical spectral regions and inverse bremsstrahlung was negligible. A more careful look at the interface conditions between the bag and the shock in air shows that on the basis of ideal gas theory, the gas in the bag is heated to 75,000 °K. Such a temperature would produce excessive ionization and make the concept of the gas bag invalid. A JPL shock tube computer program, [4] has been employed to survey some gas candidates for the bag. The program treats the gases as non-ideal and computes the pressure, temperature and composition behind the shock once the upstream conditions and shock velocity are specified. The aim is to match conditions at the gas bag-air shock interface such that there is little shock reflection. This can be accomplished if the pressures and particle velocities behind the shocks in the gas bag and in air, match. The program was employed to see how well this can be done with a variety of gases; helium, neon and air. The results of the calculations are shown in Figures 3-1, 3-2 and 3-3. Downstream pressure, temperature and electron density are plotted as a function of shock velocity for each upstream gas.

Figure 3-2 shows that for neon at 300 °K there is still a difference in matching the interface conditions (pressure and gas velocity continuous across interface). A relationship found on Page 139 of Reference [5], suggests a better match would occur if the sound velocity in neon were reduced. This can be done by reducing the temperature. Accordingly, the JPL shock program was run with neon at a temperature of 232 °K. The results as shown in Figures 3-4 through 3-6 show a much better interface match between air and neon and shows that the temperature is not too far off for a very good match.

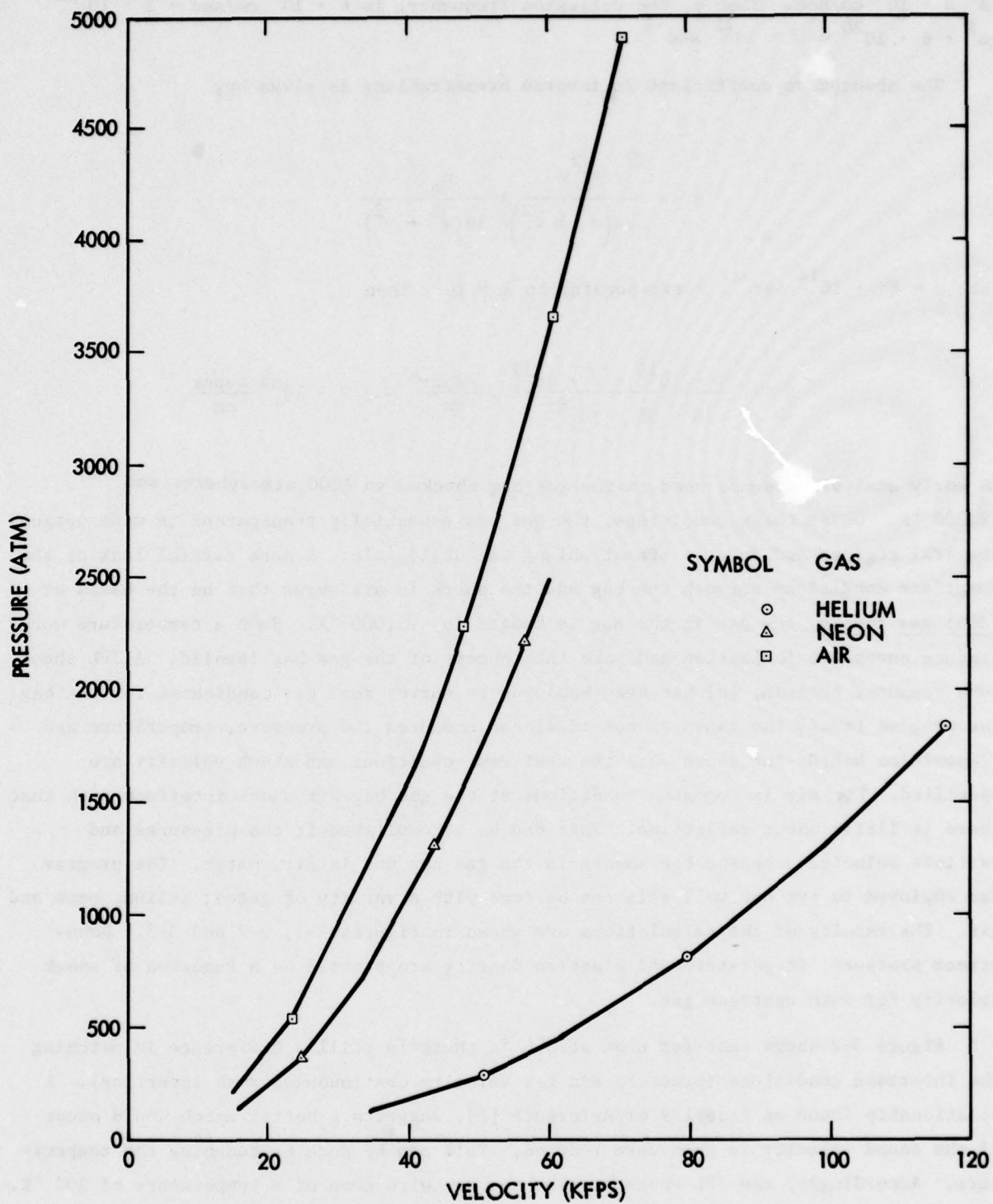


Figure 3-1. Downstream Pressure for Moving Normal Shock Upstream
Temperature = 300 °K, Upstream Pressure = 1 Atmosphere

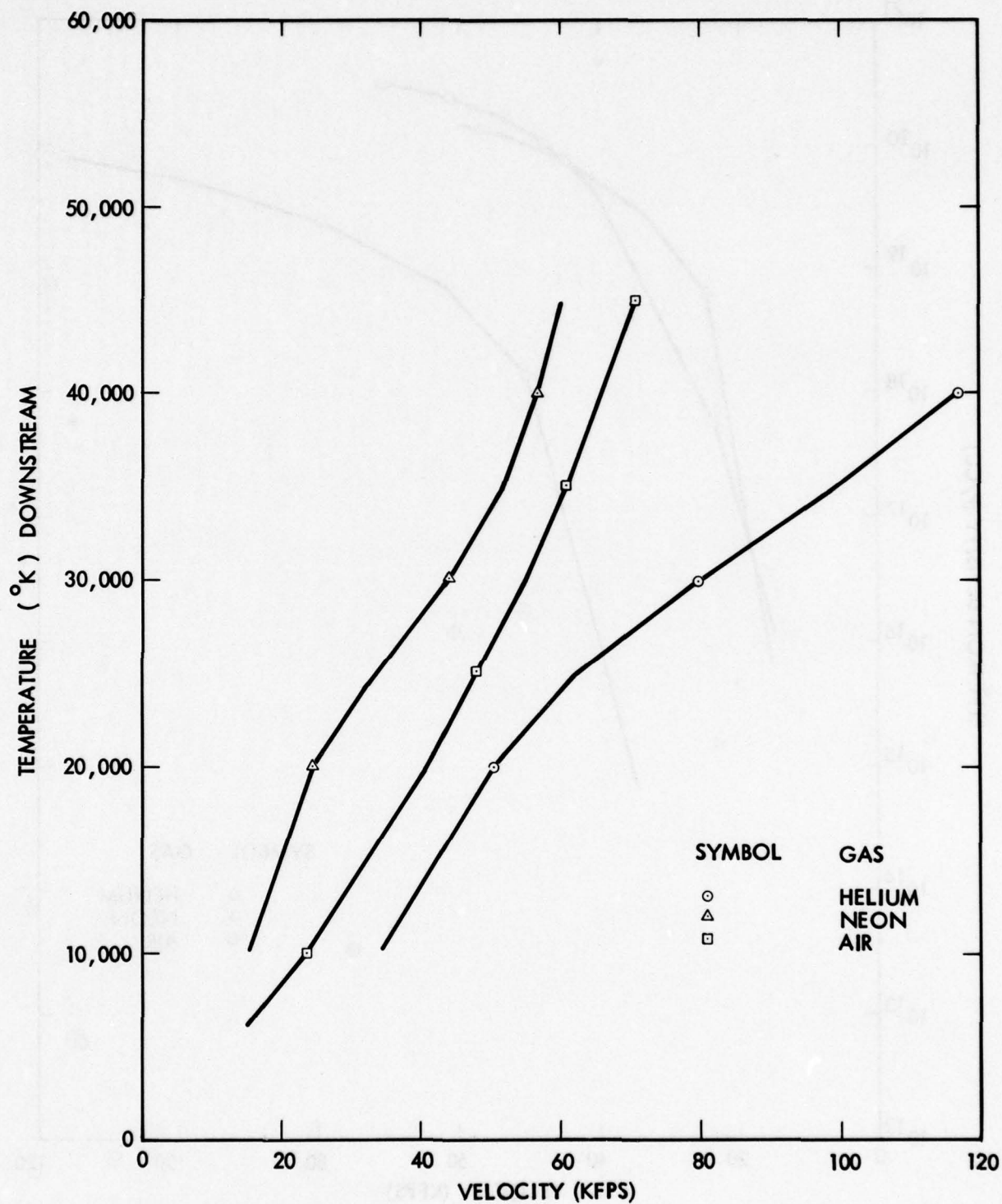


Figure 3-2. Downstream Temperature for Moving Normal Shock Upstream
Temperature = 300 °K, Upstream Pressure = 1 Atmosphere

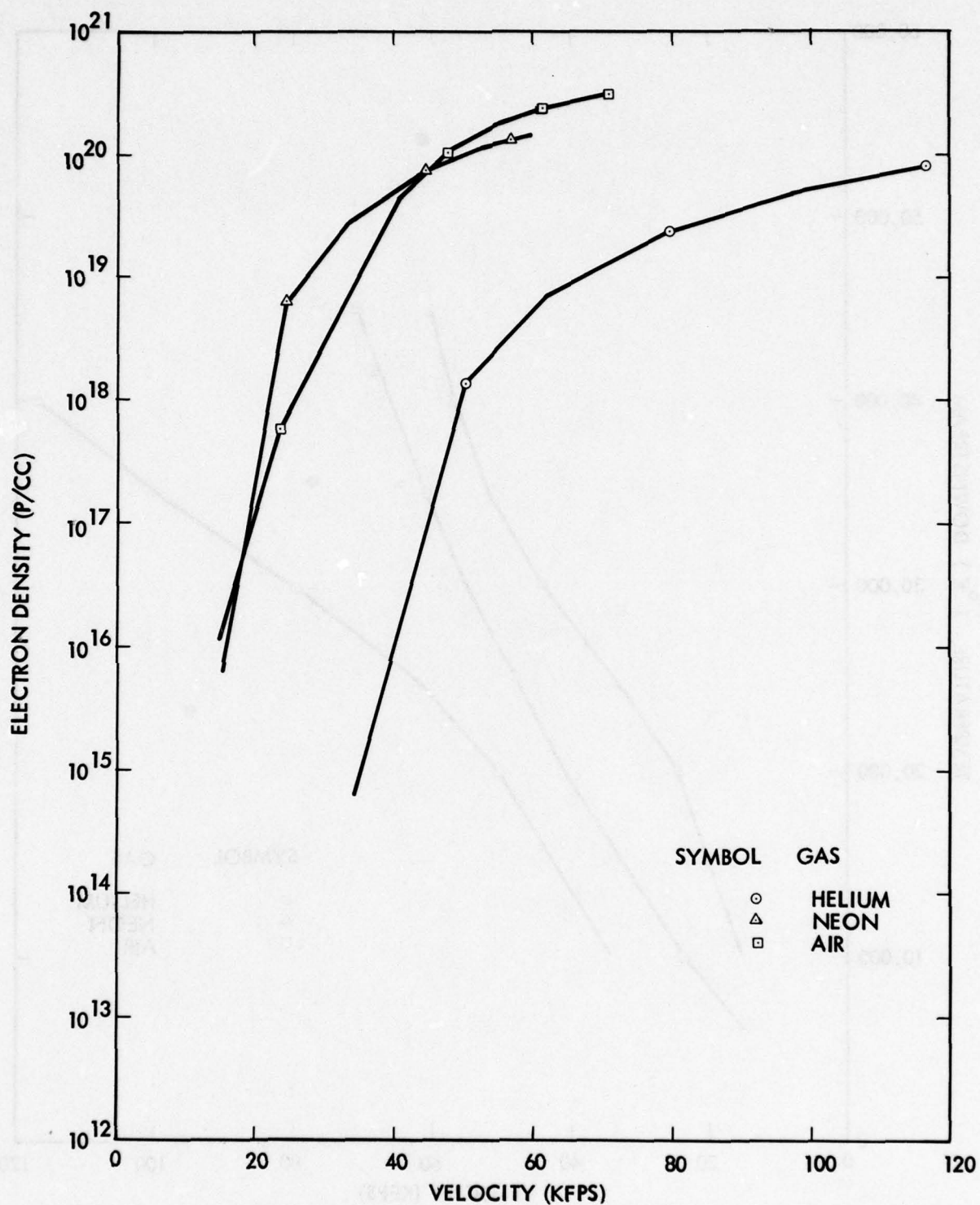


Figure 3-3. Downstream Electron Density for Moving Normal Shock; Upstream Temperature = 300 °K, Upstream Pressure = 1 Atmosphere

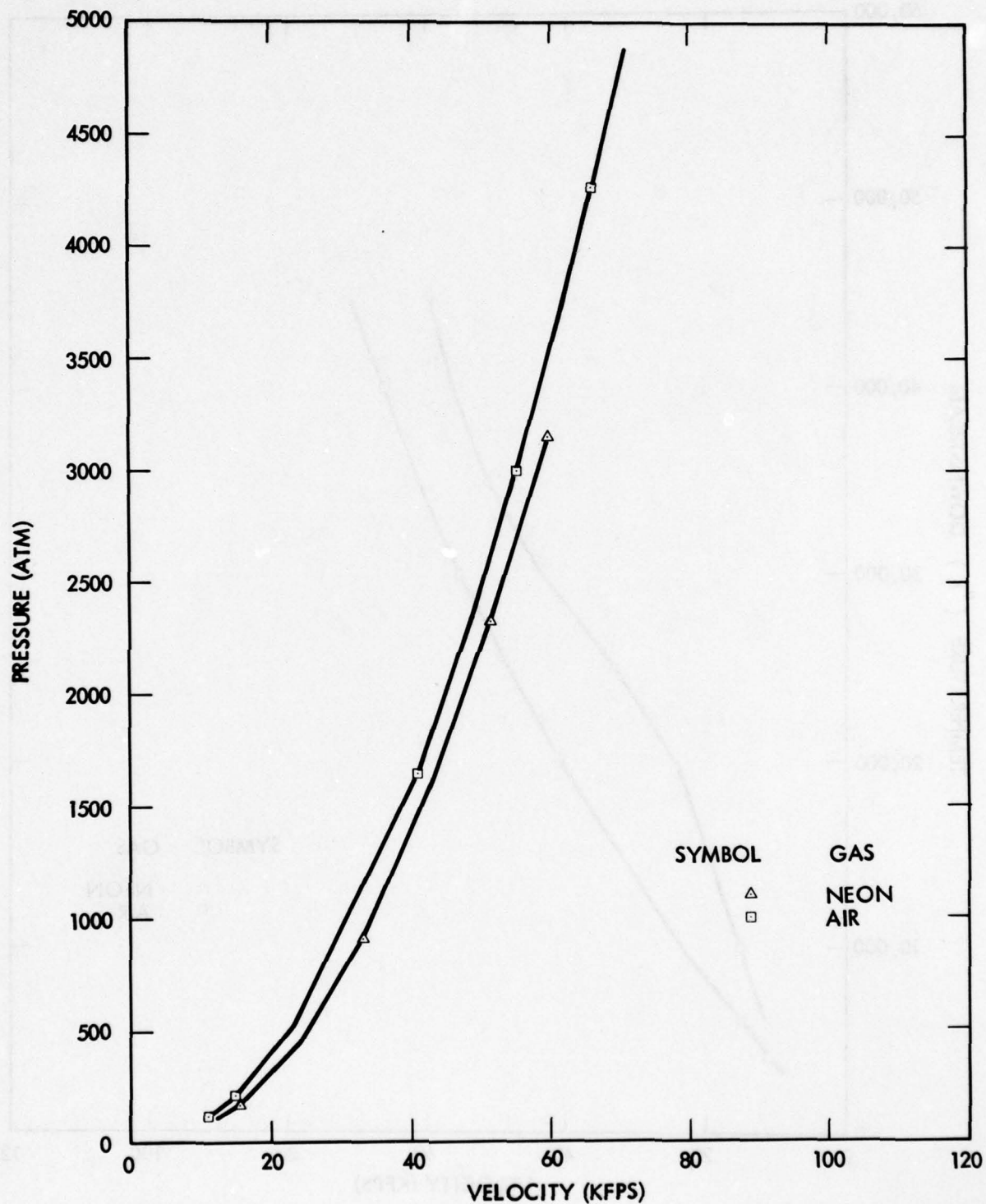


Figure 3-4 Downstream Pressure for Moving Normal Shock Upstream
Temperature = 300 °K for Air; 232 °K for Neon, Upstream Pressure = 1 Atmosphere

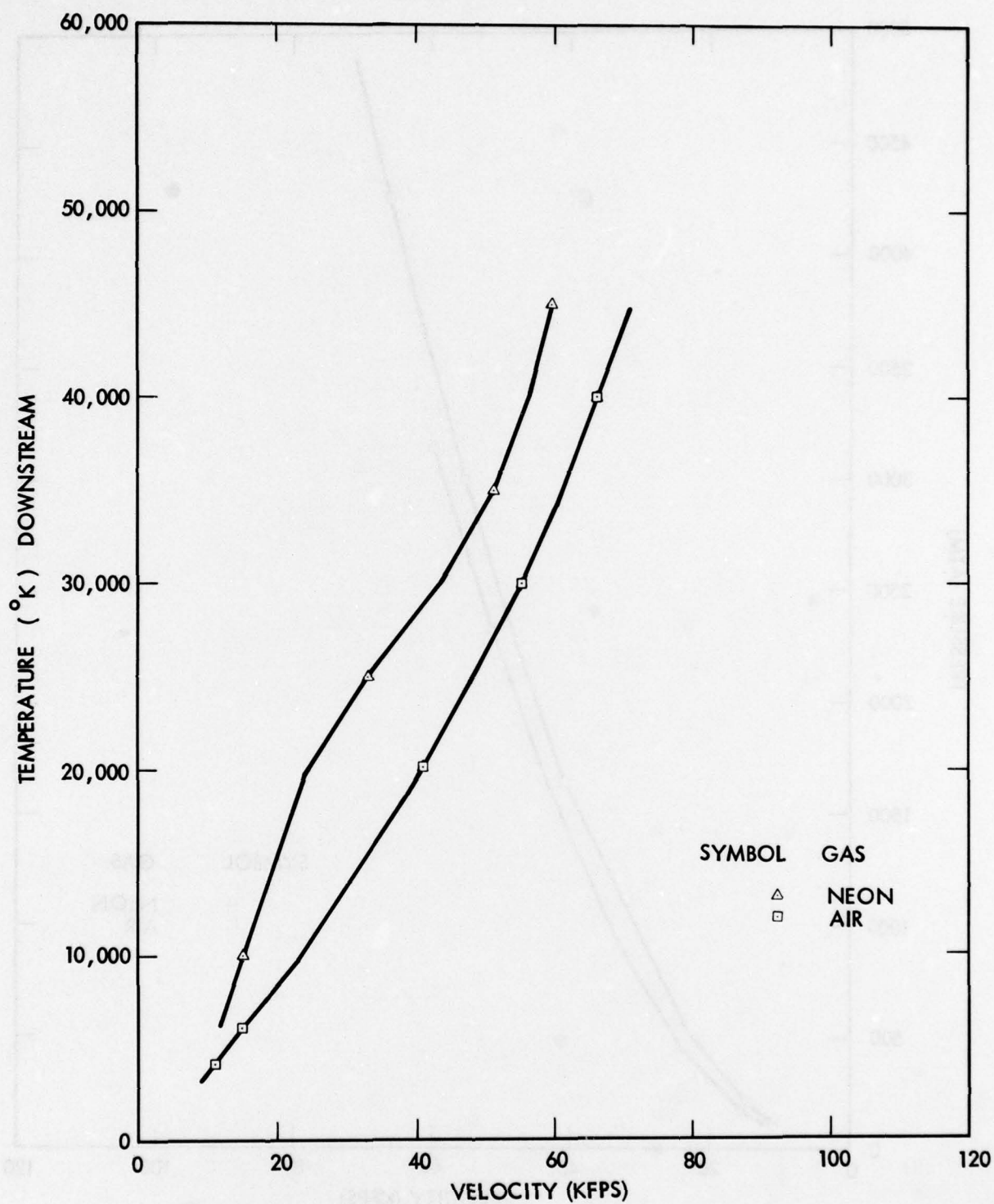


Figure 3-5. Downstream Temperature for Moving Normal Shock Upstream
Temperature = 300 °K for Air; 232 °K for Neon, Upstream Pressure = 1 Atmosphere

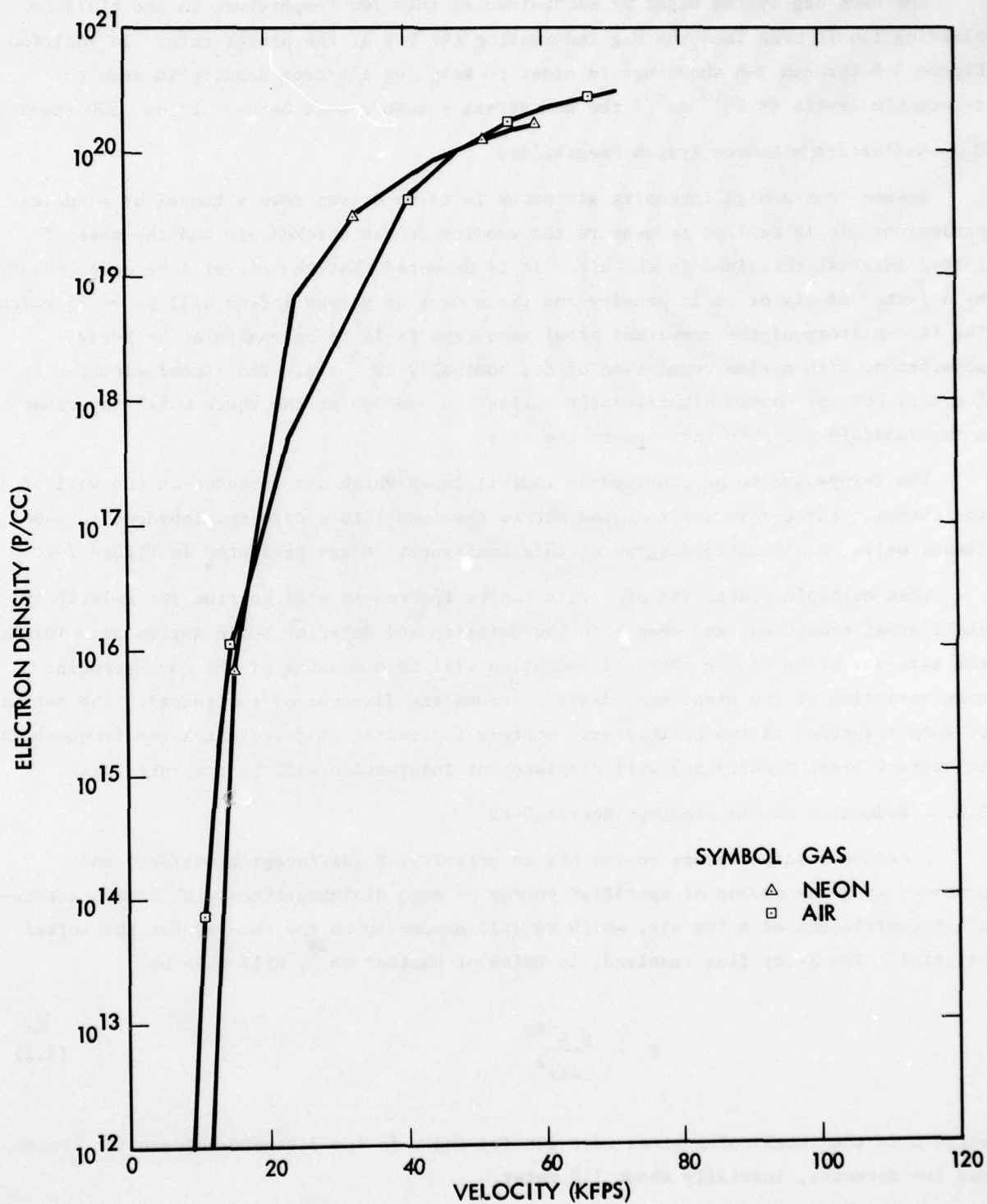


Figure 3-6. Downstream Electron Density for Moving Normal Shock Upstream Temperature = 300 °K for Air; 232 °K for Neon, Upstream Pressure = 1 Atmosphere

The neon bag system might be maintained at this low temperature in the field by bleeding liquid neon into the bag and venting the bag at the proper rate. In addition Figure 3-4 through 3-6 show that in order to keep the electron density in neon to reasonable levels ($< 10^{18} \text{ cm}^{-3}$) the downstream pressure must be kept below 500 atmospheres.

3.2 Radioisotope Source System Feasibility

Assume that a high intensity air shock is to be driven down a tunnel by a nuclear explosion. It is desired to measure the density of the shocked air and the mass of lofted material entrained in the air. It is expected that the air will be compressed by a factor of six or so in density and the amount of matter lofted will be $\sim .25 \text{ gm/cm}^3$. The time history of the resultant areal mass density is to be monitored by X-ray absorption, with a time resolution of Δt , nominally 10^{-5} sec . The tunnel diameter is 1 meter, but may change significantly during the passage of the shock which may cause a thousandfold pressure increase in the air.

The X-rays are to be provided by radioisotopes which are embedded in the wall of the tunnel. The X-rays are radiated across the tunnel to a detector imbedded in the tunnel wall. A schematic diagram of this configuration was presented in Figure 2-2.

When multiple scattering of X-rays can be ignored as will be true for relatively small areal densities, and when both the emission and detector solid angles are minimized, the time variation of the received radiation will be a measure of the corresponding time variation of the areal mass density across the diameter of the tunnel. The method of data reduction of two or more such systems (operating at different X-ray frequencies) to extract areal density and wall displacement information will be presented next.

3.2.1 Reduction of Radioisotope Source Data

Assume a radioisotope source has an activity, S (disintegrations/sec) and produces an X-ray photon of specified energy on each disintegration with a mass attenuation coefficient of β for air, which we will assume to be the same as for the lofted material. The X-ray flux received, in units of photons cm^{-2} , will then be

$$F = \frac{S e^{-\beta \mu}}{4\pi r^2} \quad (3.1)$$

where μ is the intervening areal mass density and r is the distance between the source and the detector, initially about 1.0 meter.

If r can be assumed to be constant, then monitoring the flux, F , will produce a record of $\beta \mu$ which can be solved for μ . If r cannot be taken as constant, then other

measurements have to be made. One method explored here is to use another but different radioisotope source with a different β , and make simultaneous measurements of the two fluxes with two different detectors. Equation (3.1) is rewritten for two fluxes as follows:

$$F_1 = \frac{S_1 e^{-\beta_1 \mu}}{4\pi r^2} \quad (3.2)$$

$$F_2 = \frac{S_2 e^{-\beta_2 \mu}}{4\pi r^2}$$

Then simple algebraic manipulation produces

$$\mu = -\frac{1}{(\beta_1 - \beta_2)} \ln \left[\left(\frac{F_1}{F_2} \right) \left(\frac{S_2}{S_1} \right) \right] \quad (3.3)$$

If the μ value computed from equation (3.3) is inserted into either of the equations of (3.2), then r can be solved for.

Now, F is not the quantity measured directly but N , the total number of photons received by the detector of area, A , in a time, Δt , where

$$N = FA \Delta t \quad (3.4)$$

Rewriting equation (3.3) in terms of N_1 and N_2 , it follows that:

$$\mu = -\frac{1}{(\beta_1 - \beta_2)} \ln \left[\left(\frac{N_1 A_2}{N_2 A_1} \right) (S_2/S_1) \right] \quad (3.5)$$

To assess the feasibility of this concept a estimate of the random error inherent in the method must be established. During a small time interval, Δt , the photon count, N , will fluctuate by ΔN . This happens because of the statistical nature of the disintegration and the absorption process. Due to such fluctuations, the determination of μ will be in some error. An estimate of this error now is made in general terms and subsequently, particularized to the case of two specific radioisotopes of chosen strength.

The assumption is made that Poisson statistics applies for the realization of a given value of N . Under these circumstances, the proper procedure to determine the errors in μ is to determine the mean square fluctuation in μ from Equation (3.5), assuming N_1 and N_2 are uncorrelated and obey the proper statistics. The procedure is to differentiate Equation (3.5) and replace derivatives by Δ , which signifies fluctuation.

$$\Delta\mu = - \frac{1}{(\beta_1 - \beta_2)} \left(\frac{\Delta N_1}{N_1} - \frac{\Delta N_2}{N_2} \right) \quad (3.6)$$

Now both sides of Equation (3.6) are squared and an ensemble average performed. Then the premise of ΔN_1 and ΔN_2 being uncorrelated is used to drop cross terms. The result is:

$$\langle (\Delta\mu)^2 \rangle = \frac{1}{(\beta_1 - \beta_2)^2} \left(\frac{\langle (\Delta N_1)^2 \rangle}{N_1^2} + \frac{\langle (\Delta N_2)^2 \rangle}{N_2^2} \right) \quad (3.7)$$

Here, the symbol $\langle \quad \rangle$ indicates an ensemble average.

Since Poisson statistics applies, $\langle (\Delta N_1)^2 \rangle = N_1$ and $\langle (\Delta N_2)^2 \rangle = N_2$. Thus:

$$\sqrt{\langle (\Delta\mu)^2 \rangle} = \frac{1}{(\beta_1 - \beta_2)} \sqrt{\frac{1}{N_1} + \frac{1}{N_2}} \quad (3.8)$$

Setting $P \equiv \frac{\sqrt{\langle (\Delta\mu)^2 \rangle}}{\mu}$, the fractional error and employing Equations (3.2), (3.4) and

(3.3), it follows that

$$P = \frac{1}{\mu(\beta_1 - \beta_2)} \sqrt{\frac{4\pi r^2}{\Delta t} \frac{e^{\beta_1 \mu}}{\sqrt{A_1 S_1}}} \sqrt{1 + e^{\mu(\beta_2 - \beta_1)} \left(\frac{S_1 A_1}{S_2 A_2} \right)}. \quad (3.9)$$

It is seen that, P , the fractional error in determining areal density varies as $r/\sqrt{\Delta t}$. Increasing Δt by a factor of 10 will decrease the fractional error by a factor of 3.2. P as a function of μ will have a minimum value when $\beta_1 \mu/2 \approx .6$ (assuming $\beta_1 > \beta_2$). When $[B_1 \mu/2]$ is small, then $P \sim \frac{1}{\beta_1 - \beta_2}$.

Now examine a particular case. Assume as sources 100 Curies each of Cobalt 60 (Co^{60}) and Ytterbium 169 (Yb^{169}) [half-life of 32 days], the first of which produces γ rays of 1 MeV energy and the latter produces mainly 50 KeV X-rays. Also assume $A_1 = A_2 = 10 \text{ cm}^2$ and $\Delta t = 10^{-5} \text{ sec}$. At a distance of 1.0 meter in STP air, these will produce $N_1 = N_2 = 9.4 \times 10^3$ counts on an average during the 10^{-5} sec . For 50 keV photons, $\beta_1 = .20 \text{ cm}^2/\text{gm}$ and for 1 MeV photons, $\beta_2 = .06 \text{ cm}^2/\text{gm}$. Inserting these values into Equation (3.8) and dividing by μ one obtains a fraction error prediction of:

$$P = \frac{0.0736}{\mu} \frac{r}{r_0} e^{0.1\mu} \sqrt{1 + e^{-0.14\mu}}, \quad (3.10)$$

where r_0 is the initial distance assumed to be 1.0 meter. At STP, μ for 1.0 meter of air is $.129 \text{ gm/cm}^2$. Each atmospheric density increment in a one-meter path length increases this quantity by $.129 \text{ gm/cm}^2$. The following table shows the value of P (the fractional error in μ determination) as a function of μ .

Table 3-1.

P , Fractional Error in Areal Mass Determination as Functions of Areal Mass.
(Using 100 Curie Sources of Co^{60} and Yb^{169} with 10 cm^2 Detectors and Time Resolution of 10^{-5} sec .)

$\mu \text{ (gm/cm}^2\text{)}$	$(r_0/r) \cdot P$
.322	.32
.451	.25
.581	.18
.71	.6
.84	.13
.97	.12
1.1	.10
5	.03
10	.022
15	.023
20	.028
25	.036

These errors are uncomfortably large for small values of μ , which occur when the air is only slightly compressed. A μ of .322 corresponds to a density increase of a factor of 2.5 since μ is 0.129 for one meter of air at STP. These errors, as pointed out before, can be reduced by increasing Δt (assuming the time scales of the physical processes allow such reduction). The detector area A can also be increased to decrease P ; however, the counting rate for $A = 10 \text{ cm}^2$ is already 10^8 sec^{-1} which is getting close to saturating the fastest currently available detectors. Errors could also hypothetically be reduced at small μ by employing lower energy X-ray photons than 50 keV and thus augmenting β_1 . For example, an 11 keV photon has $\beta_1 = 4 \text{ cm}^2/\text{gm}$. Using that value in Equation (3.4) gives $P = 0.016$ for a 100 Curie source at $\mu = .322$. This value of P is approximately 1/20 that in Table 3-1. Corresponding to this result, a source of 1/4 Curie at 11 keV will give the same precision as 100 Curies at 50 keV. Unfortunately, radioactive sources with strengths of the magnitude of 1 Curie at this energy are not available. The strongest available source at this energy is a Promethium-147 activated X-ray source with a target of Selenium. The output with one Curie of Pm is ~ 1 millicurie at 11 keV in a width of 1 keV.

Another example is Iodine-125 with half life 60 days and with a .027 KeV photon. At this energy $\beta = .4 \text{ cm}^2/\text{gm}$. and $P = 0.13$ for 100 Curies at $\mu = .32$. This constitutes a reduction in P by a factor of 2.45. The conclusion is that 16.5 Curies of I^{125} will be equivalent to 100 Curies of Yb^{169} .

It would appear at this stage of the analysis that the proper way to design the experiment is to relax the time requirement and use 100 Curies each of Yb^{169} and Co^{60} .

The error in r comes very simply from Equation (1.1) by taking a logarithmic derivative and using N instead of F . Thus,

$$\frac{\Delta N_1}{N_1} = -2 \frac{\Delta r}{r} - \beta_1 \Delta \mu \quad (3.11)$$

Combining Equations (3.6) and (3.4), one obtains

$$-2 \frac{\Delta r}{r} = \frac{\Delta N_1}{N_1} \left(1 - \frac{\beta_1}{\beta_1 - \beta_2}\right) + \frac{\Delta N_2}{N_2} \left(\frac{\beta_1}{\beta_1 - \beta_2}\right), \quad (3.12)$$

Squaring and averaging as before, one obtains:

$$\frac{4\langle(\Delta r)^2\rangle}{r^2} = \frac{1}{N_1} \left(1 - \frac{\beta_1}{\beta_1 - \beta_2}\right)^2 + \frac{1}{N_2} \left[\frac{\beta_1^2}{(\beta_1 - \beta_2)^2}\right], \quad (3.13)$$

or

$$\frac{2\sqrt{\langle(\Delta r)^2\rangle}}{r} = \frac{1}{\beta_1 - \beta_2} \sqrt{\frac{\beta_2^2}{N_1} + \frac{\beta_1^2}{N_2}} = \frac{\beta_1}{\sqrt{N_2}} \left(\frac{1}{\beta_1 - \beta_2}\right) \sqrt{1 + \frac{\beta_2^2 N_2}{\beta_1^2 N_1}}, \quad (3.14)$$

When $\mu = .322 \text{ gm/cm}^2$, $N_1 = 9400 = N_2$, $\beta_1 = .2$, $\beta_2 = .06$ and $[\langle(\Delta r)^2\rangle]^{1/2} \cdot r^{-1} = 0.016$. When $\mu = 20 \text{ gm/cm}^2$, $N_1 = 171.1$, $N_2 = 2823$ and $[\langle(\Delta r)^2\rangle]^{1/2} \cdot r^{-1} = 0.021$. The projected measurements thus are quite accurate over a whole array of areal mass densities.

It appears that the conceptual basis for the radioisotope source experiment is quite sound. A further, engineering systems study should be undertaken to determine if all the engineering problems outlined in the next section can be solved and implemented.

4. SUGGESTED AREAS FOR FURTHER STUDY

For both the methods outlined in this report, there remains the general problem of hardware design to implement these techniques. The proposed equipment must perform well while being subject to extremely hostile environments in and adjacent to the shock tunnel walls. Unless adequately designed, constructed and protected, the measuring devices will be subject to extreme pressure and thermal loads. The required survival time should allow for the complete passage of the shock front boundary, (~ 1 msec).

This section will identify those areas that need further study to insure the success of both the gas bag and radioisotope source methods.

4.1 Study Areas Associated with the Gas Bag and Pyrometer Experiment

4.1.1 Preheating of Downstream Air

Radiation from the shock front will preheat the air in front of the shock. This problem has not been accounted for in the computer program work to date. An effort should be undertaken to incorporate these effects into the computer code to see how the interface matching of temperature is affected.

4.1.2 Demonstration of Interface Matching

A test program should be outlined which would involve the use of TRW's shock tube to demonstrate the feasibility of interface matching using gas bags of cooled neon.

4.1.3 Determination of Optimum "Gas Bag" Material

It previously has been stated that the bag material almost certainly will vaporize upon contact with the propagating shock front. It is expected that the volume of neon gas should remain virtually intact until after the passage of the shock front. Further study is required to determine the time between evaporation of the bag material and the passage of the shock front. The effects of precursor radiation on bag survival should be examined.

4.1.4 Chemical Interaction of Vaporized Gas Bag and Air Shock Front

The atomic, molecular and ionic constituents resulting from the evaporation of the thin bag material will certainly participate to some extent in the radiative and chemical processes. Computer studies should be conducted to determine what side effects this may produce in trying to make pyrometer temperature measurements.

4.2 Study Areas Associated with the Radioisotope Source Experiment

4.2.1 Determination of Fraction of Lofted Material Entrained in the Air

The attenuation coefficient β is virtually the same for air and for SiO_2 at the X-ray photon energy of 1 MeV. At 50 KeV, however, the attenuation coefficient for SiO_2 is approximately 50% greater than that of air. Yb^{169} emits seven different specific energy X-ray photons, ranging from 50 to 308 KeV. It is thus conceivable that by using two different detectors to receive the Yb^{169} radiation, one with an aluminum filter, that the relative proportions of air and of SiO_2 could be determined. It is suggested that the feasibility and predicted precision of such a determination be investigated. Table 4-1, derived from data given in Reference [6] is presented below:

Table 4-1. Photon Emissions From Yb^{169} with Associated Absorption Coefficients* of Si, N_2 or O_2 and Al

Photon Emissions		β Si	$\beta (\text{N}_2 \text{ or } \text{O}_2)$	β Al
$\frac{-\dagger}{n}$	KeV	cm^2/gm	cm^2/gm	cm^2/gm
1.85	50	.426	.196	.368
0.45	63	.314	.18	.27
0.18	110	.18	.15	.17
0.11	131	.17	.14	.16
0.22	177	.14	.13	.14
0.35	198	.128	.12	.12
0.10	308	.108	.10	.10

*The absorption coefficients at 131 and 177 were crudely estimated from logarithmic plots in Reference 1.

\dagger number of photons emitted per disintegration

4.2.2 Selection of Detector Study

The X-ray and γ -ray detectors will have to count at a rate of $\sim 10^8 \text{ sec}^{-1}$. This rate will saturate normal NaI detectors. A plastic solution scintillator seems to have short enough decay times, but a program to research and test various detector/scintillator systems should be initiated.

4.2.3 Design Study to Narrow the Emittance and Acceptance Solid Angles

Areal densities can be computed simply only if the X-ray propagates in a narrow beam from the radioisotope source to the detector. To assure this baffles will have to be designed and incorporated into the mounting of the sources and detectors. Here a design study program would be needed.

4.2.4 Study of Source and Detector Survivability

The radioisotope sources and detectors will be subject to radiant and convective heating by the shock ionized air. Air heated to 12,000 °K (1 eV) will radiate 2 to $8 \cdot 10^4$ cal/cm² sec to the isotope source. A protective shield of aluminum 0.1 cm thick absorbing this much heat input will be vaporized in less than 10^{-3} sec. However, with a reflectivity of 90%, it will reach a temperature of only 293 °C in 1.28×10^{-3} sec. Thus, reflective sheets of aluminum (perhaps gold plated) seem adequate protection against radiative heat transfer from shock heated air. Estimates of convective heat transfer will also have to be made for survivability computations. The radioisotope source and X-ray detector will have to be constructed and mounted so they are not crushed or disintegrated by an overpressure of 1000 atmospheres. Tests should be conducted to varify the design at these extreme temperature and pressure levels.

BIBLIOGRAPHY

- [1] Crowley, B. K. et al., An Analysis of Marvel - A Nuclear Shock Tube Experiment, J. Geophysical Research, Vol. 76, No. 14, May, 1971.
- [2] Crowley, B. K. and Glenn, H. D., The Marvel Experiment, Nuclear Technology, Vol. II, July, 1971.
- [3] Glenn, H. D. and Crowley, B. K., Marvel-Nuclear Driven Shock Tube Experiment, J. Applied Physics, Vol. 41, No. 2, February, 1970.
- [4] Horton, T. E. and Menard, W. A., A Program for Computing Shock Tube Gas Dynamic Properties, JPL TR 32-1350, January, 1969.
- [5] Rudinger, G., Wave Diagrams for Non-Steady Flow in Ducts, Van Nostrand Co., Inc., Princeton, N.J., 1955.
- [6] McMester, W. H., et al., Compilations of X-ray Cross Sections, University of California, Lawrence Radiation Laboratory, UCRL-50174, Sec. II, Rev. 1, May, 1969.

DISTRIBUTION LIST

DEPARTMENT OF DEFENSE

Director
Defense Advanced Research Project Agency
ATTN: Technical Library
ATTN: STO
ATTN: NMRO
ATTN: PMO

Defense Documentation Center
Cameron Station
12 cy ATTN: TC

Director
Defense Nuclear Agency
ATTN: DDST
2 cy ATTN: SPSS
3 cy ATTN: TITL
ATTN: TISI
ATTN: SPAS
ATTN: SPTD

Commander, Field Command, DNA
ATTN: FCTMOF
ATTN: FCPR
ATTN: FCT

Chief,
Livermore Division, Field Command, DNA
Lawrence Livermore Laboratory
ATTN: FCPRL

Under Secretary of Defense for Rsch. & Engrg.
Department of Defense
ATTN: S&SS(OS)

DEPARTMENT OF THE ARMY

Deputy Chief of Staff for Rsch., Dev. & Acq.
ATTN: Technical Library

Commander
Harry Diamond Laboratories
ATTN: DELHD-NP
ATTN: DELHD-TI
ATTN: DELHD-RBH

Director
U.S. Army Ballistic Research Laboratories
ATTN: Tech. Library, Edward Baicy
2 cy ATTN: DRDAR-BLE, J. H. Keefer

Director
U.S. Army Eng. Waterways Experiment Station
ATTN: Leo Ingram
ATTN: Tech. Library
ATTN: Francis Hanes

Commander
U.S. Army Materiel Dev. & Readiness Command
ATTN: Commander

DEPARTMENT OF THE NAVY

Chief of Naval Research
ATTN: Tech. Library

Officer-in-Charge
Civil Engineering Laboratory
ATTN: Tech. Library
ATTN: W. Shaw

Commander
Naval Facilities Engineering Command
ATTN: Tech. Library

Commander
Naval Surface Weapons Center
ATTN: WX 21, Tech. Library
ATTN: Code 241, J. Petes
ATTN: WA 501, Navy Nuc. Prgrms. Off.

DEPARTMENT OF THE AIR FORCE

AF Institute of Technology, AU
ATTN: Library, AFIT, Bldg. 640, Area B

AF Weapons Laboratory, AFSC
ATTN: SUL
ATTN: DES, Ma. A. Plamondon
ATTN: DED
ATTN: DED, J. D. Renick
5 cy ATTN: S. J. Ayala

Hq, USAF/IN
ATTN: INATA

SAMSO/MN
ATTN: MNNR
ATTN: MNNH

SAMSO/DY
ATTN: DYS

SAMSO/RS
ATTN: RSSE
ATTN: RSS

DEPARTMENT OF ENERGY

Sandia Laboratories
Livermore Laboratory
ATTN: Doc. Con. for Tech. Library

Sandia Laboratories
ATTN: Doc. Con. for Luke J. Vortman
ATTN: Doc. Con. for A. J. Chabai
ATTN: Doc. Con. for 3141, Sandia Rpt. Coll.

Department of Energy
Albuquerque Operations Office
ATTN: Doc. Con. for Tech Library

DEPARTMENT OF ENERGY (Continued)

Department of Energy
Division of Headquarters Services
ATTN: Doc. Con. for Class Tech. Library

Department of Energy
Nevada Operations Office
ATTN: Doc. Con. for Tech. Library

University of California
Lawrence Livermore Laboratory
ATTN: Tech. Library

OTHER GOVERNMENT AGENCY

U.S. Department of Commerce
National Bureau of Standards
ATTN: P. S. Lederer

DEPARTMENT OF DEFENSE CONTRACTORS

Agbabian Associates
ATTN: M. Agbabian

Artec Associates, Inc.
ATTN: N. Baum

Civil/Nuclear Systems Corporation
ATTN: Robert Crawford

EG&G, Incorporated
ATTN: Tech. Library

Electromechanical Systems of New Mexico
ATTN: R. A. Shunk

General Electric Company
TEMPO-Center for Advanced Studies
ATTN: DASIAC

H-Tech Laboratories
ATTN: Bruce Hartenbaum

Kaman Sciences Corporation
ATTN: Don Sachs
ATTN: Library

DEPARTMENT OF DEFENSE CONTRACTORS (Continued)

Merritt Cases, Incorporated
ATTN: J. L. Merritt
ATTN: Technical Library

Nathan M. Newmark
Consulting Engineering Services
ATTN: Nathan M. Newmark

Physics International Company
ATTN: Doc. Con. for Coye Vincent
ATTN: Doc. Con. for Tech. Library

R & D Associates
ATTN: Tech. Library
ATTN: J. G. Lewis

SRI International
ATTN: George R. Abrahamson
ATTN: P. De Carli
ATTN: D. Keough

Systems, Science & Software, Incorporated
ATTN: Tech. Library
2 cy ATTN: Donald R. Grine

TRW Defense & Space Systems Group
ATTN: R. Doll
ATTN: L. Glatt
ATTN: P. Lieberman
ATTN: P. Molmud
ATTN: S. Pollack
ATTN: Tech. Info. Center, S-1930
3 cy ATTN: Paul Lieberman

The Eric H. Wang
Civil Engineering Research Facility
ATTN: Neal Baum
ATTN: Steve Packett